Performance Evaluation of Countermeasures Against Rupture and Protrusion of Vertically Prestressing Steel Bars in PC Girders

(PC桁の鉛直締めPC鋼棒に対する破断突出対策の性能評価)

by

Addisu Desalegne Bonger

A dissertation submitted to
Graduate School of Urban Innovation
Yokohama National University
in partial fulfillment of the requirements for the degree of
Doctor of Philosophy in Engineering

Supervised by
Akira Hosoda
Professor, Graduate School of Urban Innovation

Yokohama National University
Yokohama, Japan

August 2022

Yokohama National University, Japan

Graduate School of Urban Innovation

This thesis, written by Addisu Desalegne Bonger has been accepted by his advisor and thesis committee members. And, it is presented to Graduate School of Urban Innovation, Yokohama National University, Japan in partial fulfilment of the requirement for the degree of Doctor of Philosophy in Engineering.

Committee members:

Prof. Akira Hosoda, chair and academic supervisor

Graduate School of Urban Innovation, Yokohama National University, Japan

Prof. Koichi Maekawa, member

Graduate School of Urban Innovation, Yokohama National University, Japan

Prof. Hamed Salem, member

Structural Engineering Department, Cairo University, Egypt

Prof. Kimitoshi Hayano, member

Graduate School of Urban Innovation, Yokohama National University, Japan

Assoc. Prof. Chikako Fujiyama, member

Graduate School of Urban Innovation, Yokohama National University, Japan

ACKNOWLEDGMENTS

Firstly, I would like to express gratitude and sincere appreciation to my academic advisor Professor Akira Hosoda, Graduate School of Urban Innovation, Yokohama National University, Japan, for his comprehensive advice and suggestions, guidelines, kindly support and encouragement in this study.

The author is equally grateful to Professor Hamed Salem, Structural Engineering Department, Cairo University, Egypt, for his consistent guidance and painstaking efforts to support the author in mastering the process of numerical modeling and analysis in the Applied Element Method.

The author is grateful to Professor Koichi Maekawa and Associate Professor Chikako Fujiyama, Graduate School of Urban Innovation, Yokohama National University, Japan, for their valuable contributions and constructive comments in the Concrete Laboratory and during the research seminar discussions.

I would like to acknowledge Yokohama National University, Japan and Graduate School of Urban Innovation for granting me opportunity to pursue my doctoral studies with MEXT scholarship. I want to thank Ministry of Education, Culture, Sports, Science and Technology (Japan) for proving me scholarship to support my studies and stay in Japan.

The author extends his gratitude to Metropolitan Expressway Company, Japan for providing experimental data in this study.

The author's appreciation also goes to friends, colleagues, IMP staffs, every member of Concrete Laboratory of Yokohama National University for their kind co-operation in daily life in Japan, kindness and friendship made me precious memory in Japan.

I deeply express gratitude to my parents and my family, for their love, prayers and encouragement throughout my life.

Above all, thanks to Almighty God for his graciousness and unlimited kindness.

CONTENTS

LIST OF FIGURES

LIST OF TABLES

ABSTRACT

In Japan, some existing pre-stressed concrete bridges which were constructed in around 1970 have grout filling shortage and infiltration of water problems. Corrosion is seen as a main cause of rupture of PC bars which have been reported several times in the country. Corrosion due to insufficient grout filling can result in sudden fracture of PC bars. When a vertically prestressing steel bar in PC girders is ruptured, all the accumulated strain energy is suddenly released. The ruptured PC bar will severely damage cover concrete and asphalt pavement, and PC bars may protrude out of the structure, which may cause severe accidents. Protective measures against eruption of PC bars are necessary to avoid damage to third party.

In 2018 there were 19,657 vertically prestressing steel bars in Metropolitan Expressway (MEX) in Japan. In the same year, actual rupture of a vertically prestressing steel bar in PC girder was investigated by the authors. It was concluded that the rupture of the bar was brittle and initiated from corrosion pits, which must have been caused by cyclic drying and wetting due to the ingress of rainy water.

The principal objectives of the present research are (a) to verify the Applied Element Method (AEM) simulations by experimental results, (b) to evaluate the performance of countermeasures against rupture and protrusion of prestressing steel bars in PC girders using the AEM simulations, (c) to investigate the failure modes in the countermeasures using the AEM simulations and (d) to propose a risk management of protrusion of vertically prestressing steel bars in PC girders in MEX.

Methodology of the present research involves establishing the Applied Element Method (AEM) numerical simulation due to its advantages of simulating structural progressive collapse. The methodology follows defining material properties in the AEM simulations based on a static compression test, tension test and pull-off adhesion test. Tension softening of the materials defined in the AEM simulation using a sensitivity analysis based on a bending test. A drop-weight impact AEM simulation was used to understand the energy dissipation behavior of the materials (polyurea and steel fiber reinforced polymer cement mortar). In this study, the AEM numerical simulations were verified with the experimental results. In the process of verification, many influential parameters, such as the effects of contact stiffness between separated elements, fracture energy of concrete and asphalt pavement, mesh sensitivity, time interval sensitivity, material properties, temperature effect, and strain rate effect were investigated.

The impact energies were applied on the countermeasures either using a ruptured PC bar or using a drop weight impact test. Performance of asphalt pavements was evaluated using extreme impact energy, 4,408 J, that can cover most of rupture of vertically prestressing steel bars in MEX. Performance of asphalt pavements was also evaluated by considering low and high temperatures to simulate winter and summer conditions in Tokyo area. The effect of time dependent deterioration of asphalt pavement by reducing the thickness of asphalt pavement was also investigated. Energy absorption capacity of

polyurea and steel fiber reinforced polymer cement mortar (PCM) was investigated using a drop weight impact test.

The effect of 15 mm cover concrete (assuming bottom of a bridge girder) on preventing protrusion of PC bar was investigated. Numerical simulation of rupture and protrusion of PC bar was conducted using the Applied Element Method. The numerical simulation was verified using the experimental result. In the process of verification, many influential parameters, such as the effects of contact stiffness between elements, fracture energy of concrete, mesh sensitivity, time interval sensitivity, material properties, and strain rate effect, were investigated. The numerical simulation was required to investigate the protrusion behavior of PC bar and the failure mechanism of cover concrete. The AEM simulation results support, appropriate numerical simulation with the AEM can be conducted with appropriate interface material property between the PC bar and the sheath, considering the fracture energy of concrete, with appropriate mesh discretization, appropriate time interval, appropriate Normal Contact Stiffness Factor (*NF*), and considering strain rate effects in concrete. Cover concrete of 15 mm alone could not prevent the protrusion of a PC bar of 4.5 m rupture length.

A 3D AEM model was developed for simulating two layesrs of asphalt pavements at 0°C, 28°C and 50°C under extreme impact energy (4,408 J) generated from a ruptured prestressing steel bar. The asphalt pavement material models were calibrated using asphalt pavement bending test results. The bending properties of asphalt pavement at different temperature were numerically investigated. Interface bond material models were calibrated based on a pull-off adhesive test. The effects of temperature on asphalt pavement system on preventing the protrusion of PC bars and concrete spalling were numerically investigated. The *DIF* was employed to accurately capture the dynamic material behavior of the asphalt pavement under high loading rate. The failure mode of the asphalt pavement under 4,408 J impact energy was numerically investigated in detail. In MEX, the asphalt pavement over bridge deck has two layers. In this study, in order to simulate the worst condition in reality (time dependent deterioration, etc.), in one specimen, the cover layer was excluded and only the base layer (50 mm thickness) was investigated in terms of its performance in preventing protrusion the PC bar with 4,408 J impact energy at 20°C.

This study found that appropriate AEM simulation of rupture and protrusion of PC bar with asphalt pavement can be conducted with appropriate interface material property between the slab concrete and the asphalt pavement layers, considering the fracture energy of concrete and asphalt pavement, with appropriate mesh discretization, appropriate time interval, appropriate Normal Contact Stiffness Factor (*NF*), and considering strain rate effects both in concrete and in asphalt pavement. The asphalt pavement system used in this study, without using a steel plate and FRP sheet, with appropriate material and thickness could prevent the protrusion of the PC bar of 4.5 m rupture length. The AEM simulation results proved that the two layers of asphalt pavement with 80 mm thick at 0°C, 28°C and 50°C was effective against 4,408 J impact energy and effective against PC bar protrusion and concrete spalling.

Moreover, a single layer of guss asphalt pavement with 50 mm thick at 20°C was effective against PC bar protrusion which was around 22 mm in the AEM simulation. However, asphalt pavement fracture was observed near the anchorage area. Based on the analysis results, the effectiveness of the asphalt pavement system depends on impact energy of ruptured PC bars, material properties of asphalt pavements, material properties of interface bond materials, fracture energy, mesh discretization, strain rate and temperature.

The filure mode in the asphalt pavement at 0°C, 28°C and 50°C under 4,408 J impact energy was investigated in detail. In the two layers of asphalt pavement system at 28°C, the PC bar protrusion was prevented by ductile deformation of asphalt pavement delaminated from slab concrete. The strain energy of the PC bar was dissipated by a simultaneous action of asphalt pavement deformation, cone-shaped crack in the mortar, and interface delamination between the slab concrete and the asphalt pavement. In the two layers of asphalt pavement system at 50°C, the strain energy of the PC bar (4,408 J) was dissipated by a synchronized action of a shear-cone shaped fracture in the concrete and in the non-shrinking mortar, deformation and cracks in the asphalt pavement. In the two layers of asphalt pavement system at 0°C, the strain energy of the PC bar (4,408 J) was dissipated by a synchronized action of a shear-cone shaped fracture in the base layer and in the non-shrinking mortar, deformation and cracks in the asphalt pavement and delamination of tack coat. In the single layer (50 mm tick) of guss asphalt pavement system at 20°C, the strain energy of the PC bar (4,408 J) was dissipated by a simultaneous action of a shear-cone shaped fracture in the asphalt pavement and in the non-shrinking mortar, interface bond delamination between the concrete slab and the asphalt pavement, and cracks in the asphalt pavement. The results of the numerical simulation had a good agreement with the experimental data.

Punching tests for polyurea sheet with thickness of 3 mm, 5 mm and 10 mm under different impact loads were investigated. This study numerically investigates the effects of polyurea coating on impact resistance and on preventing concrete spalling. The results obtained are used to assess the extent of energy absorption and to identify the mode of failure of the polyurea as a function of the imposed impact conditions. The numerical simulations were verified with the experiments.

Both numerical simulations and high-speed photography measurements indicated that the polyurea sheet significantly reduced impulsive loads. Effectiveness of the polyurea sheet depends on impact energy, polyurea thickness, bond strength, primer and quality of surface concrete, etc. The constitutive model using a bi-linear material for polyurea in the drop weight AEM simulation showed good agreement with the experimental results in terms of impact resistance and failure mode. A polyurea (500 mm × 500 mm) sheet with 5 mm thickness was effective in resisting against 758 J impact energy. However, 3 mm and 10 mm thick polyurea sheets with 500 mm × 500 mm were not effective in resisting against 758 J and 3,983 J impact energy respectively.

The impact resistance of a steel fiber reinforced polymer cement mortar (PCM) against drop weight impact were investigated numerically and experimentally. Effectiveness of the PCM depended on impact energy, depth of core, material properties of the PCM and boundary conditions. The modeling of PCM in the drop weight AEM simulation showed good agreement with the experimental results in terms failure mode. The drop weight impact energy was dissipated by damages in the PCM, deflection of boundary and strain in the reinforcing bars. Both numerical simulations and high-speed photography indicated that the drop weight impact test were significantly affected by boundary conditions. The proposed boundary condition in this study greatly reduced deflection at the boundary and hence eliminate the energy absorbed by flexure.

Basic information of vertically prestressing steel bars in PC bridges in the Metropolitan Expressway (MEX) including the recent situations and onsite inspection of rupture of vertically prestressing steel bar was discussed briefly. The strategy for risk assessment of rupture and protrusion of vertically prestressing steel bar in PC brige was also addressed in detail. Moreover, risk reduction (control) interventions were explained.

CHAPTER 1

INTRODUCTION

1.1 General

Vertical PC tendons have been used primarily to enhance the shear capacity in a bridge superstructure [1]. They are used in main girder web, diaphragm, middle crossbeam, central hinge part, pier head, etc. PC bridges in which cracking is mitigated by prestress, are generally considered to be highly durable [2]. However, several problems associated with bonded post-tensioned construction occur as a result of inadequate grout injection or poor-quality grout [3]. When a vertically tightened PC bar is ruptured, all the strain energy in the PC bar is released instantly, which can damage cover concrete and asphalt pavement [4]. The instant rupture of prestressing bar sometimes results in the protrusion of a torn portion from the bridge, causing a serious public safety hazard from projecting bars and from falling concrete because such fractures can occur with no advance warning [4]. Protrusion of PC bar is very brittle and violent. Protective measure against eruption of PC bar is necessary to avoid damage to third party [5].

Steel plate and aramid FRP sheet were used on the surface of concrete as a countermeasure against protrusion of PC bar [6]. However, using steel plate and aramid fiber as a PC bar protrusion prevention takes a longer construction time, which is not recommended for Metropolitan Expressway (MEX) as the traffic volume is as large as 1,020,000 vehicles/day. Moreover, using steel plate and FRP sheet together with asphalt pavement as a PC bar protrusion prevention for a vertical PC bar is too much conservative as the strain energy of the ruptured vertical PC bar is smaller than that of rupture of horizontal PC bar.

In this research, a performance evaluation of countermeasures against rupture and protrusion of vertically prestressing steel bars in PC bridges without using a steel plate and aramid fiber is investigated. The countermeasures included asphalt pavement, polyurea and steel fiber reinforced polymer cement mortar (PCM). Numerical simulation of rupture and protrusion of PC bars with countermeasures are conducted using the Applied Element Method (AEM) due to its advantages of simulating structural progressive collapse [7].

The numerical simulation tool developed in this study is utilized for evaluating the effectiveness of countermeasures considering several practical scenarios that cannot be fully covered by experimental investigations. The numerical simulations developed in this study played a vital role in predicting experimental results. Experimental results are used for validation of numerical investigations. In the process of verification, many influential parameters, such as the effects of contact stiffness between separated elements, fracture energy of concrete, mesh sensitivity, time interval sensitivity, material properties, temperature effect, and strain rate effect are investigated.

1.2 Background of the Study

In April 2017, Metropolitan Expressway (MEX) in Japan had a total length of about 318.9 km in the Greater Tokyo Area (Fig 1.1). Routes which have been open for 30 years or more comprise about 54.3% of the total length (Fig 1.2a). The proportion of MEX occupied by structures such as elevated bridges and tunnels that require detailed maintenance and management is about 95%, which is significantly higher than other roads in other companies (Fig 1.2b). The volume of traffic is as large as 1,000,000 vehicles/day (average, FY 2019). Traffic volume of large-sized vehicles is about five times that of general roads in Tokyo's 23 wards (Fig 1.2c). The structures in MEX are aging under harsh traffic usage.

Fig. 1.1 Road network of Metropolitan Expressway (MEX)

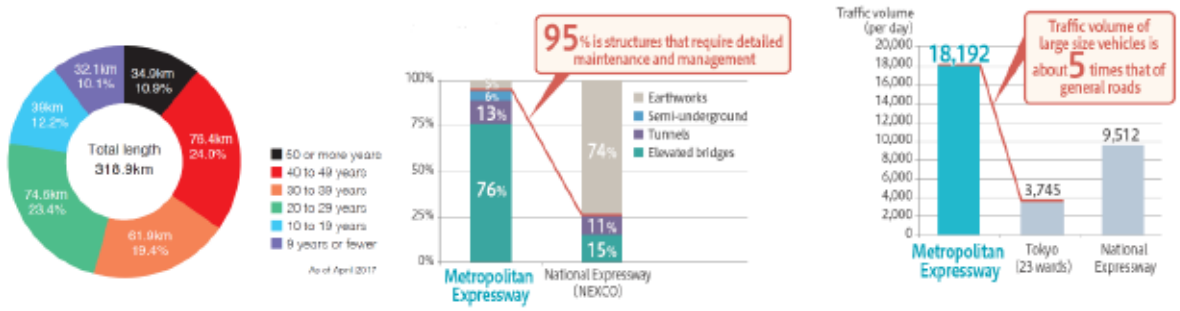

(a) Progressive aging (Percentage of years elapsed since opening)

(b) Proportion occupied by structures

(c) Heavy traffic and severe usage

Fig. 1.2 Metropolitan Expressway's recent status

As per 2018 inventory, there were 19,657 vertical PC bars in MEX as shown in Fig. 1.3a. Fig 1.3b shows the length and diameter of vertical PC bars in MEX. About 93% of the vertical PC bars have a length shorter than 3 m. Out of 11,435 vertical PC bars, counted from design drawings, about 93% have

15 mm to 60 mm concrete cover below a bridge girder and around 33.8% have 20 mm to 25 mm concrete cover above a bridge girder. Out of 19,657 vertical PC bars, 54.4% of them used in main girder web as shown in Table 1.1.

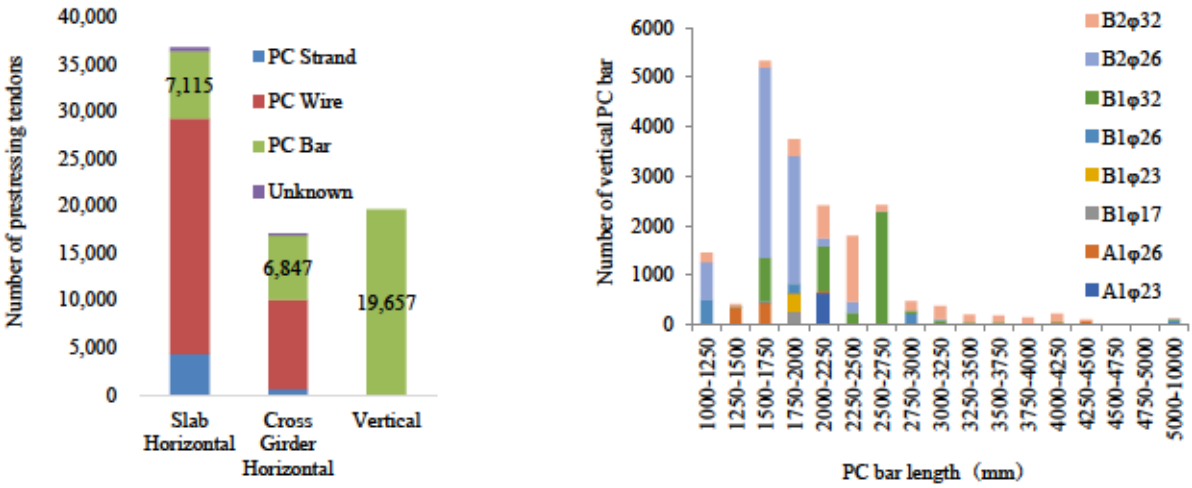

(a) Total number of prestressing tendons

(b) Vertical PC bars by length and diameter

Fig. 1.3 Number of vertical PC bars in MEX (by diameter and length)

Table 1.1 Number of vertical PC bars in Metropolitan Expressway (as per 2018 inventory)

Type of structure	Bridge part	Number of PC bars
I-Girder	Main girder web	1,322
	Notch	625
T-Girder	Notch	66
Box-Girder	Main girder web	9,370
	End transverse beam	1,428
	Notch	3,816
	Center hinge part	656
	Pier head	173
Hollow Slab	Slab	645
	Notch	1,556
Total		**19,657**

1.3 Investigation of Rupture of Vertical PC Bar in Metropolitan Expressway (MEX)

The following actual rupture of vertical PC bar was investigated in MEX in 2018. This vertical PC bar was used in a nine continuous span PC box girder bridge (construction completed in April 1984). Type of PC bar was ordinary PC steel rod B type (diameter 32 mm and length 2,620 mm). Fig. 1.4 shows the situation at the time of damage detection. Based on the digital ultrasonic test, it was guessed

that the PC steel bar ruptured at around the center of the length. After extracting the PC bar from the sheath, it was confirmed that the bar ruptured at 1,345 mm from the bottom side and detailed investigation was carried to study the rupture mechanism [8].

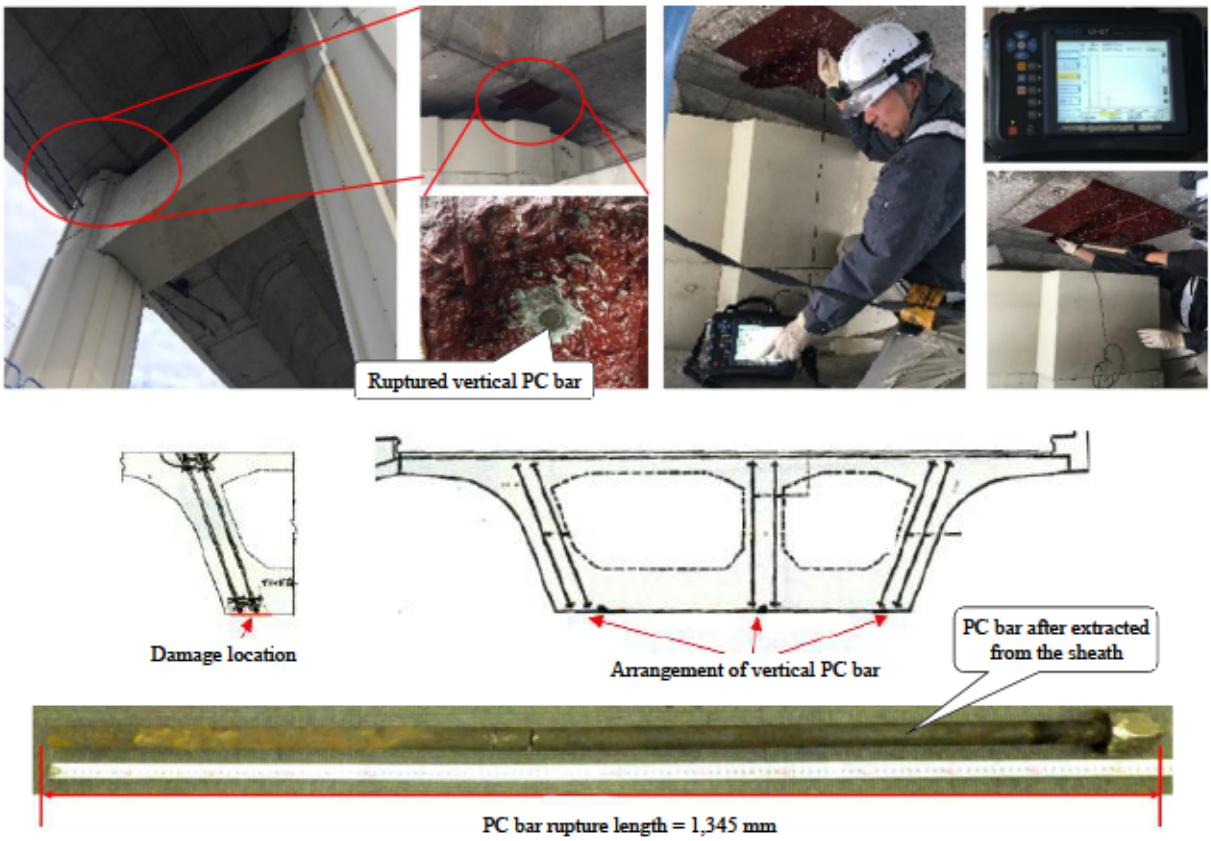

Fig. 1.4 Investigation of rupture of vertical PC bar using digital ultrasonic test

1.3.1 Surface appearance survey

Corrosion products having a thickness of about 2 mm were accumulated near broken portion than the surrounding area as shown in Fig. 1.5.

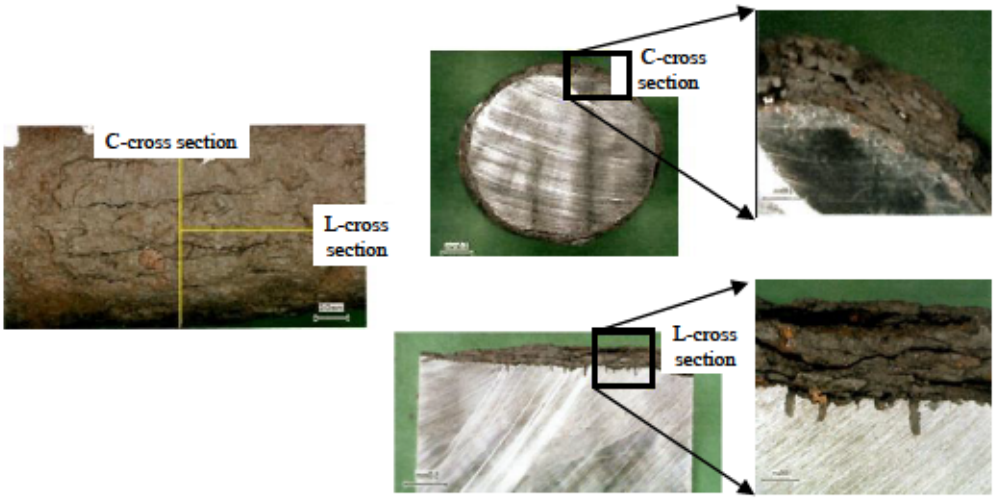

Fig. 1.5 Corrosion appearance near the PC bar fracture

1.3.2 Investigation of corrosion products

The composition of the corrosion product of the fracture surface was investigated using Energy Dispersive line analyser (EDS) attached to Scanning Electron Microscope (SEM). The result indicates almost no contribution of chlorine (CI) to the corrosion as shown in Table 1.2. Iron accounts for around 65% of corrosion product. The cause of corrosion was assumed to be infiltration of rain water.

Table 1.2 Composition corrosion products

Corrosion products	**Fe**	O	Si	Mn	Cr	P	S	**CI**	Na	K	C	Ca
Percentage	**64.8**	27.4	0.2	02	0.2	0.7	0.0	**0.1**	0.0	1.2	4.4	0.3

1.3.3 Investigation of PC bar material properties

a. Steel bar component analysis: The result is shown in Table 1.3. Phosphorus (P) and Sulphur (S) impurity concentration of the PC steel rod satisfied the composition standard of the steel rod.

Table 1.3 Chemical composition of PC steel rod (Unit mass %)

	C	Si	Mn	P	S
Sample survey	0.71	0.70	1.18	0.020	0.011
JIS Standard	-	-	-	≤ 0.030	≤ 0.035

b. Hardness test: hardness distribution with micro-Vickers hardness tester at fracture part and base material as a comparison section (7 mm away from fracture part) was measured. As shown in Fig. 1.6 there is little variation of sectional hardness, at fracture part and comparison section.

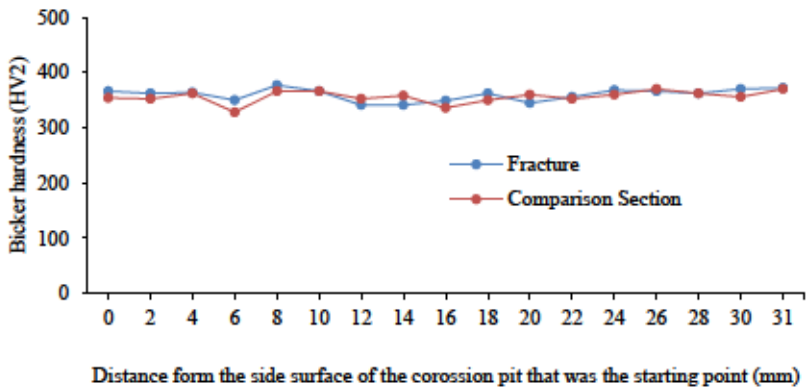

Fig. 1.6 Vickers hardness distribution curve

c. Tension test: Tensile test conducted (according to JIS Z2241) to confirm whether a PC steel rod satisfied specification or not. Then, measured values compared with PC steel bar type B (SBPR

930/1180) as specified in JIS. As shown in Table 1.4, all material characteristics meet the criteria. There was no problem of the PC bar.

Table 1.4 Tensile test results

Specimen	0.2% load	0.2% proof stress	Maximum load	Tensile strength	Elongation at break
	(KN)	(MPa)	(KN)	(MPa)	%
1	160.375	1045	186.938	1212	13.5
JIS2008 SBPR 930/1180	-	≥ 930	-	≥ 1180	≥

1.3.4 Fracture surface analysis

The fractured surface of the PC steel rod was almost perpendicular to the axial direction, and no plastic deformation was observed. The fractured surface was smooth and had no large undulations. It can be seen from Fig.1.7 that there was a stripe pattern radiating from point "a".

Therefore, it can be inferred that the fracture phenomenon of the PC steel bar was caused by the propagation of a brittle crack caused by pitting corrosion at location "a". It is estimated that the crack progressed radially from the densely packed rust area "a" (Fig A). Granular brittle fractures were observed in the macro survey (Fig E and F) and in the micro survey, a fracture surface was seen (photo H and I). "a1" is the starting of corrosion pit and progressed to "a2" ~ "d". It is estimated that the resulting brittle crack propagates and leads to rupture.

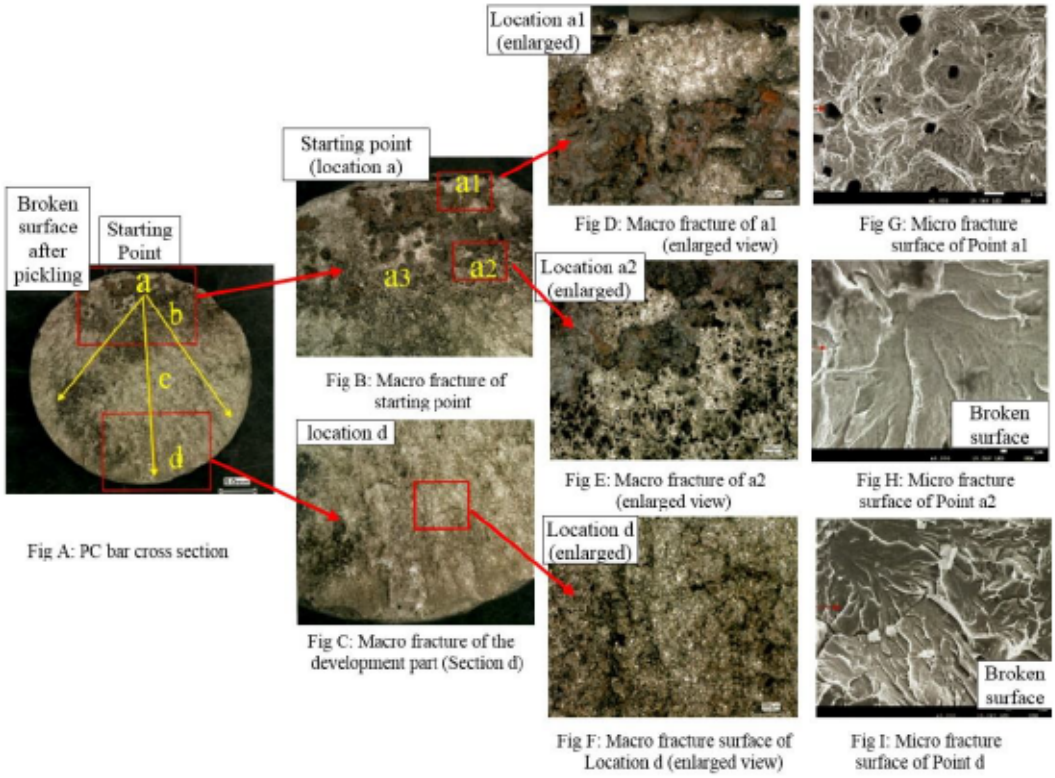

Fig. 1.7 Fracture surface analysis

1.3.5 Investigation near fracture

Many micro cracks were found at the position shown in the schematic diagram (Fig. 1.8), on the surface near the fracture surface in the circumferential direction, with many fractures.

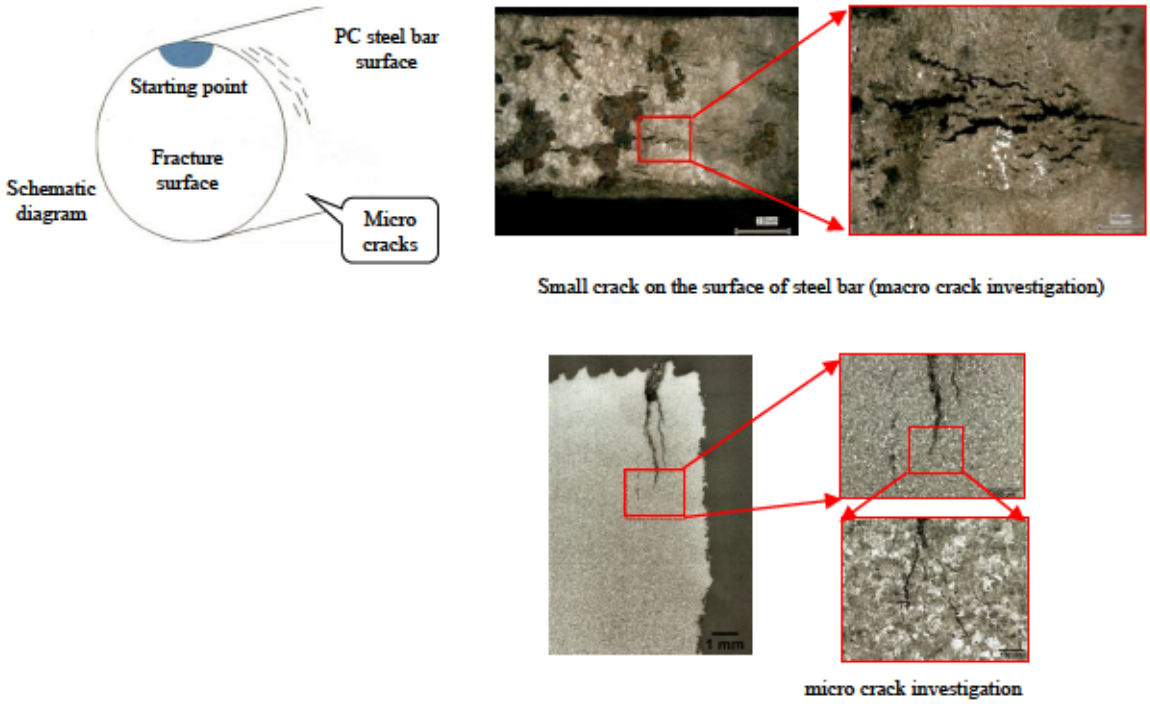

Fig. 1.8 Macro and micro cracks investigation on ruptured vertical PC bar

1.3.6 Overall damage process

From the investigation results above, it was concluded that the rupture of PC steel bar was brittle and initiated from corrosion pits which were caused by cyclic drying and wetting due to the ingress of rainy water.

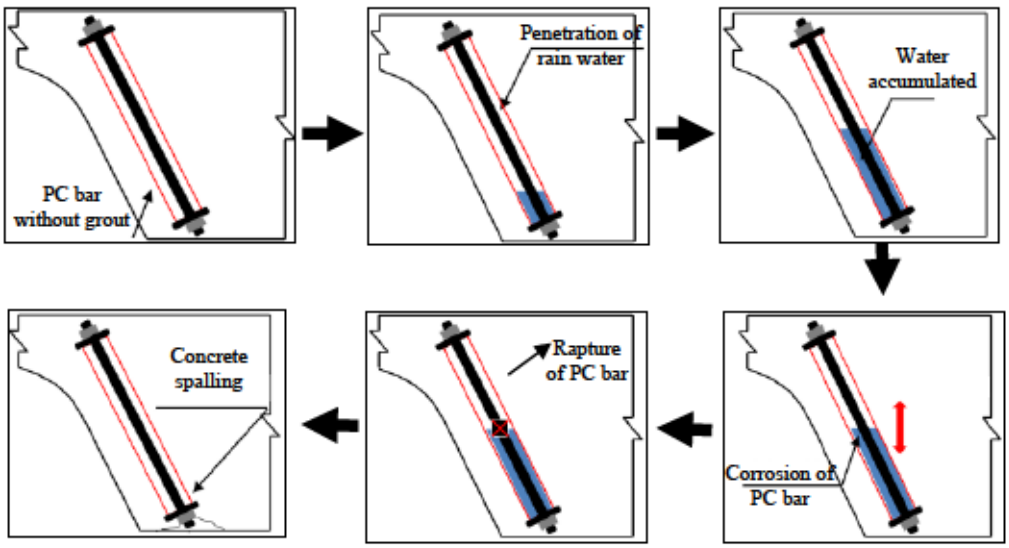

Fig. 1.9 Overall damage process

1.4 Objectives of the Study

The main objectives of the present study are:

a) To verify the Applied Element Method (AEM) simulations by experimental results.
b) To evaluate the performance of countermeasures against rupture and protrusion of prestressing steel bars in PC girders using the AEM simulations.
c) To investigate the failure modes in the countermeasures using the AEM simulations.
d) To propose a risk management of protrusion of vertically prestressing steel bars in PC girders in MEX.

1.5 Methodology of the Research

In this study, performance evaluation of countermeasures against rupture and protrusion of vertically prestressing steel bars in PC girders were conducted. The countermeasures were those applied over a bridge deck slab (including asphalt pavement and steel fiber reinforced polymer cement mortar (PCM)) and those coating materials applied below a bridge girder (including polyurea and aramid fibers). The impact energies were applied on the countermeasures either using a ruptured PC bar with 4,408 J impact energy or using a drop weight impact test. Performance of the asphalt pavements were evaluated using extreme impact energy, 4,408 J, that can cover most of rupture of vertically prestressing steel bars in the MEX. Performance of asphalt pavements were also evaluated by considering low and high temperatures to simulate winter and summer conditions in Tokyo area. The effect of time dependent deterioration of asphalt pavement by reducing the thickness of asphalt pavement was also investigated. Energy absorption capacity of polyurea and steel fiber reinforced polymer cement mortar (PCM) were investigated using a drop weight impact test.

Methodology of the present research involves establishing the Applied Element Method (AEM) numerical simulation due to its advantages of simulating structural progressive collapse. The methodology follows defining material properties in the AEM simulations based on a static compression test, tension test and pull-off adhesion test as shown in Fig. 1.10. Tension softening of the materials defined in the AEM simulation using a sensitivity analysis based on a bending test. A drop-weight impact AEM simulation was used to understand the energy dissipation capacity of the materials (polyurea and steel fiber reinforced polymer cement mortar). In this study, the AEM numerical simulations were verified with the experimental results. In the process of verification, many influential parameters, such as the effects of contact stiffness between separated elements, fracture energy of concrete and asphalt pavement, mesh sensitivity, time interval sensitivity, material properties, temperature effect, and strain rate effect were investigated.

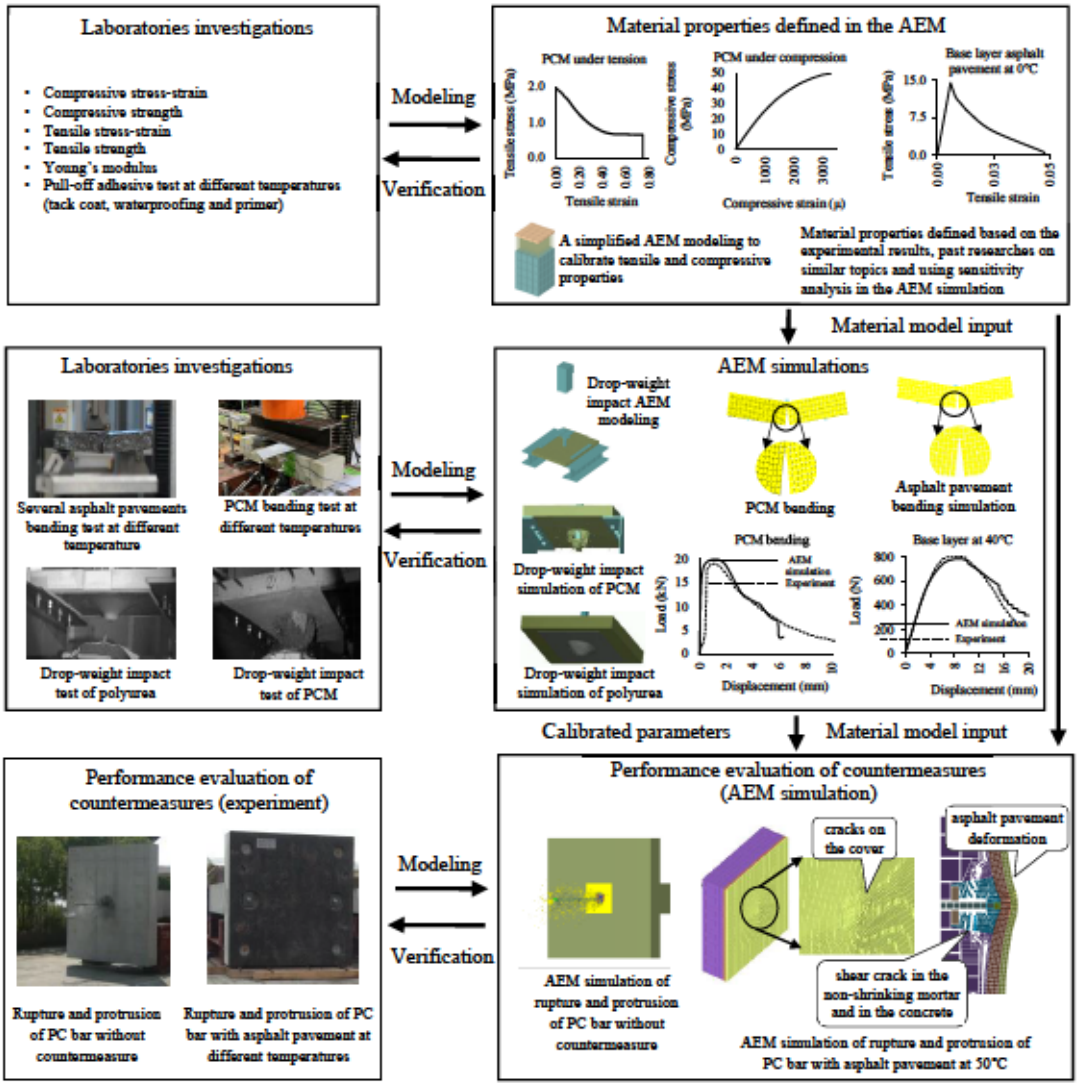

Fig.1.10 The schematic diagram of the systematic analytical scheme for AEM simulation of performance evaluation of countermeasures

1.6 Organization of the Thesis

Chapter 1: Introduction

Chapter 2: Literature review

Chapter 3: AEM simulation of rupture and protrusion of prestressing steel bar without considering countermeasure

Chapter 4: AEM simulation of rupture and protrusion of prestressing steel bar with asphalt pavement considering the effect of temperature

Chapter 5: AEM numerical simulation of dynamic punching test of polyurea sheet

Chapter 6: Drop weight impacting steel fiber reinforced PCM for investigating energy absorption capacity

Chapter 7: Risk management of protrusion of vertically prestressing steel bars in MEX

Chapter 8: Conclusions

References in Chapter 1:

[1] Transportation Research Board, "Methods of strengthening existing highway bridges," *National Cooperative Highway Research Program Report 293*, pp. 68–69, 1987.

[2] Minh H., Mutsuyoshi H., Taniguchi H., and Niitani K., "Study on chloride-induced corrosion in post-tensioned concrete beams with insufficient grout condition," *Annual Journal of Concrete Engineering*, vol. Vol. 27, no. No. 1, pp. 967–972, 2005.

[3] Reported by ACI Committee 222, "Corrosion of prestressing steels," vol. ACI222.2R, pp. 1–38, 2001.

[4] Kamada T., "The latest non-destructive inspection technologies for evaluation of grouting condition of tendon ducts in prestressed concrete beams," 2013.

[5] Harder J. and Webster N. R., "Durability of post-tensioning tendons: Canadian experience, durability of post- tensioning tendons," in *fib-IABSE Technical Report Bulletin 15. Workshop 15-16*, 2001, pp. 51–73.

[6] Hamada Y, Ishikawa Y., Mizoe M., and Miyagawa T, "Maintenance of prestressed concrete bridges, durability of post-tensioning tendons," in *fib-IABSE Technical Report, Bulletin 15. Workshop 15-1620*, 2001, pp. 109–120.

[7] Tagel-Din H. and Meguro K., "Applied element simulation for collapse analysis of structures," *Bulletin of Earthquake Resistance Structures*, vol. No. 32, pp. 113–123, 1999.

[8] Bonger A.D., Fukuhara S, Hosoda A., Salem H., Fukaya T., and Kaba K, "Rupture and protrusion of vertically tightened PC bares of PC bridges," *11th International Conference of the IFHS on Extreme Engineering, ISBN: 978-981-14-1937-9, Singapore*, pp. 161–171, Aug. 2019.

CHAPTER 2

LITERATURE REVIEW

2.1 General

Chapter 2 presents a comprehensive literature review of rupture and protrusion of prestressing steel bars (PC bars), experiences of rupture of PC bars in different countries, safety problems associated with rupture of PC bars, and countermeasures against rupture of PC bars. Moreover, the properties of countermeasure materials (concrete, asphalt pavement, interface bond materials, polyurea and steel fiber reinforced polymer cement mortar) under high loading rate are also explained. Finally, the numerical tool utilized in the present study, the Applied Element Method (AEM), is briefly discussed.

2.2 Rupture and Protrusion of PC bars

Vertically prestressing steel bars (PC bars) used in reinforced concrete box girders to increase their shear capacity [1], [2]. Vertical post-tensioning bars are occasionally added to webs, usually in the high shear zone near the piers, to control principal tension stresses and mitigate or avoid associated cracking [3]. Properly constructed post-tensioned bridges can be very durable due to the reduced cracking and multiple levels of protection for the prestressing steel. As the last level of defense for the PC bar against corrosion, the cementitious grout plays an important role in the long-term durability of the structure. Most problems associated with bonded post-tensioned construction occur as a result of inadequate grout injection or poor-quality grout [4]–[10]. This has been documented in numerous research studies and field investigations [11]–[18]. Fig. 2.1 shows grouting conditions in post-tensioned concrete. Since the mid-1980s, corrosion-related deterioration of poorly grouted and inadequately protected tendons in structures has also been well documented [19]–[24]. Failure of prestressing steel in prestressed concrete structures is usually induced by corrosion [25], [26]. Corrosion of a PC bar under stress will likely produce a sudden and sometimes volatile failure [27]. Since prestressed concrete members rely on the tensile strength of the prestressing steels to resist loads, loss of even few wires or strands per member could result catastrophic [5], [7], [19], [22], [28]. If H_2S is present in the atmosphere, or if sulfides are present in the cement or aggregate, brittle fracture of prestressing steel by stress-corrosion cracking or by hydrogen embrittlement does occur. Brittle fracture of prestressing steel by either stress corrosion or hydrogen embrittlement is especially dangerous from the safety standpoint because such fractures can occur with no prior observable macroscopic deformation of the steel and with no advance warning [29].

Fig. 2.1 Grouting conditions [27]

2.3 Experiences of Grouting Conditions and Rupture of Prestressing Bars in Different Countries

a) United Kingdom: A sample of 447 post tension PC bridges in the United Kingdom was observed and voids were found in over 50% of the bridges inspected [30]. Once corrosion is found in a tendon, it is a difficult task to quantify the level of corrosion and its location through the entire length of the tendon. Some of the multiple strands in a tendon are invisible and cannot be observed [31].

b) France: In 1994, a team of the LRPC of Aix en Provence (France) discovered the rupture and protrusion of a PC tendon due to inadequate grout filling. In 1998 PC tendon ruptured on the Saint-Cloud viaduct (France) due to insufficient grout filling. The energy brutally released during the rupture made the tendon buckle at its ends and made one of the anchoring heads move back from approximately 1 m. Rupture of PC tendon occurred in the Viviere d'Abord bridge (France) at an anchoring located in the upper part of a segment on a pier [22].

c) United States of America: Through an investigation from 1978 to 1982, 50 structures in the United States alone were found in which tendon corrosion had occurred, an average of 10 per year [32]. Of the 50 incidences reported, 10 cases of probable brittle fracture were sited. It was estimated in 1988 that, in the United States and Canada, the number of reported corrosion incidents was in the hundreds [5]. In United States, a tendon with corrosion problem in precast segmental bridges include one external tendon failure found in 1999 in the Niles Channel Bridge in Florida, two tendon failures and eleven corroded tendons discovered during the year 2000 at the Mid-Bay Bridge in Florida, and, corroded and failed vertical tendons discovered in the same year in precast segmental columns of the high-level approaches of the Sunshine Skyway Bridge. Additionally, grouting deficiencies were found in 2001 in the Sidney Lanier cable-stayed bridge in Georgia and in the Boston Central Artery bridges [6], [13]. The most obvious external evidence of corrosion damage is protrusion of tendon out of the structure. Such protrusion result when the tendon breaks and the elastic energy is released suddenly. The tendon will erupt from the slab or protrude out of the structure with a distance of several inches or several feet [33]. A 2200-car, municipally owned, cast-in-place, post-tensioned parking structure, opened in 1975 and demolished in 1994 because of severe deterioration. Broken strands were found with increasing frequency as time passed. The rate of breaks found varied from two per year initially to 36 per year less than 7 years later. There were many spalls that exposed tendons and reinforcing bar [34].

d) Canada: PC tendon breakage in a wide variety of situations was noted in Canada [35]. Failures of strands have occurred quite suddenly with a significant amount of energy released. Instances have been recorded where strands have projected from anchors or erupted in loops projecting from the top or underside of the structural slabs.

e) China: In China, insufficient grouting was also treated as one of the most serious problems in bridge construction in the 1980's [16].

f) Japan: Since 1960, a large number of prestressed concrete (PC) bridges constructed in Japan and some of them located in severe corrosive environments undergo corrosion and break of the PC

tendons due to insufficient filling of grout inside the sheath [9]. In Japan, it was found that for main cables, about 31% of total 620 investigated tendons showed imperfect grout condition ranging from minor voids to complete loss of grout [23]. In Japan, some existing bridges which were constructed in around 1970 have grout filling shortage considered as a main cause of rupture of PC steel bars, which have been reported several times in the country [36]. Fig. 2.2 shows rupture and protrusion of PC bars in Japan.

Fig. 2.2 Rupture and protrusion of PC bars in Japan [15], [36]

Table 2.1 shows, the list of ruptured PC bars of road bridges in Central Nippon Expressway Company (NEXCO), Japan. One of the main reason for rupture was insufficient grout and infiltration of water [36].

Table 2.1 Rupture of PC bars in Central Nippon Expressway Company (NEXCO), Japan [36]

Bridge name	Inspection year	Structure type	Part	Remark
O viaduct	May 1991	Continuous box girder	Floor plate side tightening	PC bar ruptured and concrete spalling
N viaduct	April 1994	Simple T girder	Floor plate side tightening	PC bar ruptured and protrusion
S viaduct	April 1994	Simple T girder	Floor plate side tightening horizontal beam side tightening	PC bar ruptured and protrusion
M bridge	May 2000	Continuous box girder	Column head vertical tightening	PC bar ruptured and pothole on the road surface
K bridge	July 2000	Continuous box girder	Horizontal beam side tightening	PC bar ruptured and protrusion
H overpass	May 2002	Simple T girder	Horizontal beam side tightening	PC bar ruptured, PCP prevents protrusion

2.4 Safety Problems Associated with Rupture of Prestressing Steel Bars (PC Bars)

Brittle fracture of prestressing steel bar by stress corrosion is dangerous from the safety standpoint because such fractures can occur with no prior observable macroscopic deformation of the steel and with no advance warning [5], [29]. The breakage of tendons sometimes results in the protrusion of a torn portion from the bridge, causing a serious public safety hazard [8], [15], [22], [28]. Rupture of PC tendons have been reported where corroded tendons have erupted from the concrete, thus also posing a risk of damage or injury from ejecting bars, falling concrete, and/ or dislodged claddings [19].

Corrosion damage in post-tensioned elements has been found in situations where no outward indications of distress were apparent [37]. This may lead some to fear that the incidence of corrosion in prestressed structures based on limited or visual inspections can be underreported, leading to a false sense of security [4]. In the spring of 2015, a condominium association in Chicago, IL, reported that a corrosion induced post tensioned tendon ruptured suddenly and a piece of concrete had fallen from the ceiling of a parking garage and broken the rear window of a vehicle parked on the second level. The potential for additional failures and eruptions to occur without warning was an unacceptable risk to the building owner [38].

If rupture of PC bar provoked any danger to a by-passer, immediate action is needed such as traffic restriction or traffic interception. Moreover, when it is judged that the advancement of deterioration inflicts damage to a third party, measures need to be taken to prevent accidents such as falling of concrete and protrusion of prestressing bars [39].

2.5 Countermeasures Against Protrusion of Prestressing Steel Bars

Prestressing Steel Bar (PC bar) protrusion potential at anchors has been seen to vary depending on concrete cover, length of PC bar, tightness of sheathing, and the location of PC bar failure. Protection measures against eruption, at anchorages or at locations with deficient concrete cover, in areas where the public could be paced at risk is necessary [35].

PC bar with a shortage of grout, re-grouting can be reliable if the steel rod is in good condition and exact location of the grout identified. But, re-injection, needs drilling holes at grout shortage location which may damage the PC bar [36]. It is very difficult to find visual evidence of corroded tendons and in some locations almost impossible. Within this limitation, countermeasures against rupture of PC bars should be developed for post-tensioned concrete bridges with corroded tendons [11]. The degree of grouting in prestressing steel that is not ruptured is not clear unless results of the detailed inspection is known. Especially when it is confirmed that the prestressing bar is ruptured, adoption of protrusion prevention method is recommended. Considerable amount of time and money is necessary for detailed inspection and re-grouting of prestressing bar in slab or transverse girders where many numbers of bars are placed. As such it is necessary adopt such methods to prevent the protrusion of

prestressing bars, so that damage to third party is avoided. Steel plate is installed at the location of pre-stressing bar and FRP sheet is bonded continuously on top of that [39]. Additional protection to the top surface of a deck slab may be provided by increased concrete cover, waterproofing with protective wearing course overlays, polymer modified concrete overlay or sealers, such as methyl methacrylate [3].

Rupture and protrusion of horizontally prestressing steel bars was investigated [40]. In this investigation, a full-scale floor slab specimen with a PC bar at different grout filling was used (Fig. 2.3). The grout filling levels were 0, 25, 50 and 75%. That was, the PC steel rod length of the unfilled part of the grout was 8, 6, 4, 2 [m] respectively. The PC bar (SBPR 930/1080) and the sheath had ϕ 23 mm and ϕ 35 mm respectively. The applied prestress force was 780MPa. After cutting of the PC steel rod, protrusion length, the condition of the fracture surface and the damage condition of the cover concrete were recorded. The experimental results after cutting of the PC steel bar are shown in Fig. 2.3. The PC bar and the nut, attached to the end of the PC bar, were protruded, and the bearing plate remained inside the cover concrete. PC bar protrusion for the grout filling levels 0, 25, 50 and 75% were 5.78 m, 4.10 m, 1.78 m and 0.00 m respectively. When the degree of grout filling increased, protrusion of PC bar decreased. In all cases the PC bars destroyed the cover concrete. A cone-shaped cover concrete fracture was observed as shown in Fig. 2.3. In this study, no grout filling in a sheath was considered to simulate the worst cases and to get a safe countermeasure against PC bar protrusion.

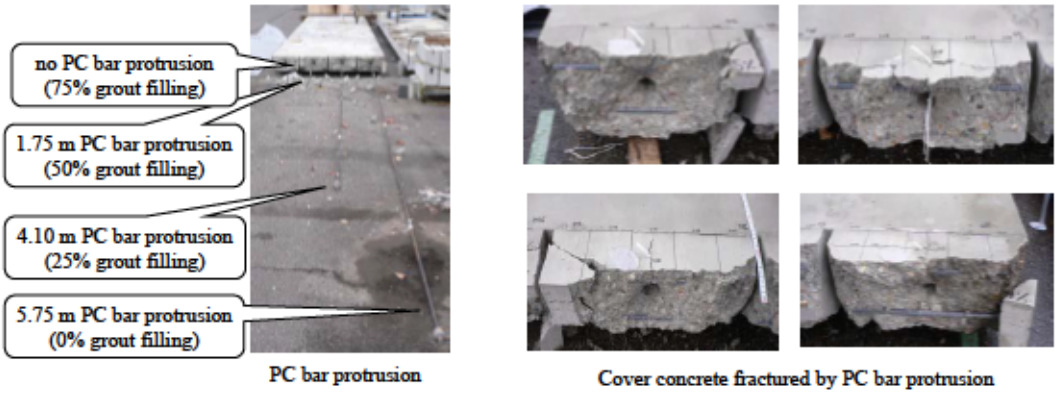

Fig. 2.3 The effect of grout filling on PC bar protrusion [40]

A rupture and protrusion of vertical PC bar was found in Central Nippon Expressway Company (NEXCO) as shown in Fig. 2.4a. The PC bar protruded and destroyed the asphalt pavement over a bridge deck slab (Fig. 2.4b). NEXCO used a conventional type of countermeasures against protrusion of PC bars as shown in Fig. 2.4c and 2.4d [36]. This type of countermeasures used asphalt pavement with steel plate, aramid fiber and waterproofing sheet. The steel plate distributed the punching shear stress from the ruptured PC bar over a wider area and reduced localized failure. Aramid fiber and waterproofing sheet attached on a cover concrete surface with adhesive to prevent concrete spalling as they are good in tensile strength, stretch performance and energy absorption. However, the steel plate

was heavy. Moreover, installation of the steel plate needed anchor drilling which took a longer construction time. More time was also needed for the adhesive material to cure. As a result, this technique was not convenient. In this study, performance of asphalt pavement without considering steel plate, aramid fiber and waterproofing sheet was investigated. Reducing construction time of countermeasures is one of the criteria in this study as traffic volume in MEX is very harsh.

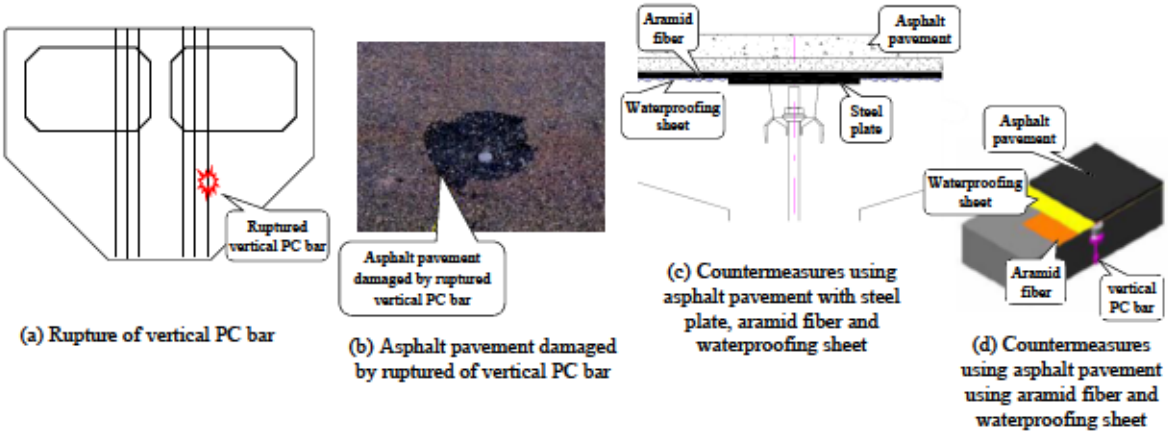

(a) Rupture of vertical PC bar

(b) Asphalt pavement damaged by ruptured of vertical PC bar

(c) Countermeasures using asphalt pavement with steel plate, aramid fiber and waterproofing sheet

(d) Countermeasures using asphalt pavement using aramid fiber and waterproofing sheet

Fig. 2.4 PC bar protrusions and countermeasures [36]

In 2009, NEXCO Central (Central Nippon Expressway Company Limited) conducted a PC bar protrusion countermeasure experiment using a 75 mm thick asphalt pavement (without steel plate and aramid fiber). The diameter of the PC bar was ϕ32 mm and the PC bar length was 4 m. The applied prestress force was 583 MPa. The experimental result showed that the asphalt pavement was not effective against PC bar protrusion. A cone-shaped fracture of asphalt pavement was observed as shown in Fig. 2.5. In this study, performance of asphalt pavement was investigated utilizing appropriate asphalt pavement materials and appropriate thickness. A countermeasure that is safe from protrusion of PC bar is one of the criteria in this study.

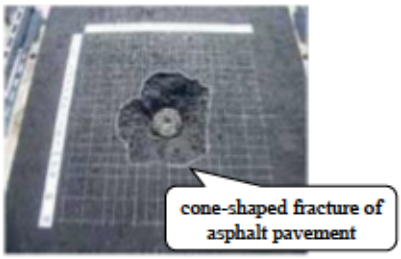

Fig. 2.5 Experimental investigation of rupture and protrusion of PC bar with asphalt pavement countermeasure by NEXCO Central [36]

A rupture and protrusion of vertical PC bar was found in East Japan Railway (JR) Company as shown in Fig. 2.6a. The PC bar protruded below the bridge girder and destroyed the cover concrete (Fig. 2.6b). The diameter of the PC bar was ϕ29 mm and the PC bar length was 3.25 m. The PC bar ruptured 1.3 m from the top of the bridge girder. JR East used a conventional type of countermeasures against protrusion of PC bars as shown in Fig. 2.6c.

(a) rupture and protrusion of PC bar

(b) cover concrete damaged by protrusion of PC bar

(c) Countermeasure using steel plate and aramid fiber

Fig. 2.6 PC bar protrusions and countermeasures using steel plate and fiber sheets (JR East)

Metropolitan Expressway Company (MEX) experimentally investigated the performance of countermeasure against rupture and protrusion of PC bars. MEX modified the conventional type countermeasure with steel plate and fiber sheets, by replacing the steel plate by a multiple layer of stainless-steel mesh. The target was to reduce construction time by avoiding steel plate and anchor drilling. The countermeasure included two layers of stainless-steel mesh, two layers of aramid fiber and two layers of FRP sheet bonded together by epoxy resin as shown in Fig 2.7. The PC bar was ϕ32 mm. The applied prestressing force was 521 kN. No grout was provided in the sheath. The PC bar ruptured at 10 m from the PC bar head. The result of the experiment indicated that, protrusion of the PC bar was only 20 mm and no major damage was found in the countermeasure. In this study, performance of asphalt pavement was investigated without utilizing stainless-steel mesh, aramid fiber and FRP sheet.

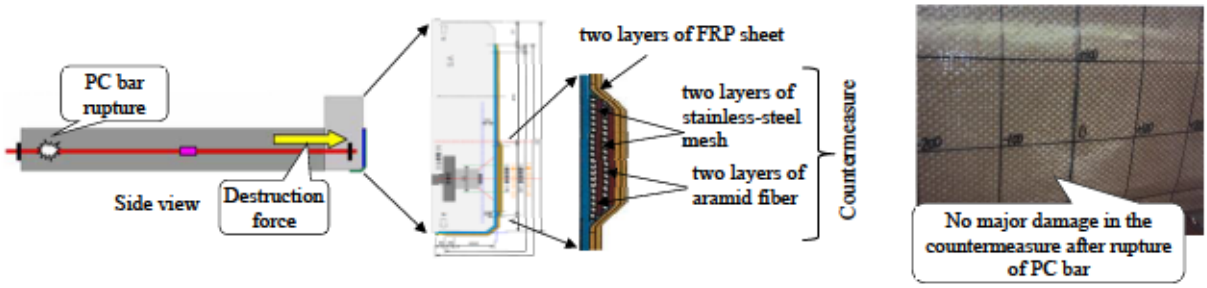

Fig. 2.7 Experiment set up for modified countermeasure [40]

A PC bar protrusion countermeasure experiment was conducted using an asphalt pavement together with two layers of aramid fiber at 20°C [36]. The diameter of the PC bar was ϕ32 mm and the PC bar length was 11.8 m. The applied prestress force was 636 kN. The PC bar rupture length was 11.0 m from the PC bar head. The experimental result showed that the asphalt pavement and the aramid fibers were destroyed around the impacting area as shown in Fig.2.8. However, no PC bar protrusion was observed.

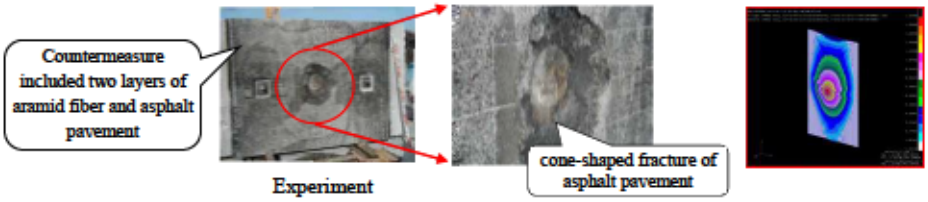

Fig. 2.8 Experimental and simulation of rupture and protrusion of PC bar with asphalt pavement [36]

2.6 Countermeasure Materials

Rupture and protrusion of prestressing steel bars (PC bar) is very violent and brutal. The sudden rupture of prestressing tendon sometimes results in the protrusion of a torn portion from the bridge, causing a serious public safety hazard from projecting bars and from falling concrete because such fractures can occur with no advance warning. Protective measures against eruption of PC bar tendon are necessary to avoid damage to third party. When a vertically prestressing steel bar is ruptured, all the strain energy in the PC bar is released instantly, which can damage the countermeasure materials. This section discusses about countermeasure material properties under high loading rate.

a) Concrete:

The response of concrete up to complete failure in tension is represented in the load-deformation relation [41]. The characteristic parameters are the ultimate strength, stiffness in the ascending branch and the fracture energy. All these properties are rate dependent. The observed response of concrete at macro level is determined by the damage initiation and damage accumulation mechanisms at meso and micro scale level. The failure process is governed by the stress condition, the ability to absorb energy in fracture and the energy flow from the surrounding material into the fracture zone.

In the fictitious crack model (Fig. 2.9), the crack initiation is controlled by the strength criterion, the maximum material strength. The material fracture energy (G_f) is the energy absorbed within a single fracture zone and equals the surface below the load-deformation curve for uniaxial tensile loading. Concrete is probably the most rate dependent structural material. The rate effects occur due to the additional resistance to damage growth at micro and meso level. The main mechanisms can be summarized as follows. In the moderate loading regime, the moisture in the capillary pores causes the dominant effect. The water adds resistance to pore-widening (Stephan effect) under dynamic loading, which results in the observed strength increase. With increasing loading rate, the inertia effects at micro level become dominant. Inertia affects the stress fields in the heterogeneous material, around the material defects and the (micro) cracks. Stress singularities decrease, and damage initiation and growth are delayed [41].

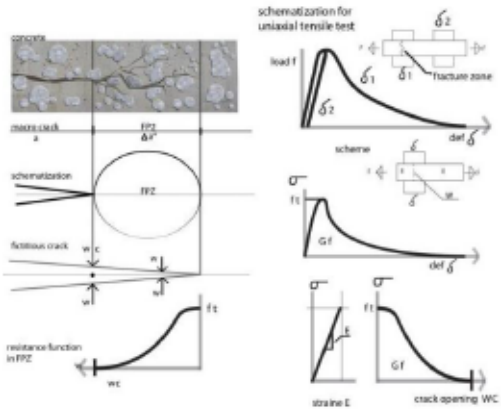

Fig. 2.9 Crack tip fracture process; fictitious crack concept [41]

The comparison of concrete in wide range of compressive and tensile strain rates is shown in Fig. 2.10a. The Dynamic Increase Factor (*DIF*), the ratio of the dynamic strength to quasi-static strength is shown in 2.10b.

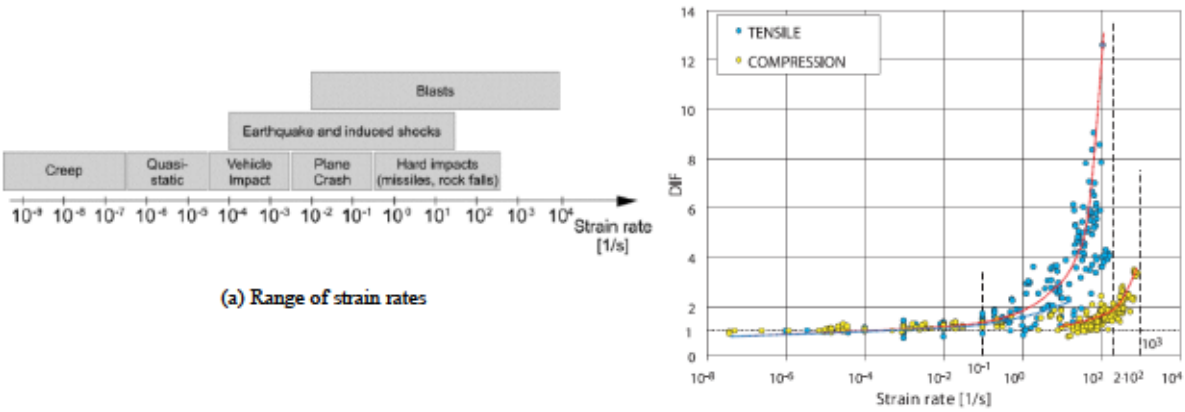

(a) Range of strain rates

(b) *DIF* of concrete

Fig. 2.10 Range of strain rates (a) [42] and strain rate effect on tensile and compressive strength of concrete (b) [43]

The strain rate effect of concrete under compression at a high load rating $\dot{\varepsilon} \leq 30s^{-1}$ and $\dot{\varepsilon} > 30s^{-1}$ can be calculated using Equation 2.1 and Equation 2.3 respectively. The strain rate effect of concrete under tension at a high load rating $\dot{\varepsilon} \leq 30s^{-1}$ and $\dot{\varepsilon} > 30s^{-1}$ can be calculated using Equation 2.2 and Equation 2.4 respectively [44].

For $\dot{\varepsilon} \leq 30s^{-1}$

$$f'_{cd}/f'_{cs} = (\dot{\varepsilon}/\dot{\varepsilon}_s)^{1.026\alpha} \tag{2.1}$$

$$f_{td}/f_{ts} = (\dot{\varepsilon}/\dot{\varepsilon}_s)^{1.016\delta} \tag{2.2}$$

$$\alpha = 1/(5 + 0.9f'_{cs}) \qquad \delta = 1/(10 + 0.6\,f'_{cs})$$

For $\dot{\varepsilon} > 30s^{-1}$

$$f'_{cd}/f'_{cs} = \gamma(\dot{\varepsilon}/\dot{\varepsilon}_s)^{1/3} \tag{2.3}$$

$$f_{td}/f_{ts} = \beta(\dot{\varepsilon}/\dot{\varepsilon}_s)^{1/3} \tag{2.4}$$

$$\gamma = 10^{(6.156\alpha-2)} \qquad \beta = 10^{(7.112\delta-2.33)}$$

Where, f'_{cd}, f_{td} : Compression and tensile strength at rapid loading,

f'_{cs}, f_{ts} : Compression and tensile strength at static loading,

$\dot{\varepsilon}$: Strain rate at rapid loading,

$\dot{\varepsilon}_s$: Strain rate at static loading (for compressive loading, $30 \times 10^{-6}s^{-1}$, for tensile loading, $3 \times 10^{-6}s^{-1}$)

Increases in the dynamic modulus, E_d expressed as Equation (2.5) [45].

$$E_d/E_s = (\varepsilon_d/\varepsilon_s)^{0.026} \quad (2.5)$$

Where, E_d : dynamic modulus,

E_s : static modulus,

ε_s : static strain rate = $30 \times 10^{-6} s^{-1}$,

ε_d : dynamic strain rate

b) Asphalt Pavement

Asphalt pavement is required to be structurally sound enough to withstand the stresses imposed on it and sufficiently thick to distribute the loads and stresses to a safe value [46]. When asphalt pavement fails to function properly, traffic safety can be seriously affected [47]. The behavior of asphalt pavement depends on temperature, loading rate, asphalt content, asphalt types, and mixtures gradation [48].

Asphalt concrete is one type of temperature sensitive mixtures [48]. Asphalt pavement suffers from the impact of temperature due to the temperature variation in different districts and environments [49]. With the decrease of temperature, the peak stress of an asphalt pavement is obviously increased and the failure mode is transferred from ductile failure to brittle failure since the asphalt changes from viscoelasticity to elastic brittleness [50]. The fracture energy of asphalt pavement increases with temperatures [51].

Temperature and strain rate of asphalt pavement have a significant effect on failure mode, mechanical characteristics and stress-strain curve [48], [49], [52]. Understanding the response and failure mode of asphalt pavement that is subjected to impact loading from the ruptured prestressing steel bar at high and low temperature is vital for traffic safety. The mechanical properties of the hot mix asphalt changed significantly under high-strain rate [53]. The failure mechanisms under the high-strain rate loading were found to be considerably different from those obtained in static testing where failure of binder was a predominant mechanism. High-strain rate loading caused trans-aggregate failures in addition to failure of the binder as shown in Fig. 2.11 [54]. For the asphalt pavement under high loading rate, the quasi-static tensile and compressive stress was increased by the respective Dynamic Increase Factor (*DIF*). *DIF* can be defined using Equation 2.6 and Equation 2.7 for the asphalt pavement under compression and tension respectively at a high loading rate [55]. Literature on fracture of asphalt pavement under high loading rate is scarce. High strain rate mechanical behavior of bituminous materials has received little attention due to inherent difficulty in testing and interpretation of results [53].

$$DIF_c = \begin{cases} 3.18 + 1.098log_{10}(\dot{\varepsilon}) + 0.1397{log_{10}}^2(\dot{\varepsilon}), & \dot{\varepsilon} \le 100s^{-1} \\ 21.39log_{10}(\dot{\varepsilon}) - 36.7, & 100s^{-1} < \dot{\varepsilon} \le 200s^{-1} \end{cases} \quad 2.6$$

$$DIF_c = \begin{cases} 1.86 + 0.1432log_{10}(\dot{\varepsilon}), & \dot{\varepsilon} \le 15s^{-1} \\ 6.06log_{10}(\dot{\varepsilon}) - 5.024, & 15s^{-1} < \dot{\varepsilon} \le 100s^{-1} \end{cases} \quad 2.7$$

Where, DIF_c: Dynamic Increase Factor under compression,

DIF_t: Dynamic Increase Factor under tension,

$\dot{\varepsilon}$: is strain rate at rapid loading

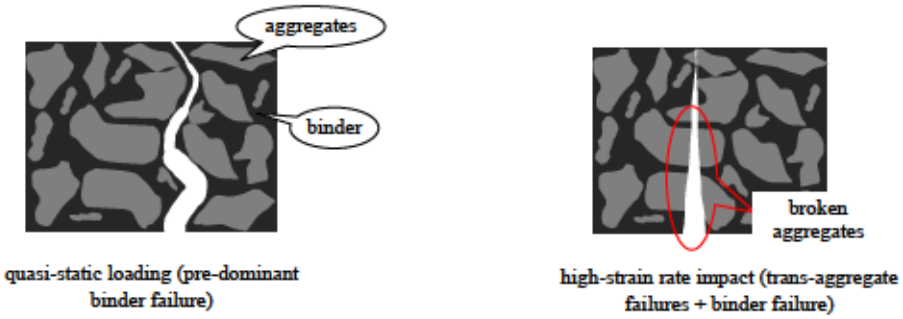

Fig. 2.11 The effect of strain rate in the failure mechanism of asphalt pavement

The fracture process zone in asphalt pavement is a nonlinear zone characterized by progressive softening, for which the stress decreases at increasing deformation [56]. The nonlinear softening zone is surrounded by a non-softening nonlinear zone, which represents material inelasticity. The fracture process behavior in certain materials classified into three types: brittle, ductile and quasi-brittle. As shown in Fig. 2.12 (reproduced from Bazant and Planas 1998), each type presents different relative sizes of those two nonlinear zones (i.e., softening and non-softening nonlinear zones) and of the structure.

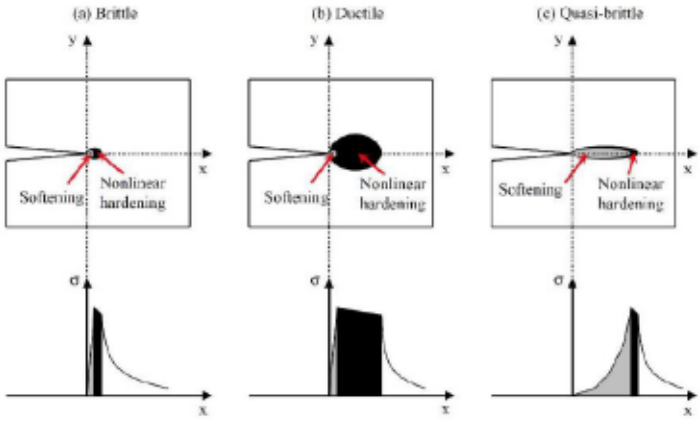

Fig. 2.12 Types of fracture process zone in asphalt pavement [56]

c) Interface Bond Materials

In this study, a waterproofing interface bond material was used at the interface between a base layer asphalt pavement and a slab concrete. A tack coat interface bond material was used at the interface between a base layer asphalt pavement and a cover layer asphalt pavement. The interface bond strength of the waterproofing and the tack coat were investigated by pull-off adhesion test at different temperatures. The pull-off adhesion test result showed that, the interface bond strength was highly temperature dependent. An Applied Element Method (AEM) numerical simulation of rupture and

protrusion of PC bar with asphalt pavement was carried out [57]. In the AEM numerical simulation, it is difficult to set appropriate material properties for interface materials directly based on experimental results. When a bond between the base layer asphalt pavement and the slab concrete had a very high bond strength, separation between the slab concrete and the asphalt base layer did not occur and it was difficult to obtain ductile asphalt pavement deformation. As a result, localized asphalt pavement failure and PC bar protrusion occurred. On the other hand, a weak interface material resulted in a total delamination between the asphalt base layer and the slab concrete in the specimen with this size, and the protrusion of PC bar could not be prevented. The details are explained in chapter 4 (Fig. 4.16).

A primer was used at the interface between a polyurea and a slab concrete [58]. The adhesive strength of the polyurea coating with a primer was experimentally investigated by pull-off adhesion test on dry concrete and it was 1.32MPa. The pull-off adhesion test was based on JIS A6909 6.10 standard. The concrete surface was smoothened by a sandpaper before applying the primer. For dry concrete, applying primers can improve adhesion results [59]. The details are explained in chapter 5 section 5.2.1.

d) Polyurea

A polyurea coating is the result of a one-step reaction between an isocyanate component and a resin blend component [59]. Polyurea is widely used as a protective coating material for structures subjected to impulsive loads [59]–[62]. Polyurea spray coating technology combines fast curing, even at very low temperatures, and water insensitivity with exceptional mechanical properties, chemical resistance and durability [59]. Their mechanical behavior at a very high strain rate is of particular interest [62], [63], because the protrusion of PC bars will generate very high strain rate in concrete and polyurea. Spraying polyurea might be applied to prevent protrusion and spalling with less construction time. FRP sheet cannot be applied well when the surface is not smooth [64], but polyurea can be applied to such surface. In this study AEM numerical simulation of dynamic punching test of polyurea was carried out using drop weight test to investigate impact resistance. The details are explained in chapter 5.

A finite-element analyses using ABAQUS/Explicit about a mechanism behind the protective benefit offered by the polyurea coating were carried out using a transient non-linear dynamics finite-element approach [61], [65], [66]. The nonlinear finite element (FE) code, LS-DYNA was used to simulate the characteristics and behavior of the polyurea coating [67]. However, in this study, a numerical model of punching test of polyurea was developed in AEM. Experimental results were used for validation of numerical investigations.

e) Steel Fiber Reinforced Polymer Cement Mortar (PCM)

A bridge deck slab, in Metropolitan Expressway (MEX) in Japan, designed according to the 1964 Steel Road Bridge Specification and the 1972 Road Bridge Specification have thin cover concrete. As

a result, severe deterioration of RC slabs became remarkable. Moreover, cover concrete can be damaged and rebar can be exposed during pavement replacement over a bridge deck slab with inaccurate flatness [68]. To restore a damaged cover concrete, a steel fiber reinforced polymer cement mortar (PCM) was developed by MEX in 2014. This newly developed PCM is an ultrahigh early strength polymer cement mortar which can be mixed and applied on the site like a shotcrete. Ultra-high early strength is required due to restrictions on construction time.

In MEX, the asphalt pavement system over a bridge deck has two layers with 80 mm thickness in total. The base layer asphalt pavement in the two layers has 50 mm thickness, and the cover layer asphalt pavement has 30 mm thickness. The asphalt pavement system was effective against 4,408 J impact energy from a ruptured vertically prestressing steel bar of ϕ 32 mm [57]. However, in a bridge deck slab with damaged cover concrete, the PCM has been used not only to restore damaged cover concrete but also as a 50 mm thick base layer together with a 30 mm thick asphalt pavement cover layer. The PCM is also expected to be effective against the protrusion of vertically prestressing steel bar. An impact energy of 4,408 J can cover most of the strain energies of vertically tightened PC bars in MEX. In this study, in order to fundamentally investigate the energy absorption capacity of the PCM, a drop weight impact test was conducted with 1,494 J energy.

In this study, a numerical model of drop weight impact of PCM was investigated using the Applied Element Method (AEM). The results of numerical simulations are discussed and compared with experimental results. The details are explained in chapter 6.

For steel fiber reinforced concrete under high loading rate, the compressive strength, and tensile strength should be increased with the increase in strain rate. In this study, the empirical Equation (2.8) and Equation (2.9) [69] to calculate the Dynamic Increase Factor (*DIF*) of PCM under compression and under tension, respectively, were applied in the AEM numerical simulation.

$$CDIF = \begin{cases} (\dot{\varepsilon}/\dot{\varepsilon}_s)^{1.026\delta} & \dot{\varepsilon} \leq 53s^{-1} \\ 0.6608\gamma_s(\dot{\varepsilon}/\dot{\varepsilon}_s)^{\frac{7}{20}} & \dot{\varepsilon} > 53s^{-1} \end{cases} \tag{2.8}$$

Where, $CDIF$: compressive Dynamic Increase Factor,

$\dot{\varepsilon}_s$: static strain rate $3 \times 10^{-5}\mathrm{s}^{-1}$,

$\dot{\varepsilon}$: strain rate ranged from $3 \times 10^{-5}\mathrm{s}^{-1}$ to $300\mathrm{s}^{-1}$,

$\delta = 1/(5 + 0.9f_c)$,

$log\gamma_s = 6.156\delta - 2$,

f_c : static compressive strength

$$TDIF = \begin{cases} (\dot{\varepsilon}/\dot{\varepsilon}_s)^{0.95\delta} & \dot{\varepsilon} \leq \dot{\varepsilon}_s s^{-1} \\ 0.71\beta(\dot{\varepsilon}/\dot{\varepsilon}_s)^{\frac{1}{3}} & \dot{\varepsilon} > \dot{\varepsilon}_s s^{-1} \end{cases} \tag{2.9}$$

Where, $TDIF$: tensile Dynamic Increase Factor,

$\dot{\varepsilon}_s$: static strain rate $1 \times 10^{-6} s^{-1}$,

$\dot{\varepsilon}$: dynamic strain rate,

$\delta = 1/(1 + 0.8 f_c)$,

$log\beta = 6.65\delta - 2.141$,

f_c : static compressive strength

2.7 Applied Element Method (AEM)

Applied Element Method (AEM) is based on dividing the structural members into virtual elements connected through springs (Fig. 2.13a). The two elements are assumed to be connected by one normal and two shear springs located at contact points, which are distributed around the element's edges. Each spring entirely represents the stresses, strains, deformations, and failure of a certain portion of the structure as shown in Fig. 2.13b [70]–[74]. Stiffness matrix components are determined by applying a unitary displacement to a Degrees of Freedom (DOF) while keeping the remaining DOF's fixed (Fig. 2.13c). The forces needed to generate this configuration are the stiffness matrix components, which are equal to the summation of the contributions of the springs surrounding the element. The contribution of the contact spring shown in Fig 2.13c to DOFs u1, u2, and u3 is shown in Fig 2.13d. This Equation shows one-quarter of the element stiffness matrix [71]. Applied Element Method (AEM) was proven to be the method that can track the structural collapse behavior passing through all stages of the application of loads with reliable accuracy in reasonable CPU time: elastic stage, crack initiation and propagation in tension-weak materials, reinforcement yielding, element separation, element collision (contact), and collision with the ground and with adjacent structures [74], [75].

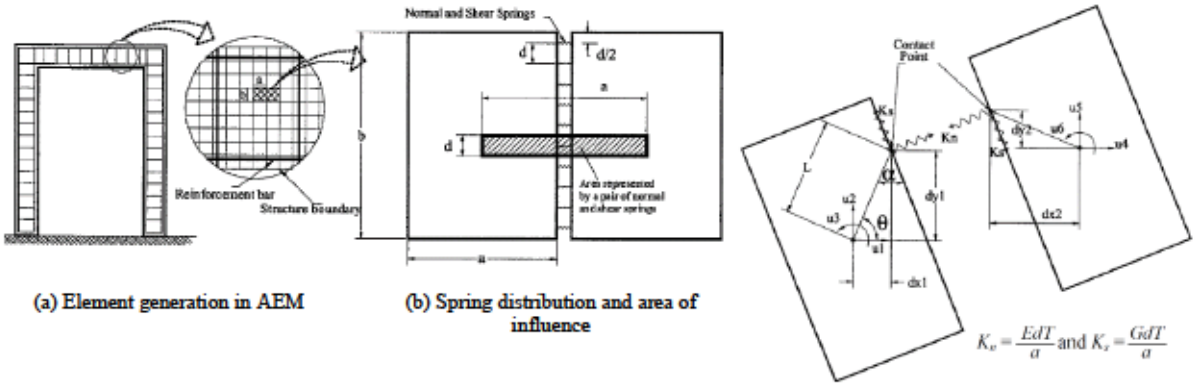

(a) Element generation in AEM

(b) Spring distribution and area of influence

Where: d is the distance between springs, T the element thickness, the length of the representative area, E the material Young's modulus, and G the material shear modulus.

(c) Element shape, contact point, degrees of freedom and spring stiffness

$$\begin{bmatrix} Sin^2(\theta+\alpha)K_n + Cos^2(\theta+\alpha)K_s & -K_nSin(\theta+\alpha)Cos(\theta+\alpha) + K_sSin(\theta+\alpha)Cos(\theta+\alpha) & Cos(\theta+\alpha)K_sLSin(\alpha) - Sin(\theta+\alpha)K_nLCos(\alpha) \\ -K_nSin(\theta+\alpha)Cos(\theta+\alpha) + K_sSin(\theta+\alpha)Cos(\theta+\alpha) & Sin^2(\theta+\alpha)K_s + Cos^2(\theta+\alpha)K_n & Cos(\theta+\alpha)K_nLCos(\alpha) + Sin(\theta+\alpha)K_sLSin(\alpha) \\ Cos(\theta+\alpha)K_sLSin(\alpha) - Sin(\theta+\alpha)K_nLCos(\alpha) & Cos(\theta+\alpha)K_nLCos(\alpha) + Sin(\theta+\alpha)K_sLSin(\alpha) & L^2Cos^2(\alpha)K_n + L^2Sin^2(\alpha)K_s \end{bmatrix}$$

(d) Stiffness matrix

Fig. 2.13 Modeling of structure in AEM [71]

The solution for dynamic problems adopts the step-by-step integration (Newmark beta) method. For nonlinear dynamic phenomenon, the numerical solution can be obtained by a sufficiently small-time interval. The time interval required for stable dynamic analysis is a function of element mass and contact stiffness [72]–[75]. Fig. 2.14 shows flow of analysis in the AEM.

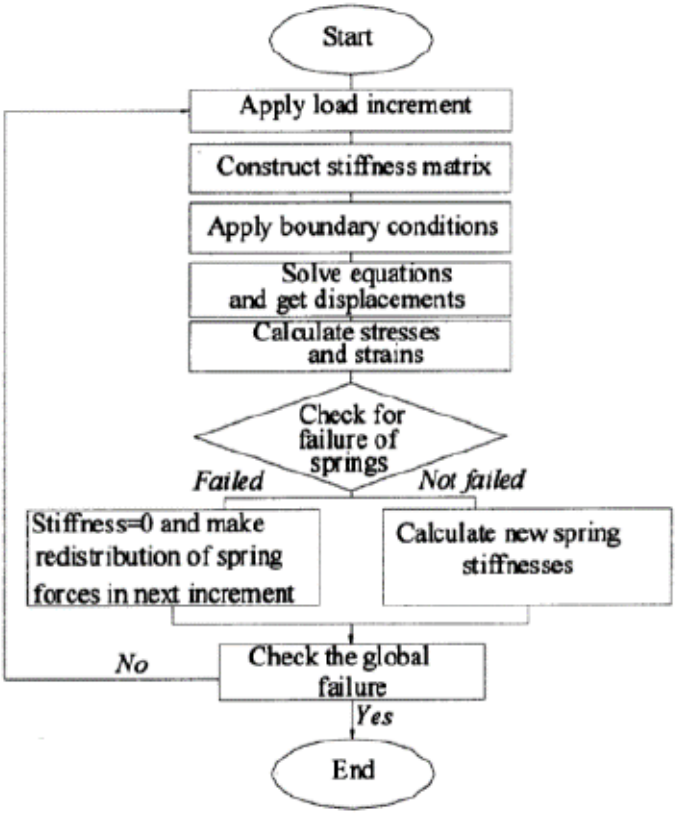

Fig. 2.14 Flow of analysis [72]

The overall equilibrium set of equations for elastic loading conditions is as follows [73];

$$K_G \Delta = F \tag{2.10}$$

Where, K_G: global stiffness matrix,

Δ: displacement vector,

F: the applied load vector

The overall equilibrium set of equations for static large deformation analysis is as follows [71];

$$K \Delta U = \Delta f + R_m + R_G \tag{2.11}$$

Where, K: nonlinear stiffness matrix,

ΔU: incremental displacement vector,

Δf: incremental load vector,

R_m: residual force vector due to cracking or incompatibility between spring strains and stresses,

R_G: residual force vector due to geometrical changes in the structure during loading

The general dynamic equation of motion in small deformation range is [74]:

$$M\Delta\ddot{U} + C\Delta\dot{U} + K\Delta U = \Delta f(t) - M\Delta\ddot{U}_G \qquad (2.12)$$

Where, M: mass matrix,

C: damping matrix,

K: nonlinear stiffness matrix,

$\Delta f(t)$: incremental applied load vector,

ΔU: incremental displacement vector,

$\Delta\dot{U}$, $\Delta\ddot{U}$ and $\Delta\ddot{U}_G$: incremental velocity, acceleration and gravity acceleration vectors, respectively

The general dynamic equation of motion in large deformation case is [74]

$$M\Delta\ddot{U} + C\Delta\dot{U} + K\Delta U = \Delta f(t) + R_m + R_G \qquad (2.13)$$

Where, M: mass matrix,

C: damping matrix,

K: nonlinear stiffness matrix,

$\Delta f(t)$: incremental applied load vector,

ΔU: incremental displacement vector,

$\Delta\dot{U}$ and $\Delta\ddot{U}$: incremental velocity and acceleration vectors, respectively

R_m: residual force vector due to cracking or incompatibility between spring strains and stresses,

R_G: residual force vector due to geometrical changes in the structure during loading

Nonlinear path-dependent constitutive models are used for simulating concrete and reinforcing bars in AEM. For concrete in compression, the elastoplastic and fracture model of Maekawa and Okamura is adopted [76], while linear stress–strain relationship is adopted in tension up to reaching the crack stage, where the stresses fall to zero for concrete as shown in Fig. 2.15a. For concrete springs, the relationship between shear stress and shear strain is assumed to remain linear till the cracking of concrete. Then, the shear stresses drop down as shown in Fig. 2.15b. The level of drop of shear stresses depends on the aggregate interlock and friction at the crack surface [75]. The reinforcing bars are modeled as bare bars for the envelope following the model of Menegotto and Pinto [77] for the inner cyclic loops.

In this study, numerical simulation of rupture and protrusion of vertically prestressing steel bar was conducted using the Applied Element Method (AEM) due to its advantages of simulating structural progressive collapse [70]–[74]. In this study, a nonlinear structural analysis software 'Extreme Loading for Structure (ELS)' [75] based on AEM is used. Many research papers have been published on the successful use of AEM to simulate structural progressive collapse [78]–[84].

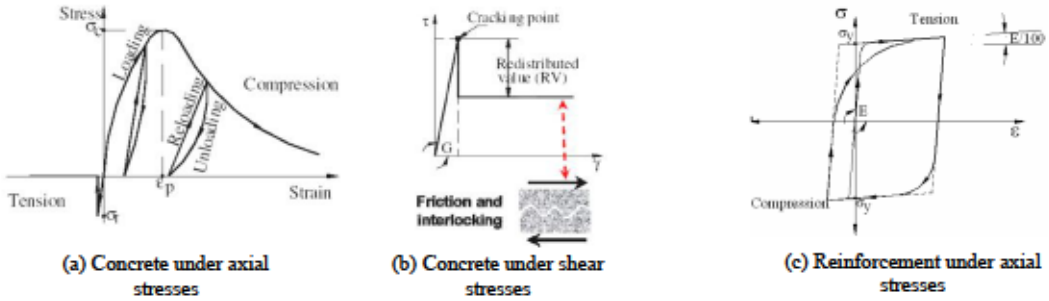

(a) Concrete under axial stresses (b) Concrete under shear stresses (c) Reinforcement under axial stresses

Fig. 2.15 Constitutive models for concrete and reinforcement used in Extreme Loading for Structure (ELS) [75]

References in Chapter 2:

[1] Transportation Research Board, "Methods of strengthening existing highway bridges," *National Cooperative Highway Research Program Report 293*, pp. 68–69, 1987.

[2] OECD (Organization for Economic Co-operation and Development), "Bridge rehabilitation and strengthening," *OECD, Scientific Expert Group*, p. 103, 1983.

[3] John C.P.E. and Alan M.P.E., "Post-tensioning tendon installation and grouting manual," *U.S. Department of Transportation Federal Highway Administration (FHWA), FHWA-NHI-13-026, Version 2*, p. 5, 2013.

[4] ACI, "Corrosion of prestressing steels," *Reported by ACI Committee 222, ACI 222.2R*, pp. 1–38, 2001.

[5] Podolny W., "Corrosion of prestressing steels and its mitigation," *Journal of the Prestressed Concrete Institute, V. 27, Issue. 5*, pp. 34–55, 1992.

[6] Freyermuth C. L., "Status of the durability of post-tensioning tendons in the United States," *Durability of Post-tensioning tendons. fib-IABSE Technical Report, Bulletin 15. Workshop 15-16*, pp. 43–50, 2001.

[7] Täljsten B., Paulsson B., and Elfgren L., "Prestressed concrete bridges condition assessment and future challenges," *Luleå University of Technology, Department of Civil, Environmental and Natural Resources Engineering, BBT 2017-011, Trafikverket, TRV 2018/28332, ID 6686*, pp. 13–20, 2019.

[8] Nishi H., Otsuka T., Kamei K., and Onishi H., "Risk assessment about the maintenance of the PC bridge in Tozai line," *Journal of the Society of Material Science, Japan, V.67, No.2*, pp. 163–169, 2018.

[9] Isuru W., Hiroshi M., and Toshihiro Y., "Effects of tendon rupture and re-grouting on the flexural behavior of prestressed concrete beams," *10th International Conference on Short and Medium Span Bridges Quebec City, Quebec, Canada, 154*, pp. 1–10, 2018.

[10] Aoki K., Umitsu M., and Igo Y., "Strategies for improvement approach in Japan," *Durability of Post-tensioning tendons. fib-IABSE Technical Report, Bulletin 15*, pp. 263–227, 2001.

[11] Youn S. and Kim E., "Deterioration of bonded post-tensioned concrete bridges and research topics on the strength evaluation in ISARC."

[12] Vector, "Post-tensioned structures solutions for repair and protection," *Vector Construction, Vector Corrosion Technologies and Vector Corrosion Services*, pp. 2–11, 2019.

[13] R. M. Salas, Schokker A. J., West J. S., Breen J. E., and Kreger M. E., "Conclusions, recommendations and design guidelines for corrosion protection of post-tensioned bridges," *U.S. Department of Transportation Federal Highway Administration and Texas Department of Transportation, Research Report 0-1405-9*, pp. 1–73, 2004.

[14] Jungwirth D., "Problems, solutions and developments for post-tensioning tendons from the German point of view," *Durability of Post-tensioning tendons. fib-IABSE Technical Report, Bulletin 15. Workshop 15-16*, pp. 11–24, 2001.

[15] Nagata Y., Shiratori A., Ito T., and Ueki H., "Diagnosis for grouted condition of transverse prestressing tendon in PC bridges in-service using impact elastic wave methods," *Concrete Research and Technology, Vol. 25*, pp. 57–64, 2014.

[16] Wang L., Zhang X., Zhang J., Ma Y., Xiang Y., and Liu Y., "Effect of insufficient grouting and strand corrosion on flexural behavior of PC beams," *Construction and Building Materials 53*, pp. 213–224, 2014.

[17] Fuzier J.P., "Development of grout and grouting techniques," *Durability of Post-tensioning tendons. fib-IABSE Technical Report, Bulletin 15. Workshop*, pp. 173–194, 2001.

[18] Clark G., "Strategies for improvement -approach in Europe- the UK strategy and fib developments," *Durability of Post-tensioning tendons. fib-IABSE Technical Report, Bulletin 15. Workshop,* pp. 221–226, 2001.

[19] Fallis G., Ball J.C., and Moad A., "Innovative corrosion evaluation system for unbonded post-tensioned cables," *Concrete Repair Bulletin*, pp. 7–8, 2007.

[20] Poston R. W. and West J. S., "North American strategies for improving bonded post-tensioned concrete construction," *Durability of Post-tensioning tendons. fib-IABSE Technical Report, Bulletin 15. Workshop 15-16,* pp. 245–255, 2001.

[21] Sprinkel M.M., "VDOT experience with grouts and grouted post-tensioned tendons," *Journal of Posttensioning Institute*, pp. 51–61, 2015.

[22] Godart B., "Status of durability of post tension tendons in France," *Durability of Post-tensioning tendons. fib-IABSE Technical Report, Bulletin 15. Workshop,* pp. 25–42, 2001.

[23] Mutsuyoshi H., "Present situation of durability of post-tensioned PC bridges in Japan," *Durability of Post-tensioning tendons. fib-IABSE Technical Report, Bulletin 15. Workshop*, pp. 75–88, 2001.

[24] Wicke M., "Repair and strengthening of damaged tendons and structures," *Durability of Post-tensioning tendons. fib-IABSE Technical Report, Bulletin 15. Workshop,* 2001.

[25] Japan Society of Civil Engineers, "Standard specifications for concrete structures, materials and construction," vol. No. 16, 2007.

[26] Proverbio E. and Bonaccorsi L.M., "Failure of prestressing steel induced by crevice corrosion in prestressed concrete structures," University of Messina Italy, 9DBMC-2002 Paper 026, 2002.

[27] Wada Y., Kimura Y., and Hanai T., "Study on grout conditions of existing prestressed concrete bridges", Accessed: Apr. 06, 2022. [Online]. Available: https://www.pwri.go.jp/eng/ujnr/tc/g/pdf/28/28-8-4_Wada.pdf

[28] Kamada T., "The latest non-destructive inspection technologies for evaluation of grouting condition of tendon ducts in prestressed concrete beams," 2013.

[29] Moore D.G., Klodt D.T., and Hensen R.J., "Protection of steel in prestressed concrete bridges, National Cooperative Highway Research Program Report 90," Colorado, 1970.

[30] Woodward R., "Durability of post-tensioned tendons on road bridges in the UK," *Durability of Post-tensioning tendons. fib-IABSE Technical Report, Bulletin 15. Workshop 15-16* , pp. 1–10, 2001.

[31] Jeon C., Nguyen C.D., and Shim C., "Assessment of mechanical properties of corroded prestressing strands," *Journal of Applied Science, Appl. Sci. 2020, 10, 4055; doi:10.3390/app10124055*, 2020.

[32] Schupack M. and Suarez M. G., "Some recent corrosion embrittlement failures of prestressing systems in the United States," *Journal of the Prestressed Concrete Institute, V. 27, No. 2*, pp. 38–55, 1982.

[33] ACI, "Corrosion and repair of unbonded single strand tendons," *Reported by ACI Committee 423, ACI 423.4R*, pp. 1–20, 1998.

[34] Chacos G.P., "Progressive deterioration caused by poor quality control and inadequate maintenance: the sad tale of a doomed parking structure," *Journal of Posttensioning Institute*, pp. 55–58, 2009.

[35] Harder J. and Webster N.R., "Durability of post-tensioning tendons: Canadian experience," *Durability of Post-tensioning tendons. fib-IABSE Technical Report, Bulletin 15. Workshop*, pp. 51–73, 2001.

[36] Central NEXCO (Central Nippon Expressway Company Ltd.), "Technical data on countermeasures for rupture of PC steel bar," 2009.

[37] Krauser L., "Repairs, modifications, and strengthening with post-tensioning," *Journal of Posttensioning Institute, V-4, No. 1*, pp. 24–40, 2006.

[38] Naso T.R., "A stitch in time saves nine: a post tensioning repair case study," *Journal of Post Tensioning Institute, V. 13, No. 2*, pp. 53–60, 2017.

[39] Hamada Y, Ishikawa Y., Mizoe M., and Miyagawa T, "Maintenance of prestressed concrete bridges, durability of post-tensioning tendons," in *fib-IABSE Technical Report, Bulletin 15. Workshop 15-1620*, 2001, pp. 109–120.

[40] Kimura Y., Tanaka Y., and Nakamura H., "Research on confirmation method of grout filling of PC bridge," 2009.

[41] Weerheijm J and Vegt I., "The dynamic fracture energy of concrete. Review of test methods and data comparison," *Korea Concrete Institute*, pp. 419–427, 2010.

[42] Riisgaard B., Ngo T., Mendis P., Georgakis C.T., and Stang H., "Dynamic Increase Factors for high performance concrete in compression using Split Hopkinson pressure bar," *Fracture Mechanics of Concrete and Concrete Structures http://www.cprosam.dk/*, 2007.

[43] Balokhonov R.R., Romanova V.A., and Schwab E.A., "the Influence of the Strain Rate on the Strength of the coating-substrate composition. Numerical modeling," *Nanoscience and Technology: An International Journal, Vol. 2, No. 3*, pp. 231–253, 2011.

[44] Oo H., Kano K., and Shinai S., "Comparative analysis of concrete and UFC construction subjected to impact loading," *J. Taisei Corp. No. 39*, 2006.

[45] Bischoff P.H. and Perry S.H., "Compressive behavior of concrete at high strain rates," *Materials and Structures Vol. 24, No. 6*, pp. 425–450, 1991.

[46] Wada S. A., "Bituminous pavement failures," *Int. Journal of Engineering Research and Applications ISSN: 2248-9622, Vol. 6, Issue 2, (Part - 4)*, pp. 94–100, 2016.

[47] Zenonas K., "Deterioration of bridge deck roadway members. Part I: site investigations," *The Baltic Journal of Road and Bridge Engineering, ISSN 1822-4288 online, Vol I, No 4*, pp. 177–184, 2006.

[48] Si W., Li N., Ma B, Tian Y., and Zhou X., "Temperature response to tensile characteristics of the hot asphalt mixtures," *KSCE Journal of Civil Engineering (2016) 20(4)*, pp. 1336–1346, 2016.

[49] Wei S., Ning L., Biao M., Yu-xiang T., and Xue-yan Z., "Temperature response to tensile characteristics of the hot asphalt mixtures," *KSCE Journal of Civil Engineering (2016) 20(4): DOI 10.1007/s12205-015-0688-2*, pp. 1336–1346, 2006.

[50] Bonger A.D., Hosoda A., Salem H., and Fukaya T., "Numerical simulation of asphalt pavement countermeasure at high temperature against protrusion of vertical PC bars using Applied Element Method," *Proc. of the 13th fib International PhD Symposium in Civil Engineering, ISSN: 2617-4820, ISBN: 978-2-940643-11-0, Paris, France*, pp. 144–151, 2021.

[51] Ding B., Xiaolong Z., Zixin P., and Xiang L., "Evaluation of fracture resistance of asphalt mixtures using the single-edge notched beams," *Advances in Materials Science and Engineering, Volume 2018, Article ID 8026798.*, 2018.

[52] Rui T., Zhenpeng Y., Guoqing L., Furong L., and Wenbin T., "Uniaxial dynamic compressive behaviors of hydraulic asphalt concrete under the coupling effect between temperature and strain rate," *MDPI Journals, Materials 2020, 13, 5348; doi:10.3390/ma13235348*, 2020.

[53] Tekalur S. A., Shukla A., Sadd M., and Lee K. W., "Mechanical characterization of a bituminous mix under quasi-static and high strain rate loading," *Construction and Building Materials, Vol. 23*, pp. 1795–1802, 2009.

[54] Bonger A. D, Hosoda A., Salem H., and Fukaya T., "Impact analysis of asphalt pavement against PC bar protrusion using Applied Element Method," *11th International Conference on Bridge Maintenance, Safety and Management*, ISBN 978-1-032-35623-5, DOI: 10.1201/9781003322641-15, 157-165, Barcelona, Spain, 2022.

[55] Jun W., Liang L., Xiuli D., and Xuemei L., "Numerical study on the asphalt concrete structure for blast and impact load using the Karagozian and case concrete model," *Journal of Applied Science, 2017, 7, 202; doi:10.3390/app7020202*, 2017.

[56] Kim Y., "Cohesive zone model to predict fracture in bituminous materials and asphaltic pavements: state of the art review pavements," *International Journal of Pavement Engineering 12:4,* pp. 343–356, 2011.

[57] Bonger A.D, Hosoda A., Salem H., and Fukaya T., "Numerical simulation of rupture and protrusion of vertically tightened PC steel bars in PC girders with asphalt pavement using Applied Element Method," *Journal of Japan Society of Civil Engineers*, vol. 10, pp. 145–161, 2022.

[58] Bonger D. A., Hosoda A., Salem H., and Fukaya T., "Numerical simulation of dynamic punching test of polyurea using Applied Element Method," *Japan Concrete Institute*, Vol.43, No.1., pp. 1103–1108, Nagoya, Japan, 2021.

[59] Broekaert M., "Polyurea spray coatings, the technology and latest developments," *Huntsman International LLC., Belgium,* 2002.

[60] Yi J., Boyce M.C., Lee G.F., and Balizer E., "Large deformation rate-dependent stress–strain behavior of polyurea and polyurethanes," *Polymer 47, Issue 1*, pp. 319–329, 2006.

[61] Bodin C., "Energy storage and dissipation in polyurea composites," *Massachusetts Institute of Technology, Master thesis, USA*, pp. 3–27, 2013.

[62] Cui J., Shi Y., Zhang X., Huang W., and Ma M., "Experimental study on the tension and puncture behavior of spray polyurea at high strain rates," *Polymer 93 (2020) 106863*, pp. 1–11, 2020.

[63] Sarva S.S., Deschanel S., Boyce M.C., and Chen W., "Deformation of polyurea: Where does the energy go?," *Polymer 105 (2016)*, pp. 227–233, 2016.

[64] Shimamoto K. and Yashiro K., "Spalling prevention method for tunnel lining using polyurea resin," *Railway Technical Research Institute, Vol. 58, No. 3*, pp. 217–222, 2017.

[65] Grujicic M., Pandurangan B., He T., Cheeseman B.A., Yen C.F., and Randow C.L, "Computational investigation of impact energy absorption capability of polyurea coatings via deformation-induced glass transition," *Materials Science and Engineering A 527*, pp. 7741–7751, 2010.

[66] Fallon C., "Blast and impact response of elastomer-coated concrete," *Peterhouse University of Cambridge, Doctoral thesis*, p. 96, 2018.

[67] Raman S. N., Jamil M., Ngo T., Mendis P., and Pham T., "Retrofitting of RC panels subjected to blast effects using elastomeric polymer coatings," *Proceedings of the Concrete Solutions, 5th International Conference on Concrete Repair. Belfast, UK.*, pp. 353–360, 2014.

[68] Aoki S. and Someya A., "Reinforcing effect of PCM pavement on deteriorated RC deck," *Pavement, Vol.56, No.1*, pp. 17–22, 2021.

[69] Yang L., Lin X., and Gravina R.J., "Evaluation of Dynamic Increase Factor models for steel fiber reinforced concrete," *Construction and Building Materials 190*, pp. 632–644, 2018.

[70] Tagel-Din H. and Meguro K., "Applied element simulation for collapse analysis of structures," *Bulletin of Earthquake Resistance Structures*, vol. No. 32, pp. 113–123, 1999.

[71] Meguro K. and Tagel-Din H, "Applied Element Method used for large displacement structural analysis," *Journal of Natural Disaster Science, Vol. 24, No. 1*, pp. 25–34, 2002.

[72] Tagel-Din H. and Meguro K., "Nonlinear simulation of RC structures using Applied Element Method," *Journal of Doboku Gakkai Ronbunshu, Vol. 17, No. 654*, pp. 13–24, 2000.

[73] Tagel-Din H. and Meguro K., "Applied Element Method for structural analysis, theory and application for linear materials," *Journal of Doboku Gakkai Ronbunshu, No. 647*, pp. 31–45, 2000.

[74] Tagel-Din H. and Meguro K., "Applied Element Method for dynamic large deformation analysis of structures," *Structural Eng. / Earthquake Eng., JSCE, Vol. 17, No. 2*, pp. 215–224, 2000.

[75] Extreme Loading for Structures, "Applied Science International," *Available at: http://www.Extreme Loading for Structures (ELS)*, 2017.

[76] Maekawa K., "The deformational behavior and constitutive question of concrete using the elasto-plastic fracture model," *J Fac Eng Univ Tokyo (B). 1983;37(2)*, pp. 253–328, 1983.

[77] Menegotto M. and Pinto PE, "Method of analysis for cyclic loaded R. C. plane frame including changes in geometry and non-elastic behavior of elements under combined normal force and bending," *Proceedings of IABSE Symposium on Resistance and Ultimate Deformability of Structures Acted on by Well Defined Repeated Loads 1986;11*, pp. 15–22, 1973.

[78] Helmy H., Salem H., and Mourad S., "Progressive collapse assessment of framed reinforced concrete structures according to UFC guidelines for alternative path method," *Engineering Structures, Vol. 42*, pp. 127–141, 2012.

[79] Salem H. and Helmy H, "Numerical investigation of collapse of the Minnesota I-35W bridge," *Engineering Structures, Vol. 59*, pp. 635–645, 2014.

[80] Salem H., Mohssen S., Kosa K., and Hosoda A., "Collapse analysis of Utatsu Ohashi bridge damaged by Tohoku tsunami using Applied Element Method," *Journal of Advanced Concrete Technology, Vol. 12*, pp. 388–402, 2014.

[81] Elshaer A., Mostafa H., and Salem H., "Progressive collapse assessment of multistory reinforced concrete structures subjected to seismic actions," *KSCE Journal of Civil Engineering, Vol. 21*, pp. 184–194, 2016.

[82] Garofano A. and Lestuzzi P, "Seismic assessment of a historical masonry building in Switzerland: The "Ancien Hôpital De Sion," *International Journal of Architectural Heritage, Vol. 10*, pp. 975–992, 2016.

[83] Cismasiu C., Ramos A. P., Moldovan I. D., Ferreira D. F., and Filho J. B., "Applied element method simulation of experimental failure modes in RC shear walls," *Computers and Concrete, Vol. 19 (4)*, pp. 365–374, 2017.

[84] Zerin A., Hosoda A., Salem H., and Amanat K., "Seismic performance evaluation of masonry infilled reinforced concrete buildings utilizing verified masonry properties in Applied Element Method," *Journal of Advanced Concrete Technology, Vol. 15*, pp. 227–243, 2017.

CHAPTER 3

AEM SIMULATION OF RUPTURE AND PROTRUSION OF PRESTRESSING STEEL BAR WITHOUT CONSIDERING COUNTERMEASURE

3.1 General

In this chapter, the effect of 15 mm cover concrete (assuming bottom of a bridge girder) on preventing protrusion of prestressing steel bar (PC bar) was investigated. Numerical simulation of rupture and protrusion of PC bars was conducted using the Applied Element Method. The numerical simulations were verified with the experimental results. In the process of verification, many influential parameters, such as the effects of contact stiffness between elements, fracture energy of concrete, mesh sensitivity, time interval sensitivity, material properties, and strain rate effect, were investigated. The numerical simulation was required to investigate the protrusion behavior of PC bar and the failure mechanism of cover concrete.

3.2 Experimental Program

a) Details of specimen

The details of the specimen with 15 mm cover concrete simulating the bottom of a bridge girder is shown in Fig. 3.1. PC bar rupture length was 4.5 m. In MEX, there are very few vertical PC bars longer than 4.5 m. The diameter of the PC bar tendon was ϕ32 mm and that for the sheath was ϕ45 mm. The sheath was not grouted. Cover concrete was 15 mm.

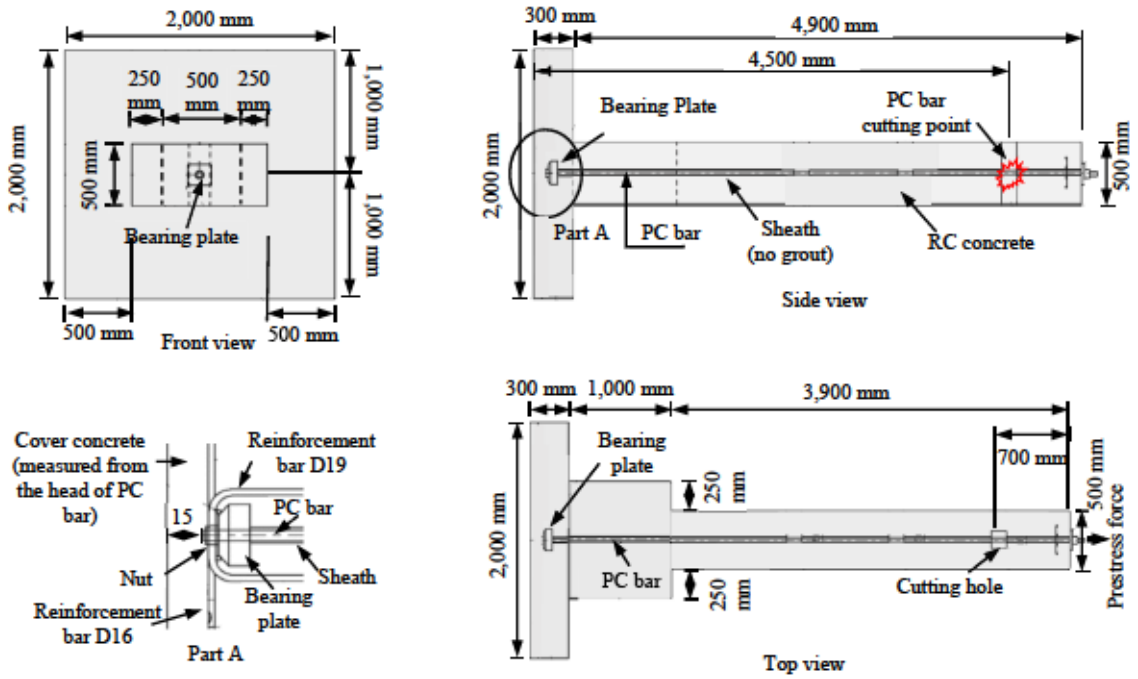

Fig. 3.1 Specimen details with 15 mm cover concrete [1]

b) Materials

The concrete had a compressive strength of 40 MPa. The PC bar tendon was standard steel bar: SBPR930/1180 (class B2 in JIS). The applied prestress force, after the prestress loss due to relaxation, creep and shrinkage, was 591 kN (0.6Pu). Strain energy of the PC bar was 4,408 J. Non-shrinking mortar was used in the anchor zone, whose compressive strength was 60 MPa.

c) Testing procedure

Fig. 3.2 shows the experimental setup. The PC bar was inserted into the sheath. The PC bar had no contact with the sheath during prestressing. The sheath was not grouted. Tension force was applied to the PC bar. The PC bar was cut using a grinder at 4.5 m from the PC bar head. Then, the protrusion of the PC bar and concrete spalling were investigated.

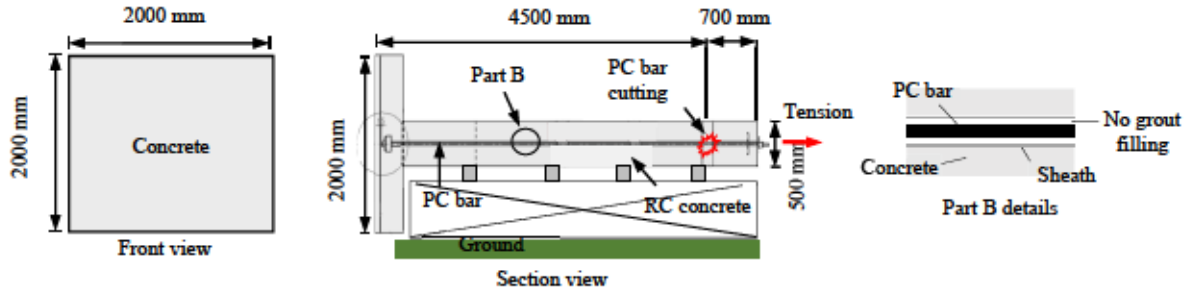

Fig. 3.2 Experimental setup for the specimen with 15 mm cover concrete [1]

3.3 Element Contact in the Extreme Loading for Structure (ELS)

In ELS, elements may separate and contact, re-contact again, or contact other elements (Fig. 3.3a). When two elements with different material properties collide, the spring properties are governed by the material with softer properties [2]. When contact occurs between elements, three contact springs are added at each contact point; one normal spring and two shear springs. The stiffness values for the normal contact spring and the shear contact spring are shown in Equation (3.1) and (3.2). Those springs are linear springs that transfer energy between the elements as shown in Fig. 3.3b and Fig. 3.3c.

The contact normal spring stiffness is calculated as:

$$K_n = E\ NF\ D \qquad (3.1)$$

Where, K_n: (N/mm) contact normal spring stiffness,

E: (N/mm^2) Young's Modulus of softer material of the two collided elements,

NF: normal contact stiffness factor,

D: (mm) the distance between the centers of contacting elements

The contact shear spring stiffness is calculated as:

$$K_s = G\ SF\ D \qquad (3.2)$$

Where, K_s: (N/mm) contact shear spring stiffness,

G: (N/mm^2) shear Modulus of softer material of the two collided elements,

SF: shear contact stiffness factor,

D: (mm) the distance between the centers of contacting elements

When shear force is larger than (*friction coefficient* × *Normal force*), the shear stiffness is multiplied by the minimum shear stiffness factor (0.001).

Contact Spring Unloading Stiffness Factor (n) express the effect of energy dissipation during contact. Referring to Fig. 3.3d, the ratio between unloading and loading stiffness is defined as n. For example, a value of unity for n means no energy dissipation during collision, while a value of 2 means half the kinetic energy is lost due to collision.

In ELS, friction coefficient (μ) is available for all material models. It is effective when the contact springs between elements are generated (Fig. 3.3e).

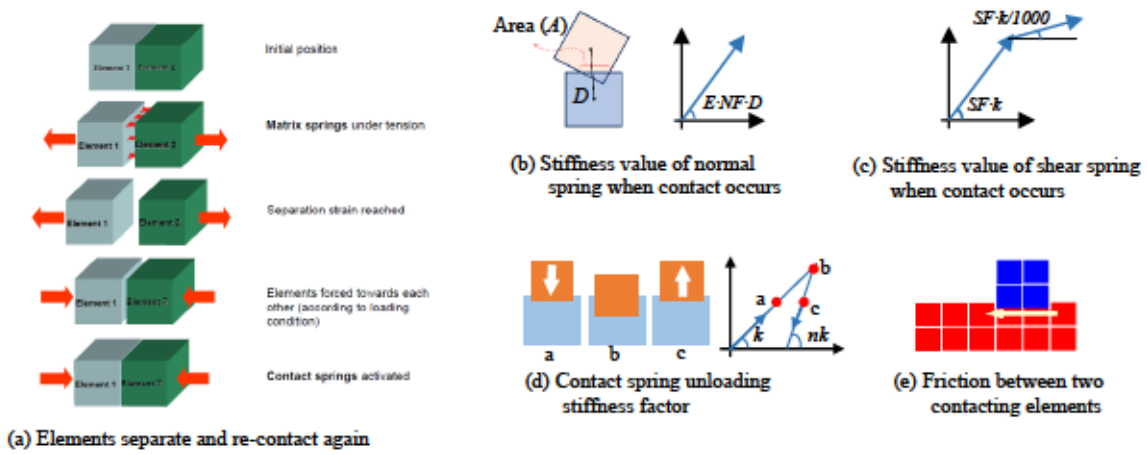

(a) Elements separate and re-contact again

(b) Stiffness value of normal spring when contact occurs

(c) Stiffness value of shear spring when contact occurs

(d) Contact spring unloading stiffness factor

(e) Friction between two contacting elements

Fig. 3.3 Element contacts in ELS [2]

3.4 Sensitivity Analysis for Element Contact and Time Interval

a) Element Contact Sensitivity Analysis

The contact between the PC bar and the sheath has an effect on PC bar protrusion. In the experiment of the specimen shown in Fig. 3.1, after the rupture of the PC bar, a camera was inserted into the sheath to detect the contact between the PC bar and the sheath. Eight contact locations were detected as shown in Fig. 3.4a. At locations 1 to 4, the PC bar contacted the sheath with no severe damage. While the PC bar was protruding in the sheath, the gravity pulled the PC bar down and impacted the sheath with more damage at locations 5, 6, 7, and 8. At location 5, the PC bar contacted the sheath on the top surface of the sheath; however, at locations 6, 7, and 8, the contact was on the bottom surface of the sheath (Fig. 3.4b). Similarly, element contact between the PC bar and the sheath was observed in the numerical simulation [1] as shown in Fig. 3.4c. After the rupture of the PC bar, the distribution of normal force in the PC bar was not constant. This could be explained by a dynamic

wave transmission along the bar due to sudden loss of its axial force. This caused the PC bar to be energetic and unstable while protruding in the sheath. When the PC bar moved inside the sheath, gravity pulled the PC bar down and made contact with the sheath.

The effects of element contacts were investigated using a simplified model [1]. This simplified model (Fig. 3.5) was prepared based on the details shown in Fig. 3.1, where the concrete and the reinforcement bars were removed to reduce analysis time. In this case, the bearing plate and the sheath were completely restrained. Rupture length was 4.5 m from the PC bar head. The "bearing material" in ELS, which can transfer only compression, was used for the interface between the PC bar and the sheath, and for the interface between the PC bar and the bearing plate. Table 3.1 shows the geometry and materials of the simplified model.

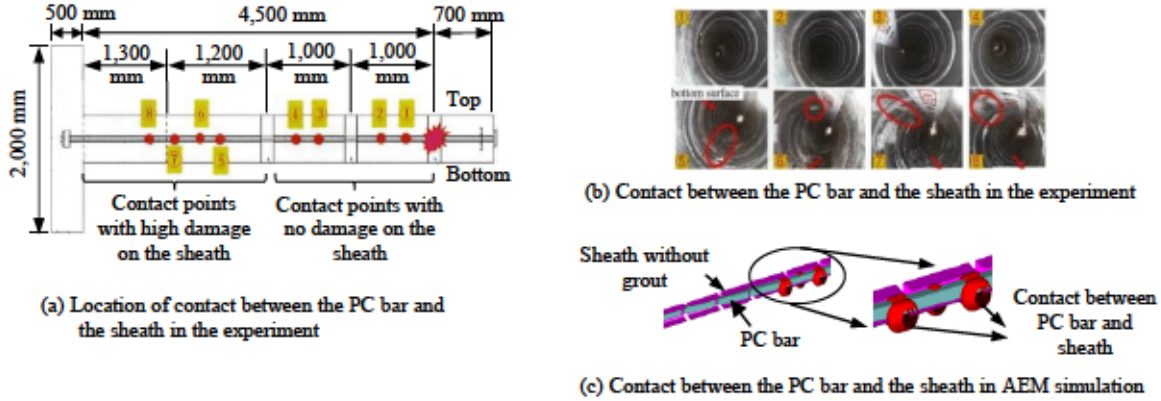

(a) Location of contact between the PC bar and the sheath in the experiment

(b) Contact between the PC bar and the sheath in the experiment

(c) Contact between the PC bar and the sheath in AEM simulation

Fig. 3.4 Contact between the PC bar and the sheath

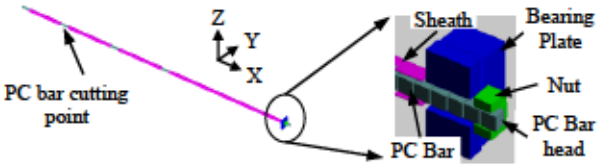

Fig. 3.5 Simplified numerical model to study the effect of element contact

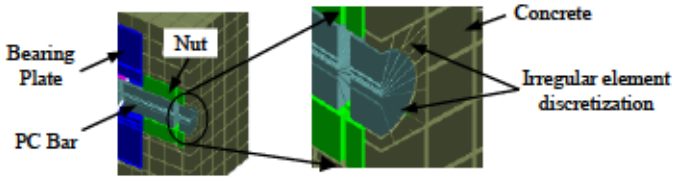

Fig. 3.6 Irregular element discretization in ELS

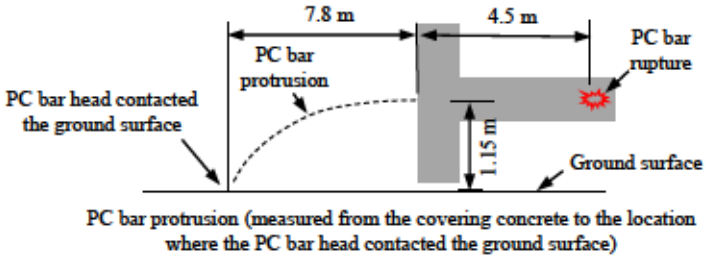

Fig. 3.7 Illustration of PC bar protrusion in the experiment

Table 3.1 Geometry and materials for simplified model

Objects	Geometry		Element size (mm)	Material
	Cross section in Y and Z axis (mm)	Length along X axis (mm)		
PC bar	28.36 × 28.36	5,336	28.36 × 28.36 × 28.36	High strength steel
Nut	62 × 62	34	34 × 62 × 62	
Bearing plate	160 × 160 (40 × 40 hole)	84	84 × 160 × 160	Normal steel
Sheath	40 × 40	5,060	126 × 40 × 40	

In this study, a rectangular-shaped PC bar, sheath, and nut were used to avoid irregular element discretization. When the concrete intersected with round-shaped PC bar and nut, irregular-shaped elements formed as shown in Fig. 3.6. This had effect on shear crack formation in the concrete when the PC bar impacted with the concrete. However, when a rectangular PC bar and sheath were used, the contacting area between the PC bar and the sheath was larger than the contacting area between the round PC bar and sheath. The contacting area between the PC bar and the sheath had an effect on PC bar protrusion. Therefore, appropriate contact parameters should be used to accurately obtain the PC bar protrusion as shown in Fig. 3.7.

From parametric study using the simplified model (Fig.3.5), it was found that the element contact parameters (coefficient of friction (μ), normal contact stiffness factor (*NF*), shear contact stiffness factor (*SF*), and contact spring unloading stiffness factor (n)) had noticeable effects on the PC bar protrusion [1]. When one of the element contact parameter was evaluated, the other element contact parameters were fixed as default values. For example, when *NF* value of the PC bar was evaluated at 1.0E-0.8, the other contact parameters (*SF*, μ and n) of the PC bar and *NF*, *SF*, μ, and n of sheath, bearing plate and ground surface were set to the default values. In ELS, the default values of the element contact parameters (*NF*, *SF*, μ, and n) are 1.0E-0.4, 1.0E-0.5, 0.8, and 2, respectively. The following charts show the effects of element contact on protrusion of the PC bar. In this study, the PC bar protrusion length was measured from the surface of covering concrete (Fig. 3.7).

The results of this parametric study indicated that the *NF* values of the PC bar smaller than around 1.0×10^{-6} had a significant effect on the PC bar protrusion. The PC bar protrusion was around 8,000 mm when the *NF* value was less than 1.0×10^{-8}. The PC bar protrusion decreased to 870 mm when the *NF* value was greater than 1.0×10^{-6} as shown in Fig. 3.8a. Setting a very high contact stiffness value of the PC bar causes a large shock force to transfer between the PC bar and the sheath, which results in a very small PC bar protrusion. Setting a low contact stiffness value causes underestimation of transmitted forces when elements collide, which results in a very large PC bar protrusion and

penetration of PC bar into the sheath. From this parametric study, *NF* value of 0.5×10^{-8} for the PC bar gave a result close to the experiment as shown in Fig. 3.7. However, *NF* values of the sheath, the bearing plate, and the bearing interface material had little effect on the PC bar protrusion.

After setting the *NF* value of the PC bar as 0.5×10^{-8}, further investigation was carried out for *SF*, μ, and n. The *SF* value of the PC bar and the ground surface material (bearing material) had a significant effect on PC bar sliding over the ground surface. The *SF* value of the PC bar and of the ground surface material smaller than 1.0×10^{-7} resulted in larger sliding of the PC bar over the ground surface between 13,000 mm and 15,000 mm as shown in Fig. 3.8b. On the other hand, μ and n had little effect on the PC bar protrusion.

From the element contact analysis, it can be concluded that the *NF* of the PC bar affects the PC bar movement inside the sheath and over the ground surface and the *SF* of the ground surface material affects the PC bar sliding over the ground surface. Therefore, appropriate values should be set for contact spring stiffness.

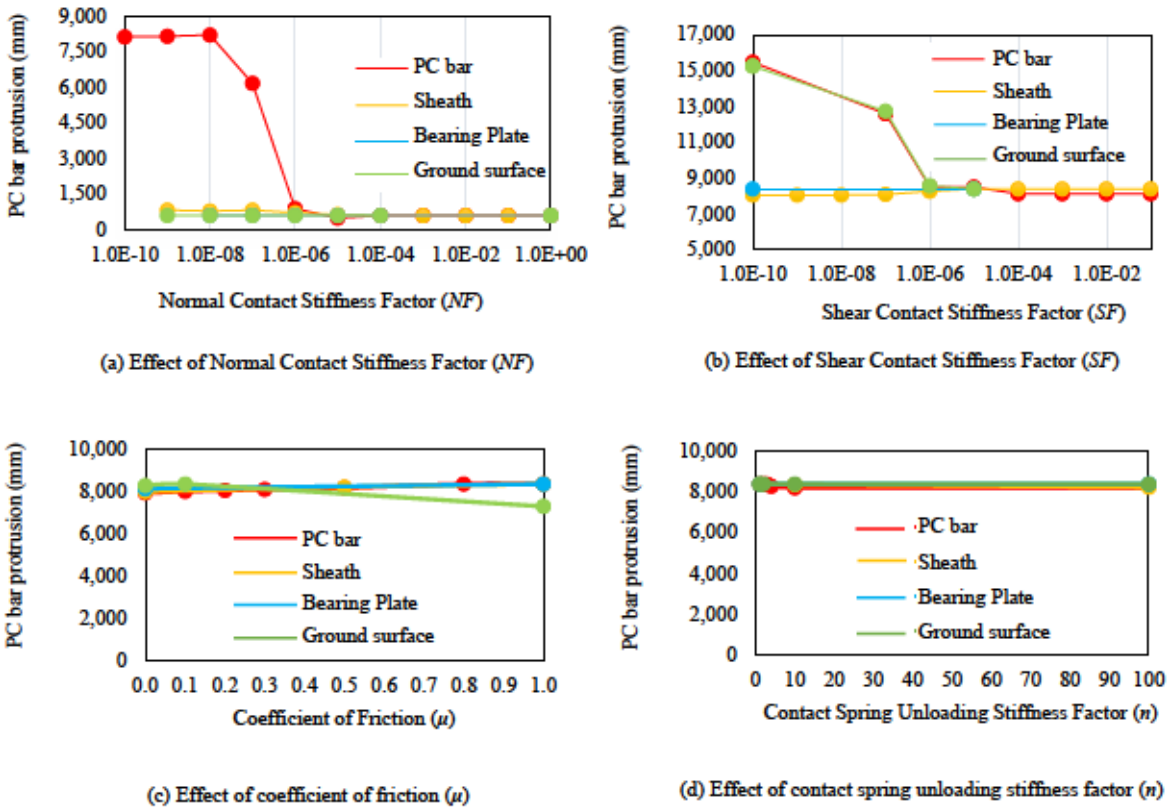

Fig. 3.8 The effects of element contacts on PC bar protrusion [1]

b) Sensitivity Analysis of Time Interval

The impact force of the PC bar on cover concrete is a transient force applied in a very short time. Therefore, a sensitivity study was carried out to obtain the largest possible time increment that can be used without affecting the results. Small time interval is necessary for accurate simulation, but it will significantly increase the simulation time.

In the analysis, three stages of loading were provided. The first one was static loading to account for prestressing stage, while the second and the third ones were dynamic to simulate the rupture of the PC bar and its impact on cover concrete. In the second stage, the rupture of the PC bar was simulated by suddenly removing one element of the PC bar at the cut point. The first dynamic stage had a duration of 0.7 s with a time interval of 5.0×10^{-6} s and the second dynamic stage had a duration of 0.4 s with a time interval of 1.0×10^{-3} s were found appropriate by sensitivity analysis. During the first dynamic stage, the PC bar was energetic, and the cover concrete was under a high loading rate and it was necessary to use smaller time interval for accurate simulation. On the other hand, during the second dynamic stage, most of the energy of the PC bar was dissipated, and the crushing of concrete was almost finished. To save on simulation time, a larger time interval (1.0×10^{-3} s) was used for the second dynamic stage without affecting the result.

3.5 Verification of AEM Simulation

AEM numerical simulation was made for the specimen shown in Fig. 3.1. Geometry and materials of the PC bar, the bearing plate, the nut, and the sheath are shown in Table 3.1. The interface material between the sheath and the PC bar and that between the bearing plate and the PC bar were modeled using "bearing material" (a material that can transfer only compression). On the other hand, the interface material between concrete and other metal materials (the PC bar, the nut, the bearing plate, and the sheath) was modeled as normal concrete (40 MPa compressive strength).

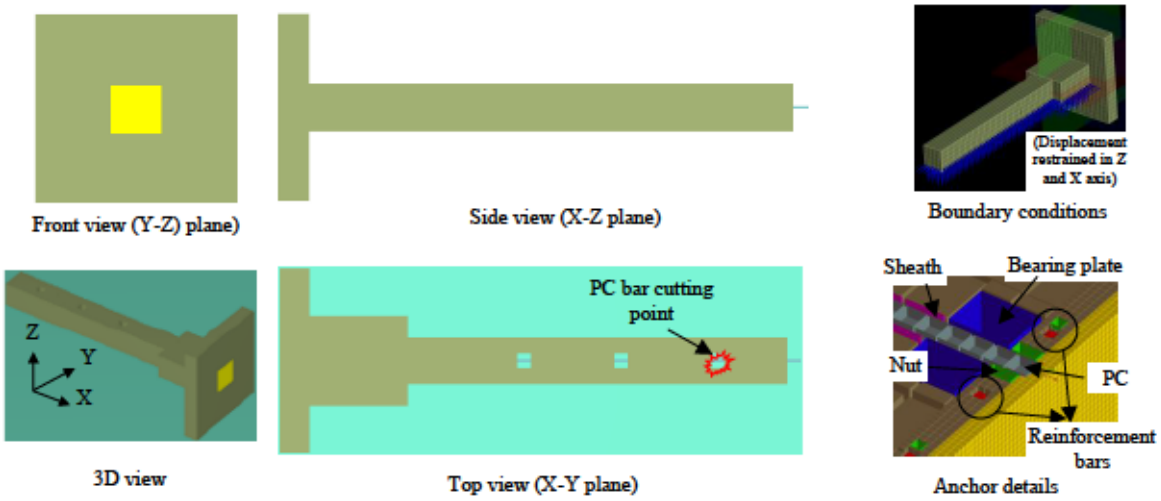

Fig. 3.9 AEM numerical simulation [1]

In this research, ELS version 6 was used as a nonlinear structural analysis tool. In this version, for modelling concrete under compression, the model of Maekawa, including unloading and reloading, is adopted [3]. However, for modeling of concrete under tension, fracture energy (G_f) was not considered. According to this model, the concrete tensile stress suddenly drops to zero after reaching the tensile strength as shown in Fig. 3.10a. To overcome this drawback and to consider the contribution of fracture

energy of concrete in tension, the tensile strength (f_t) was increased to an equivalent tensile strength (f_{t_e}) to consider fracture energy in the numerical simulation as shown in Fig. 3.10b. The equivalent tensile strength (f_{t_e}) can be calculated from the fracture energy of concrete using Equation (3.3). Fracture energy of the normal concrete can be obtained from the maximum aggregate size using Equation (3.4) [4]. Fig. 3.10c shows the tension softening curve adjusted based on finite element length [5]. Based on this method, fracture energy dependent on mesh size was considered in this research. Consideration of fracture energy using this method improved energy absorption of concrete (Fig. 3.11).

$$G_f = \left(\frac{f_{t\_e} + f_t}{2}\right)\left(\frac{f_{t\_e} - f_t}{E}\right) \cdot l \tag{3.3}$$

Where, G_f: (N/mm) fractur energy,

E: (N/mm^2) Young's Modulus of concrete,

f_{t_e}: (N/mm^2) equivalent tensile strength,

l: (mm) element size

$$G_f = 10(d_{\max})^{1/3}(f'_{ck})^{\frac{1}{3}} \tag{3.4}$$

Where G_f: (N/m) fracture energy,

$d_{\max}$: (mm) maximum aggregate size,

f'_{ck}: (N/mm^2) compressive strength

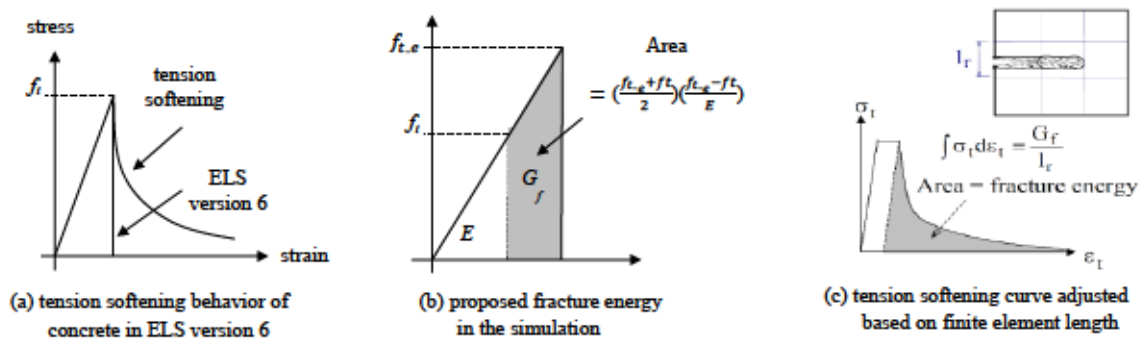

(a) tension softening behavior of concrete in ELS version 6

(b) proposed fracture energy in the simulation

(c) tension softening curve adjusted based on finite element length

Fig. 3.10 Consideration of fracture energy of concrete in ELS Version-6

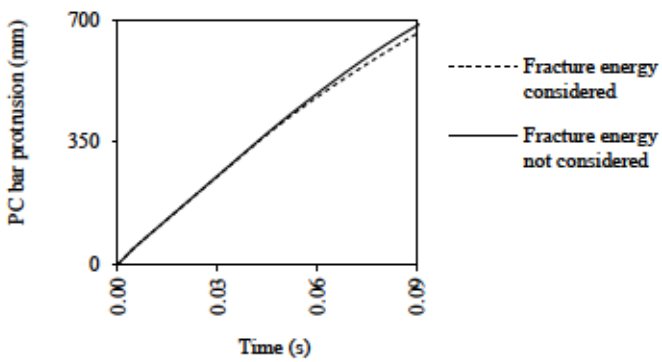

Fig. 3.11 Effect of proposed fracture energy of concrete on PC bar protrusion (PC bar ruptured at 1 m)

Fig. 3.12 shows the protrusion of the PC bar and concrete spalling both in the experiment and in the numerical simulation at different times. The protrusion of the PC bar was very fast and energetic. At around 0.4 s after the rupture, the PC bar was fully outside of the sheath. The numerical simulation showed that, at 0.584 s, the PC bar made first contact with the ground surface (7.1 m from the cover concrete). On the other hand, the experiment showed that the PC bar made first ground contact at around 0.6 - 0.7 s (7.8 m from the cover concrete). The AEM numerical simulation showed good agreement with experimental results in terms of protrusion behavior.

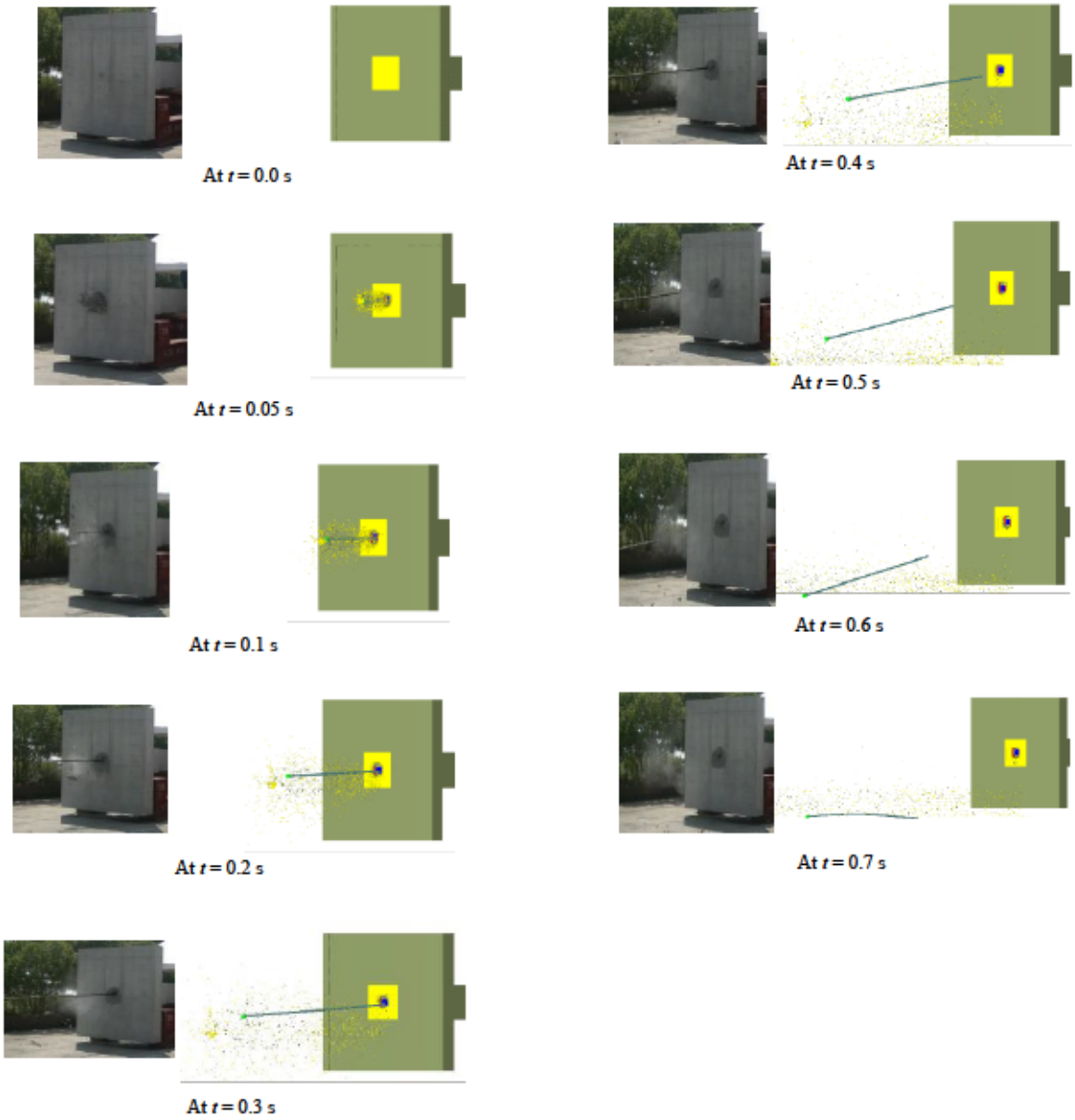

Fig. 3.12 AEM numerical simulation about protrusion of PC bar [1]

The 15 mm cover concrete was destroyed and spalled. The cover concrete spalling had a size of around 40 cm × 43 cm area (Fig. 3.13a). The concrete spalling was limited to the center of the specimen. One of the reasons could be the large amount of reinforcing bars in the cover concrete, which were arranged to prevent damaging during prestressing.

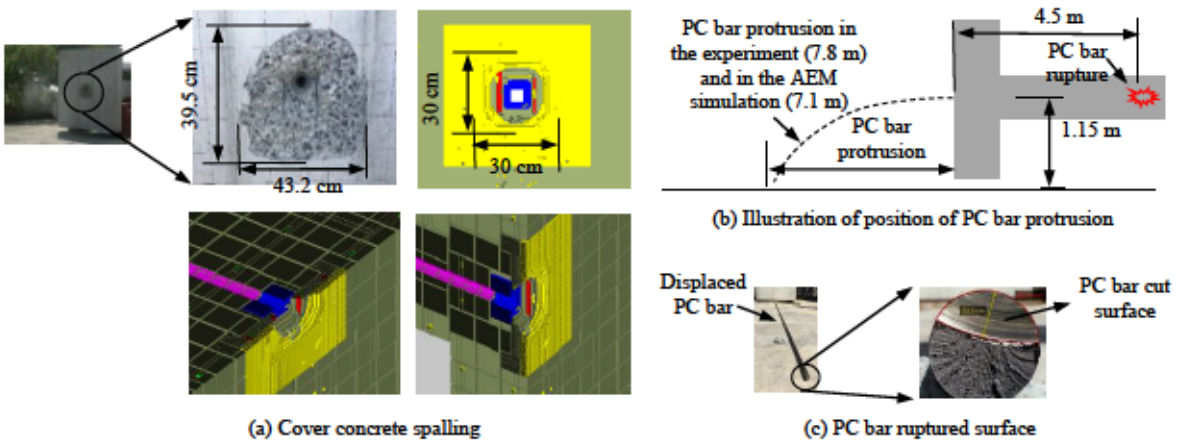

(a) Cover concrete spalling

(b) Illustration of position of PC bar protrusion

(c) PC bar ruptured surface

Fig. 3.13 Cover concrete spalling, illustration of PC bar protrusion and PC bar ruptured surface [1]

Fig. 3.14a shows the progress of the protrusion of the PC bar. The velocity of the PC bar was also investigated. The investigation results indicated that the velocity of the PC bar was fluctuating (not steady throughout the dynamic stage (Fig. 3.14b). The main reason was that the distribution of normal force in the PC bar was not constant throughout the time. This could be explained by a dynamic wave transmission along the bar due to sudden loss of its axial force.

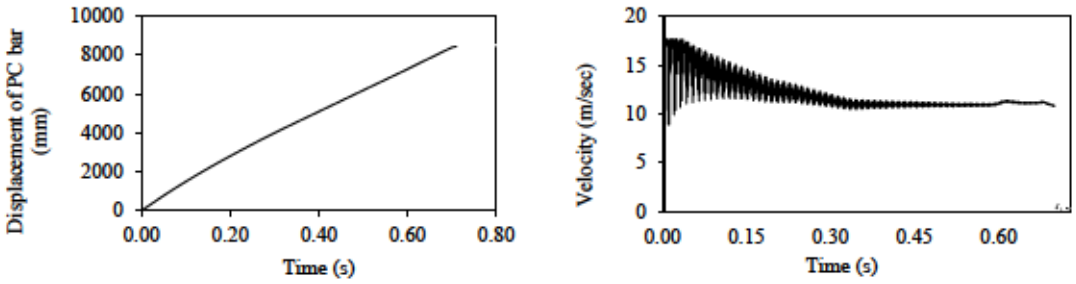

(a) Protrusion of PC bar (AEM numerical simulation)

(b) Velocity of PC bar (AEM numerical simulation)

Fig. 3.14 Protrusion of PC bar and velocity of PC bar [1]

The strain rate was checked in the numerical simulation results for the normal spring between the PC bar and the cover concrete and between the nut and the cover concrete. The average maximum strain rate for the spring between the PC bar and the cover concrete was found to be 97.7/s and that for the spring between the nut and the cover concrete was 89.7/s. For plain concrete under high loading rate, the compressive strength, tensile strength, and elastic modulus should be increased with an increase in strain rate [6]. The dynamic increase factors (*DIF*), the ratio of the dynamic strength to quasistatic strength, of concrete under compression and tension at a high loading rate (strain rate > 30/s) can be calculated using Equation (2.3) and (2.4) [7]. In the numerical simulation, for the normal spring between the PC bar and the cover concrete and between the nut and the cover concrete, the quasistatic compressive and tensile strengths and Young's Modulus of concrete were multiplied by the respective *DIF* as shown in Table 3.2. For example, 83.6 MPa, a product of 40 MPa quasistatic strength and *DIF* of 2.09, was used as compressive strength for the spring between the PC bar and the cover concrete.

Table 3.2 The Dynamic Increase Factors [8]

Material Properties	Dynamic Increase Factor (*DIF*)	
	Springs between PC bar and cover concrete	Springs between nut and cover concrete
Young's modulus	1.48	1.47
Tensile strength	2.42	2.35
Compressive strength	2.09	2.03

3.6 Summary of Chapter 3

Based on experimental and numerical simulation using the Applied Element Method to study the rupture and protrusion of prestressing steel bar, the following conclusions were obtained:

- Appropriate numerical simulation with the AEM can be conducted with appropriate interface material property between the PC bar and the sheath, considering the fracture energy of concrete, with appropriate mesh discretization, appropriate time interval, appropriate Normal Contact Stiffness Factor (*NF*), and considering strain rate effects in concrete.
- Cover concrete of 15 mm alone could not prevent the protrusion of a PC bar of 4.5 m rupture length.

References in Chapter 3:

[1] Bonger A.D, Hosoda A., Salem H., and Fukaya T., "Numerical simulation of rupture and protrusion of vertically tightened PC steel bars in PC girders with asphalt pavement using Applied Element Method," *Journal of Japan Society of Civil Engineers*, vol. 10, pp. 145–161, 2022.

[2] Extreme Loading for Structures, "Applied Science International," *Available at: http://www.Extreme Loading for Structures (ELS)*, 2017.

[3] Maekawa K. and Okamura H, "The deformational behavior and constitutive equation of concrete using the elasto-plastic and fracture model," *Journal of the Faculty of Engineering, The University of Tokyo (B), Vol. 37 (2)*, pp. 253–328, 1983.

[4] JSCE, "Standard specifications for concrete structures (design)," *Guideline for concrete, Tokyo: JSCE, ISBN 978-4-8106-0777-2*, p. 42, 2017.

[5] Maekawa K., Pimanmas A., and Okamura H., "Non-linear mechanics of reinforced concrete," *CRC Press*, pp. 29–31, 2003.

[6] Bischoff P.H. and Perry S.H., "Compressive behavior of concrete at high strain rates," *Materials and Structures Vol. 24, No. 6*, pp. 425–450, 1991.

[7] Oo H., Kano K., and Shinai S., "Comparative analysis of concrete and UFC construction subjected to impact loading," *J. Taisei Corp. No. 39*, 2006.

[8] Bonger, A., Hosoda, A., Hamed, S., Kaba, K., "Numerical simulation of rupture protrusion of vertically tightened PC steel bars using Applied Element Method." *Internet Journal of Society for Social Management Systems*, Vol.12 Issue 1 sms19-3671, ISSN: 844 2432-552X, pp.107-116, Tokyo, Japan, 2019.

CHAPTER 4

AEM SIMULATION OF RUPTURE AND PROTRUSION OF PRESTRESSING STEEL BAR CONSIDERING ASPHALT PAVEMENT

4.1 General

A 3D Applied Element Method (AEM) model was developed for simulating asphalt pavement at 0°C, 28°C and 50°C under extreme impact energy (4,408 J) generated from a ruptured prestressing steel bar. The asphalt pavement material models were calibrated using asphalt pavement bending test results. The bending properties of asphalt pavement at different temperature were numerically investigated. The effects of temperature on asphalt pavement system on preventing the protrusion of PC bars and concrete spalling were numerically investigated. The *DIF* was employed to accurately capture the dynamic material behavior of the asphalt pavement under high loading rate. The failure mode of the asphalt pavement under 4,408 J impact energy was numerically investigated in detail.

In the MEX, the asphalt pavement over bridge deck has two layers. In this study, in order to simulate the worst condition in reality (time dependent deterioration), in one specimen, the cover layer was excluded and only the base layer was investigated in terms of its performance in preventing the protrusion PC bars with 4,408 J impact energy at 20°C.

4.2 AEM Simulation of Rupture and Protrusion of Prestressing Steel Bar with Asphalt Pavement at 28°C (Normal Temperature)

4.2.1 Experimental Program

a) Details of Specimen

The details of the specimen with 80 mm thick asphalt pavement simulating the top of a bridge girder are shown in Fig. 4.1. PC bar rupture length was 4.5 m. The diameter of the PC bar tendon was ϕ32 mm and that for the sheath was ϕ45 mm. The sheath was not grouted. Cover thickness was 0 mm (cover thickness was measured between head of the PC bar and the cover concrete) simulating the worst situation in reality. Two-layered asphalt pavement was provided in this specimen. The asphalt pavement system had a total thickness of 80 mm with 2 m × 2 m area. The base layer (guss asphalt pavement) in the two layers had a thickness of 50 mm, and the cover layer had a thickness of 30 mm. Fig. 4.2 shows the fabrication of this specimen. The base layer and the cover layer were placed over a 2 m × 2 m RC concrete (the first part) and compacted layer by layer. Then, it was transported to the experiment site and connected to the second part of the specimen. The two RC concrete parts were connected using connecting PC bars (ϕ32 mm). A coupler was used to connect the main PC bar tendons. The coupler did not affect the experimental results.

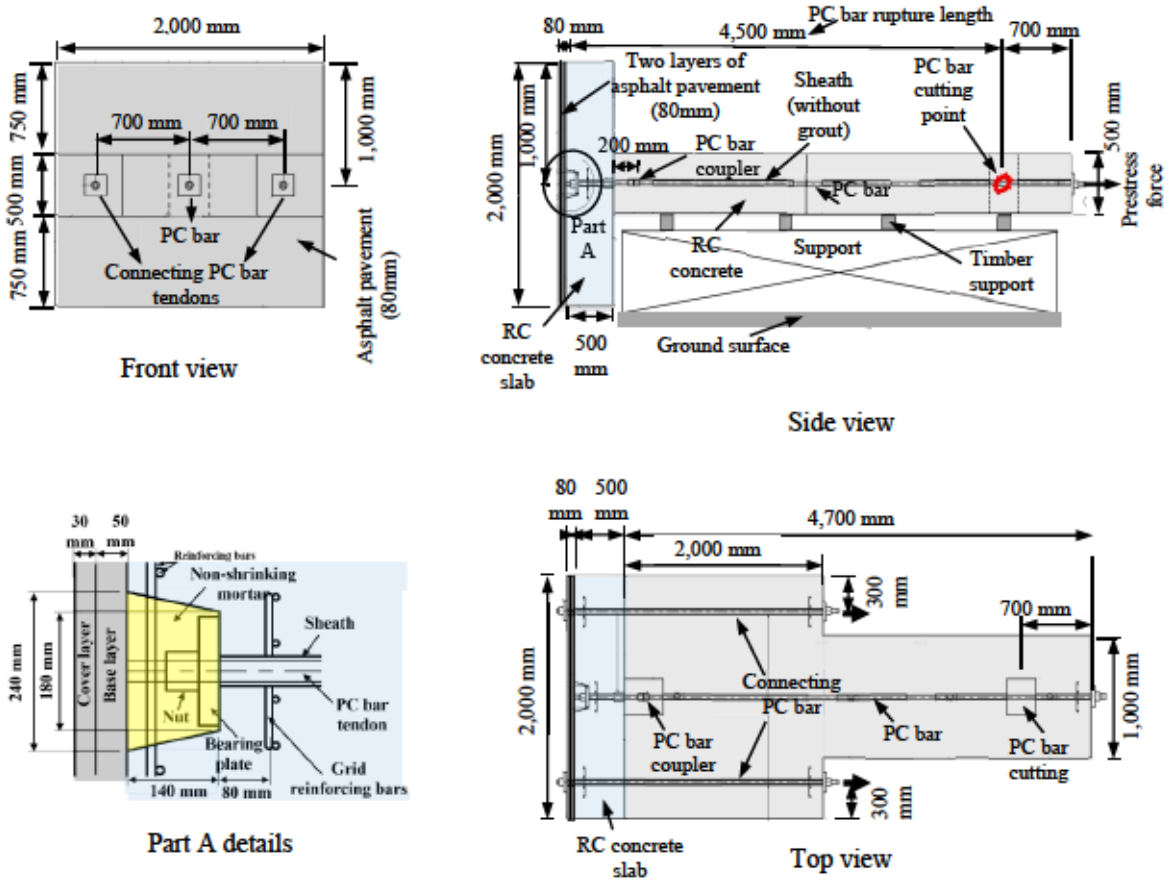

Fig. 4.1 Specimen details with 80mm thick asphalt pavement [1]

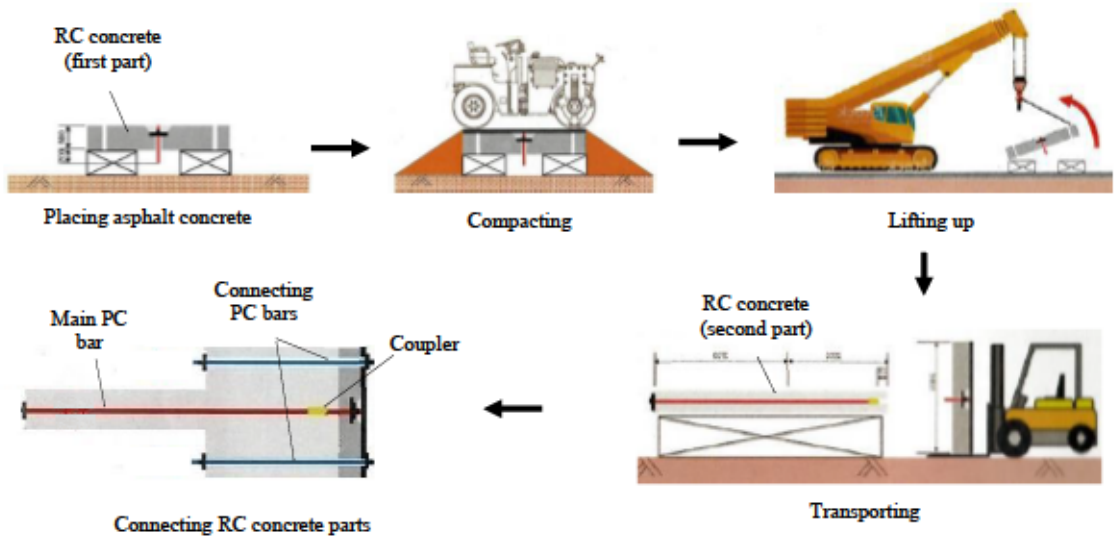

Fig. 4.2 Fabrication of the specimen with 80 mm thick asphalt pavement [1]

b) Materials

The concrete had a compressive strength of 40 MPa. The PC bar was standard steel bar: SBPR930/1180 (class B2 in JIS). The applied prestress force, after the prestress loss due to relaxation, creep and shrinkage, was 591 kN ($0.6P_u$). Strain energy of the PC bar was 4,408 J. The two asphalt

pavement layers (cover layer and guss asphalt base layer) had different material properties. Bending tests for asphalt materials were conducted in this study. Non-shrinking mortar was used in the anchor zone, whose compressive strength was 60 MPa.

c) Testing Procedure

Fig. 4.3 shows the experimental procedure for the specimen shown in Fig. 4.1. The main PC bar and the connecting PC bars were inserted into the sheath. The main PC bar and the connecting PC bars had no contact with the sheath during prestressing. The sheath was not grouted. Tension force was applied to the main PC bar and the connecting PC bars. Non-shrinking mortar was placed in the anchor zone. The main PC bar was cut using a grinder at 4.5 m from the PC bar head. Then, the effectiveness of the asphalt pavement system was investigated.

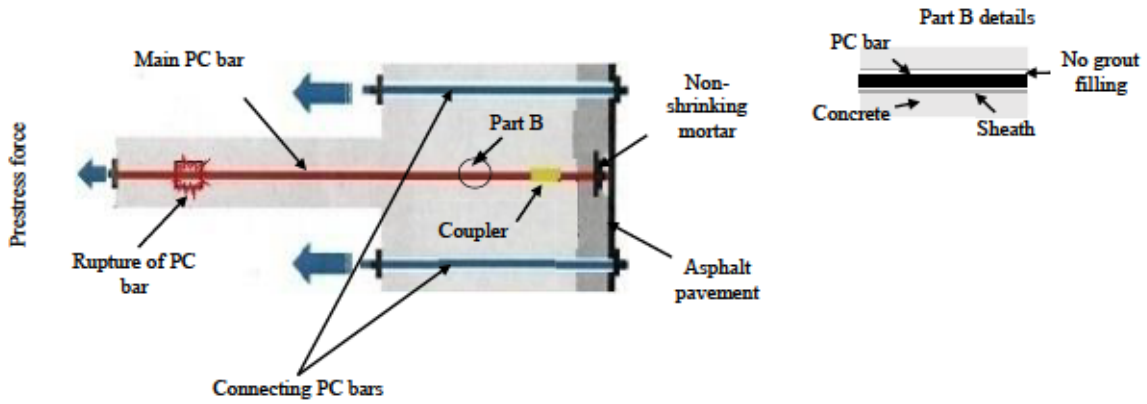

Fig. 4.3 Experimental procedure for the specimen with 80 mm thick asphalt pavement

4.2.2 Verification of AEM Simulation

a) Bending Test of Asphalt Concrete at 20°C

AEM numerical simulation was carried out for the base layer asphalt material and the cover layer asphalt material to calibrate tensile stress – tensile strain relationships for the two asphalt materials. The asphalt specimens had a dimension of 300 mm × 100 mm × 50 mm (Fig. 4.4a). The load was applied at the midspan. The distance between the pinned supports was 200 mm (each pinned support was 100 mm from the midspan). In the numerical simulation, the asphalt pavement had an element size of 5 mm × 5 mm × 5 mm. The applied displacement was 20 mm. In this section, the asphalt pavement materials were simulated using a bilinear model with softening range, which was the most appropriate material in ELS. Fig. 4.4c and Fig. 4.4e show the tensile stress–tensile strain relationships for the base layer and the cover layer in the AEM simulation. The numerical simulation was verified with the experiment. The experiment was carried out at a temperature of 20°C.

The relationships between load and displacement are shown in Fig. 4.4d and Fig. 4.4f. In AEM simulation of the base layer asphalt pavement, the observed maximum load was 11,138 N at a displacement of 2.51 mm. And the first crack was observed at this maximum load on the bottom surface

at the midspan of the specimen. After that, the load suddenly dropped to zero without showing additional deformation. It showed brittle failure.

On the other hand, in the cover layer asphalt pavement, the observed maximum load in the numerical simulation was 1,059 N at a displacement of 6.95 mm. The first crack on the bottom surface of the specimen at the midspan was observed at a load of 697 N and at a displacement of 11.40 mm. After that, the crack gradually propagated upward until the complete collapse of the specimen. The cover layer showed a relatively lower capacity with a larger deformation.

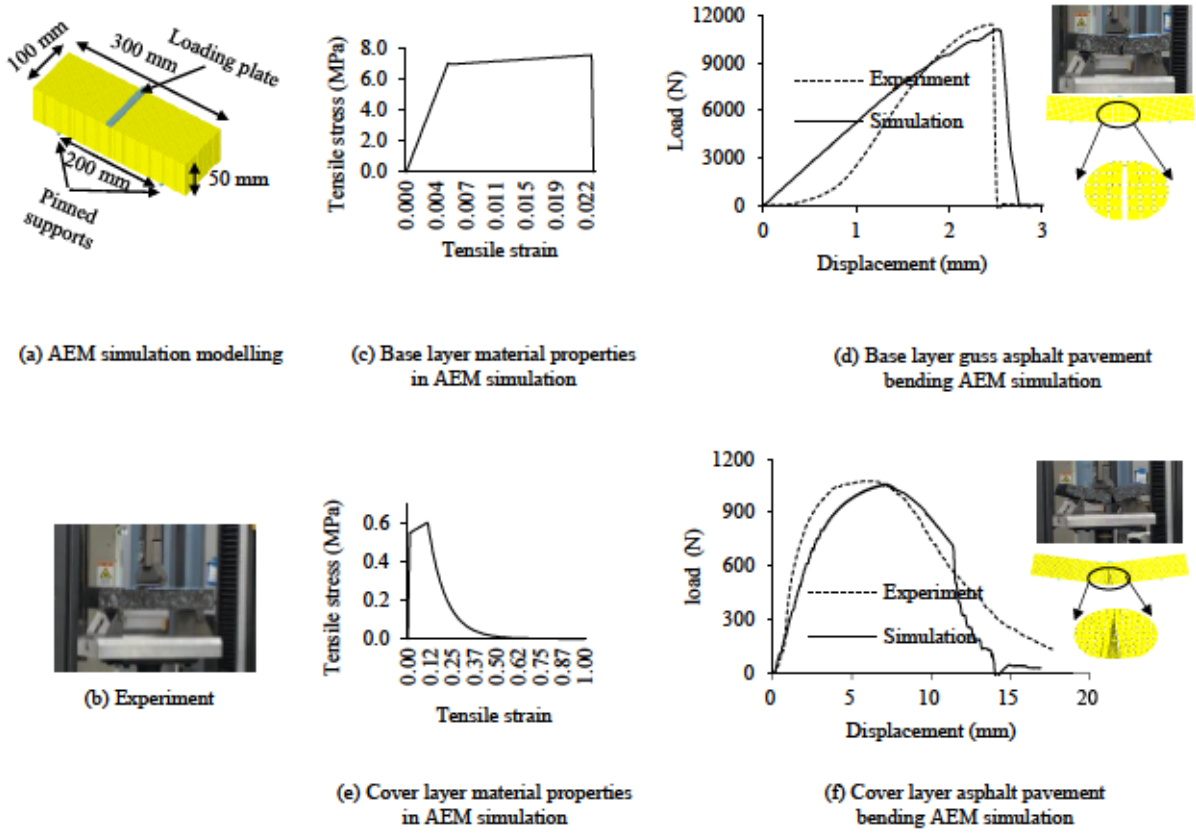

(a) AEM simulation modelling

(b) Experiment

(c) Base layer material properties in AEM simulation

(d) Base layer guss asphalt pavement bending AEM simulation

(e) Cover layer material properties in AEM simulation

(f) Cover layer asphalt pavement bending AEM simulation

Fig. 4.4 Asphalt pavement bending test and material properties of cover layer and base layer [1]

b) Verification of AEM Simulation with Two Layers of Asphalt Pavement at 20°C

AEM numerical simulation was carried out for the specimen explained in Fig. 4.1. The details of the modeling are shown in Fig. 4.5. The details of loading stages were already explained in section 3.4.2.

The interface material between the PC bar and the non-shrinking mortar, between the nut and the non-shrinking mortar, and between the bearing plate and the non-shrinking mortar was modeled as mortar with compressive strength of 60 MPa. The base layer and the cover layer were modeled as bilinear materials (material properties are shown in Fig. 4.4c and e). Similarly, the interface materials between the slab concrete and the base layer and between the cover layer and the base layer were modeled as bilinear materials.

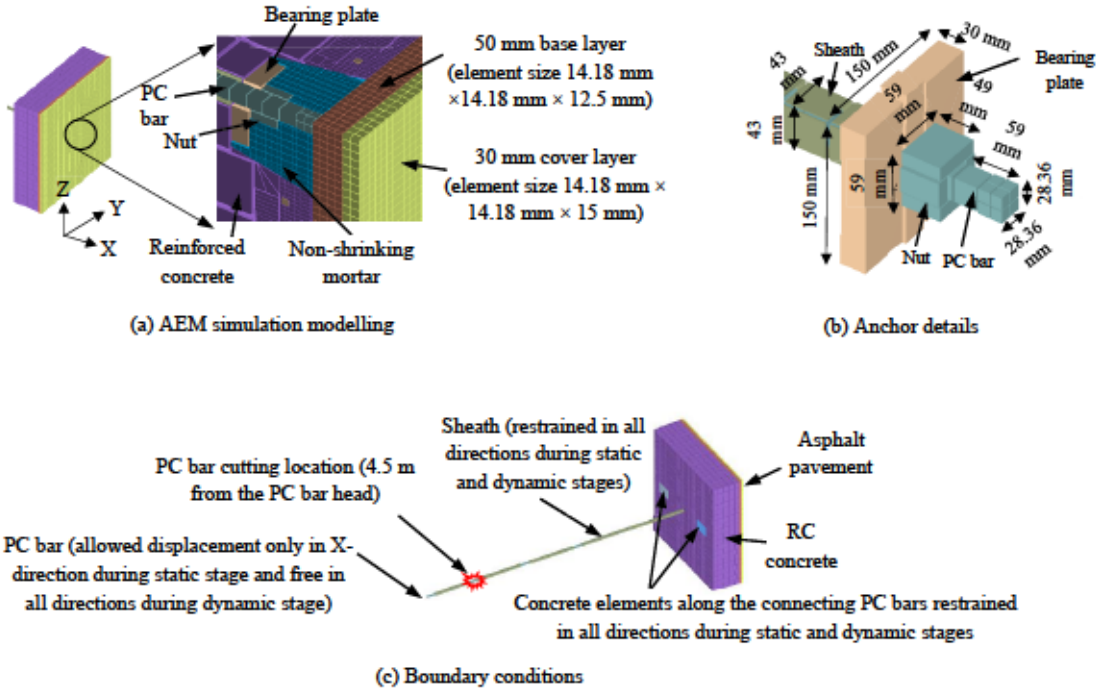

Fig. 4.5 Modeling for AEM simulation considering asphalt pavement

It is difficult to set appropriate material properties for interface materials directly based on experimental results. When a bond between the base layer and the slab concrete had a very high yield strength, separation between the slab concrete and the asphalt base layer did not occur and it was difficult to obtain ductile asphalt pavement deformation. As a result, localized asphalt pavement failure and PC bar protrusion occurred as shown in Fig. 4.6a. On the other hand, a weak interface material resulted in a total delamination between the asphalt base layer and the slab concrete in the specimen with this size, and the protrusion of PC bar could not be prevented as shown in Fig. 4.6b.

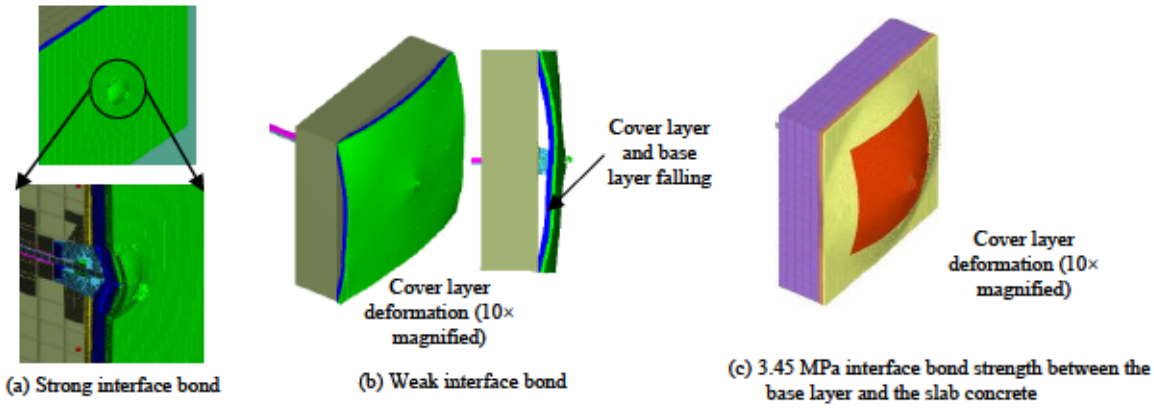

Fig. 4.6 The effects of bond at interface between asphalt base layer and slab concrete on the asphalt pavement deformation and on the failure mode [1]

Asphalt pavement pull-off test was carried out to measure the interface bond strength between the slab concrete and the base layer asphalt pavement as shown in Fig. 4.7. The pull-off strength was 0.4 MPa at a temperature of 28°C. However, using a 0.4 MPa bond strength between the base layer and the

slab concrete in the numerical simulation resulted in total delamination between the slab concrete and the asphalt pavement. The asphalt pavement fell down as shown in Fig. 4.6b. The bond was lost due to the impact energy of the PC bar and the shear stress from self-weight of the asphalt pavement.

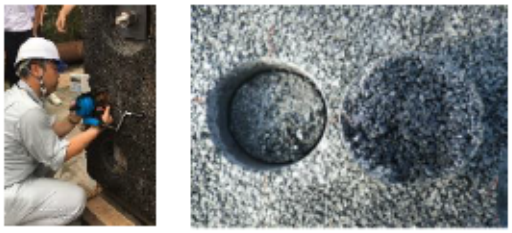

Fig. 4.7 Asphalt pavement pull-off test [1]

Therefore, in the numerical simulation it is necessary to use an appropriate interface material between the base layer and the slab concrete and between the base layer and the cover layer to obtain asphalt pavement deformation without total delamination (Fig. 4.8). In the numerical simulation, the bond strength of the interface material between the base layer and the slab concrete was calibrated as 3.45 MPa and gave a result closer to the experiment as shown in Fig. 4.6c. This bond strength increment might be associated with the effect of strain rate as the bond delaminated at a high loading rate.

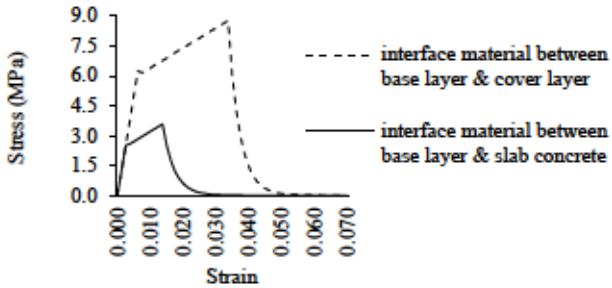

Fig. 4.8 Interface bond materials in the AEM simulation [1]

In the numerical simulation, mesh sensitivity of the asphalt pavement was investigated to obtain appropriate asphalt pavement deformation and failure mode. A 12.5 mm × 14 mm × 14 mm element size for the base layer and a 15 mm × 14 mm × 14 mm element size for the cover layer were used over the area of 1,600 mm × 1,600 mm as shown in red area in Fig. 4.9c. The main reason for this meshing was that the asphalt pavement deformation was larger in the red area. For the rest of the asphalt pavement, a 12.5 mm × 20 mm × 20 mm element size for the base layer and a 15 mm × 20 mm × 20 mm element size for the cover layer were used as shown in the yellow area in Fig. 4.6c.

The normal contact stiffness factor (*NF*), explained in section 3.4.1, of the asphalt pavement materials affects the interaction between the PC bar and the asphalt pavement and energy transfer between them. Providing a very high contact stiffness value causes a large shock force transferred between elements, while providing a low contact stiffness value causes a reduction in the transmitted force when elements collide Fig. 4.10a and b.

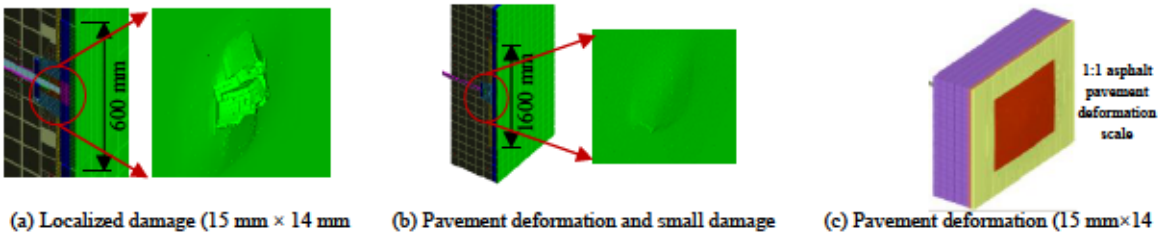

(a) Localized damage (15 mm × 14 mm × 14 mm cover layer and 12.5 mm × 14 mm × 14 mm base layer element size over 600 mm × 600 mm area)

(b) Pavement deformation and small damage (15 mm ×14 mm × 14 mm cover layer and 12.5 mm × 14 mm × 14 mm base layer element size over 1,600 mm × 1,600 mm area and 30 mm × 100 mm × 100 mm cover layer and 50 mm × 100 mm × 100 mm base layer element size for other part)

(c) Pavement deformation (15 mm×14 mm × 14 mm cover layer and 12.5 mm × 14 mm × 14 mm base layer element size over 1,600 mm × 1,600 mm area and 15 mm × 20 mm × 20 mm cover layer and 12.5 mm × 20 mm × 20 mm base layer element size for other part)

Fig. 4.9 Mesh division for appropriate simulation with less time [1]

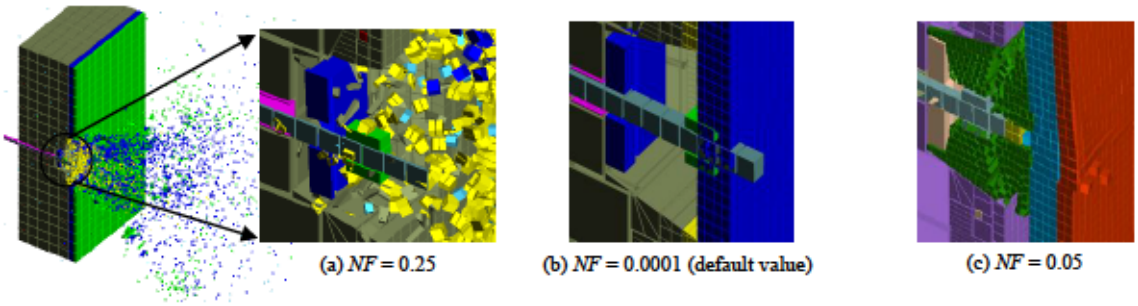

(a) $NF = 0.25$ (b) $NF = 0.0001$ (default value) (c) $NF = 0.05$

Fig. 4.10 The effect of *NF* on energy transfer between the PC bar and the asphalt pavement [1]

Therefore, the normal contact stiffness factor (*NF*) should have a reasonable value. The numerical simulation with *NF* value of 0.05 and shear contact stiffness factor (*SF*) value of 0.001 for the base layer and the cover layer gave a result closer to the experiment as shown in Fig. 4.10c. On the other hand, for the mortar, *NF* value of 0.1 and *SF* value of 0.01 were used in the numerical simulation.

The mechanical properties of the hot mix asphalt (HMA) changed significantly under high-strain rate. The failure mechanisms under the high-strain rate loading were found to be considerably different from those obtained in static testing where failure of binder was a predominant mechanism [2], [3]. High-strain rate loading caused trans-aggregate failures in addition to failure of the binder [2]. When the PC bar protruded, the asphalt pavement was fractured under a high loading rate. It was necessary to consider the effect of strain rate in the numerical simulation. For the asphalt pavement under high loading rate, the yield stress and the elastic modulus were increased by the respective *DIF*.

Table 4.1 The Dynamic Increase Factors [1]

Material Properties	Dynamic Increase Factor (*DIF*)	
	Springs between the base layer elements	Springs between the cover layer elements
Yield stress	2.39	6.00
Young modulus	1.48	1.58

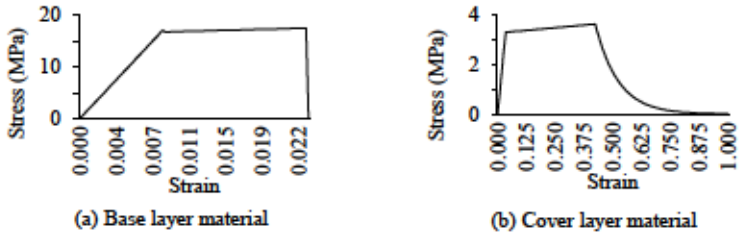

Fig. 4.11 Material properties of cover layer and base layer after considering strain rate [1]

In this study, the empirical equations (Equation 2.3 and 2.4) to calculate the *DIF* of concrete were also applied for the asphalt pavements as literature on similar studies on asphalt materials is scarce. High-strain rate mechanical behavior of bituminous materials has received little attention due to inherent difficulty in testing and interpretation of results [2]. The *DIF* was calculated and considered in the numerical simulation by following the same procedure as in section 3.5. The *DIF* was considered for the base layer and for the cover layer inside the red area of 1,600 mm ×1,600 mm as shown in Fig. 4.9c. Material properties of the base layer and the cover layer after considering strain rate effect are shown in Fig. 4.11a and Fig. 4.11b. The Dynamic Increase Factors (*DIF*) that were calculated based on Equation 2.3 and 2.4 are shown in Table 4.1.

c) Result and Discussion

Immediately after the rupture of the PC bar, stress in the non-shrinking mortar was generated from the head of the nut and cracking was propagated diagonally with an angle of 35° from the vertical axis. This stress distribution resulted in a cone-shaped crack in the mortar (Fig. 4.12). As the PC bar tendon pushed the mortar forward, both the base layer and the cover layer asphalt pavement deformed together. At the same time, separation was observed at the interface between the slab concrete and the asphalt base layer as shown in Fig. 4.13b and Fig. 4.13d. Separation was not observed between the two asphalt pavement layers. Small cracks were also observed on the surface of the cover layer asphalt pavement near the center of the PC bar as shown in Fig. 4.13a and Fig. 4.13c.

The displacement of the PC bar in the numerical simulation was observed in Fig. 4.14b. The maximum PC bar protrusion was 46 mm at 0.0169 s. After that, the PC bar moved in the reverse direction. Finally, the PC bar stopped moving at a protrusion of 9 mm after 0.18 s.

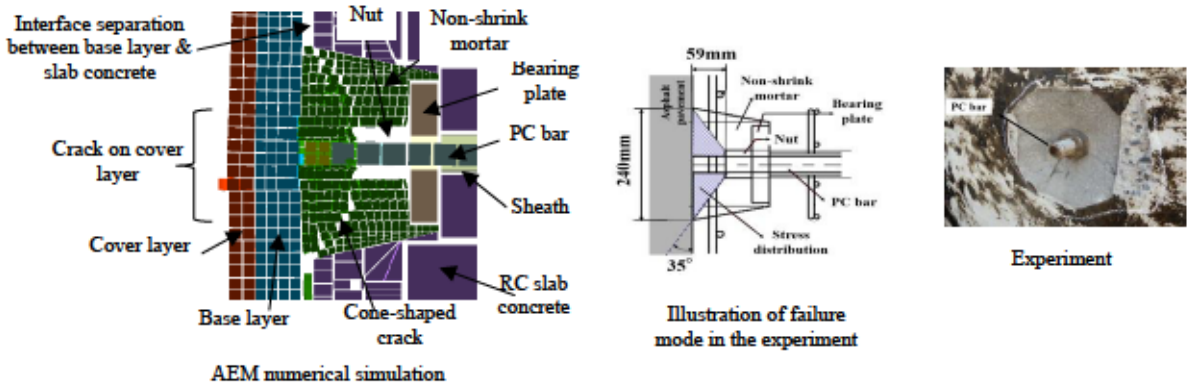

Fig. 4.12 Failure mechanism after rupture of the PC bar [1]

Deformation of the asphalt pavement was measured on the cover layer along the centerline of the connecting PC bars. In the numerical simulation, the asphalt pavement deformation was measured at 0.0169 s when maximum PC bar protrusion was observed, and at 0.10 s, 0.15 s, and 0.1828 s when PC bar protrusion was stopped (around 9 mm) as shown in Fig. 4.14c. The asphalt pavement deformation at 0.1828 s is shown in Fig. 4.14a. The maximum asphalt pavement deformation was observed at 0.0169 s when the PC bar protrusion was maximum. After 0.0169 s, all strain energy of the PC bar (4,408 J) was dissipated by the asphalt pavement and the PC bar moved in the reverse direction. Similarly, after 0.0169 s the asphalt pavement deformed in the reverse direction. Both the experiment and the numerical simulation showed that the maximum cover layer deformation was observed at the center of the section and deformation was decreasing towards the edges in the section. The experiment showed 23 mm residual deformation at the center of cover layer and 3 mm deformation at 600 mm from the center on both sides. In the numerical simulation, at 0.1 s, 0.15 s, and 0.1828 s, the maximum cover layer deformation was around 16 mm at the center of the section and gradually decreased towards the edge of the cover layer.

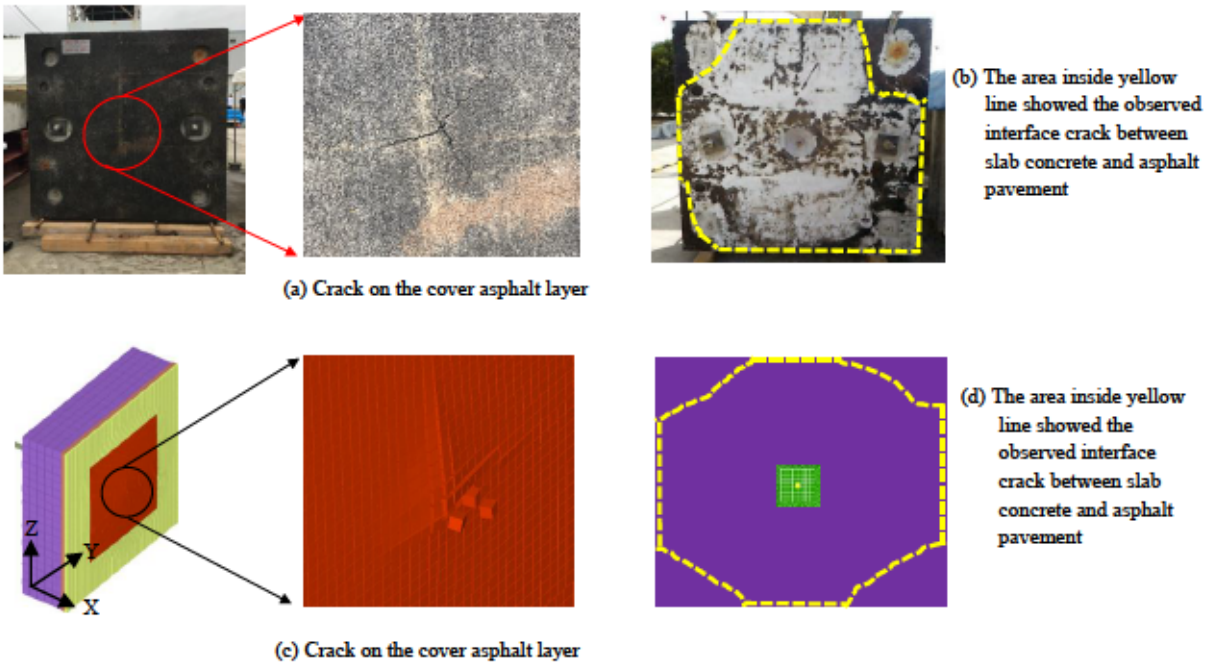

Fig. 4.13 Asphalt pavement crack & interface separation, experiment (a & b) and numerical simulation at 0.1828 s (c & d) [1]

The cover layer deformation was asymmetry in the experiment and in the numerical simulation. In the numerical simulation, at 0.1 s, the cover layer deformation was 4 mm at 1,000 mm from the center of cover layer, but the deformation was 0 mm at -1,000 mm. On the other hand, at 0.1828 s, the cover layer deformation was 0 mm at 1,000 mm from the center of cover layer, but the deformation was 8 mm at -1,000 mm. Both at 0.1 s and at 0.1828 s, the PC bar protrusion (Fig. 4.14b) was around 9 mm and the interface bond delamination between the base layer and the slab concrete (Fig. 4.13d) was the

same. The difference in cover layer deformation at 0.1 s and at 0.1828 s was due to the shock wave (which originated at the center of the cover layer when the PC bar impacted the asphalt pavement) and due to its reflection at the free boundary. As a result, the cover layer was deformed inward and outward around the edge at different times. However, this deformation must be decreasing with time according to the dissipation of strain energy.

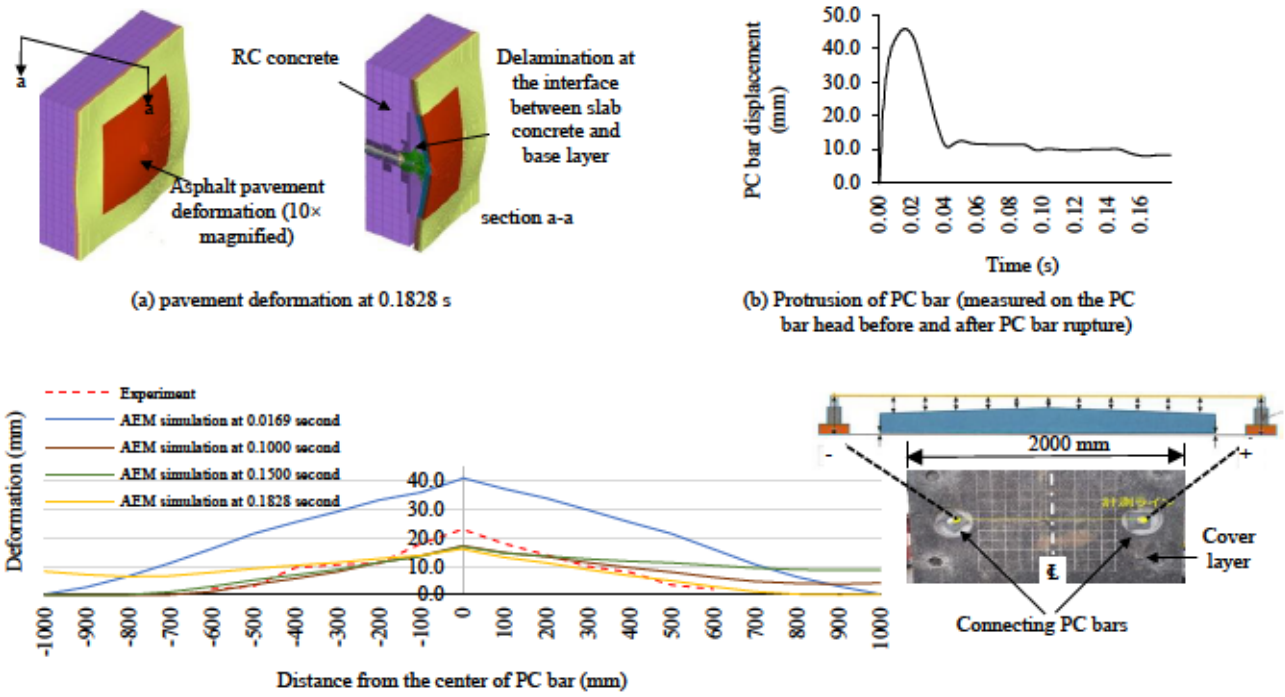

(a) pavement deformation at 0.1828 s

(b) Protrusion of PC bar (measured on the PC bar head before and after PC bar rupture)

(c) Asphalt pavement deformation

Fig. 4.14 Asphalt pavement deformation and protrusion of the PC bar [1]

From this investigation, the asphalt pavement system was proven effective in preventing PC bar protrusion and concrete spalling. The effectiveness of the asphalt pavement system depends on so many factors, such as energy of ruptured PC bars, material properties of asphalt pavements including time-dependent deterioration, temperature, etc. The numerical simulation tool developed in this study will be utilized for detailed investigation of the protrusion behavior and for evaluating the effectiveness of countermeasures.

4.2.3 Summary of Section 4.2

Based on experimental and numerical simulation using the Applied Element Method to study the rupture and protrusion of vertically prestressed steel bar with asphalt pavement, the following conclusions were obtained:

- Appropriate numerical simulation with the AEM can be conducted with appropriate interface material property between the slab concrete and the asphalt pavement layers, considering the

fracture energy of concrete, with appropriate mesh discretization, appropriate time interval, appropriate Normal Contact Stiffness Factor (*NF*), and considering strain rate effects both in concrete and in asphalt pavement.

- The asphalt pavement system with appropriate material and thickness could prevent the protrusion of the PC bar of 4.5 m rupture length and concrete spalling. The experimental results proved that the asphalt pavement system used in this study, without using a steel plate and FRP sheet, was effective against 4,408 J impact energy. The effectiveness of the pavement system was also confirmed in the numerical simulation.
- In the asphalt pavement system, the PC bar protrusion was prevented by ductile deformation of asphalt pavement delaminated from slab concrete. The strain energy of the PC bar was dissipated by a simultaneous action of asphalt pavement deformation, cone-shaped crack in the mortar, and interface delamination between the slab concrete and the asphalt pavement.

4.3 AEM Simulation of Rupture and Protrusion of Prestressing Steel Bar with Asphalt Pavement at 50°C (High Temperature)

Asphalt concrete is one type of temperature sensitive mixtures. Asphalt pavement suffers from the impact of temperature due to the temperature variation in different districts and environments [4]. Fig. 4.15 shows a temperature distribution in an asphalt pavement over a bridge deck. The measurement was carried out on 9th of August 2006 in Shimane prefecture (Japan). August is one of the hottest months in Japan. Temperature was recorded on the asphalt pavement surface, at the interface between the cover layer and the base layer and at the interface between the base layer and the deck slab as shown in a, b and c respectively in Fig 4.15. The maximum recorded temperature at a, b and c was 63°C at 13:00, 55°C at 13:40 and 48°C at 14:40 respectively. The maximum ambient temperature was 36°C at 13:00. However, in this section the target temperature of the materials was 50°C.

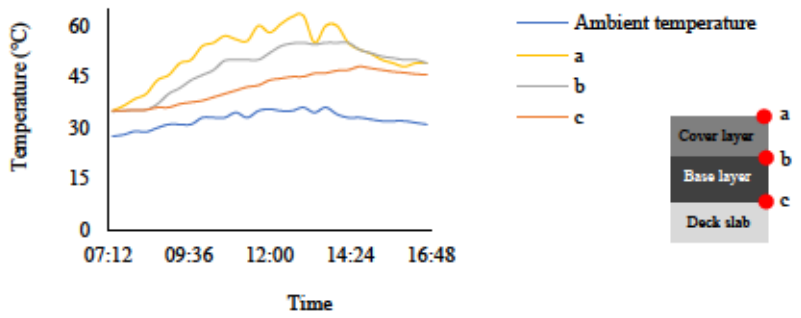

Fig. 4.15 Temperature gradient on asphalt pavement over a bridge deck slab

4.3.1 Experimental Program

a) Details of Specimen

The details of the specimen in this section are the same as section 4.2.1 as shown in Fig. 4.1 and Fig. 4.2.

b) Materials

The materials used in this section were the same as section 4.2.1 However, the following modification were made:

- The guss asphalt base layer was replaced by a modified type fine particle asphalt mixture. This asphalt pavement is more ductile than guss asphalt pavement at room temperature. However, in the bending test, the guss asphalt pavement exhibited a higher strength. The base layer asphalt pavement used in this section is denser than the porous cover layer asphalt pavement.
- The interface bond material between the concrete slab and the base layer asphalt pavement was replaced by waterproofing interface material.
- The performance of asphalt pavement was investigated at high temperature (50°C).

Three-point bending tests for the base layer asphalt pavement and the cover layer asphalt pavement were conducted. The asphalt specimen had a dimension of 300 mm × 100 mm × 50 mm. The experiment was carried out at a temperature of 40°C. In the base layer bending experiment, the observed maximum load was 807.17 N at a displacement of 8.13 mm. In the cover layer bending test, the observed maximum load was 522.36 N at a displacement of 7.49 mm. The first crack was observed at the maximum load on the bottom surface at the mid span of the base layer and the cover layer specimens. After that, the crack gradually propagated upward until the complete collapse of the specimens. At 40°C, the base layer and the cover layer showed a ductile failure. The details are presented in section 4.3.2.

Waterproofing was used to bind the base layer and the concrete slab and tack coat was used to bind the base layer and the cover layer. A pull-off adhesion test was carried out on the asphalt pavement as shown in Fig. 4.16 to investigate the bond strength of the waterproof and the tack coat at 50°C and 0°C. Three pull-off adhesion tests were conducted for the waterproofing as well as for the tack coat. The speed of pull-off was 60 mm/minute. The maximum load at the time of destruction was measured. At 50°C the average bond strength of the waterproofing and the tack coat was 0.37 MPa and 0.15 MPa respectively (Fig. 4.16). At 0°C the average bond strength of the waterproofing and the tack coat was 2.36 MPa and 2.11 MPa respectively. The waterproofing and the tack coat are highly temperature dependent materials.

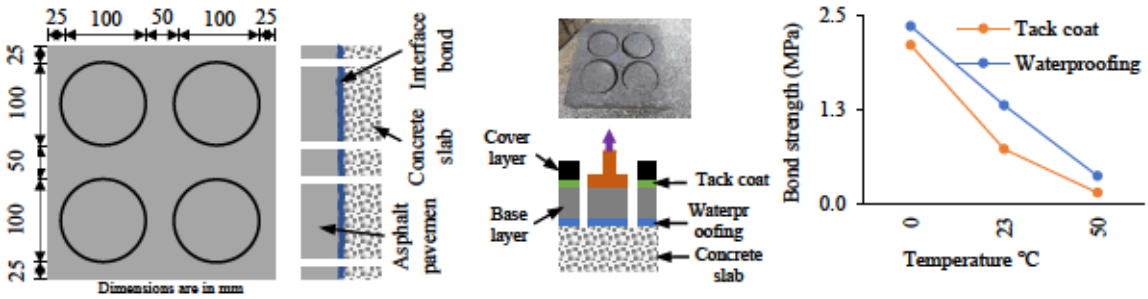

Fig. 4.16 Pull-off adhesion test of tack coat and waterproofing [5]

c) Testing Procedures

Before the experiment was carried out at a full-scale level, there had been a concern that, at 50°C the base layer and the cover layer might fell down by shear stress due to self-wight of the base layer and cover layer placed vertically (Fig. 4.17a). A small-scale specimen with the base layer and the cover layer was kept in a chamber at a constant temperature of 60°C for 40 hours (Fig. 4.17b). In the small-scale specimen, the waterproofing was used at the interface between the base layer and the concrete slab. No delamination was observed at the waterproofing. The density of the cover layer and the base layer was 2,052 kg/m^3 and 2,385 kg/m^3 respectively. The total mass of the base layer and the cover layer on the full-scale specimen was 724 kg (Fig. 4.17a). In the full-scale specimen, shear stress at the waterproofing due to self-weight of the base layer and the cover layer was 0.00177 MPa. On the other hand, the shear strength of the waterproofing at 50°C was 0.16 MPa. It was confirmed that, in the full-scale specimen, self-weight of the base layer and the cover layer would not result in a slip at waterproofing at 50°C

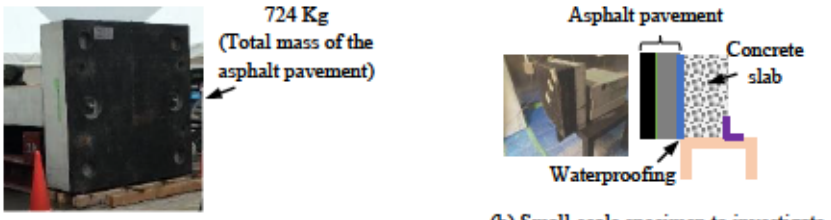

(a) Full-scale specimen with asphalt pavement

(b) Small-scale specimen to investigate peel-off at waterproofing at 60°C

Fig. 4.17 Investigation of interface bond delamination due to self-weight of asphalt pavement at high temperature

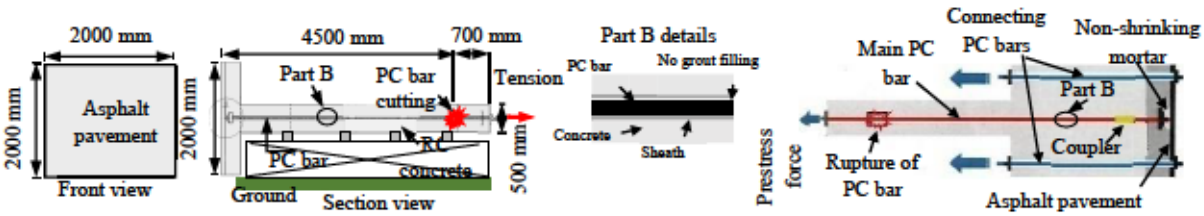

Fig. 4.18 Experimental procedure [5]

(a) Specimen kept in a temporary chamber to maintain constant temperature

(b) At high temperature

Fig 4.19 Temperature distribution in the base layer and the cover layer when the PC bar ruptured [5]

Fig. 4.18 shows the experimental procedure. Tension force was applied to the main PC bar and the connecting PC bars. The main PC bar and the connecting PC bars had no contact with the sheath

during prestressing. The sheath was not grouted. During rupture of PC bar with asphalt pavement at high temperature, the specimen was kept in a temporary chamber to maintain the target temperature (50°C) (Fig. 4.19a). A jet heater was used to apply heat to the specimen until the target temperature was maintained to simulate a summer condition in Tokyo area. The PC bar was raptured when the temperature at the surface of the cover later, at the tack coat and at the waterproofing was 55°C, 50°C and 46°C respectively as shown in Fig. 4.19b. The ambient temperature was 29°C. Temperature was measured using thermocouple. When the required temperature was maintained, the PC bar was cut using a grinder at 4.5 m from the PC bar head. Then, the effectiveness of the asphalt pavement was investigated.

4.3.2 Verification of AEM Simulation

a) Bending Test of Asphalt Concrete at 40°C

AEM numerical simulation was carried out for the asphalt material (Fig. 4.20a) to calibrate tensile stress-tensile strain relationship. The load was applied at the midspan. The distance between the pinned supports were 200 mm (each pinned support was 100 mm from the mid span) as shown in Fig. 4.20a. In the numerical simulation, the asphalt specimens had an element size of 5 mm × 5 mm × 5 mm. The applied displacement was 5 mm. In this study, the asphalt pavement material was simulated using a user defined bilinear model which shows softening behavior after tensile strength. The softening behavior depended on element size and fracture energy.

Fig. 4.20b shows the tensile stress-tensile strain relationship of the base layer. Fig. 4.20c shows the load and displacement relationship of the base layer. In the numerical simulation, the observed maximum load was 783.70 N at a displacement of 9.16 mm. On the other hand, in the base layer bending experiment, the observed maximum load was 807.17 N at a displacement of 8.13 mm. The first cracking was observed at the maximum load on the bottom surface at the mid span of the specimen. After that, the crack gradually propagated upward until the complete collapse of the specimens. The base layer showed a larger deformation before collapse.

Fig. 4.21a shows the tensile stress-tensile strain relationship of the cover layer. Fig. 4.21b shows the load and displacement relationship of the cover layer. In the cover layer bending simulation, the observed maximum load was 506.01 N at a displacement of 7.08 mm. On the other hand, in the cover layer bending experiment, the observed maximum load was 522.36 N at a displacement of 7.49 mm. The failure mode was the same as the base layer bending test.

The fracture energy of asphalt pavement increases with the increase of temperature [6]. According to the AEM simulation, the fracture energy of the base layer and the cover layer at 40°C was 3.2 N/mm and 1.15 N/mm respectively (Fig 4.20b and Fig. 4.21a). A similar AEM simulation was carried out for the base layer and the cover layer at 0°C and the fracture energy of the base layer and the cover layer

was 0.49 N/mm and 2.75 N/mm respectively. The fracture energy of the cover layer decreased with the increase of temperature. One of the reasons was the performance of the cover layer significantly deteriorated at high temperature.

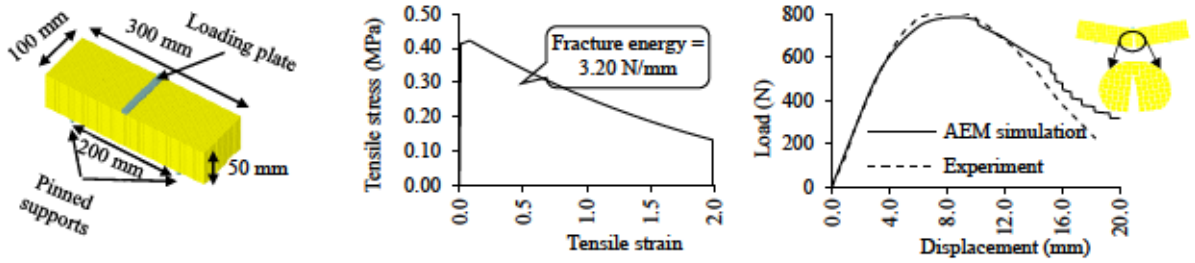

(a) AEM modelling of asphalt pavement bending

(b) base layer material property at 40°C

(c) base layer load-displacement curve at 40°C

Fig. 4.20 Relationship between load and displacement of the base layer at 40°C [5]

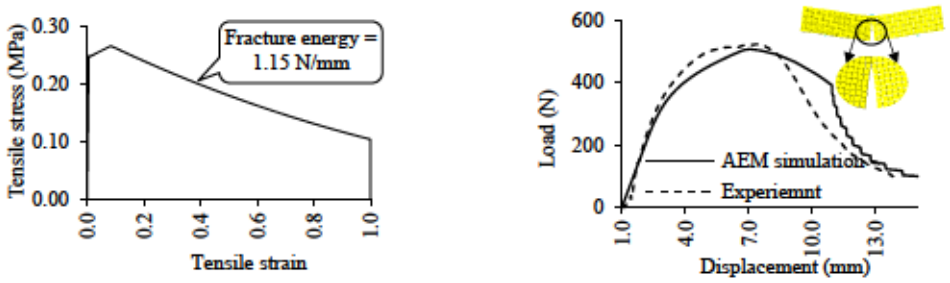

(a) cover layer material property at 40°C

(b) cover layer load-displacement curve at 40°C

Fig. 4.21 Relationship between load and displacement of the cover layer at 40°C [5]

b) Verification of AEM Simulation with Two Layers of Asphalt Pavement at 50°C

AEM numerical simulation was carried out for the specimen explained in Fig. 4.1 The details of the modelling are shown in Fig. 4.5. The details of loading stages were explained in section 3.4.2. In the AEM simulation, it is difficult to set appropriate material properties for interface materials directly based on experimental results. In the numerical simulation it is necessary to use an appropriate interface bond materials to obtain appropriate failure mode [1]. In the AEM simulation at 50°C, the interface materials between the slab concrete and the base layer (waterproofing) and between the base layer and the cover layer (tack coat) were modeled as shown in Fig. 4.22. The interface bond strength of the waterproofing and the tack coat were defined using the interface bond experiment as shown in Fig. 4.16. In this study, the tension softening behavior of the waterproofing and the tack coat were found appropriate by sensitivity analysis.

In this section the *DIF* of the base layer and the cover layer asphalt pavement under compression and tension at a high loading rate was calculated using Equation 2.6 and Equation 2.7 respectively [7]. In the numerical simulation, for a normal spring between the asphalt pavement elements, the quasi-static tensile and compressive stress were automatically multiplied by the respective *DIF*. The same *DIF* – strain rate equation (Equation 2.6 and Equation 2.7) was assumed for the interface bond materials

(waterproofing membrane and tack coat). In this section, two identical AEM simulations with and without considering strain rate effect were carried to show the applicability of Equation 2.6 and Equation 2.7 in the AEM simulation as shown in Fig 4.23a. The AEM simulation without considering strain rate resulted in PC bar protrusion. However, the AEM simulation with considering strain rate gave a good result as shown in Fig 4.23b. The details of the AEM simulation results with considering strain rate are explained next in the results and discussion.

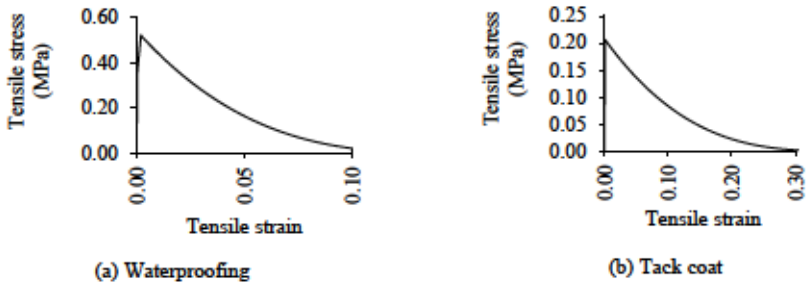

Fig. 4.22 Interface bond material properties at 50°C in the AEM simulation

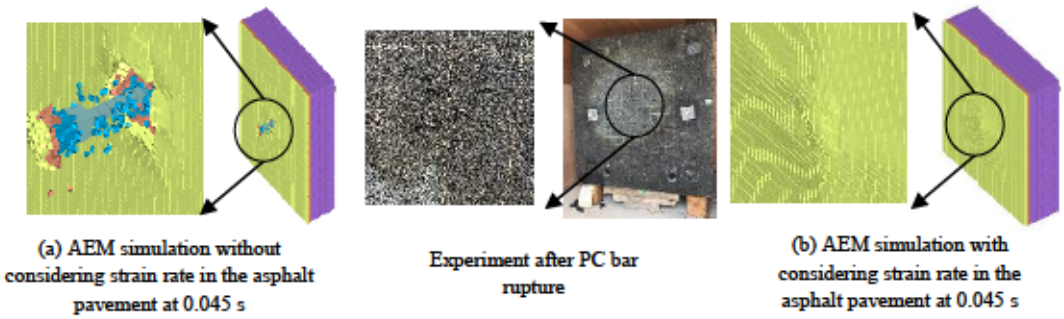

Fig. 4.23 The effect of strain rate in the failure mode of asphalt pavement in the AEM simulation at 50°C

c) Result and Discussion

The impact resistance of the asphalt pavement is discussed. Photographs were taken after the impact; a crack in the asphalt pavement, in the concrete and in the non-shrinking mortar, crater area in the concrete and in the mortar, asphalt pavement deformation and final state of the PC bar protrusion were measured as damage criteria. The PC bar protrusion was measured to determine the actual displacement of the PC bar into the asphalt pavement. The PC bar protrusion was measured at the head of the PC bar before and after rupture of the PC bar.

When the PC bar ruptured, all the strain energy of the PC bar (4,408 J) was released instantly. The head of the PC bar with the nut impacted the asphalt pavement and the non-shrinking mortar with a high loading rate. When the PC bar impacted the asphalt pavement, a very high stress was developed near the impact area, forming a shear-cone shaped fracture zone. Stress generated from the head of the nut propagated diagonally and created a cone shaped crack in the non-shrinking mortar and in the concrete (Fig. 4.24a). To investigate the extent of shear cone shaped fracture in the concrete, the base layer and the cover layer were removed in the experiment as shown in area *A* in Fig. 4.24b. Around 800

mm × 800 mm concrete crater area was found (Fig. 4.24c). Fig. 4.24d shows the profile of the concrete crater. The crater profile was measured from the covering concrete. The maximum concrete crater depth was observed at the center of the PC bar and gradually decreasing towards the edges. A similar concrete crater was found in the AEM simulation. The maximum concrete crater depth in the experiment and in the AEM simulation was 45 mm and 83 mm respectively as shown in Fig. 4.24d.

The impact of the PC bar induced a compressive shock wave on the front face of the asphalt pavement. The shock wave propagated through the thickness of the asphalt pavement and reflected from the rear free surface of the asphalt pavement as tensile wave. At the rear free surface of the asphalt pavement, the total stresses of the compression wave and the reflected tension wave exceeded the tensile capacity of the asphalt pavement and produced small cracks in the cover layer asphalt pavement as shown in Fig. 4.24b.

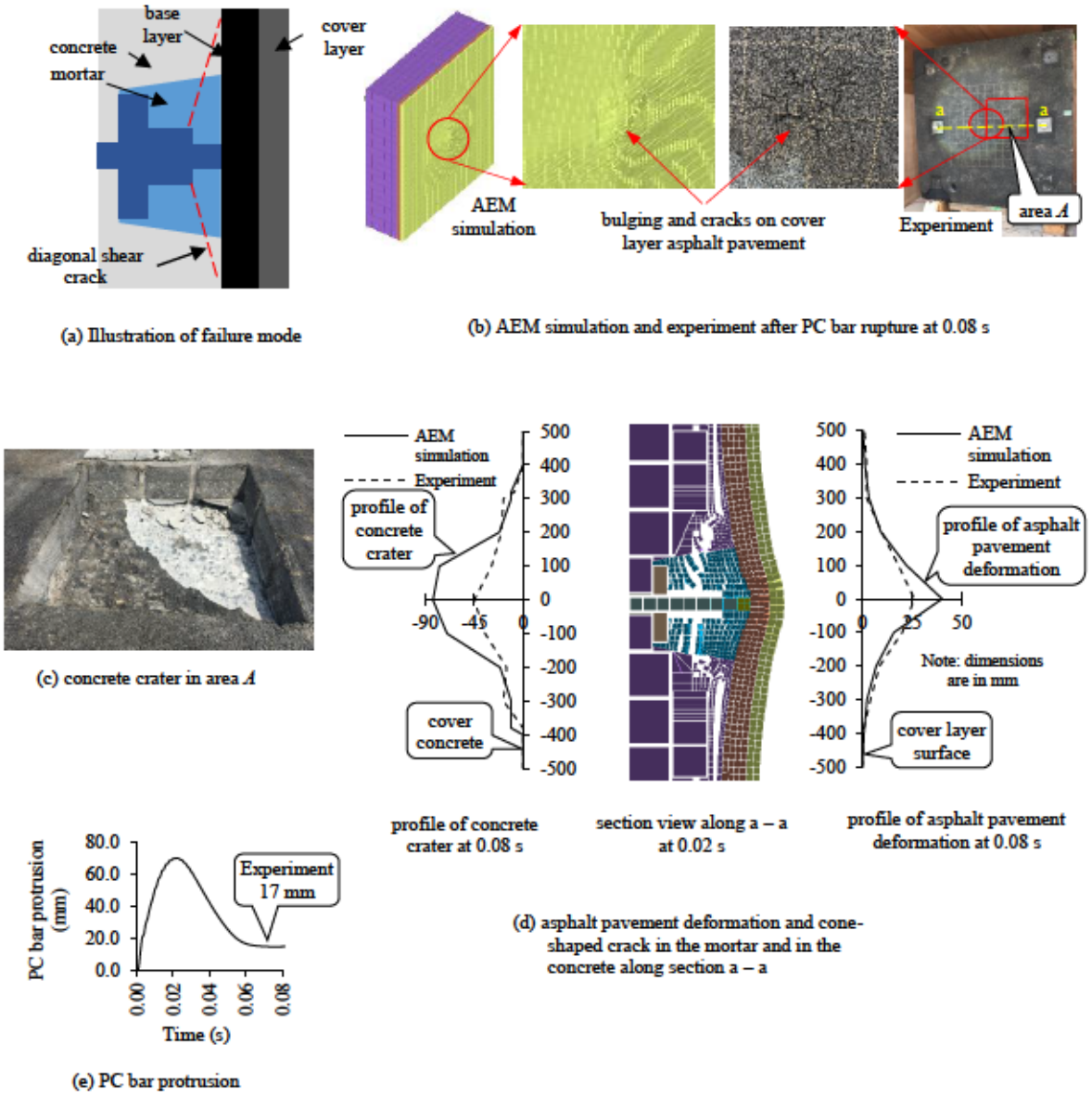

(a) Illustration of failure mode

(b) AEM simulation and experiment after PC bar rupture at 0.08 s

(c) concrete crater in area *A*

(d) asphalt pavement deformation and cone-shaped crack in the mortar and in the concrete along section a – a

(e) PC bar protrusion

Fig. 4.24 Failure modes in the asphalt pavement and in the concrete after PC bar rupture [5]

Deformation of the asphalt pavement was measured on the cover layer along the centerline of the connecting PC bars (as shown in Fig. 4.24b along a – a). In the numerical simulation, the asphalt pavement deformation was measured at 0.08 s when the PC bar protrusion was stopped as shown in Fig. 4.24d. Both the experiment and the numerical simulation showed that the maximum cover layer deformation was observed at the center of the section and deformation was decreasing towards the edges in the section. The experiment showed 26 mm residual deformation at the center of the cover layer and 0 mm deformation at 500 mm from the center. In the numerical simulation, the maximum residual cover layer deformation was around 40 mm at the center of the section and gradually decreased towards the edges of the cover layer. In the AEM numerical simulation and in the experiment, there was no delamination between the base layer and the concrete slab, and between the base layer and the cover layer.

The displacement of the PC bar in the numerical simulation was observed in Fig. 4.24e. Between 0.00 – 0.022 s, the PC bar impacted the asphalt pavement and protruded forward. The maximum PC bar protrusion was 70 mm at 0.022 s. At 0.022 s, the PC bar lost all of its strain energy. After that, the PC bar moved in the reverse direction however, the cracks and the crater continue to extend because of inertia. Finally, the PC bar stopped moving at a protrusion of 15 mm after 0.065 s. On the other hand, the PC bar displacement in the experiment was 17 mm.

The base layer and the cover layer showed smaller strengths during the quasi-static bending test as shown in Fig. 4.21. Similarly, the waterproofing membrane and the tack coat exhibited smaller bond strengths during the pull-off adhesion test as shown in Fig. 4.16 and Fig. 4.22. Moreover, increasing temperature significantly deteriorated the strength of the base layer, the cover layer and the interface bond materials. However, these materials exhibited a greater resistance during high loading impact. One of the reasons can be, the strength of the base layer, the cover layer and the interface bond materials were greatly enhanced by the strain rate. Moreover, the fracture energy and the deformability of the base layer increased with temperature. Most of the 4,408 J impact energy were dissipated by the deformation of the base layer and the cover layer, cracks in the cover layer and fracture of the concrete and the non-shrinking mortar. The base layer, the cover layer and the interface bond materials were intact after the impact except minor cracks on the cover layer near the PC bar.

4.3.3 Summary of Section 4.3

A 3D AEM model was developed using ELS for simulating asphalt pavement under 4,408 J impact energy at 50°C. Two layers of asphalt pavement with 80 mm thick was used to stop protrusion of the PC bar. The constitutive model using a user defined bilinear model with softening behavior after tensile strength for the base layer and the cover layer in the AEM simulation showed good agreement with the experimental results in terms of impact resistance and failure mode. The asphalt pavement material models were calibrated based on the asphalt pavement bending test results. The employed *DIF*

of the asphalt pavements accurately captured the dynamic material behavior of the asphalt pavement under high loading rate. The experimental results proved that the asphalt pavement system at 50°C used in this study was effective against 4,408 J impact energy and effective against the PC bar protrusion which was measured as 17 mm in the experiment. The effectiveness of the pavement system was also confirmed in the numerical simulation. Appropriate numerical simulation with the AEM can be conducted using appropriate modelling of asphalt pavement materials. The strain energy of the PC bar (4,408 J) was dissipated by a synchronized action of a shear-cone shaped fracture in the concrete and in the non-shrinking mortar, deformation and cracks in the asphalt pavement. The results of the numerical simulation had a good agreement with the experimental data.

4.4 AEM Simulation of Rupture and Protrusion of Prestressing Steel Bar with Asphalt Pavement at 0°C (Low Temperature)

4.4.1 Experimental Program

a) Details of Specimen

The details of the specimen in this section were the same as section 4.3.1.

b) Materials

The materials used in this section were the same as section 4.3.1. However, in this section, mechanical behavior of asphalt pavements was investigated at low temperature (at 0°C). Three-point bending tests for the base layer asphalt pavement and the cover layer asphalt pavement were conducted at 0°C. In the base layer bending test at 0°C, the observed maximum load was 12.86 kN at a displacement of 1.35 mm. In the cover layer bending test at 0°C, the observed maximum load was 3.50 kN at a displacement of 2.15 mm. In all of the bending tests, the first crack was observed at the maximum load on the bottom surface at the mid span of the base layer and cover layer specimens. After that, the crack gradually propagated upward until the complete collapse of the specimens. At 0°C, the base layer showed a brittle failure. However, the cover layer showed a ductile failure. The details of AEM numerical simulation of the base layer and the cover layer are presented in section 4.4.2.

c) Testing Procedures

Rupture of PC bar with asphalt pavement at low temperature was conducted when the ambient temperature was -1.52°C to simulate a winter condition in Tokyo area. One day before the experiment, the specimen was kept outside a room at an ambient temperature. The PC bar was ruptured when the temperature at the surface of the cover later, at the tack coat and at the waterproofing was -0.75°C, -0.60°C and 0.53°C respectively as shown in Fig. 4.25.

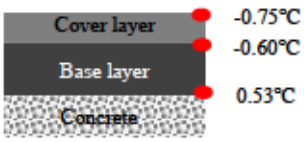

Fig. 4.25 Temperature distribution in the base layer and cover layer when the PC bar ruptured

4.4.2 Verification of AEM Simulation

a) Bending Test of Asphalt Concrete at 0°C

AEM numerical simulation was carried out for the asphalt material to calibrate tensile stress-tensile strain relationship. The asphalt specimen dimension, element size, the loading and boundary conditions is shown in Fig. 4.20a. In this study, the asphalt pavement material was simulated using a user defined material model, which was the most appropriate material in ELS, which shows softening behavior after reaching tensile strength. The softening behavior depended on element size and fracture energy. The user defined materials allowed a user to consider strain rate effect and fracture energy. Fig. 4.26a and Fig. 4.27a shows the tensile stress-tensile strain relationships for the base layer and the cover layer in the AEM simulation respectively.

The relationship between load and displacement of the base layer and the cover layer at 0°C are shown in Fig. 4.26b and Fig. 4.27b respectively. In the base layer, the observed maximum load was 13.1 kN at a displacement of 1.32 mm. In the cover layer, the observed maximum load was 3.31 kN at a displacement of 1.67 mm. Both in the base layer and in the cover layer, the first cracks were observed at the maximum loads on the bottom surface at the mid span of the specimens. After that, the cracks gradually propagated upward until the complete collapse of the specimens. The base layer showed brittle failure however, the cover layer showed a deformation. According to the base layer bending AEM simulation, the estimated fracture energy of the base layer at 0°C was 0.49 N/mm (Fig. 4.26a). However, the fracture energy of the cover layer 0°C was 2.75 N/mm (Fig. 4.27a).

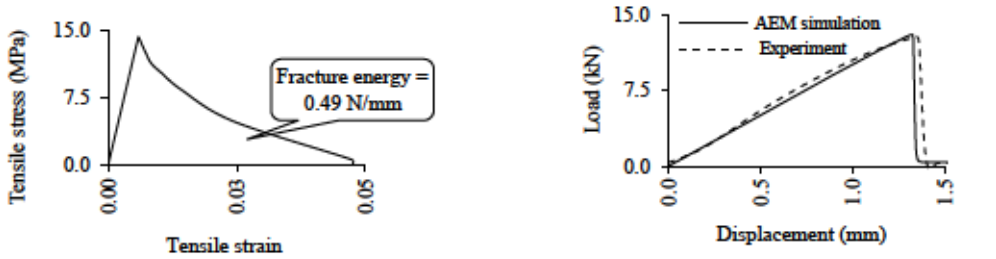

(a) Base layer material property at 0°C

(b) Base layer load-displacement curve at 0°C

Fig. 4.26 Base layer asphalt pavement bending at 0°C [8]

(a) Cover layer material property at 0°C

(b) Cover layer load-displacement curve at 0°C

Fig. 4.27 Cover layer asphalt pavement bending at 0°C [8]

b) Verification of AEM Simulation with Two Layers of Asphalt Pavement at 0°C

AEM numerical simulation was carried out for the specimen explained in Fig. 4.1 The details of the modelling are shown in Fig. 4.5. The details of loading stages were explained in section 3.4.2. When the interface bonds (tack coat and waterproofing) had a very high bond strength, interface separation would be difficult. However, a weak interface material resulted in a total delamination of base layer and cover layer. Therefore, in the numerical simulation it is necessary to use an appropriate interface bond materials to obtain appropriate failure mode [1]. In the AEM simulation at 0°C the interface materials between the slab concrete and the base layer (waterproofing) and between the base layer and the cover layer (tack coat) were modeled as shown in Fig. 4.28. The interface bond strength of the waterproofing and the tack coat were defined using the interface bond experiment as shown in Fig. 4.16. In this study, the tension softening behavior of the waterproofing and the tack coat were found appropriate by sensitivity analysis.

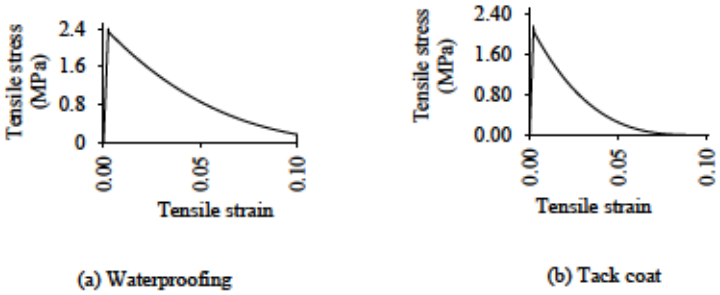

Fig 4.28 Interface bond material properties of waterproofing and tack coat at 0°C in the AEM simulation

In this section the *DIF* of the base layer and the cover layer asphalt pavement under compression and tension at a high loading rate was calculated using Equation 2.6 and Equation 2.7 respectively [6]. In the numerical simulation, for a normal spring between the asphalt pavement elements, the quasi-static tensile and compressive stress were automatically multiplied by the respective *DIF*. The same *DIF* – strain rate equation (Equation 2.6 and Equation 2.7) was assumed for the interface bond materials (waterproofing membrane and tack coat). Literature on fracture of asphalt pavement under high loading rate is scarce. High strain rate mechanical behavior of bituminous materials has received little attention due to inherent difficulty in testing and interpretation of results [2].

c) Result and Discussion

The effectiveness of two layers of asphalt pavement in preventing protrusion of the PC bar with 4,408 J of impact energy at 0°C was investigated. The impact resistance of the asphalt pavement is discussed. High speed camera captured slow motion during impact. Photographs were taken after the impact; a crack in the asphalt pavement and in the non-shrinking mortar, asphalt pavement deformation, tack coat delamination and final state of the PC bar protrusion were measured as damage criteria. The PC bar protrusion was measured to determine the actual displacement of the PC bar into the asphalt pavement. The PC bar protrusion was measured at the head of the PC bar before and after rupture of

the PC bar. Fig. 4.29a and Fig. 4.29b shows the AEM simulation and experimental results. The experiment results were used to validate the AEM numerical simulation.

When the PC bar ruptured, all the strain energy of the PC bar (4,408 J) was released instantly. The head of the PC bar with the nut impacted the asphalt pavement and the non-shrinking mortar with a high loading rate. When the PC bar impacted the asphalt pavement, a very high stress was developed near the impact area, forming a shear-cone shaped fracture zone. Stress generated from the head of the nut propagated diagonally and created a cone shaped crack in the non-shrinking mortar and in the base layer (Fig. 4.29c and Fig. 4.29d). Minor cracks in the cover layer asphalt pavement were observed as shown in 4.29a and Fig. 4.29b. To investigate the extent of shear cone shaped crack in the base layer, the base layer and the cover layer were removed in the experiment as shown in area *B* in 4.29b. It was found that the shear cone shaped crack in the base layer extended to around 450 mm from the center of the specimen as shown in Fig. 4.29d. A similar shear cone shaped crack in the base layer was found in the AEM simulation as shown in Fig. 4.29e. The shear cone shaped crack in the base layer reached to around 300 mm from the center of the specimen. The diagonal shear cracks in the base layer might be associated with small fracture energy and brittleness of the base layer due to low temperature. Multiple cracking was observed in the non-shrinking mortar, in the base layer and in the cover layer (Fig. 4.29e).

The impact of the PC bar induced a compressive shock wave on the front face of the asphalt pavement. The shock wave propagated through the thickness of the asphalt pavement and reflected from the rear free surface of the asphalt pavement as tensile wave. At the rear free surface of the asphalt pavement, the total stresses of the compression wave and the reflected tension wave exceeded the tensile capacity of the asphalt pavement and produced small cracks in the cover layer asphalt pavement as shown in Fig. 4.29a and Fig. 4.29b.

As the PC bar pushed the mortar forward, both the base layer and the cover layer asphalt pavement deformed together. Deformation of the asphalt pavement was measured on the cover layer along the centerline of the connecting PC bars (as shown in Fig. 4.29b along b – b). In the numerical simulation, the asphalt pavement deformation was measured at 0.076 second when the PC bar protrusion was stopped as shown in Fig. 4.29e. Both the experiment and the numerical simulation showed that the maximum cover layer deformation was observed at the center of the section and deformation was decreasing towards the edges in the section. The experiment showed 9 mm residual deformation at the center of the cover layer and 0 mm deformation at 500 mm from the center. In the numerical simulation, the maximum residual cover layer deformation was around 35 mm at the center of the section and gradually decreased towards the edges of the cover layer. At the same time, tack coat delamination was also observed around the impacting area in the experiment and in the AEM simulation. Around ϕ 40 mm and ϕ 30 area of tack coat was delaminated in the experiment and in the AEM simulation respectively.

The displacement of the PC bar in the numerical simulation was observed in Fig. 4.30. Between 0.00 – 0.013 second, the PC bar impacted the asphalt pavement and protruded forward. The maximum PC bar protrusion was 42.33 mm at 0.013 second. At 0.013 second, the PC bar lost all of its strain energy. After that, the PC bar moved in the reverse direction, however the cracks extended because of inertia. Finally, the PC bar stopped moving at a protrusion of 25.92 mm after 0.076 second.

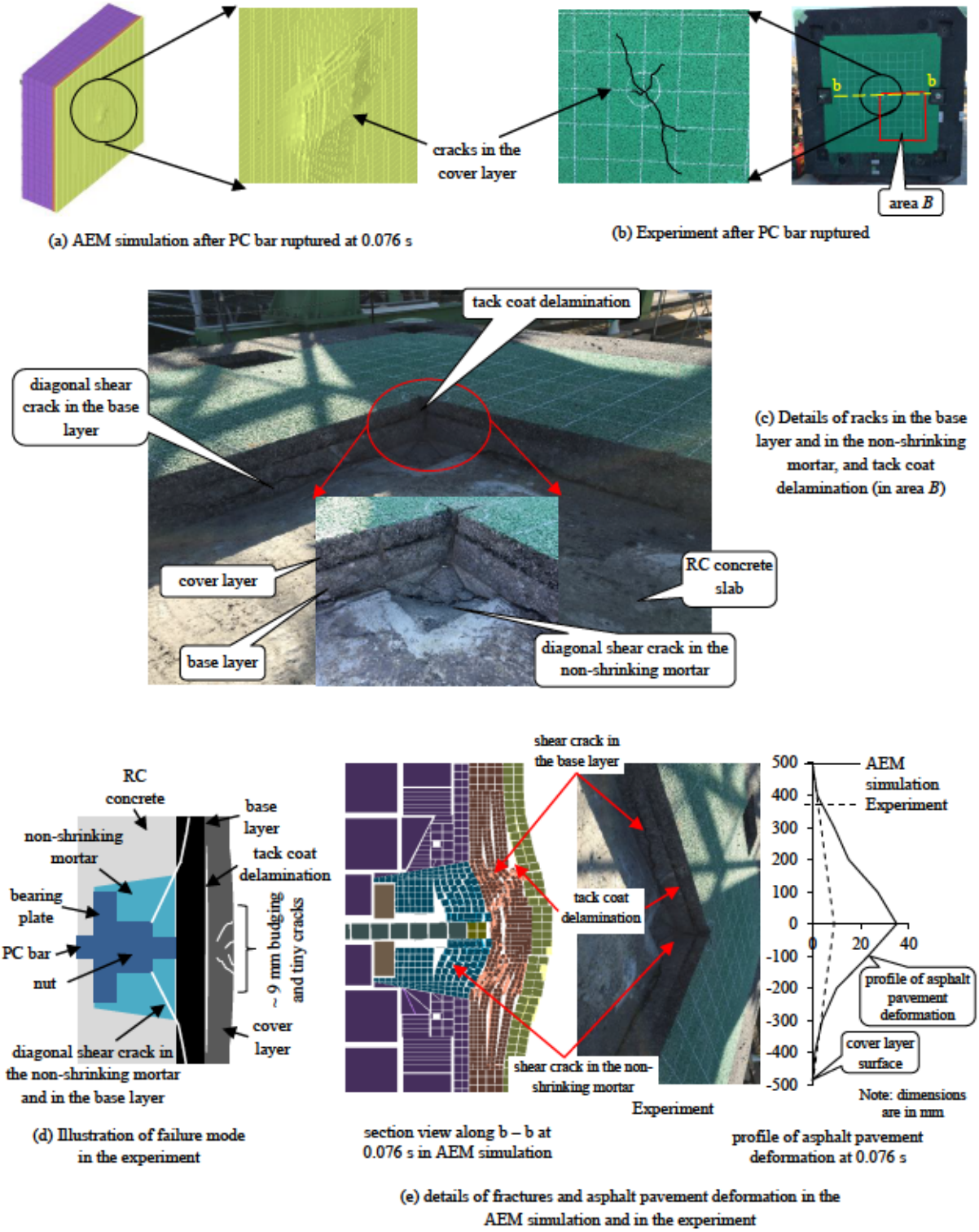

(a) AEM simulation after PC bar ruptured at 0.076 s

(b) Experiment after PC bar ruptured

(c) Details of racks in the base layer and in the non-shrinking mortar, and tack coat delamination (in area *B*)

(d) Illustration of failure mode in the experiment

section view along b – b at 0.076 s in AEM simulation

profile of asphalt pavement deformation at 0.076 s

(e) details of fractures and asphalt pavement deformation in the AEM simulation and in the experiment

Fig. 4.29 Failure modes in the asphalt pavement after PC bar ruptured at 0°C [8]

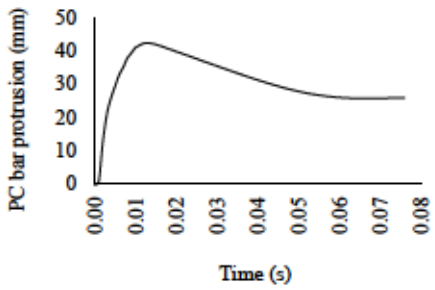

Fig. 4.30 PC bar protrusion in the AEM simulation [8]

The asphalt pavement system in the AEM simulation at 0°C exhibited a great resistance during high loading impact. One of the reasons can be, the formation of multiple cracking during the impact increased the fracture surface and energy dissipation. Another reason can be the quasi-static strength of the base layer, the cover layer and the interface bond materials were enhanced during low temperature. Most of the 4,408 J impact energy were dissipated by the diagonal shear cracks in the base layer and in the non-shrinking mortar, cracks in the cover layer, tack coat delamination and deformation of the base layer and the cover layer. In overall, the asphalt pavement system at 0°C dissipated the impact energy of the PC bar without any major damage.

4.4.3 Summary of Section 4.4

A three-dimensional nonlinear dynamic analysis using the AEM was developed for simulating the impact resistance of the asphalt pavement against PC bar protrusion. Low temperature was considered on the asphalt pavement to simulate winter condition at 0°C. Extreme impact energy, 4,408 J that can cover most of rupture of vertical PC bars in MEX, was applied on the asphalt pavement. Two layers of asphalt pavement with 80 mm thick was used to stop protrusion of PC bar. The user defined material constitutive model was implemented for the asphalt pavement. The asphalt pavement material model was calibrated based on the asphalt pavement bending test. The interface bond material model was calibrated based on the pull-off adhesive test. The *DIF* was employed to accurately capture the dynamic material behavior of the asphalt pavement under high loading rate. The AEM simulation results support the following conclusions.

The effectiveness of the asphalt pavement system against 4,408 J impact energy at 0°C in preventing PC bar protrusion was proven in the numerical simulation. The asphalt pavement system with appropriate material and thickness could prevent the protrusion of the PC bar of 4.5 m rupture length. The results of the numerical simulation had a good agreement with the experimental data in terms of failure mode.

Based on the analysis results, the effectiveness of the asphalt pavement system depends on impact energy of ruptured PC bars, material properties of asphalt pavements, material properties of interface bond materials, fracture energy, mesh discretization, strain rate and temperature.

At 0°C the strain energy of the PC bar (4,408 J) was dissipated by a synchronized action of a shear-cone shaped fracture in the base layer and in the non-shrinking mortar, deformation and cracks in the asphalt pavement and delamination of tack coat.

4.5 AEM Simulation of Rupture and Protrusion of Prestressing Steel Bar without Considering Cover Layer Asphalt Pavement at 20°C (Normal Temperature)

In Metropolitan Expressway (Japan), the asphalt pavement over a bridge deck has two layers with 80 mm thickness in total. The base layer in the two layers has 50 mm thickness, and the cover layer has 30 mm thickness. In this section, the cover layer was excluded to account for the effect of asphalt pavement deteriorations and to simulate the worst condition in reality. Only the base layer (guss asphalt pavement) was investigated in terms of its performance in preventing the protrusion of the PC bar tendons with 4,408 J impact energy at 20°C. Understanding the response and failure mode of asphalt pavement that is subjected to impact loading from the ruptured PC bar is vital for safety management. The objective of this section is to numerically investigate the effects of base layer asphalt pavement on preventing the protrusion of PC bars and concrete spalling. Experimental results are used for verification of numerical investigations. The results of numerical simulations are discussed and compared with experimental results.

Facilities for experimentally testing structures under high-velocity impact loading are very expensive, and the experimental process is time consuming. Therefore, these facts restrict experimental studies in this area. Recently, the effectiveness of numerical simulation has been increased with much less computational effort. When analytical results are experimentally verified, numerical predictions can reduce experimental costs [9].

4.5.1 Experimental Program

a) Details of Specimen

The details of the specimen in this section were the same as section 4.2.1a. However, in this section, the cover layer asphalt pavement was excluded. Only the guss asphalt pavement (50 mm thickness base layer) was used as a countermeasure.

b) Materials

The materials used in this section were the same as section 4.2.1b.

c) Testing Procedures

The details of the testing procedures in this section were the same as section 4.2.1c.

4.5.2 Verification of AEM Simulation

a) Bending Test of Guss Asphalt Base Layer at 20°C

Material properties and bending test of guss asphalt pavement (base layer) at 20°C (Fig 4.4).

b) Verification of AEM Simulation with One Layer of Guss Asphalt Pavement at 20°C

AEM numerical simulation was carried out for the specimen explained in Fig. 4.1. The details of the modeling are shown in Fig. 4.5. The details of loading stages were already explained in section 3.4.2. However, in this study the cover layer asphalt pavement (30 mm thick) was excluded to simulate the worst condition in reality and only the base layer with 50 mm thickness and 2 m × 2 m area was investigated in terms of its performance in preventing the protrusion of vertically tightened PC bar tendons with 4,408 J impact energy at 20°C (Fig. 4.31).

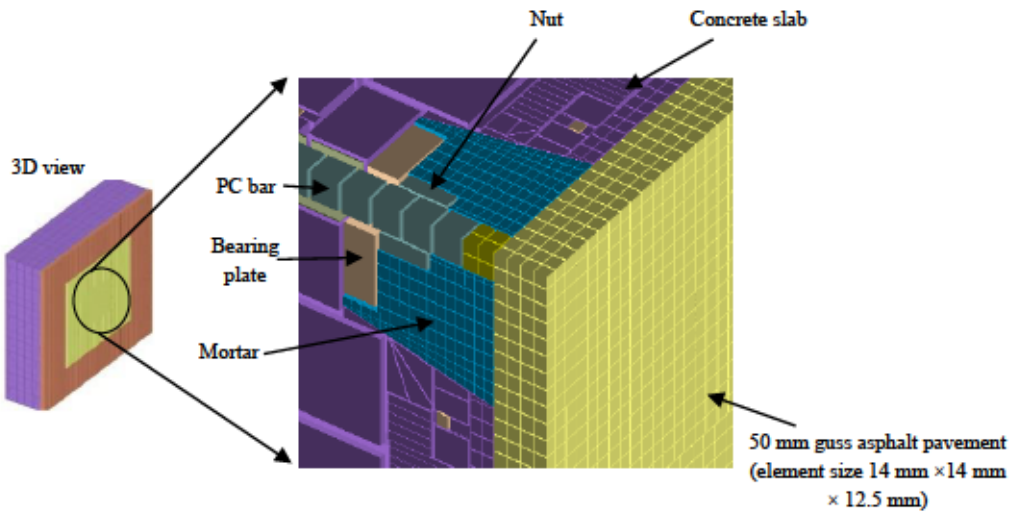

Fig. 4.31 Modeling for AEM numerical simulation considering guss asphalt pavement

When the PC bar protruded, the asphalt pavement was fractured under a high loading rate. The failure mechanisms under the high-strain rate loading were found to be considerably different from those obtained in static testing where failure of binder was a predominant mechanism [2]. High-strain rate loading caused trans-aggregate failures in addition to failure of the binder as shown in (Fig. 2.11). It was necessary to consider the effect of strain rate in the numerical simulation. For the asphalt pavement under high loading rate, the yield stress and the elastic modulus was increased by the respective Dynamic Increase Factor (*DIF*).

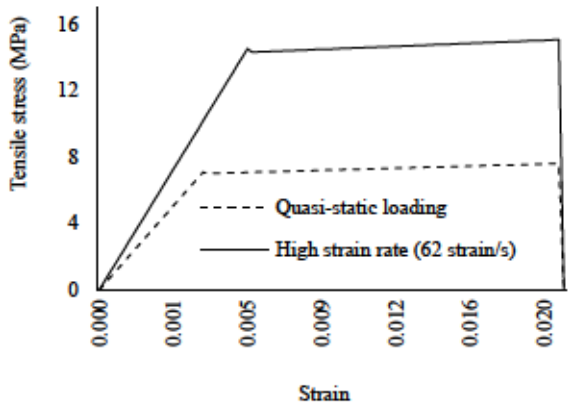

Fig. 4.32 Material properties of asphalt pavement in tension after considering strain rate [10]

The strain rate was checked in the numerical simulation result at the center of the asphalt pavement for a normal spring between asphalt pavement elements. It was found that, the average maximum strain rate was 62 s^{-1}. The *DIF* of the asphalt pavement under compression and tension at a high loading rate (strain rate > 30 s^{-1}) can be calculated using Equation 2.3 and Equation 2.4 [11]. The *DIF* for Young's modulus can be calculated using Equation 2.5 [12]. In the numerical simulation, for a normal spring between the asphalt pavement elements, the quasi-static yielding stress and the Young's Modulus were multiplied by the respective *DIF*. The *DIF* of a normal spring between the asphalt pavement elements was 2.00 for the yield stress and 1.46 for the Young's Modulus. Material properties of the asphalt pavement after considering strain rate effect is shown in Fig. 4.32.

4.5.3 Result and Discussion

The impact resistance performance of the asphalt pavement is discussed. Photographs were taken after the impact; cracks in the asphalt pavement and in the non-shrinking mortar, crater area, interface bond delamination between the asphalt pavement and the concrete slab and final state of the PC bar protrusion were measured as damage criteria. The PC bar protrusion was measured to determine the actual displacement of the PC bar into the asphalt pavement. The PC bar protrusion was measured at the head of the PC bar before and after the rupture of the PC bar. An image analysis was used to determine irregular crater areas.

When the PC bar was ruptured, all the strain energy of the PC bar (4,408 J) was released instantly. A stress wave was generated at the cut point and propagating along the PC bar and impacted the asphalt pavement and the non-shrinking mortar with a high loading rate. When the PC bar impacted the asphalt pavement, a very high stress was developed near the impact area, forming a shear-cone shaped fracture zone. Stress generated from the head of the nut propagated diagonally and created a cone shaped crack in the non-shrinking mortar. Similarly, stress generated from the head of the PC bar propagated diagonally and created a cone shaped crack in the asphalt pavement (Fig. 4.33). In addition, the impact of the PC bar induced compressive shock wave on the front face of the asphalt pavement and reflected from the rear free surface of the asphalt pavement as tensile wave. At the rear free surface of the asphalt pavement, the total stresses of the compression wave and the reflected tension wave exceeded the tensile capacity of the asphalt pavement and produced a rear crater (~ 0.04 m^2) (Fig. 4.33d).

A trans-aggregate failure in addition to a binder failure was observed on the cracked surface of the asphalt pavement as shown in Fig. 4.33d. This clearly indicated that, the asphalt pavement was fractured under a high loading rate. To simulate the strain rate effect in the numerical simulation, the yield strength and the Young's modulus of the asphalt pavement springs between the asphalt pavement elements were multiplied by the *DIF* to enhance the material properties as explained in section 3.5.2b.

As the PC bar tendon protruded forward, interface bond separation was observed at the interface between the asphalt pavement and the concrete slab as shown in Fig. 4.34. According to the numerical

simulation, bond separation in around 3.6 m^2 (90%) of interface area was observed. A similar interface bond delamination was also observed in the experiment. Deformation of the asphalt pavement was insignificant due to the brittleness of the material. As a result, guss asphalt pavement crack was observed as shown in Fig. 4.35.

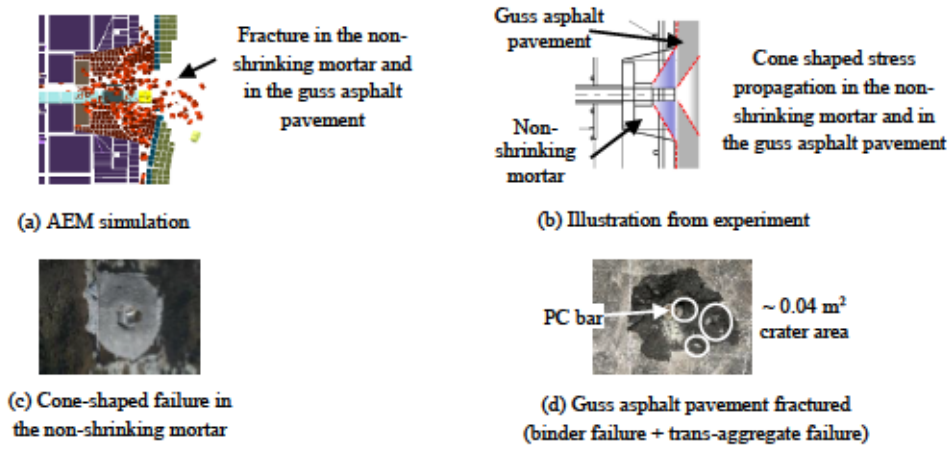

Fig. 4.33 Failure mechanism after rupture of the PC bar [10]

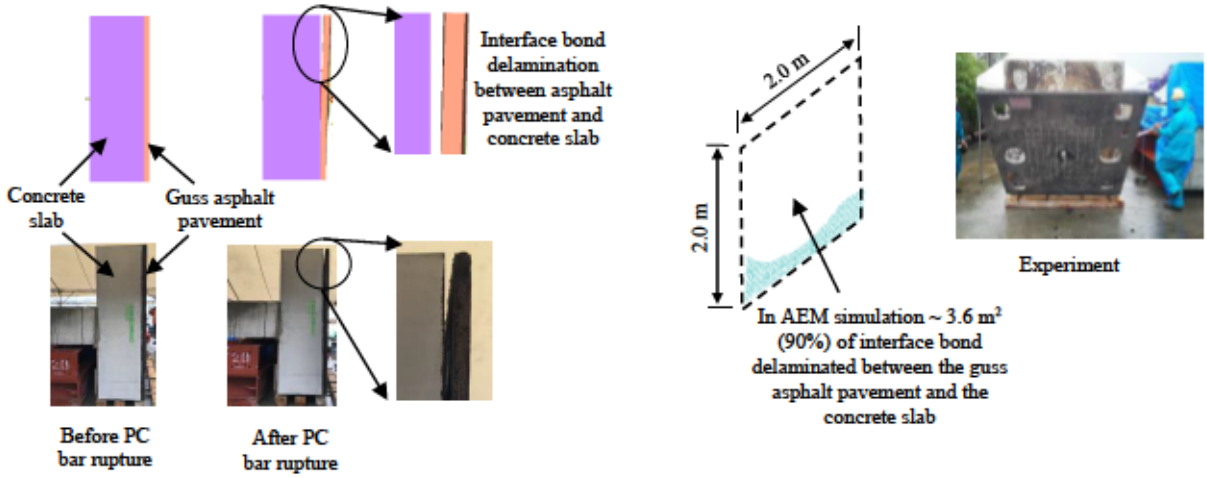

Fig. 4.34 Interface bond separation between asphalt pavement and concrete slab [10]

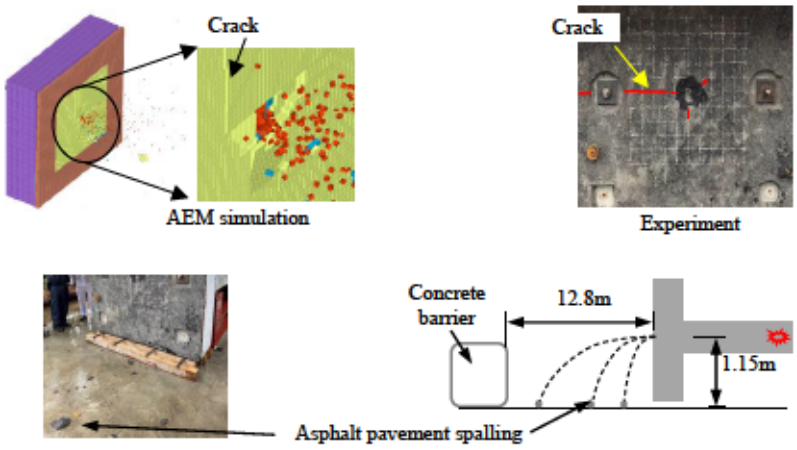

Fig. 4.35 Guss asphalt pavement fracture and spalling of small pieces after rupture of the PC bar [10]

The displacement of the PC bar in the numerical simulation was shown in Fig. 4.36 with solid line. Between 0.00 – 0.025 s, the PC bar impacted the asphalt pavement and protruded forward. The maximum PC bar protrusion was 90 mm at 0.025 s. At 0.025 s, the PC bar lost all of its kinetic energy. After that, the PC bar moved in the reverse direction, however the cracks and the crater continue to propagate. Finally, the PC bar stopped moving at a protrusion of 22 mm after 0.09 s. On the other hand, the PC bar displacement in the experiment was 72mm.

To investigate the importance of including rapid loading effect, numerical simulation was repeated neglecting the strain-rate effect (*DIF*) as illustrated in Fig. 4.37b. The numerical simulation results indicated more fracture in asphalt layer and showed that the maximum PC bar protrusion was 291 mm at 0.041 s and kept increasing (dotted line in Fig. 4.36). However, considering strain rate, the PC bar protrusion was 73 mm at 0.041 s. In the numerical simulation, energy dissipation of the asphalt pavement was enhanced after considering strain rate.

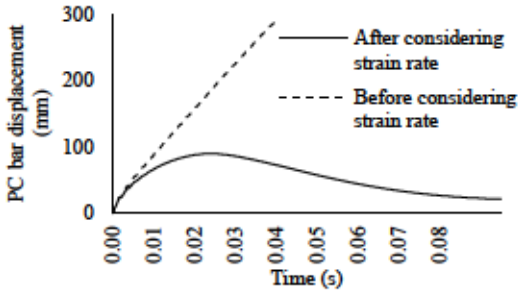

Fig. 4.36 PC bar protrusion in the AEM simulation [10]

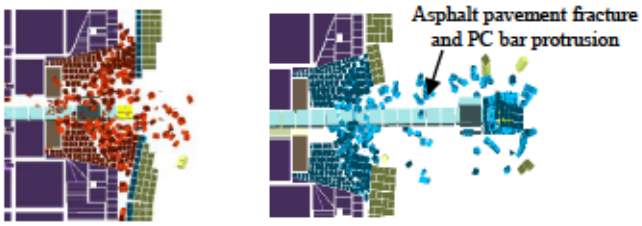

(a) AEM simulation after considering strain rate

(b) AEM simulation without considering strain rate

Fig. 4.37 The effect of strain rate on asphalt pavement failure mode (AEM numerical simulation) [10]

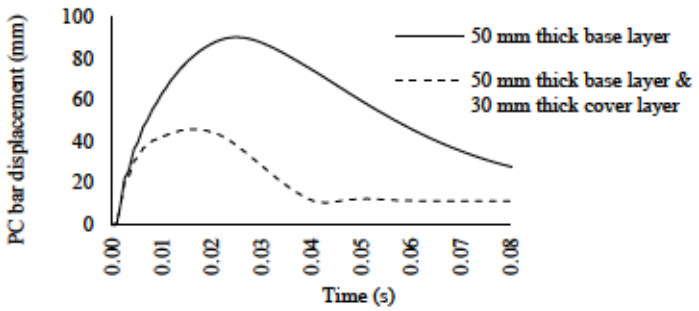

Fig. 4.38 Protrusion of PC bar with one layered asphalt pavement and with two layered asphalt pavements [10]

The PC bar protrusion of AEM simulation with the base layer asphalt pavement (only one layer) and the PC bar protrusion of AEM simulation with two layers of asphalt pavement (details are shown in section 4.2.2c and Fig. 4.14b) are shown in Fig. 4.38. From the chart, it can be clearly seen that, the two layered asphalt pavement system dissipated more energy of the PC bar.

In this study, numerical simulation with the guss asphalt pavement base layer (50 mm thickness) was carried out using the Applied Element Method (AEM) neglecting 30 mm cover layer asphalt pavement to account for time-dependent severe deterioration in the asphalt pavement. The numerical investigation showed 22 mm PC bar protrusion and asphalt pavement fracture near the PC bar. However, significant amount of energy of the PC bar was dissipated. MEX has its high-quality asphalt pavement standard. Asphalt pavement inspections and maintenances are carried out regularly for safety. Severe deterioration of asphalt pavement is seldom seen in MEX. However, as a safety management, it was necessary to investigate the impact performance of the asphalt pavement considering the extreme deterioration case.

4.5.4 Summary of Section 4.5

In the current study, the impact resistance of the asphalt pavement against PC bar protrusion was numerically investigated. 3D AEM model was developed using ELS for simulating asphalt pavement under 4,408 J impact energy. Only a single layer of guss asphalt pavement with 50 mm thick was used to simulate the worst condition in reality. A bi-linear material constitutive model was implemented for the asphalt pavement. The asphalt pavement material model was calibrated based on the bending test of an asphalt specimen. *DIF* was employed to accurately capture the dynamic material behavior of the asphalt pavement under high loading rate. Appropriate numerical simulation with the AEM can be conducted using appropriate interface material properties between the concrete slab and the asphalt pavement layer. The AEM simulation results supported the following conclusions.

- The results of the numerical simulation showed good agreement with the experimental results.
- The strain energy of the PC bar (4,408 J) was dissipated by a simultaneous action of a shear-cone shaped fracture in the asphalt pavement and in the non-shrinking mortar, interface bond delamination between the concrete slab and the asphalt pavement, and cracks in the asphalt pavement.
- Asphalt pavement fracture was observed near the anchorage area. However, the asphalt pavement was effective against the PC bar protrusion which was around 22 mm in the AEM simulation.

4.6 Summary of Chapter 4

A three-dimensional nonlinear dynamic analysis using the AEM was developed for simulating the impact resistance of the asphalt pavement against PC bar protrusion. Two layers of asphalt pavement

with 80 mm thick was used to stop protrusion of the PC bar at 0°C, 28°C and 50°C. Moreover, only a single layer of guss asphalt pavement with 50 mm thick was used to simulate the worst condition in reality (time dependent deterioration). Extreme impact energy, 4,408 J that can cover most of rupture of vertical PC bars in MEX, was applied on the asphalt pavement. The asphalt pavement material model was calibrated based on the asphalt pavement bending test. The interface bond material model was calibrated based on the pull-off adhesive test. The *DIF* was employed to accurately capture the dynamic material behavior of the asphalt pavement under high loading rate. The AEM simulation results support the following conclusions.

- Appropriate numerical simulation with the AEM can be conducted with appropriate interface material property between the slab concrete and the asphalt pavement layers, considering the fracture energy of concrete and asphalt pavement, with appropriate mesh discretization, appropriate time interval, appropriate Normal Contact Stiffness Factor (*NF*), and considering strain rate effects both in concrete and in asphalt pavement.
- The asphalt pavement system used in this study, without using a steel plate and FRP sheet, with appropriate material and thickness could prevent the protrusion of the PC bar of 4.5 m rupture length. The AEM simulation results proved that the two layers of asphalt pavement with 80 mm thick at 0°C, 28°C and 50°C was effective against 4,408 J impact energy and effective against PC bar protrusion and concrete spalling. Moreover, a single layer of guss asphalt pavement with 50 mm thick at 20°C was effective against PC bar protrusion which was around 22 mm in the AEM simulation. However, asphalt pavement fracture was observed near the anchorage area.
- Based on the analysis results, the effectiveness of the asphalt pavement system depends on impact energy of ruptured PC bars, material properties of asphalt pavements, material properties of interface bond materials, fracture energy, mesh discretization, strain rate and temperature.
- In the two layers of asphalt pavement system at 28°C, the PC bar protrusion was prevented by ductile deformation of asphalt pavement delaminated from slab concrete. The strain energy of the PC bar was dissipated by a simultaneous action of asphalt pavement deformation, cone-shaped crack in the mortar, and interface delamination between the slab concrete and the asphalt pavement.
- In the two layers of asphalt pavement system at 50°C, the strain energy of the PC bar (4,408 J) was dissipated by a synchronized action of a shear-cone shaped fracture in the concrete and in the non-shrinking mortar, deformation and cracks in the asphalt pavement.
- In the two layers of asphalt pavement system at 0°C, the strain energy of the PC bar (4,408 J) was dissipated by a synchronized action of a shear-cone shaped fracture in the base layer and

in the non-shrinking mortar, deformation and cracks in the asphalt pavement and delamination of tack coat.

- In the single layer (50 mm tick) of guss asphalt pavement system at 20°C, the strain energy of the PC bar (4,408 J) was dissipated by a simultaneous action of a shear-cone shaped fracture in the asphalt pavement and in the non-shrinking mortar, interface bond delamination between the concrete slab and the asphalt pavement, and cracks in the asphalt pavement.
- The results of the numerical simulation had a good agreement with the experimental data.

References in Chapter 4:

[1] Bonger A.D, Hosoda A., Salem H., and Fukaya T., "Numerical simulation of rupture and protrusion of vertically tightened PC steel bars in PC girders with asphalt pavement using Applied Element Method," *Journal of Japan Society of Civil Engineers*, vol. 10, pp. 145–161, 2022.

[2] Tekalur S. A., Shukla A., Sadd M., and Lee K. W., "Mechanical characterization of a bituminous mix under quasi-static and high strain rate loading," *Construction and Building Materials, Vol. 23*, pp. 1795–1802, 2009.

[3] Rui T., Zhenpeng Y., Guoqing L., Furong L., and Wenbin T., "Uniaxial dynamic compressive behaviors of hydraulic asphalt concrete under the coupling effect between temperature and strain rate," *MDPI Journals, Materials 2020, 13, 5348; doi:10.3390/ma13235348*, 2020.

[4] Wei S., Ning L., Biao M., Yu-xiang T., and Xue-yan Z., "Temperature response to tensile characteristics of the hot asphalt mixtures," *KSCE Journal of Civil Engineering (2016) 20(4): DOI 10.1007/s12205-015-0688-2*, pp. 1336–1346, 2006.

[5] Bonger, A., Hosoda, A., Hamed, S. and Fukaya, T., "AEM simulation of impact resistance of asphalt pavement on PC bridge caused by rupture of vertical PC bars at high temperature," *6th fib International Congress*, Oslo, Norway, 2022 (in press).

[6] Ding B., Xiaolong Z., Zixin P., and Xiang L., "Evaluation of fracture resistance of asphalt mixtures using the single-edge notched beams," *Advances in Materials Science and Engineering, Volume 2018, Article ID 8026798.*, 2018.

[7] Jun W., Liang L., Xiuli D., and Xuemei L., "Numerical study on the asphalt concrete structure for blast and impact load using the Karagozian and case concrete model," *Journal of Applied Science, 2017, 7, 202; doi:10.3390/app7020202*, 2017.

[8] Bonger, A., Hosoda, A., Hamed, S. and Fukaya, T., "Applied Element Method analysis of asphalt pavement on PC bridge under the coupling effect between impact from ruptured vertical PC bars and temperature." *International Journal of Impact Engineering*, manuscript No. IE-D-22-00652, 2022 (under review).

[9] Tai Y.S., "Flat ended projectile penetrating ultra-high strength concrete plate target," *Theoretical and Applied Fracture Mechanics 51, doi: 10.1016/j.tafmec.2009.04.005*, pp. 117–128, 2009.

[10] Bonger, A., Hosoda, A., Hamed, S. and Fukaya, T., "Impact Analysis of Asphalt Pavement Against PC Bar Protrusion Using Applied Element Method." *11th International Conference on Bridge Maintenance, Safety and Management*, ISBN 978-1-032-35623-5, DOI: 10.1201/9781003322641-15, 157-165, Barcelona, Spain, 2022.

[11] Oo H., Kano K., and Shinai S., "Comparative analysis of concrete and UFC construction subjected to impact loading," *J. Taisei Corp. No. 39*, 2006.

[12] Bischoff P.H. and Perry S.H., "Compressive behavior of concrete at high strain rates," *Materials and Structures Vol. 24, No. 6*, pp. 425–450, 1991.

CHAPTER 5

NUMERICAL SIMULATION OF DYNAMIC PUNCHING TEST OF POLYUREA SHEET USING APPLIED ELEMENT METHOD

5.1 General

In this chapter, punching tests for polyurea sheet with thickness of 3 mm, 5 mm and 10 mm under different impact loads were investigated. This chapter numerically investigates the effects of polyurea coating on impact resistance and on preventing concrete spalling. The results obtained are used to assess the extent of energy absorption and to identify the mode of failure of the polyurea as a function of the imposed impact conditions. It was found in this study that 3 mm and 10 mm thick polyurea sheet with 500 mm × 500 mm area could not withstand 758 J and 3,983 J impact energy, respectively. However, 5 mm thick polyurea sheet could withstand 758 J impact energy [1]. Effectiveness of the polyurea sheet depended on impact energy, polyurea thickness, bond strength, and material properties of polyurea and primer. The numerical simulation tool developed in this study will be utilized in the future for evaluating the effectiveness of polyurea sheet against rupture and protrusion of PC bar tendon and concrete spalling in PC bridges.

5.2 Experimental Programs

5.2.1 Materials

a) Polyurea

Mechanical properties of aromatic polyurea are shown in Table 5.1. Tensile strength and elongation of the polyurea were obtained from experimental investigation based on JIS K 6251. Two kinds of liquids were mixed by collision using a spray gun, forming coating of 3 mm, 5 mm and 10 mm thickness.

Table 5.1 Mechanical properties of polyurea

Properties	Values
Tensile strength (MPa)	22
Elongation (%)	300
Durometer hardness (D type)	51
Tear Resistance (N/mm)	90
Volume resistivity (Ω.cm)	10^7

b) Adhesive

For dry concrete, applying primers can improve adhesion results [2]. The adhesive strength of the polyurea coating with a primer was experimentally investigated by pull-off adhesion test on dry

concrete and it was 1.32 MPa. The pull-off adhesion test was based on JIS A6909 6.10 standard. The concrete surface was smoothened by a sandpaper before applying the primer. During this test, a concrete cohesive failure was observed due to poor-quality surface concrete despite adhesive failure was expected. However, according to Japanese highway company guidelines, the specified value for the adhesive strength of spalling prevention material is more than 1.5 MPa [3].

c) Concrete

A prefabricated concrete product based on JIS A 5372 was used.

5.2.2 Loading Method

A numerical simulation of rupture and protrusion of PC bar was conducted by the authors using AEM [4]. The prestress force after prestress loss was 591 kN (0.6Pu). The PC bar tendon used was a 5.0 m standard steel bar: SBPR930/1180 (class B2 in JIS). PC bar rupture length was 4.5 m measured from the PC bar head. Strain energy of the PC bar was 4,408 J [4].

In this study, the impact energies were decided by taking 17% (758 J) and 90% (3,983 J) of the strain energy of the 4.5 m PC bar mentioned above. The experiments were carried out using a drop weight test instrument as shown in Fig 5.1. Three types of punching tests were conducted with different impact loading and with different polyurea thickness as shown in Table 5.2. The kinetic energy of the drop weight at impact in Case 1 and Case 2 was 758 J which represents 17% of the strain energy of the PC bar, while the impact energy in Case 3 was 3,983 J which represents 90% of the strain energy of the PC bar.

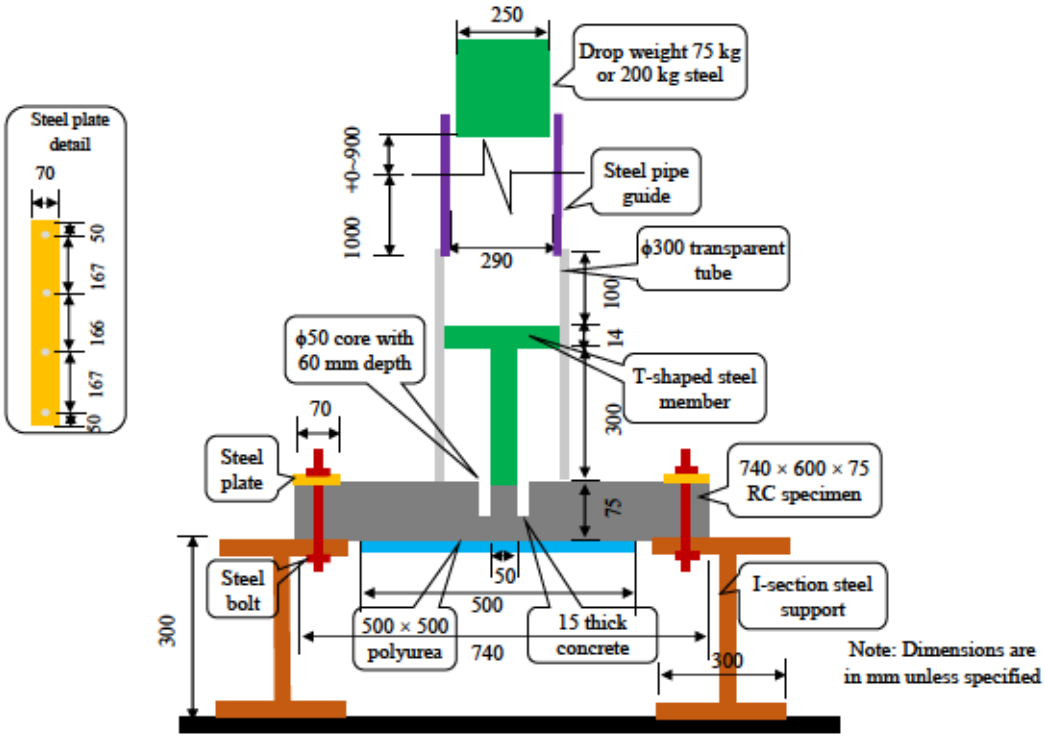

Fig. 5.1 Drop weight test [1]

Table 5.2 Types of polyurea punching punchout test [1]

Cases	Thickness of polyurea (mm)	Drop weight (kg)	Drop height (m)	Impact energy (J)
Case 1	3	75	1	758
Case 2	5	75	1	758
Case 3	10	200	2	3,983

5.2.3 Testing Procedure

A reinforced concrete specimen, 740 mm × 600 mm × 75 mm, with coring at the center of the specimen was provided. The core had inner diameter of 50 mm and outer diameter of 55 mm and 60 mm depth. 15 mm thick concrete remained below the core. The bottom surface of the concrete specimen was smoothened by a sandpaper before applying a primer. A primer was used to attach a 500 mm × 500 mm polyurea on the bottom surface of the concrete specimen. The concrete specimen was fixed with I-section steel support using steel plates and bolts as shown in Fig 5.1. A T-shaped steel member was attached to the center of the specimen to transfer the impact load to the concrete and to the polyurea. Deformation and failure processes of the polyurea under high-speed punching were recorded with the aid of a high-speed camera.

5.3 AEM Simulation of Punching Test of Polyurea

5.3.1 AEM Simulation Modeling

In this study, a non-linear structural analysis software "Extreme Loading for Structure (ELS)" based on AEM was used. AEM numerical simulation was conducted for the drop weight test explained in Fig. 5.1. The details of the modeling of the punching test are shown in Fig. 5.2. The reinforced concrete specimen was fixed at its edges at the bottom as shown in Fig. 5.2b (marked with yellow color). The drop weight was free in all degrees of freedom as it falls under gravity. The T-shaped steel member was free to move only in z-direction.

In the analysis, two stages of loading were provided. The first one was static to account for boundary conditions and self-weight of polyurea, concrete and steel, while the second one was dynamic to simulate the drop weight and its impact to concrete and polyurea. The initial condition of the weight drop stage was zero initial velocity. In the AEM simulation, a concrete with assumed compressive strength of 40 MPa was used. Element size of the concrete specimen below the core was 5 mm × 5 mm × 3.75 mm as shown in Fig. 5.2c. Element size of other parts of the concrete specimen was 15 mm × 15 mm × 15 mm. A 500 mm × 500 mm polyurea sheet was attached under the concrete specimen. The polyurea material was modeled as shown in Fig 5.3b. The interface material between the concrete specimen and the polyurea was the nonlinear material shown in Fig 5.4b. The "bearing material" in ELS which can transfer only compression was used for the interface between the concrete specimen

and the T-shaped steel. A normal steel material was used for the drop weight and the T-shaped steel member.

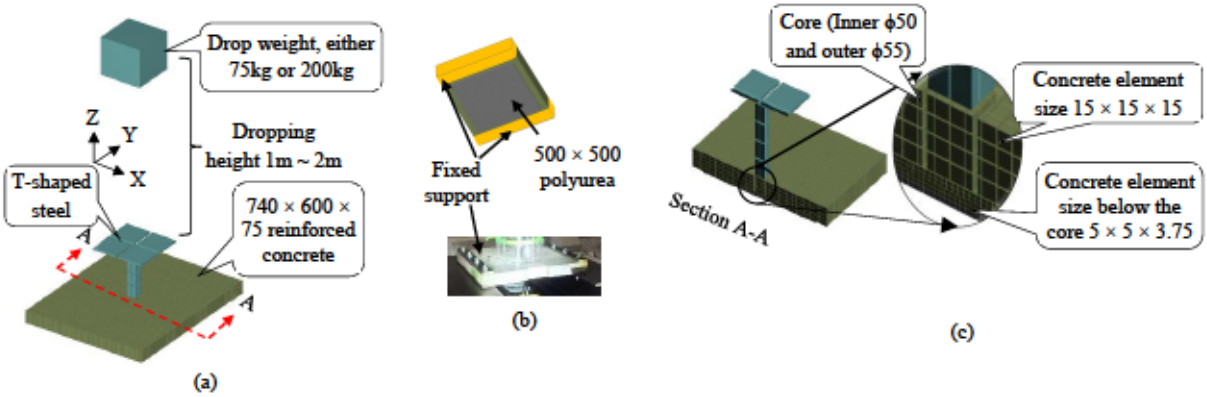

Fig. 5.2 AEM simulation modelling [1]

5.3.2 AEM Simulation of Case 1 (Using 3 mm Thick Polyurea)

In Case 1, 3 mm thick polyurea was attached to the concrete specimen. The element size of the polyurea was 3 mm × 5 mm × 5 mm. The drop weight had a mass of 75 kg and fell from 1 m height. The kinetic energy of the drop weight at impact was 758 J (17% of the strain energy of the PC bar). In the numerical simulation, the dynamic stage had a duration of 0.7 s (0.46 s to account for the drop weight free fall time + 0.24 s for impact and destruction). The time interval was 0.0002 s.

For polyurea under tension, the relationship between tensile stress and strain was modeled to be approximately bilinear with strain hardening [5]. In the drop weight AEM simulation, the constitutive model of the polyurea until ultimate strength (22 MPa) was implemented through a bilinear material. The Young's Modulus (250 MPa) and yield stress (16 MPa) of polyurea was calibrated from the drop weight AEM simulation (Fig. 5.5). To show the stress-strain curve of a polyurea, a simple tension test was carried out using AEM as shown in Fig 5.3. In the simple tension test (Fig 5.3a), a bilinear material simulating polyuria was used between the concrete and the steel plate. The concrete was fixedly supported. Tension force was applied on the steel plate. The stress-strain curve of the simulate polyurea is shown in Fig 5.3b. In the initial region, the stress increases proportionally to the strain. After that the material starts to yield. Then the stress still increases linearly but much more slowly until ultimate strength (22 MPa) at a strain of 2.55. Finally, a perfect plastic deformation was followed from a strain of 2.55 to a strain of 3.00.

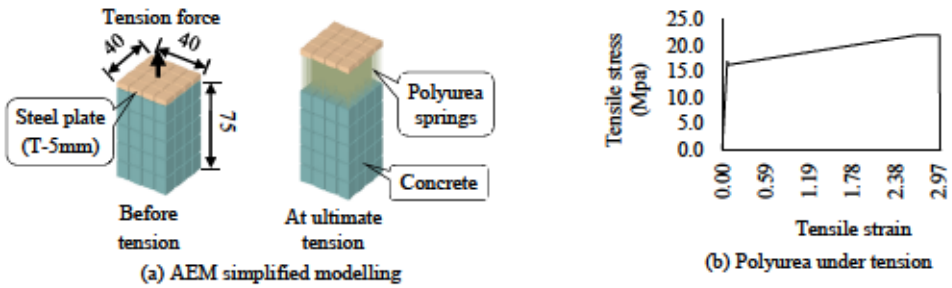

Fig. 5.3 AEM simulation of polyurea under tension [1]

In the drop weight AEM simulation, a nonlinear material showing softening behavior after reaching the maximum stress was used to simulate adhesive between the polyurea and the concrete specimen. The adhesive used in the pull-off adhesion test and in the drop weight experiment was similar. However, the pull-off strength (1.32 MPa) from the pull-off adhesion test was small as a concrete cohesive failure was observed due to poor-quality surface concrete despite adhesive failure was expected. Using adhesive strength from the pull-off adhesion test in the drop weight AEM simulation resulted in a total delamination of polyurea despite the experiment as shown in Fig 5.5. However, a similar drop weight AEM simulation with a 3.4 MPa adhesive strength withstand 758 J impact energy without total delamination and showed good agreement with the experimental result (Fig 5.5). This might be associated with the strain rate effect in the adhesive. In this study, the adhesive strength of 3.4 MPa was found appropriate. A simple tension test was conducted using AEM to show the stress-strain curve of this material as shown in Fig 5.4. In this test, a linear material which shows softening behavior after tensile strength was used between the concrete and the polyurea. The Young's Modulus (4,500 MPa) of the primer was calibrated from the drop weight AEM simulation (Fig. 5.5). The concrete was fixedly supported. Tension force was applied on the polyurea element. The stress-strain curve is shown in Fig 5.4b. The maximum tensile stress was 3.4 MPa and after that stress softening took place.

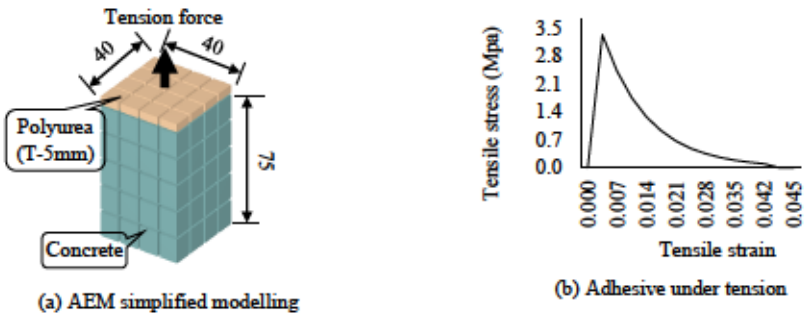

(a) AEM simplified modelling

(b) Adhesive under tension

Fig. 5.4 AEM simulation of adhesive material [1]

The polyurea punching test result shown in Fig. 5.5. Figure 5.5a shows the progressive failure of polyurea and concrete spalling both in the experiment and in the numerical simulation at different time. The concrete under the core crushed instantly after the impact. After that, the polyurea started elongation. In the numerical simulation, a vertical deformation of polyurea was measured. The maximum vertical deformation before cracking appeared in the polyurea was 60 mm at 0.48 s as shown in Fig. 5.5c. In the experiment, a high-speed camera measured the maximum polyurea deformation of 70 mm. While the polyurea was elongated, the primer between the polyurea and the concrete was delaminated in 280 mm × 280 mm area. Delamination area of the primer in the experiment was 275 mm × 250 mm. After the partial delamination, the polyurea couldn't stretch any longer and was torn, and crushed concrete was observed as shown in Fig. 5.5b and Fig. 5.5d.

In the numerical simulation, the kinetic energy of the drop weight was measured to assess the energy absorption of polyurea as shown in Fig. 5.6. From 0.00 s to 0.458 s, the drop weight was freely falling. From 0.458 s to 0.460 s, the concrete below the core was crushed, and the kinetic energy of the

drop weight suddenly dropped from 758 J to 342 J. After that, the polyurea elongated from 0.46 s to 0.50 s and the kinetic energy of the drop weight gradually decreased from 342 J to 130 J. At 0.48 s, first crack was observed in the polyurea. At 0.50 s, the polyurea was torn apart and no longer resisted against the impact loading. The drop weight and the T-shaped steel member freely fell until they impacted the ground surface.

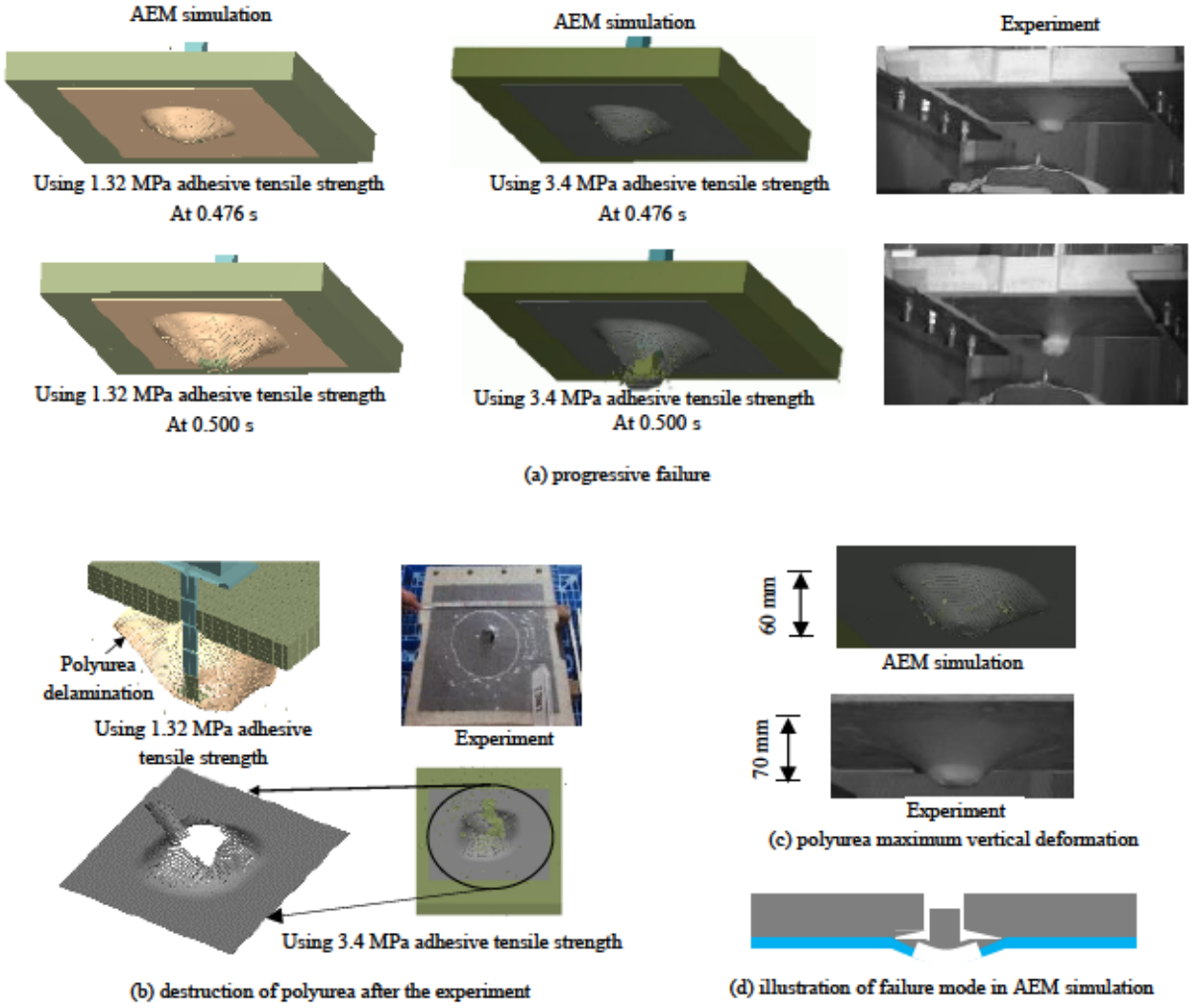

Fig. 5.5 Polyurea punching test (3 mm thick polyurea) [1]

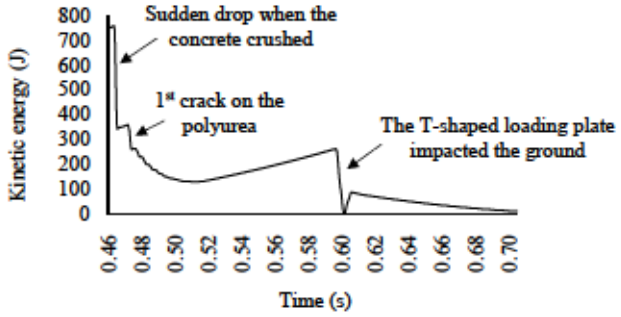

Fig. 5.6 Kinetic energy of the drop weight (Case 1) [1]

In this investigation, a 500 mm × 500 mm polyurea with 3 mm thickness couldn't prevent the protrusion simulating 17% strain energy of the PC bar protrusion of 4.5 m length.

5.3.3 AEM Simulation of Case 2 (Using 5mm Thick Polyurea)

In Case 2, 5 mm thick polyurea was attached to the concrete specimen. The simulation model in this case is the same as in Case 1 except that the element size of the polyurea was 5 mm × 5 mm × 5 mm.

Fig. 5.7a shows the progressive deformation of polyurea both in the experiment and in the numerical simulation at different time. The concrete under the core crushed instantly after the impact. After that, the polyurea started elongation. Fig. 5.7b shows the deformed polyurea after the experiment. In the numerical simulation, a vertical deformation of polyurea was measured. The maximum vertical deformation was 87 mm at 0.52 s as shown in Fig. 5.7c. In the experiment, the maximum vertical deformation measured by the high-speed camera was 85 mm. While the polyurea was elongated, the primer between the polyurea and the concrete was delaminated in 410 mm × 410 mm area. The delamination area of the primer in the experiment was 355 mm × 380 mm. After 0.52 s, the drop weight lost all of its kinetic energy and the polyurea recovered from the maximum deformation. Concrete spalling and cracking in the polyurea were not observed. The illustration of failure mode in AEM simulation is shown in Fig. 5.7d.

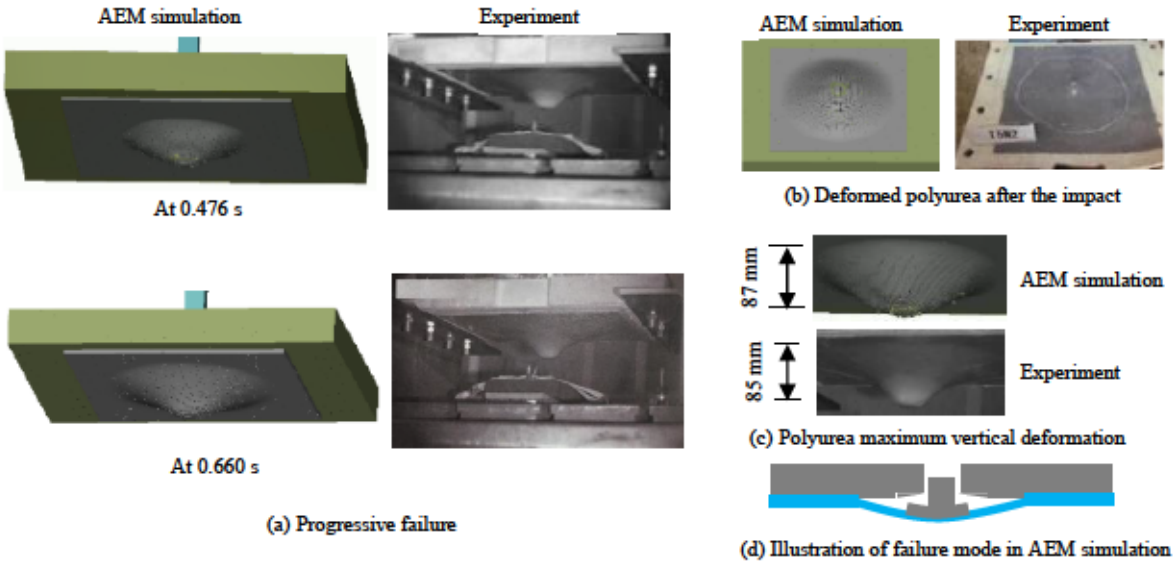

Fig. 5.7 Polyurea punching test (5 mm thick polyurea) [1]

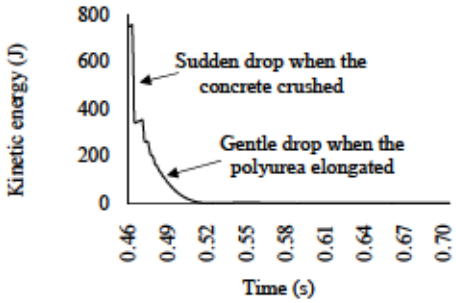

Fig. 5.8 Kinetic energy of the drop weight (Case 2) [1]

In the numerical simulation, the maximum speed of the drop weight at impact was 4.49 m/s and the kinetic energy was 758 J. From 0.458 s to 0.460 s, the speed of the drop weight was suddenly dropping from 4.49 m/s to 3.00 m/s as the concrete was crushing. At the same time interval, the kinetic energy of the drop weight suddenly dropped from 758 J to 340 J as shown in Fig. 5.8. From 0.46 s to 0.52 s, the polyurea elongated gradually until the kinetic energy of the drop weight decreased from 340 J to 0 J.

In this investigation, a 500 mm × 500 mm polyurea sheet with 5 mm thickness could prevent the protrusion simulating 17% strain energy of the PC bar protrusion of 4.5 m length.

5.3.4 AEM Simulation of Case 3 (Using 10mm Thick Polyurea)

In Case 3, 10 mm thick polyurea was attached to the concrete specimen. The element size of the polyurea was 5 mm × 5 mm × 5 mm. The drop weight had a mass of 200 kg and fell from 2 m height. The kinetic energy of the drop weight at impact was 3,983 J (90% of the strain energy of the PC bar). In the numerical simulation, the dynamic stage had a duration of 1.0 s. Two dynamic stages were used. The first one was to account for free falling, while the second one was to simulate the drop weight impact to the concrete and the polyurea. The 1st dynamic stage had a duration of 0.64 s with a time interval of 0.01. The 2nd dynamic stage had a duration of 0.36 s with a time interval of 0.00015.

Fig. 5.9a shows the progressive failure of polyurea and concrete spalling both in the experiment and in the numerical simulation at different time. Similar to Case 1 and Case 2, the concrete under the core crushed instantly after the impact. After that, the polyurea started elongation. In the numerical simulation, the vertical deformation of polyurea was measured. The maximum vertical deformation before the polyurea was fully delaminated was 100 mm at 0.67 s as shown in Fig. 5.9b. In the experiment, the maximum polyurea deformation measured by the high-speed camera was 116 mm. At 0.67 s, the polyurea sheet was totally delaminated resulting in falling down caused by the cohesive failure of skin layer of the concrete specimen as shown in the illustration Fig. 5.9c. No crack was observed in the polyurea.

In the numerical simulation, the maximum speed of the drop weight at impact was 6.31 m/s and the kinetic energy was 3,983 J. From 0.64 s to 0.65 s, the speed of the drop weight was suddenly dropping from 6.31 m/s to 5.62 m/s as the concrete was crushing. At the same time interval, the kinetic energy of the drop weight suddenly dropped from 3,983 J to 3,160 J as shown in Fig. 5.10. From 0.65 s to 0.67 s, the polyurea elongated gradually until the kinetic energy of the drop weight further decreased from 3,160 J to 1,376 J. After 0.67 s the kinetic energy of the drop weight gradually increasing due to gravity as the polyurea and the concrete no longer resisted against the impact load.

In this investigation, 500 mm × 500 m polyurea sheet with 10 mm thickness couldn't prevent the protrusion simulating 90% strain energy of the PC bar protrusion of 4.5 m length.

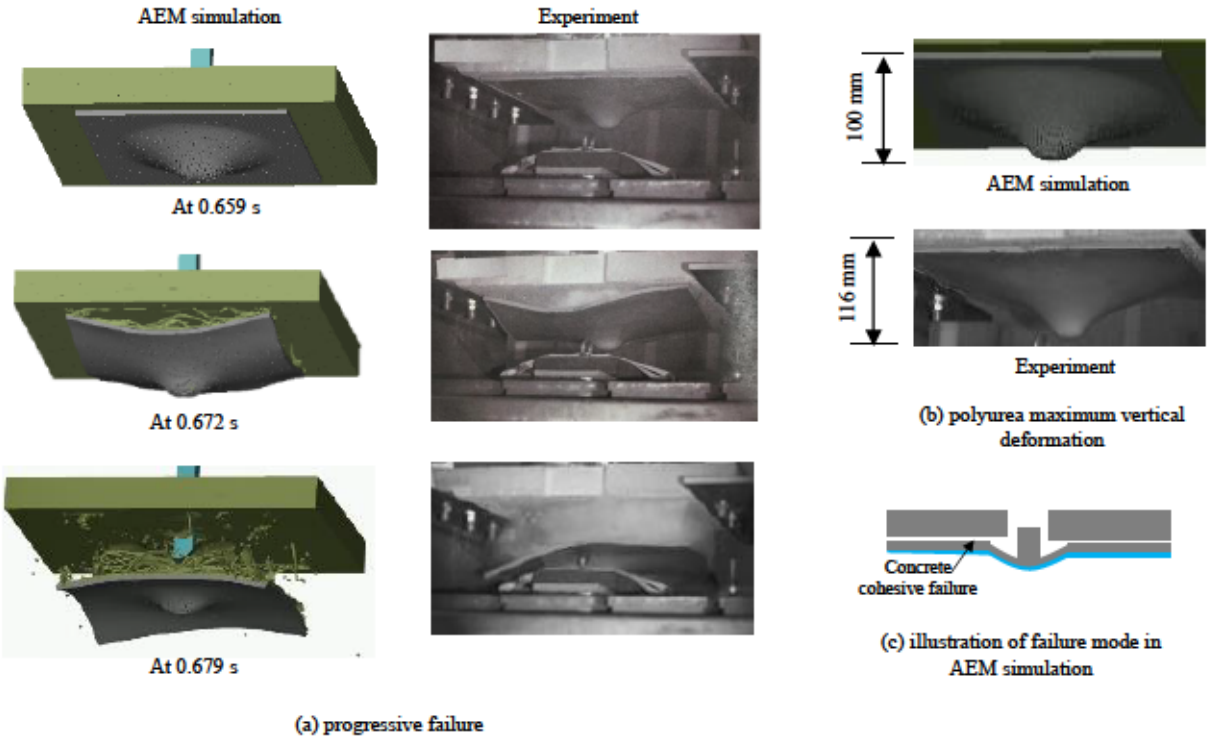

Fig. 5.9 Polyurea punching test (10 mm thick polyurea) [1]

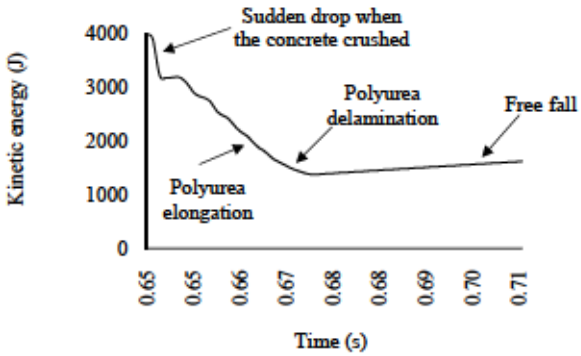

Fig. 5.10 Kinetic energy of the drop weight (Case 3) [1]

In our future investigation, the surface quality of the concrete specimen in the experiment will be improved to avoid concrete cohesive failure during impact. The numerical simulation tool developed in this study will be utilized for evaluating the effectiveness of polyurea against rupture and protrusion of PC bar tendon and concrete spalling in PC bridges.

5.4 Summary of Chapter 5

In this study, the effects of polyurea coating on impact resistance and concrete spalling were numerically investigated. Punching tests of polyurea with a thickness of 3 mm, 5 mm and 10 mm under different impact loads were numerically investigated. The numerical simulations were verified with the experiments. Based on the results obtained in the present work, the following main summary remarks and conclusions can be drawn:

- Both numerical simulations and high-speed photography measurements indicated that the polyurea sheet significantly reduced impulsive loads.
- Effectiveness of the polyurea sheet depends on impact energy, polyurea thickness, bond strength, primer and quality of surface concrete, etc.
- The constitutive model using a bi-linear material for polyurea in the drop weight AEM simulation showed good agreement with the experimental results in terms of impact resistance and failure mode.
- A polyurea (500 mm × 500 mm) sheet with 5 mm thickness was effective in resisting against 758 J impact energy. However, 3 mm and 10 mm thick polyurea sheets with 500 mm × 500 mm were not effective in resisting against 758 J and 3,983 J impact energy respectively.

References in Chapter 5:

[1] Bonger D. A., Hosoda A., Salem H., and Fukaya T., "Numerical simulation of dynamic punching test of polyurea using Applied Element Method," *Japan Concrete Institute*, Vol.43, No.1., pp. 1103–1108, Nagoya, Japan, 2021.

[2] Broekaert M., "Polyurea spray coatings, the technology and latest developments," *Huntsman International LLC., Belgium,* 2002.

[3] Shimamoto K. and Yashiro K., "Spalling prevention method for tunnel lining using polyurea resin," *Railway Technical Research Institute, Vol. 58, No. 3*, pp. 217–222, 2017.

[4] Bonger A.D, Hosoda A., Salem H., and Fukaya T., "Numerical simulation of rupture and protrusion of vertically tightened PC steel bars in PC girders with asphalt pavement using Applied Element Method," *Journal of Japan Society of Civil Engineers*, vol. 10, pp. 145–161, 2022.

[5] Cui J., Shi Y., Zhang X., Huang W., and Ma M., "Experimental study on the tension and puncture behavior of spray polyurea at high strain rates," *Polymer 93 (2020) 106863*, pp. 1–11, 2020.

CHAPTER 6

DROP WEIGHT IMPACTING STEEL FIBER REINFORCED PCM FOR INVESTIGATING ENERGY ABSORPTION CAPACITY

6.1 General

This chapter evaluated the impact resistance of a steel fiber reinforced polymer cement mortar (PCM) against drop weight impact. Effectiveness of the PCM depended on impact energy, depth of core, and material properties of the PCM. Moreover, the experimental and simulation results reveal that boundary conditions of the test significantly affected the impact resistance of the target PCM. The results of the Applied Element Method (AEM) numerical simulation showed a good agreement with the experimental data and can be used for further research.

6.2 Steel Fiber Reinforced Polymer Cement Mortar (PCM)

Cover concrete can be damaged and rebar can be exposed during pavement replacement over a bridge deck slab with inaccurate flatness [1]. To restore a damaged cover concrete, a steel fiber reinforced polymer cement mortar (PCM) was developed by MEX in 2014 (Fig. 6.1). The PCM is an ultrahigh early strength polymer cement mortar which can be mixed and applied on the site like a shotcrete. Ultra-high early strength is required due to restrictions on construction time.

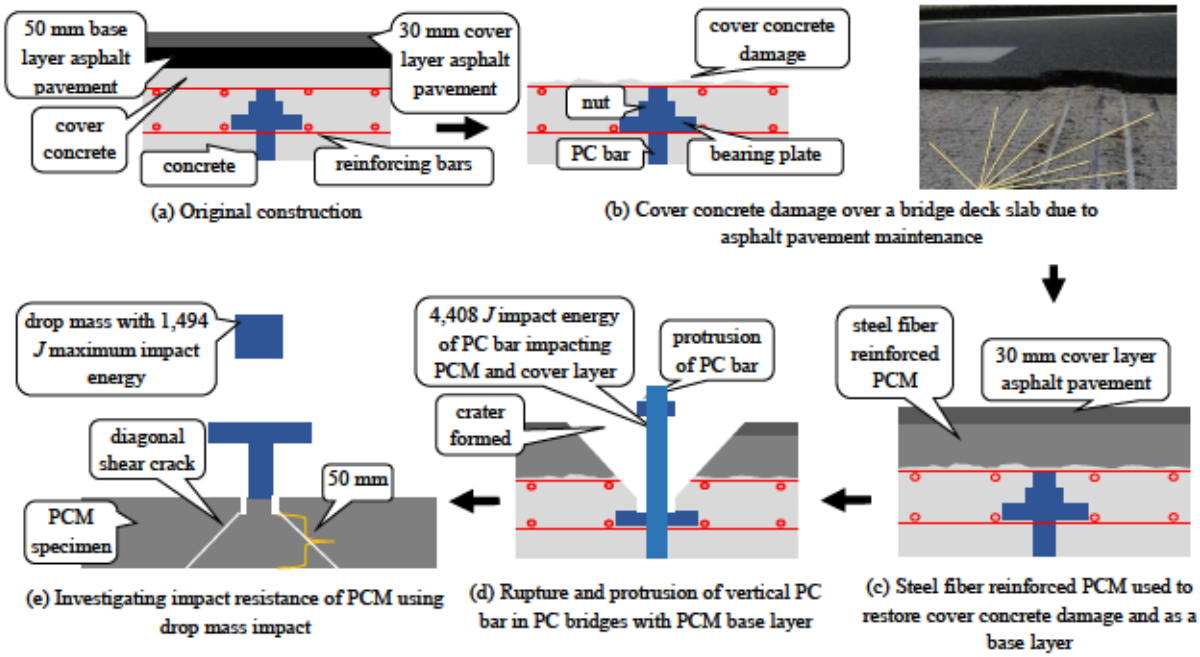

Fig. 6.1 Illustration of relationship between protrusion of PC bar and drop mass impact on PCM [2]

In a bridge deck slab with damaged cover concrete, the PCM has been used not only to restore damaged cover concrete but also as a 50 mm thick base layer together with a 30 mm thick asphalt pavement cover layer (Fig. 6.1). The PCM is also expected to be effective against the rupture of vertical

PC bar. An impact energy of 4,408 J can cover most of the strain energies of vertically tightened PC bars in MEX. In this study, in order to fundamentally investigate the energy absorption capacity of the PCM, drop mass impact test is conducted with 1,494 J energy.

In this chapter, a numerical model of drop weight impact of PCM is investigated using the Applied Element Method (AEM). The results of numerical simulations are discussed and compared with experimental results.

In this chapter, three PCM specimens under different impact loads are investigated using a drop-weight impact test. The results obtained are used to assess the extent of energy absorption and to identify the mode of failure of the PCM as a function of the imposed impact conditions. The numerical model developed in this study will be utilized in the future for evaluating the effectiveness of PCM against rupture and protrusion of PC bars in PC bridges.

6.3 Experimental Program

The following sections describe the materials used and details of the experiments.

6.3.1 Materials

a) PCM pre-mix Powder

A mixture of high early strength cement powder and an aggregate with a maximum size of 5mm.

b) Steel Fiber

JIS G 3532 was used (ϕ 0.6 mm, 30 mm length, hooked-ends type, ≥ 600 MPa tensile strength and 67 mg/piece).

c) Polymer Emulsion (Lion Bond A)

JIS A 6204 was used.

d) Water

JIS A 5308 Annex C was used.

6.3.2 Mix Proportion

The mix proportion is shown in Table 6.1. The slump should be 10 ± 3.0 cm.

Table 6.1 PCM mix proportion [2]

Unit amount (kg / m^3)				Retarder
PCM pre-mix powder	Lion bond A	Steel fiber	Water	0.2% of PCM pre-mix powder
1950	93	147	100	

Fig. 6.2 shows ingredients of steel fiber reinforced polymer cement mortar (PCM). Fig. 6.3 shows mixing and casting of the PCM. The first mixing procedure was adding water and lion bond A and mix. Then, add and dissolve retarder. Gradually add PCM pre-mix powder while mixer rotates. Then, mix for about 1 minute. Gradually add steel fibers while mixer rotates. Finally, mix for about 1 to 2 minutes. Setting time was 40 minutes. For a cylindrical specimen, the compaction was made using a steel rod (ϕ16mm and 500 mm / 600mm) with hemispherical round tip. When a cylindrical specimen was ϕ100mm, a ϕ28 mm steel rod can be used. However, for a beam specimens' compaction was made using internal vibrator as per JIS A 8610.

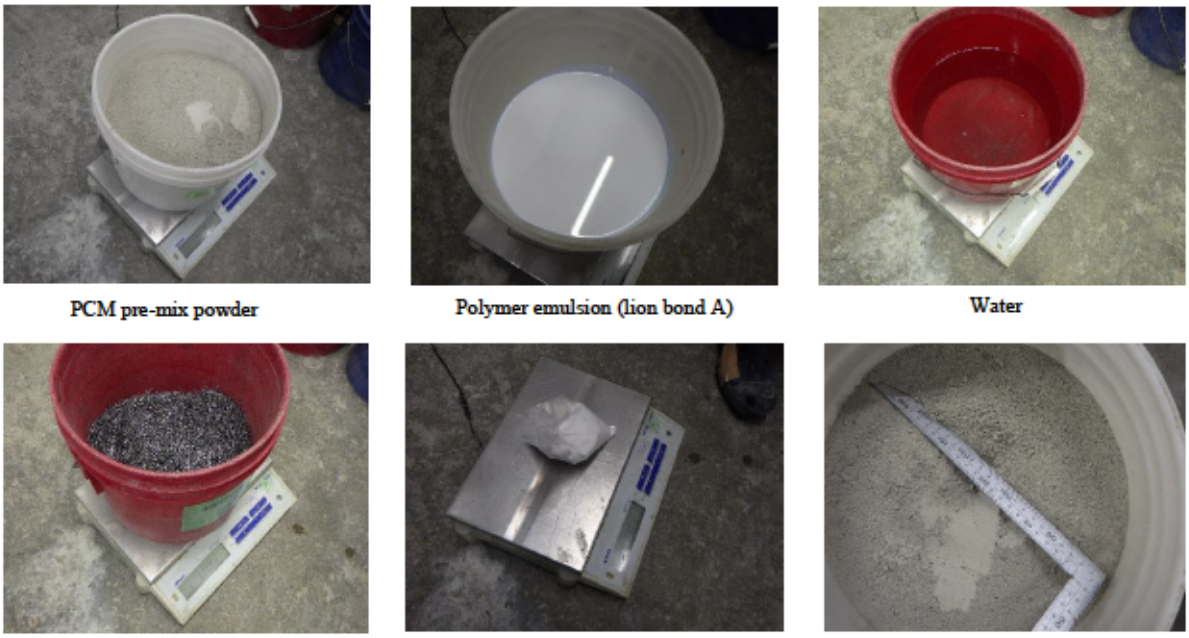

PCM pre-mix powder | Polymer emulsion (lion bond A) | Water

Steel fiber | Retarder | PCM maximum aggregate size ≤ 5

Fig. 6.2 Steel fiber reinforced PCM materials

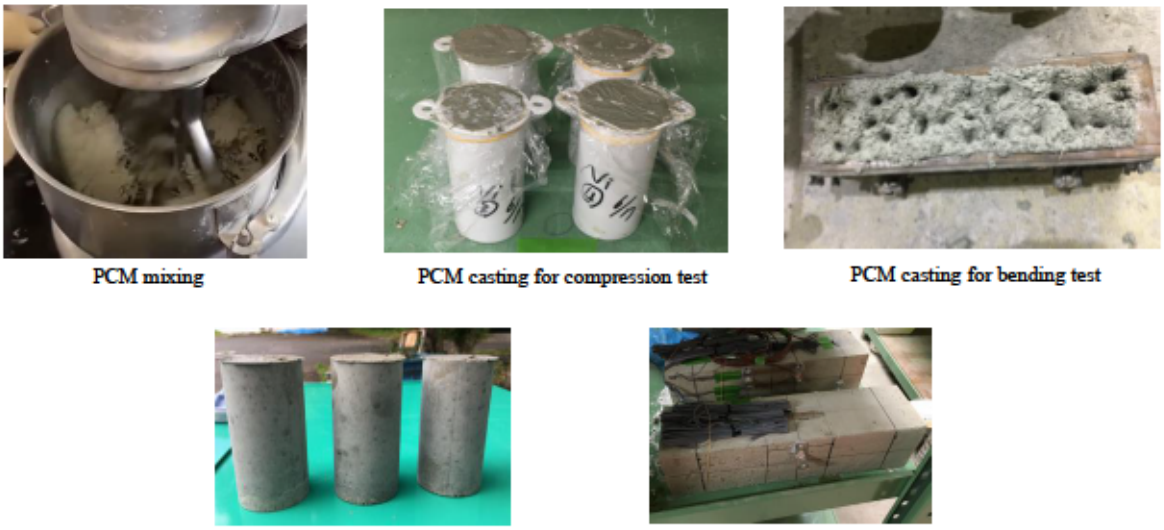

PCM mixing | PCM casting for compression test | PCM casting for bending test

Hardened PCM cylindrical specimens | Hardened PCM beam specimen

Fig. 6.3 PCM mixing and casting

6.3.3 Curing Condition and Strength Development

JIS A 1132 was used for demolding and curing condition of PCM specimens for compression, tension and bending tests.

PCM compressive strength development was investigated using a cylindrical specimen (ϕ50 mm and 100 mm height). A compressive strength was measured at 3 hours, 1 day, 7 days, 14 days and 28 days using three specimens at each time as shown in Fig 6.4. An average compressive strength of 29 MPa was obtained at 3 hour age as the PCM is high early strength material. The minimum requirement for a PCM compressive strength at 3 hour is 12 MPa. After 3 hours the strength development was increasing gradually toward compressive strength of 50 MPa at 28 days.

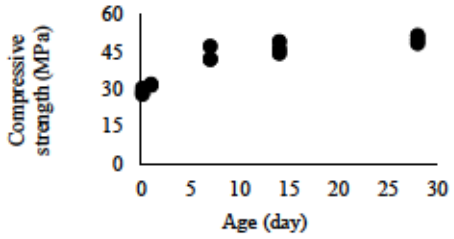

Fig. 6.4 PCM compressive strength development [2]

6.3.4 PCM Compression, Tension and Bending Test

A compressive and a tensile strength of PCM (using three specimens for each test) were tested as per JIS A 1108 and JIS A 1132 respectively. The compressive stress – compressive strain curve of the PCM and the tensile stress – tensile strain curve of the PCM are shown in Fig 6.5. The PCM static modulus of elasticity under compression was determined as per JIS A 1149 and it was 26,698 MPa. The elastic modulus of the PCM shall not exceed 28,000 MPa in practice.

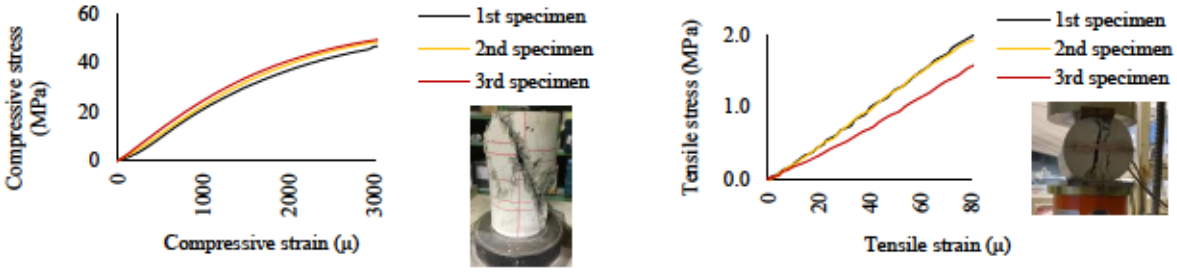

Fig. 6.5 PCM compressive and tensile strength [2]

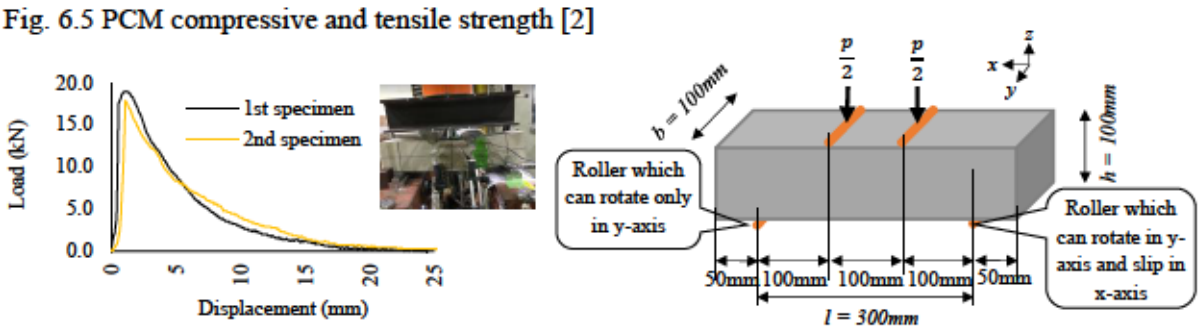

Fig. 6.6 Load – displacement of PCM [2]

A four-point bending strength of the PCM was tested as per JSCE-G552-2013 using two specimens. The load – displacement of the PCM is shown in Fig 6.6.

6.3.5 PCM Specimens for Drop-Weight Impact Test

Three identical PCM specimens were provided with a dimension of 1,000 mm × 740 mm × 75 mm as shown in Fig 6.7. Fig. 6.8 shows PCM slab casting and curing conditions. Slump test was caried out for the PCM slabs and it was 2.5 cm (Fig. 6.9). The slump value was smaller than the quality control value (10 ± 3.0 cm). However, this had no effect on the strength. A core (inner ϕ50 mm and outer ϕ55 mm) was drilled at the center of the specimen (Fig. 6.9). The depth of the core was 25 mm. 50 mm thick PCM remained below the core. Eight drilled holes with ϕ25 mm were made to connect the specimen with the support during a drop weight test. The specimens were reinforced with ϕ10 mm (SD295) reinforcing bars. Before the experiment it was assumed that there would be no deflection of the I-section steel support and punching shear would occur within 300 mm × 300 mm area (an area free from reinforcing bars). The reinforcing bars were provided only to prevent the specimens from damage during transport and not to had an effect on the energy dissipation of the PCM.

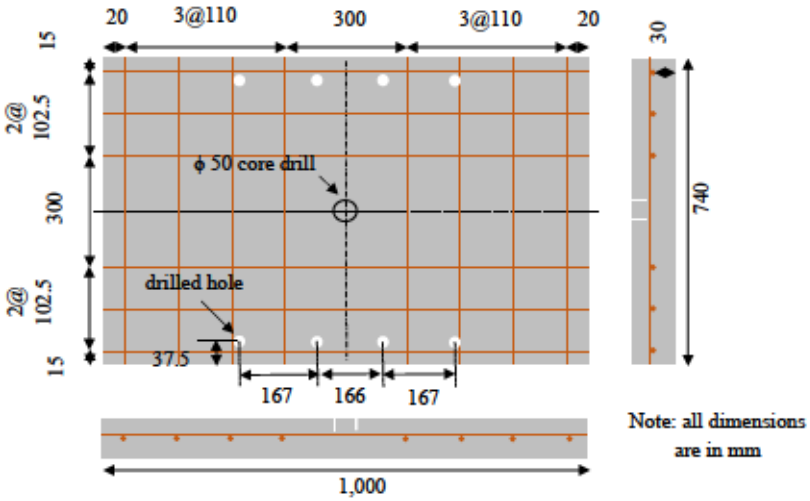

Fig. 6.7 Details of steel fiber reinforced PCM slab [2]

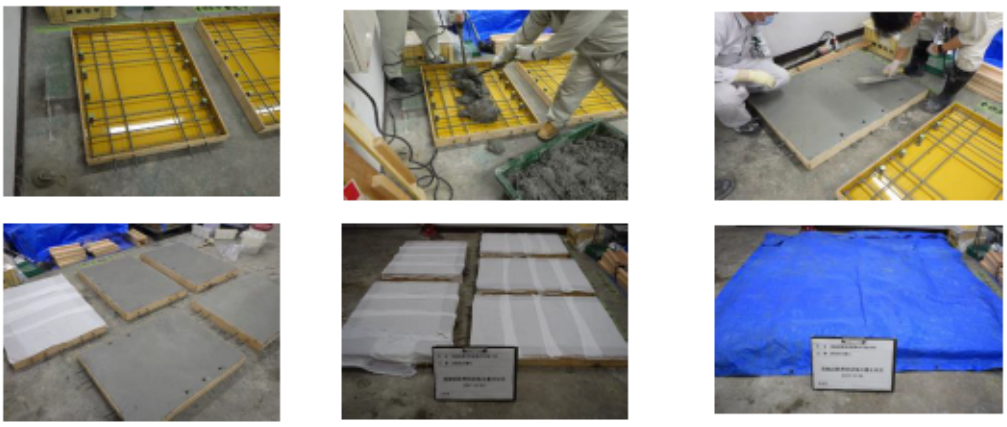

Fig. 6.8 PCM slab casting and curing

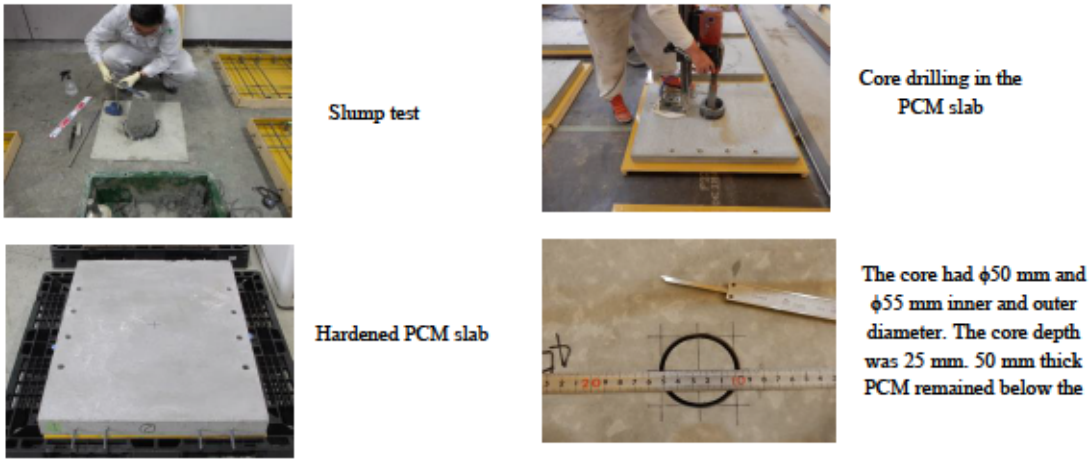

Fig. 6.9 Slump test of the PCM slab and core drilling

6.3.6 Drop Weight Impact Testing Setup

The experiments were carried out using a drop weight test instrument as shown in Fig 6.10. The PCM specimen was connected with the I-section steel support using steel plates, bolts and nuts as shown in Fig 6.10. A T-shaped steel member was attached to the center of the specimen to transfer the impact load to the PCM.

6.3.7 Loading Method

The applied impact energies on the PCM specimens are shown in Table 6.2. The first PCM specimen was impacted with 758 J and 1,494 J. Failure processes of the PCM under high-speed punching were recorded with the aid of a high-speed camera.

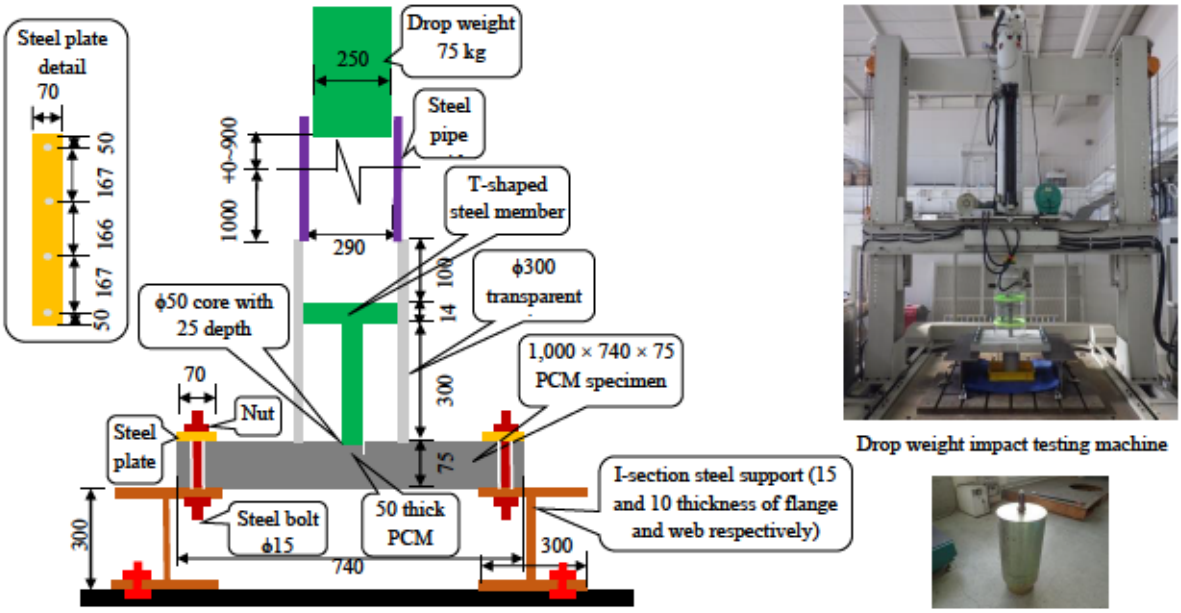

Note: all dimensions are in mm unless specified

Fig. 6.10 Setup of drop weight impact test [2]

Table 6.2 Types of drop weight impact test [2]

PCM specimens	Drop weight (kg)	Drop height (m)	Impact energy (J)
first specimen	75	1.03	758
		2.03	1,494
second specimen	75	1.53	1,126
third specimen	75	1.83	1,346

6.4 Experimental Results of Drop Weight Impact

The first PCM specimen was impacted with 758 J. After the impact, the authors carefully investigated the experimental result and found no apparent damage in the PCM. Then, the authors decided to impact the PCM once again with 1,494 J. In this case however, the PCM was perforated and produced a rear crater as shown in Fig. 6.11a. Multiple cracks were also observed beyond the central area of the PCM (300 mm × 300 mm) as shown in Fig. 6.11b.

After a carful investigation of the experimental results of the first PCM specimen, the authors decided to impact the second PCM specimen with 1,126 J. The experimental result showed a minor penetration and crack of rear as shown in Fig. 6.11a. Multiple cracks were also observed beyond the central area of the PCM (300 mm × 300 mm) as shown in Fig. 6.11b.

Similarly, after a carful investigation of the experimental results of the second PCM specimen, the authors decided to increase the impact energy to 1,346 J for the third PCM specimen. The experimental result showed a minor penetration and crack of rear as shown in Fig. 6.11a. However, significant cracks were observed beyond the central area of the PCM (Fig. 6.11b).

All the impact energy was supposed to be dissipated by the PCM. However, the reinforcing bars also dissipated some amount of impact energy as cracks propagated in the reinforcing bars area. The reinforcing bars were not provided to dissipate impact energy, but just to prevent damage on the PCM specimens during transport, etc. The authors tried to understand the reason behind cracks beyond the center of the PCM specimens. After a carful investigation of a high-speed camera, the authors found out that there was a deflection of the I-section steel support. Deflection of the I-section steel support made the PCM specimen to be bended during impact. Bending of the PCM specimens during drop weight impact was also revealed by the high-speed camera. Those cracks of the PCM specimens resulted from bending of the PCM specimens. Due to the unforeseen boundary deflection, additional impact energy was dissipated by the PCM bending cracks and boundary deflection. To investigate the extent of cracks, the PCM specimens were dissected along the centerline as shown in Fig. 6.11b. And, it was revealed that, cracks were observed beyond the 300 mm × 300 mm area. Similar results were

also revealed by AEM simulations as will be explained in the next section with the details of AEM simulation.

first PCM specimen second PCM specimen third PCM specimen

(a) PCM specimens after drop weight impact test

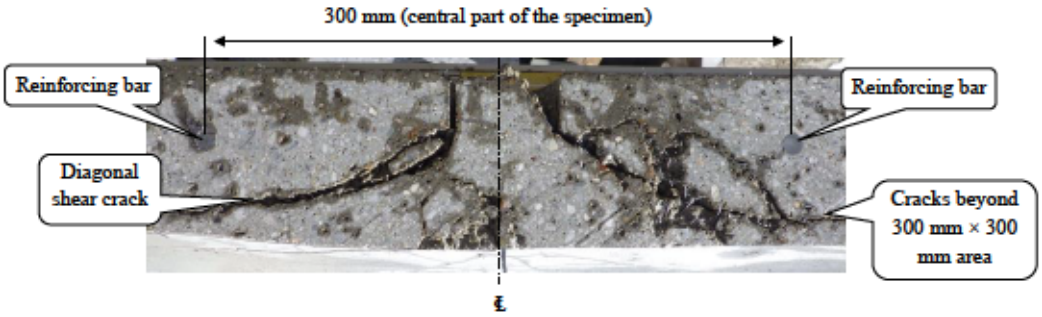

(b) section view of the second PCM specimen

Fig. 6.11 Crack pattern in the PCM specimens [2]

6.5 AEM Simulation of PCM Drop Weight Impact

6.5.1 Simulation with Applied Element Method (AEM)

In this study, a non-linear dynamic structural analysis software "Extreme Loading for Structure (ELS)" based on AEM was used [3].

6.5.2 AEM Simulation Modeling

AEM numerical simulation was conducted for the drop weight test explained in Fig. 6.10. The details of the modeling of the punching test are shown in Fig. 6.12. The drop weight was free in all degrees of freedom as it falls under gravity. The T-shaped steel member was free to move only in z-direction.

In the analysis, two stages of loading were provided. The first one was static to account for the self-weight of PCM and steel, while the second one was dynamic to simulate the drop weight and its impact to PCM. Table 6.3 shows durations and time intervals of dynamic stage. Duration in the dynamic stage was further divided into two. The first duration was to account for the drop weight free fall time while

the second duration was to account for impact simulation. The initial condition of the weight drop stage was zero initial velocity.

When designing model mesh in the AEM, it is generally recommended to use cube-shape elements and small size elements at locations of stress concentrations. Moreover, in AEM, cracks propagate at element boundary and finer elements are recommend in shear dominant failure. Fig. 6.13 shows the effect of element size on the PCM failure mode. Element size of the PCM specimen below the core was 5 mm × 5 mm × 5 mm (in 300 mm × 300 mm area) as the maximum aggregate size in the PCM was 5 mm and shear stress was concentrated (Fig. 6.12). However, element size of other parts of the PCM specimen was 15 mm × 15 mm × 15 mm to reduce computational time.

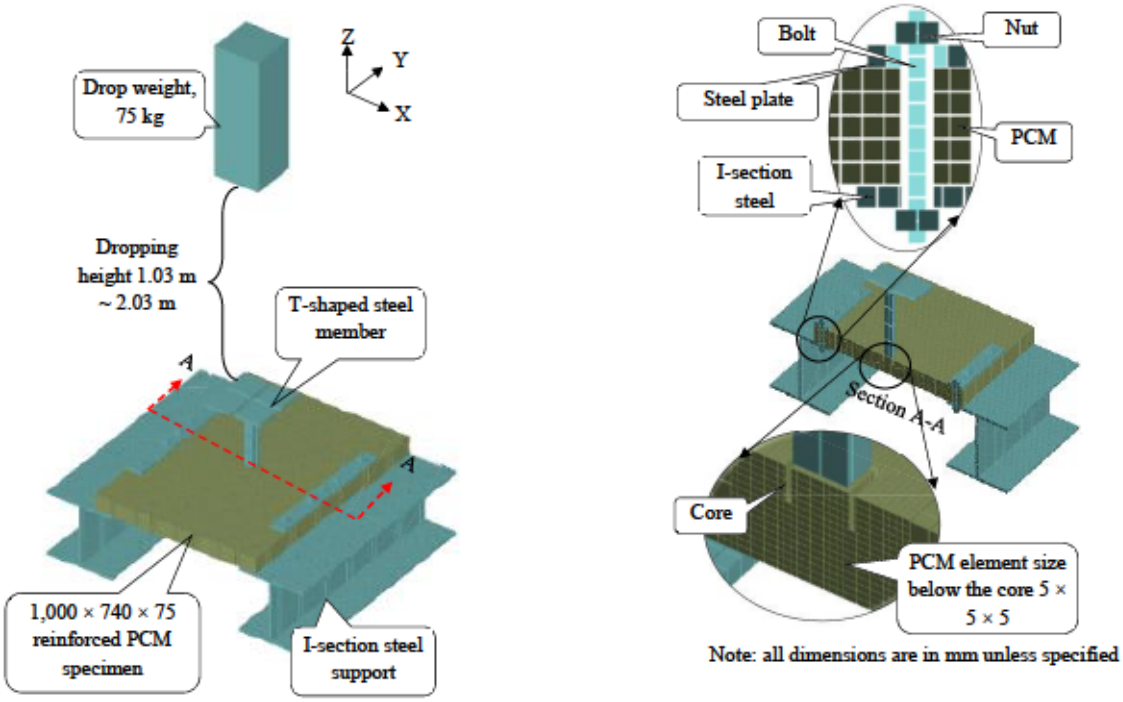

Fig. 6.12 AEM simulation modelling [2]

Table 6.3 Duration and time interval (dynamic stage) [2]

PCM specimens	Duration (s)	Time interval	Remark
first specimen	0 – 0.458	0.1	free fall
	0.458 – 0.493	0.001	1st impact
	0.493 – 1.136	0.1	free fall
	1.136 – 1.171	0.001	2nd impact
second specimen	0 – 0.5585	0.1	free fall
	0.5585 – 0.6385	0.001	impact
third specimen	0 – 0.600	0.1	free fall
	0.600 – 0.680	0.001	impact

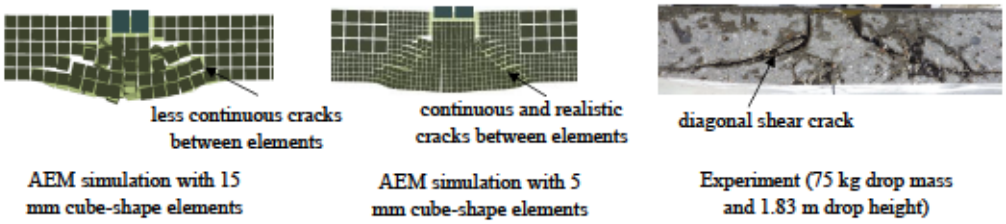

Fig. 6.13 The effect of element size on failure mode [2]

Material properties of the PCM under compression and under tension was assigned as shown in Fig. 6.5, and under shear as shown in Fig. 6.14. The "bearing material" in ELS, which can transfer only compression, was used for the interface between the PCM specimen and the T-shaped steel member, between the PCM specimen and the steel plate, between the PCM specimen and the I-section steel support, between the I-section steel support and the nut, and between the steel plate and the nut. The interface material between the PCM specimen and the reinforcing bars was a PCM. A normal steel material was used for the drop weight, the T-shaped steel member, the steel plate, the nut, and I-section steel support. The interface material between the nut and the bolt was a normal steel. There was a 5 mm gap between the PCM and the bolt.

6.5.3 AEM Simulation of PCM Bending

AEM numerical simulation of PCM bending was carried out to calibrate post – peak tensile stress –tensile strain relationship that depends on fracture energy and element size. The detail of the PCM bending specimen is shown in Fig. 6.6. In the numerical simulation, the PCM had an element size of 5 mm × 5 mm × 5 mm as the maximum aggregate size in the PCM was 5 mm. The applied displacement was 10 mm. In this study, the PCM material was simulated using a user defined material (a material that is defined by a user). PCM behaviors under tension until the peak stress and under compression were defined as shown in Fig. 6.5. PCM under shear was defined as shown in Fig. 6.14 [4]. Fig. 6.14 show the tensile stress–tensile strain relationships of the PCM including tension softening. The PCM tension softening was calibrated using the PCM bending simulation (Fig. 6.15). Calibrated fracture energy of the PCM was 2.13 N/mm. The load – displacement relationship of the PCM is shown in Fig. 6.15. The PCM shows a high stiffness until the peak load. However, after the peak load the PCM shows a significant deformation before elements were fully separated due to the presence of steel fibers. The numerical simulation was verified with the experiment.

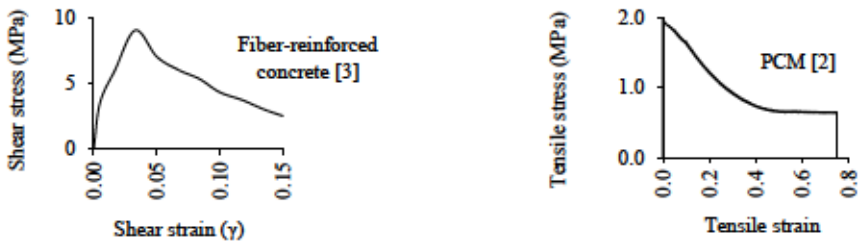

Fig. 6.14 Stress – strain relationship of the PCM

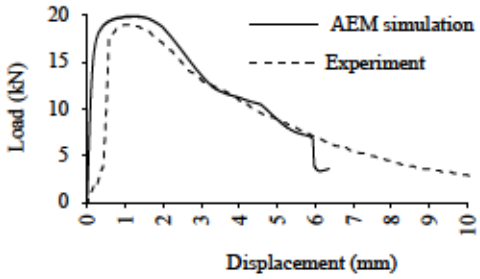

Fig. 6.15 Relationship between load – displacement [2]

6.5.4 Strain Rate in the Numerical Simulation

For steel fiber reinforced concrete under high loading rate, the compressive strength, and tensile strength should be increased with the increase in strain rate. In this chapter, the empirical Equation (2.8) and (2.9) [5] to calculate the Dynamic Increase Factor (*DIF*) of PCM under compression and under tension, respectively, were applied in the numerical simulation. Similar *DIF* empirical equations were utilized for the three PCM specimens (Fig. 6.12) in the AEM simulation.

To show the applicability of the empirical Equation (2.8) and (2.9) for the PCM in the AEM numerical simulation, a numerical simulation of drop mass impact on PCM was carried out with and without considering strain rate effect. The simulation without considering strain rate resulted in perforation of the PCM, which was different from the experimental result as shown in Fig. 6.16. However, the simulation with considering strain rate gave a nice result.

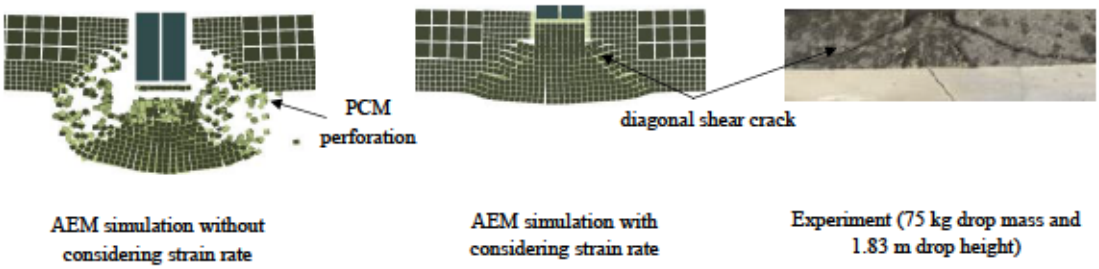

Fig. 6.16 The effect of strain rate on the PCM [2]

6.5.5 AEM Simulation of Drop Weight Impact

a) Drop Weight Impact on the First PCM Specimen

In the numerical simulation, the first PCM specimen was impacted twice. The first impact was 758 J while the second impact was 1,494 J. In the numerical simulation, the kinetic energy of the drop weight was measured to assess the energy absorption of the PCM as shown in Fig. 6.17a. The curve shows the kinetic energy from 0.000 s to 0.493 s of the drop weight during the first impact. The drop weight was freely falling from 0.000 s to 0.458 s. From 0.458 s to 0.493 s the drop weight impacted the PCM and the kinetic energy of the drop weight suddenly dropped from 758 J to 0 J. During impacting, the PCM was bended due to deflection of the I-section steel support as shown in Fig. 6.17b. No major

damage was observed in the PCM. However, strain contour was observed beyond the central part of the specimen.

The drop weight fell from a height of 2.03 m to impact the PCM for the second time as the PCM specimen was intact during the first impact. The drop weight was freely falling from 0.493 s to 1.136 s as shown in Fig. 6.17a. From 1.136 s to 1.137 s the drop weight impacted the PCM and the kinetic energy of the drop weight dropped from 1,494 J to 256 J. The PCM was perforated and produced a rear crater. During impacting, the PCM bended due to deflection of the I-section steel support and resulted bending cracks as shown in Fig. 6.17c and Fig. 6.17d. Significant cracking represented by large strain contours was observed beyond the central part of the specimen. The failure mechanism can be explained as, at the moment of contact, flared shear cracks are formed immediately in a region in the periphery of the impact. Additionally, the compressive wave reflected from the rear face of the PCM changes to a tensile wave that interacts with the compressive wave and produces a rear crater. At the same time, the bending cracks propagated from the impacting area towards the support. Fig. 6.17e shows the PCM specimen during the first impact and the second impact.

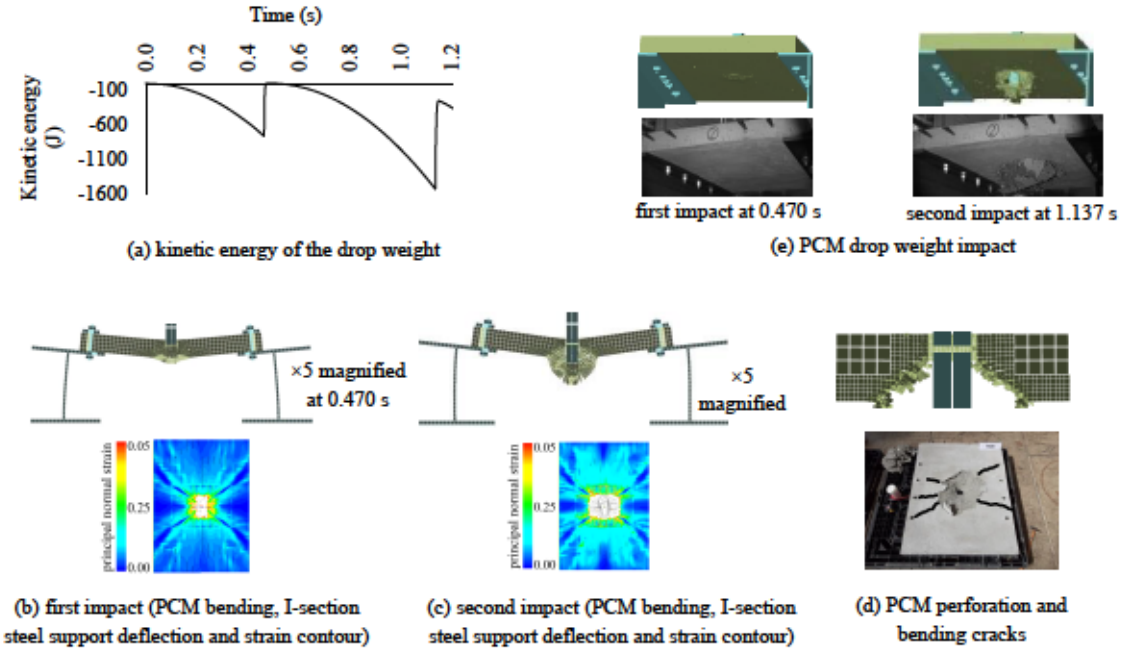

Fig. 6.17 Drop – weight impact on the first PCM specimen [2]

b) Drop Weight Impact on the Second PCM Specimen

The kinetic energy of the drop weight at impact was 1,126 J. Fig. 6.18a shows, the kinetic energy of the drop weight in the numerical simulation. The drop weight was freely falling from 0.000 s to 0.5585 s. From 0.5585 s to 0.6385 s the drop weight impacted the PCM and the kinetic energy of the drop weight suddenly dropped from 1,126 J to 0 J. The PCM was penetrated and produced crack of rear. During impacting, the PCM bended due to deflection of the I-section steel support and resulted bending cracks as shown in Fig. 6.18a and Fig. 6.18b. Significant cracking represented by large strain

contours was observed beyond the central part of the specimen. Fig. 6.18b shows the PCM specimen during impact.

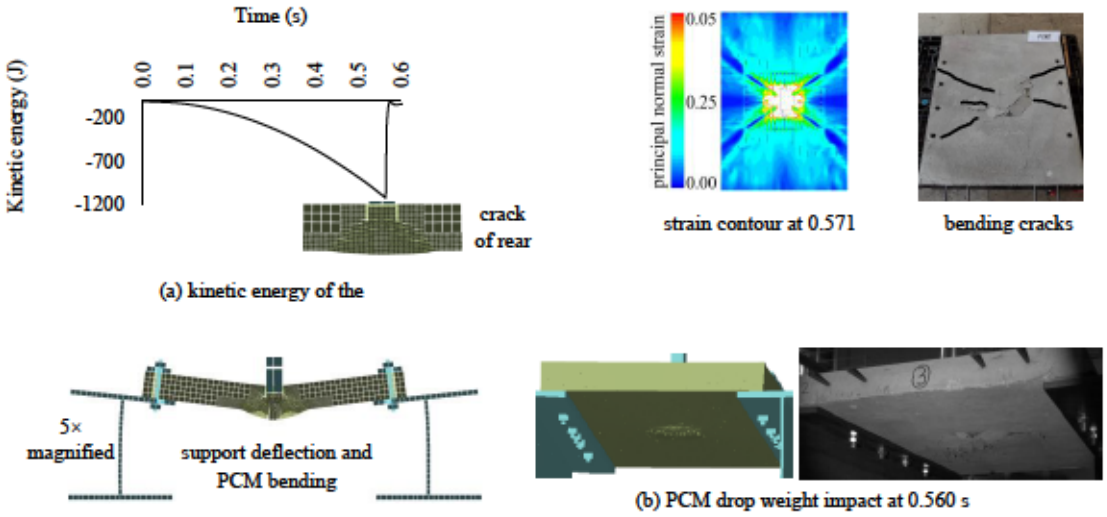

Fig. 6.18 Drop – weight impact on the second PCM specimen [2]

c) Drop Weight Impact on the Third PCM Specimen

The kinetic energy of the drop weight at impact was 1,346 J. Fig. 6.19a shows, the kinetic energy of the drop weight in the numerical simulation. The drop weight was freely falling from 0.000 s to 0.600 s. From 0.600 s to 0.680 s the drop weight impacted the PCM and the kinetic energy of the drop weight suddenly dropped from 1,346 J to 0 J. The PCM was penetrated and produced crack of rear. Similarly, during impacting, the PCM was bent due to deflection of the I-section steel support, which resulted in bending cracks as shown in Fig. 6.19a. and Fig. 6.19b. Significant cracking represented by large strain contours was observed beyond the central part of the specimen. Fig. 6.19b shows the PCM specimen during impact.

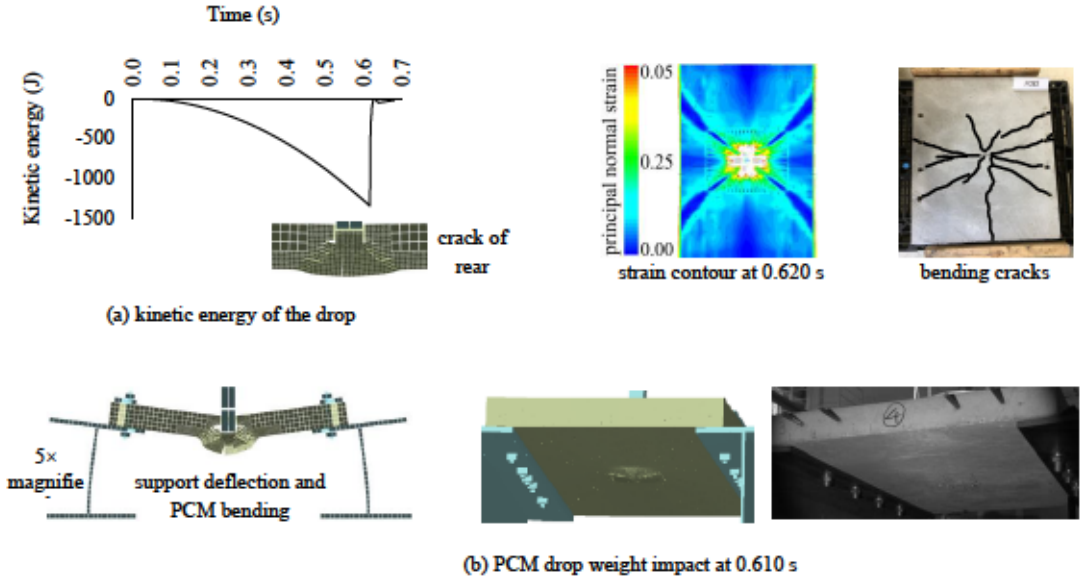

Fig. 6.19 Drop – weight impact on the third PCM specimen [2]

In all of the PCM drop weight impact test, bending cracks were observed in the PCM specimen due to the unforeseen deflection of I-section steel support. Bending of PCM specimen and deflection of the I-section steel support also revealed in the AEM simulations and in the experiment. The impact energy of the drop weight was dissipated by damages in the PCM specimen, deflection of I-section steel support and reinforcing bars.

d) Proposed Boundary Condition

To improve deflection of the I-section steel support in the drop weight impact experiment, the authors investigated a PCM drop weight impact AEM simulation using I-section steel support with stiffeners as shown in Fig. 6.20a. The interface material between the PCM slab and the bolt was PCM mortar. The interface material between the PCM slab and the I-section steel support was bearing material with a higher coefficient of friction to avoid lateral slip between them. This AEM simulation was identical with the PCM drop weight impact on the third PCM specimen (Fig. 6.20b). However, stiffeners were provided in the I-section steel support to enhance against the deflection. The AEM simulation showed that providing stiffeners in the I-section steel support significantly reduced bending of the PCM specimen and deflection of the I-section steel support. Strains beyond the central part of the specimen was also significantly reduced as shown in Fig. 6.20a.

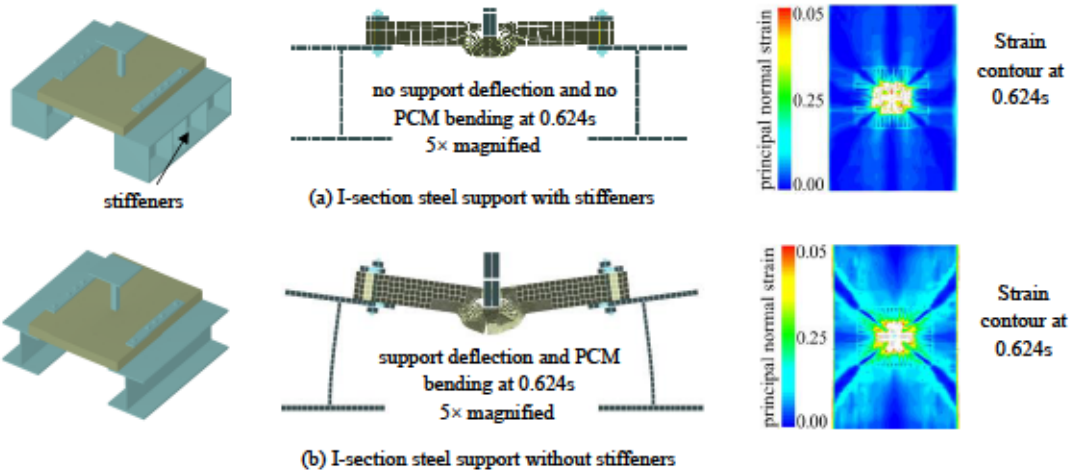

Fig. 6.20 Proposed boundary (AEM simulation) [2]

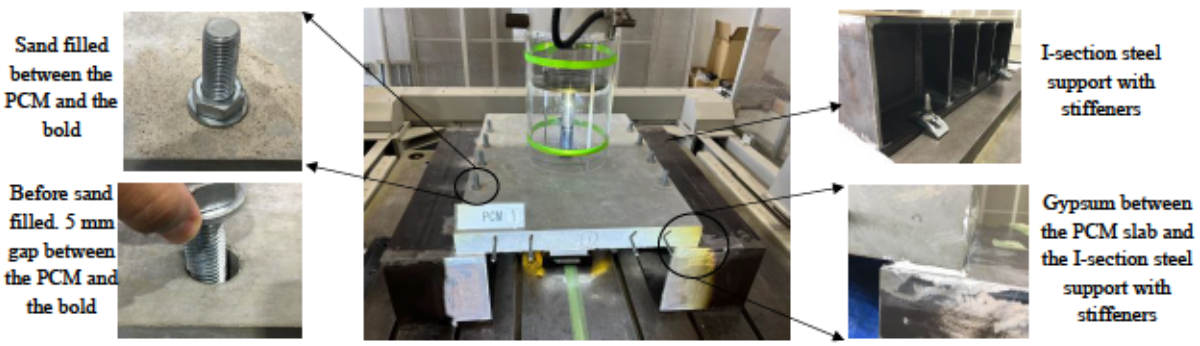

Fig. 6.21 Drop weight impact experiment on the PCM with proposed boundary condition

6.5.6 Experimental Investigation of PCM Drop Weight Impact using the Proposed Boundary Condition

PCM drop weight impact experiment was carried out using the proposed boundary conditions (Fig. 6.20). The objective of this particular experiment was to show the AEM simulation actually predicted the experiment or not. Moreover, to utilize the proposed boundary conditions for future drop weight impact experiment without boundary deflection and bending of a specimen. In this experiment the impact energy was 1,126 J (75 kg drop weight fell from 1.54 m height). In this experiment the PCM slab, the impact energy and the experimental procedures were the same as the drop weight impact experiment of the second PCM slab as shown in Fig. 6.11a. The experimental result the second PCM slab showed a minor penetration and crack of rear as shown in Fig. 6.11a. Multiple cracks were also observed beyond the central area of the PCM (300 mm × 300 mm) as shown in Fig. 6.11b.

However, the experiment in this section, the boundary conditions enhanced to avoid deflection of I-section steel support, bending of the PCM slab and bending cracks in the PCM slab as shown in Fig. 6.21. Stiffeners were provided in the I-section steel support to avoid deflection of the I-section steel support. Sand was filled between the PCM slab and the bolt to avoid lateral motion of the PCM slab. Gypsum was provided between the PCM slab and the steel support to avoid lateral slip of the PCM and to fix the PCM slab with the steel support. By utilizing the proposed boundary conditions, all the impact energy would be dissipated by the PCM.

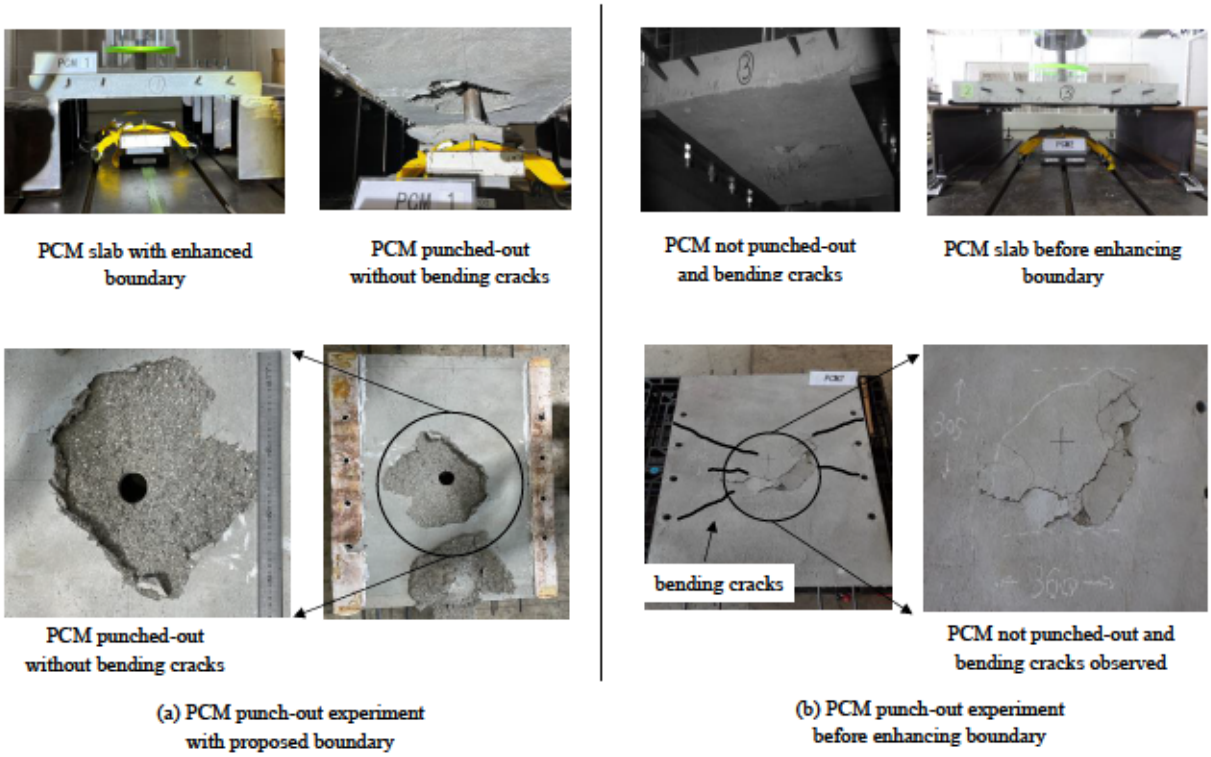

Fig. 6.22 The effect of boundary condition on the failure mode of PCM punch-out (75 kg drop weight fell from 1.54 m height)

Fig. 6.22a shows the PCM drop weight impact experiment using the proposed boundary conditions. The PCM was perforated and produced a rear crater. The high-speed camera clearly revealed that, the PCM was punched-out without any deflection of the steel support, without any lateral slip between the PCM slab and the steel support and without any bending of the PCM slab. After the impact, the bottom surface of the PCM was investigated and bending cracks were not found. It can be concluded that all the impact energy was dissipated by the PCM slab. The failure mode was pure punching shear. Fig. 6.23 shows a progressive collapse of the PCM punched-out. The AEM simulation accurately predicted the experiment interns of the proposed boundary conditions.

For reference Fig. 6.22b shows the PCM drop weight impact experiment without applying the proposed boundary conditions. In this case the PCM was not punched-out as certain amount of impact energy was dissipated by bending cracks and deflection of the I-section steel support in addition to damages in the PCM slab.

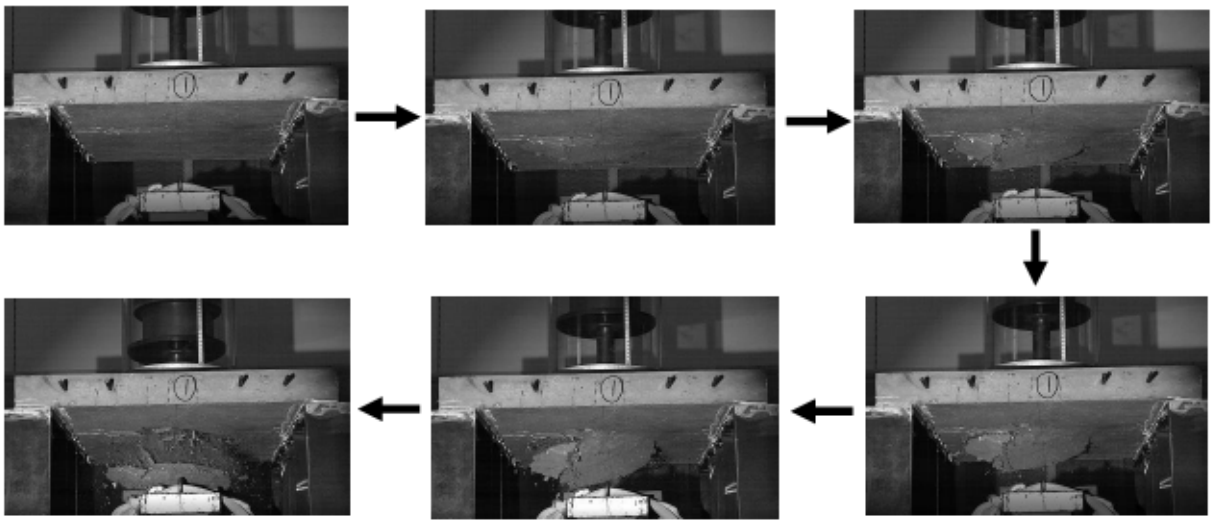

Fig. 6.23 Progressive collapse of PCM punch-out (experiment) using the proposed boundary conditions

In this study, the author has learned the importance of the high speed-camera during high loading experiment. Without the high speed-camera, it was impossible to identify the unforeseen boundary deflection. In future investigation of the energy dissipation of the PCM, the proposed boundary will be utilized. The numerical simulation tool developed in this study will be utilized for evaluating the effectiveness of PCM against rupture and protrusion of PC bar tendon in PC bridges.

6.6 Summary of Chapter 6

Based on the results obtained in the present work, the following main summary and conclusions can be drawn:

- The effect of PCM on impact resistance were investigated numerically and experimentally.

- The modeling of PCM in the drop weight AEM simulation showed good agreement with the experimental results in terms failure mode.
- Both numerical simulations and high-speed photography indicated that the drop weight impact test were significantly affected by boundary conditions.
- The drop weight impact energy was dissipated by damages in the PCM, deflection of boundary and strain in the reinforcing bars.
- The proposed boundary condition in this study greatly reduced deflection at the boundary and hence eliminate the energy absorbed by flexure.

References in Chapter 6:

[1] Aoki S. and Someya A., "Reinforcing effect of PCM pavement on deteriorated RC deck," *Pavement, Vol.56, No.1*, pp. 17–22, 2021.

[2] Bonger, A., Ni, S., Hosoda, A. and Hamed, S., "Drop weight impacting steel fiber reinforced PCM for investigating energy absorption capacity." *JCI Annual Convention*, Vol. 44, No.2, pp. 757-762, Chiba, Japan, 2022.

[3] Extreme Loading for Structures, "Applied Science International," *Available at: http://www.Extreme Loading for Structures (ELS)*, 2017.

[4] Ngo T., Park J., Pyo S., and Kim D., "Shear resistance of ultra-high-performance fiber-reinforced concrete," *Construction and Building Materials 151*, pp. 246–257, 2017.

[5] Yang L., Lin X., and Gravina R.J., "Evaluation of Dynamic Increase Factor models for steel fiber reinforced concrete," *Construction and Building Materials 190*, pp. 632–644, 2018.

CHAPTER 7

RISK MANAGEMENT OF PROTRUSION OF VERTICALLY PRESTRESSING STEEL BARS IN MEX

7.1 General

Rupture of vertical PC bar in PC bridge can damage cover concrete and asphalt pavement and it may provoke a serious public safety hazard from projecting bars and from falling concrete because such fractures can occur with no advance warning. This chapter briefly discussed about a basic information of vertical PC bars in Metropolitan Expressway (MEX) including the recent situations and onsite inspection of rupture of vertical PC bars. The strategy for risk assessment of rupture of vertical PC bars is also addressed in detail. Moreover, risk reduction (control) interventions are explained. The numerical simulation tools developed in this study are utilized for PC bar protrusion risk reduction interventions.

7.2 Basic Information of Vertically Prestressing Steel Bars in MEX

a) Current Situation

The structures in MEX in Japan are aging under harsh traffic usage. For example, in S62 Kawaguchi Line (Adachi – Nishiaraijuku), constructed in 1987, there were around 6,000 vertical PC bars (as per 2018 inventory). In S39 No. 3 Shibuya Line (Shibuya – Dogenzaka) and No. 4 Shinjuku Line (Otemachi - Hatsudai), constructed in 1964, there were around 1,500 vertical PC bars (as per 2018 inventory). According to the investigation in 2018 [1], there were 19,657 vertical PC bars in MEX, 54.4% of which were used in the webs of main girders. About 93% of the vertical PC bars had a length shorter than 3 m. Table 7.1 and Fig. 7.1 shows number of vertical PC bars in MEX by diameter and length. Out of 11,435 vertical PC bars, counted from design drawings, about 93% of them have 15 mm to 60 mm cover concrete below a bridge girder and around 33.8% of them have 20 mm to 25 mm cover concrete above a bridge girder. However, in this study, cover concrete was not considered in the investigation of performance evaluation of countermeasures against rupture of ungrouted vertical PC bars to simulate the worst scenarios in practice.

b) Onsite Inspection

Actual rupture of a vertical PC bar was investigated by the authors as explained in chapter 1. PC bar was ordinary PC steel bar JIS B type (diameter 32 mm and length 2,620 mm). After extracting the PC bar from the sheath, it was confirmed that the bar was ruptured at 1,345 mm from the bottom side and detailed investigation was carried out to study the rupture mechanism. It was concluded that the rupture of the bar was brittle and initiated from corrosion pits, which must have been caused by cyclic drying and wetting due to the ingress of rainy water (Fig. 1.9).

Table 7.1 Number of vertical PC bars in Metropolitan Expressway (as per 2018 inventory)

PC bar length (mm)	PC bar type								
	B1ϕ17	A1ϕ23	B1ϕ23	A1ϕ26	B1ϕ26	B2ϕ26	B1ϕ32	B2ϕ32	Total
1000-1250	0	0	0	0	496	764	0	200	1,460
1250-1500	0	0	0	340	5	0	14	64	423
1500-1750	0	0	0	444	30	3,845	877	138	5,334
1750-2000	288	0	336	4	194	2,578	6	344	3,750
2000-2250	0	642	0	36	0	158	908	667	2,411
2250-2500	0	0	0	8	0	222	236	1,335	1,801
2500-2750	0	0	0	16	0	16	2,264	122	2,418
2750-3000	0	0	0	8	216	0	54	202	480
3000-3250	0	0	0	8	0	32	76	259	375
3250-3500	0	0	0	20	0	0	24	160	204
3500-3750	0	0	0	12	0	0	32	140	184
3750-4000	0	0	0	0	0	0	16	128	144
4000-4250	0	0	0	44	0	0	16	160	220
4250-4500	0	0	0	64	0	0	8	40	112
4500-4750	0	0	0	0	0	4	8	0	12
4750-5000	0	0	0	0	0	0	8	0	8
5000-10000	0	0	0	0	84	8	28	8	128
Total	288	642	336	1,004	1,025	7,627	4,575	3967	19,464
Low risk of PC bar protrusion	288	642	336	1,004	941	7,619	4,531	3,959	19,320
High risk of PC bar protrusion	0	0	0	0	84	8	44	8	144

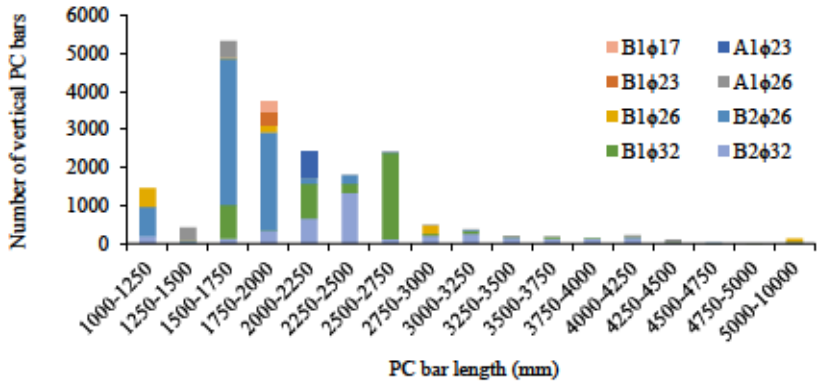

Fig. 7.1 Number of vertical PC bars in MEX (by diameter and length)

7.3 Risk Assessment of Rupture of Vertically Prestressing Steel Bars in MEX

When a vertical PC bar is ruptured, all the strain energy in the PC bar is released instantly, which can damage cover concrete and asphalt pavement. The strain energy in the PC bar depended on diameter of PC bars, class (type) of PC bars, elastic modulus of PC bars, prestressing force and PC bar ruptured length. Table 7.2 and Fig. 7.2 shows the strain energy of PC bars with different PC bar type, diameter and rupture length. The energy stored in the PC bar is calculated from the applied tension force by Equation 7.1. For this equation, PC bar is arranged in a straight line, and energy loss due to bending is not considered. In this study, the type of PC bar which was utilized to investigate the performance of PC bar was a standard steel bar: SBPR930/1180 (class B2 in JIS). The applied prestress force, after the prestress loss due to relaxation, creep and shrinkage, was 591 kN. Strain energy of the PC bar was 4,408 J (4.4 kN·m). The 4.4 kN·m PC bar strain energy can cover the PC bar strain energies highlighted in green color in Table 7.2. The PC bar strain energies highlighted in red color in Table 7.2 were not covered in this study (Fig. 7.2). In MEX, out of 19,464 vertical PC bars only 144 of vertical PC bars had a strain energy exceeded 4,408 J (4.4 kN·m). That is the strain energy of the PC bar considered in this study can cover 99.26% of the total vertical PC bars as shown in Table 7.1.

$$U = P^2L/2EA \qquad 7.1$$

Where, U: strain energy in PC bar (N·m)

P: tensile force of PC bar (N),

L: PC bar length (m),

E: Young's modulus of PC bar (N/mm^2),

A: area of PC bar (mm^2)

As explained in chapter 4, the two layered asphalt pavement was effective against 4,408 J (4.4 kN·m) impact energy at different temperatures. If this asphalt pavement applied over a PC bridge deck slab, the risk of PC bar protrusion will be very low for 19,320 vertical PC bars (99.26%) as shown in Table 7.1 and Fig. 7.3. However, the risk of PC bar protrusion will be higher for 144 vertical PC bars (0.74%) as shown in Table 7.1 and Fig. 7.3.

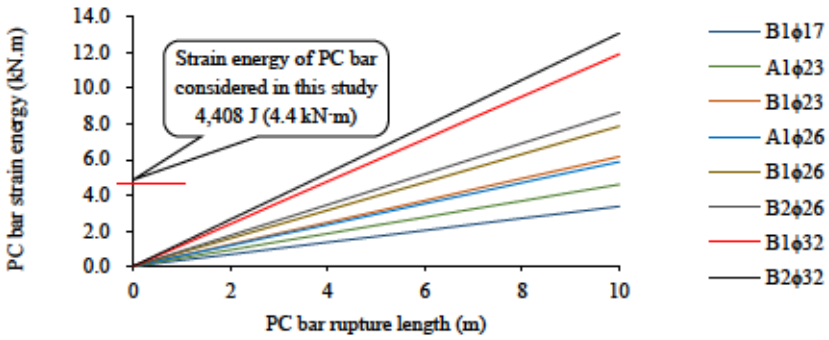

Fig. 7.2 The strain energy released by raptured PC bars

Table 7.2 The strain energy released by raptured PC bars

ϕ	17	23	23	26	26	26	32	32
PC bar type	B1ϕ17	A1ϕ23	B1ϕ23	A1ϕ26	B1ϕ26	B2ϕ26	B1ϕ32	B2ϕ32
A_p (mm^2)	227.0	415.5	415.5	530.9	530.9	530.9	804.2	804.2
σ (N/mm^2)	770	665	770	665	770	807	770	807
P_e (N) = $A_p\sigma$	174,790	276,308	319,935	353,049	408,793	428,436	619,234	648,989
E_p (N/mm^2)	20,0000	20,0000	20,0000	20,0000	20,0000	20,0000	20,0000	20,0000
PC bar rupture length (m)	PC bar strain energy (kN.m)							
0	0	0.00	0.00	0.00	0.00	0.00	0.00	0.00
1	0.34	0.46	0.62	0.59	0.79	0.86	1.19	1.31
2	0.67	0.92	1.23	1.17	1.57	1.73	2.38	2.62
3	1.01	1.38	1.85	1.76	2.36	2.59	3.58	3.93
4	1.35	1.84	2.46	2.35	3.15	3.46	4.77	5.24
5	1.68	2.30	3.08	2.93	3.93	4.32	5.96	6.55
6	2.02	2.76	3.70	3.52	4.72	5.19	7.15	7.86
7	2.36	3.22	4.31	4.11	5.51	6.05	8.34	9.17
8	2.69	3.67	4.93	4.70	6.30	6.91	9.54	10.47
9	3.03	4.13	5.54	5.28	7.08	7.78	10.73	11.78
10	3.36	4.59	6.16	5.87	7.87	8.64	11.92	13.09

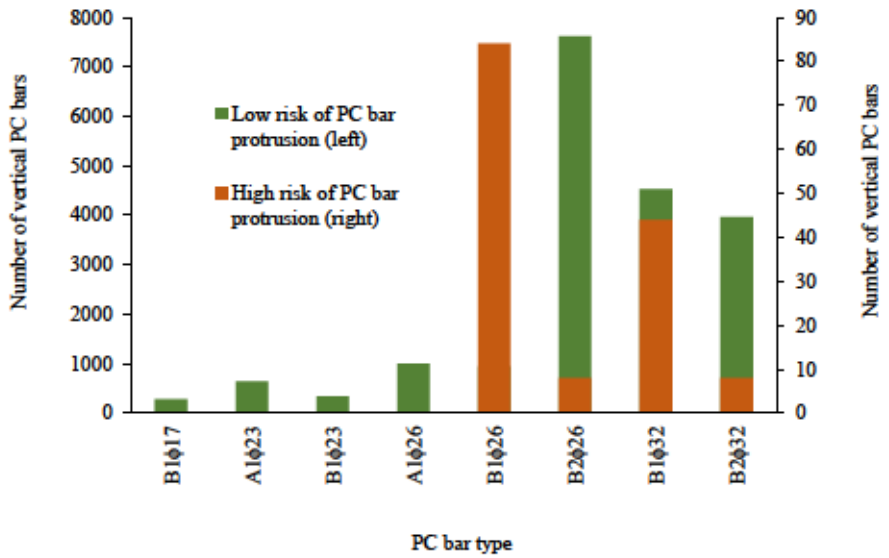

Fig. 7.3 Risk of vertical PC bar protrusion in MEX

7.4 Risk Analysis of Prestressing Steel Bar Protrusion using AEM Numerical Simulation

Fig. 7.4 shows application of the AEM simulations in the preparation of a PC bar protrusion prevention guideline. The PC bar protrusion prevention guideline prepared in this study can be applied only for the asphalt pavement over a bridge deck slab. The PC bar protrusion prevention guideline for a countermeasure below a bridge girder was not included in this study. Performance of the asphalt pavement against PC bar protrusion was investigated using AEM simulations by considering different PC bar rupture length, different temperatures and defects in the asphalt pavement system as shown in Fig. 7.4. These cases were considered in the AEM simulations which were verified with the experimental results. Then the damages in the asphalt pavement due an impact from a ruptured vertical PC bar was evaluated according to the MEX pavement damage rating standard. These enabled to decide the damages in the asphalt pavement would be safe for traffic or not. In this study, the damage criterions included length of PC bar protrusion and damage condition in the asphalt pavement system (cracks, deformation, potholes etc.). Finally, a PC bar protrusion prevention guideline prepared.

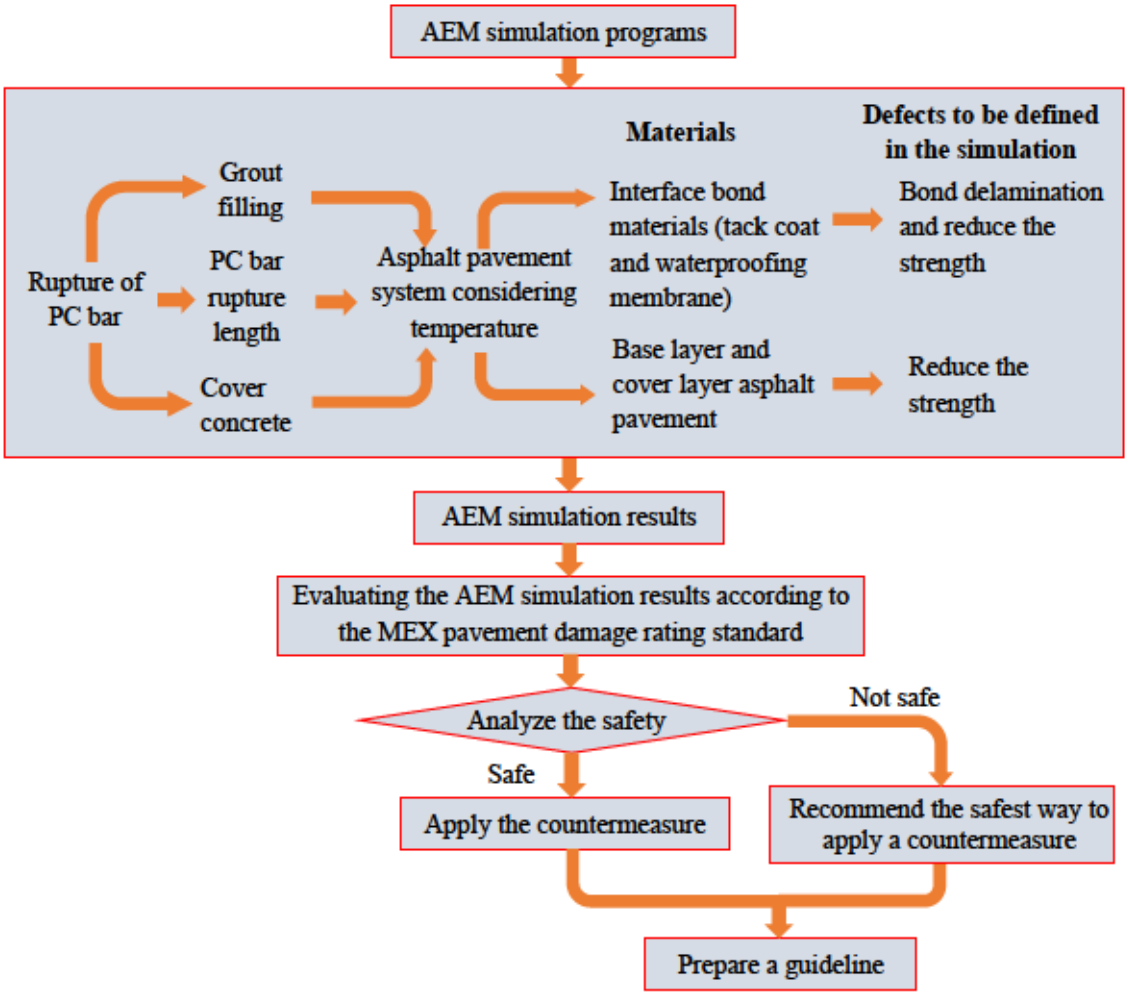

Fig. 7.4 Application of the AEM simulations in the preparation of PC bar protrusion prevention guideline

Following the flow chart shown in Fig. 7.4, numerous AEM simulations were carried out by considering several cases. The target was to prepare a safety guideline to mitigate PC bar protrusion over a bridge deck slab. The safety guideline included a kind of countermeasures to be applied over a bridge deck slab according to the PC bar length. The guideline identified the most influential materials which contributed in dissipation of strain energy of the PC bar. Moreover, the guideline sat a safety margin in terms of interface bond delamination and strength reduction of the countermeasure materials. The safety margins were sat using the AEM simulations by considering a localized interface bond delamination and / or by reducing the strength of the interface bond materials and the asphalt pavements. The AEM simulations by considering a safety margin were carried out to simulate time dependent deterioration in the asphalt pavements system, poor workmanship during application, poor quality material, etc. Strength reduction of the interface bond materials and the asphalt pavements were simulated by reducing the original strength under tension, compression and shear by some percentage. Moreover, different PC bar rupture length was considered to simulate the effect of PC bar impact energy in the PC bar protrusion and damages in the asphalt pavements.

a) AEM Simulation of Rupture of PC Bar with Two Layers of Asphalt Pavement at 0°C by Considering Bond Delamination and Strength Reduction in the Asphalt Pavement System

Fig 7.5 – Fig. 7.12 shows AEM simulation results of rupture of PC bar with two layers of asphalt pavement at 0°C by considering several cases. These cases were considered in the experimentally verified AEM simulation of rupture of PC bar with two layers of asphalt pavement at 0°C as explained in Section 4.4 (Fig. 4.29 and Fig. 4.30).

Fig. 7.5 shows the effect of waterproof membrane delamination in the PC bar protrusion and damage in the asphalt pavements. These AEM simulations (Case 1 – 3 of Fig. 7.5) were the same as the AEM simulation shown in Fig. 4.29 except the waterproof membrane delamination was considered. In Case 1 of Fig. 7.5, a 487 mm × 487 mm (5.9%) of waterproof membrane delamination was considered. In this case the asphalt pavement near the impacting area was severely fractured and the maximum PC bar protrusion was 139.7 mm. In Case 2 of Fig. 7.5, a 240 mm × 240 mm (1.4%) of waterproof membrane delamination was considered. In this case also the asphalt pavement near the impacting area was severely fractured and the maximum PC bar protrusion was 72.6 mm. In Case 3 of Fig. 7.5, only a 487 mm × 487 mm (5.9%) of waterproof membrane was considered. In an area outside of the 487 mm × 487 mm, the waterproof membrane was not considered. In this case however, minor cracks were observed in the asphalt pavement near the impacting area and the maximum PC bar protrusion was 50.6 mm.

Fig. 7.6 shows the effect of tack coat delamination in the PC bar protrusion and damage in the asphalt pavements. These AEM simulations (Case 1 – 3 of Fig. 7.6) were the same as the AEM simulation shown in Fig. 4.29 except the tack coat delamination was considered. In Case 1 - 2 of Fig. 7.6, a 487 mm × 487 mm (5.9%) and a 240 mm × 240 mm (1.4%) of tack coat delamination was

considered respectively. In both cases the asphalt pavement near the impacting area was severely fractured and the maximum PC bar protrusions were 109.3 mm and 69.9 mm respectively. In Case 3 of Fig. 7.6, only a 487 mm × 487 mm (5.9%) of tack coat was considered. In an area outside of the 487 mm × 487 mm, the tack coat was not considered. In this case however, minor cracks were observed in the asphalt pavement near the impacting area and the maximum PC bar protrusion was 44.8 mm.

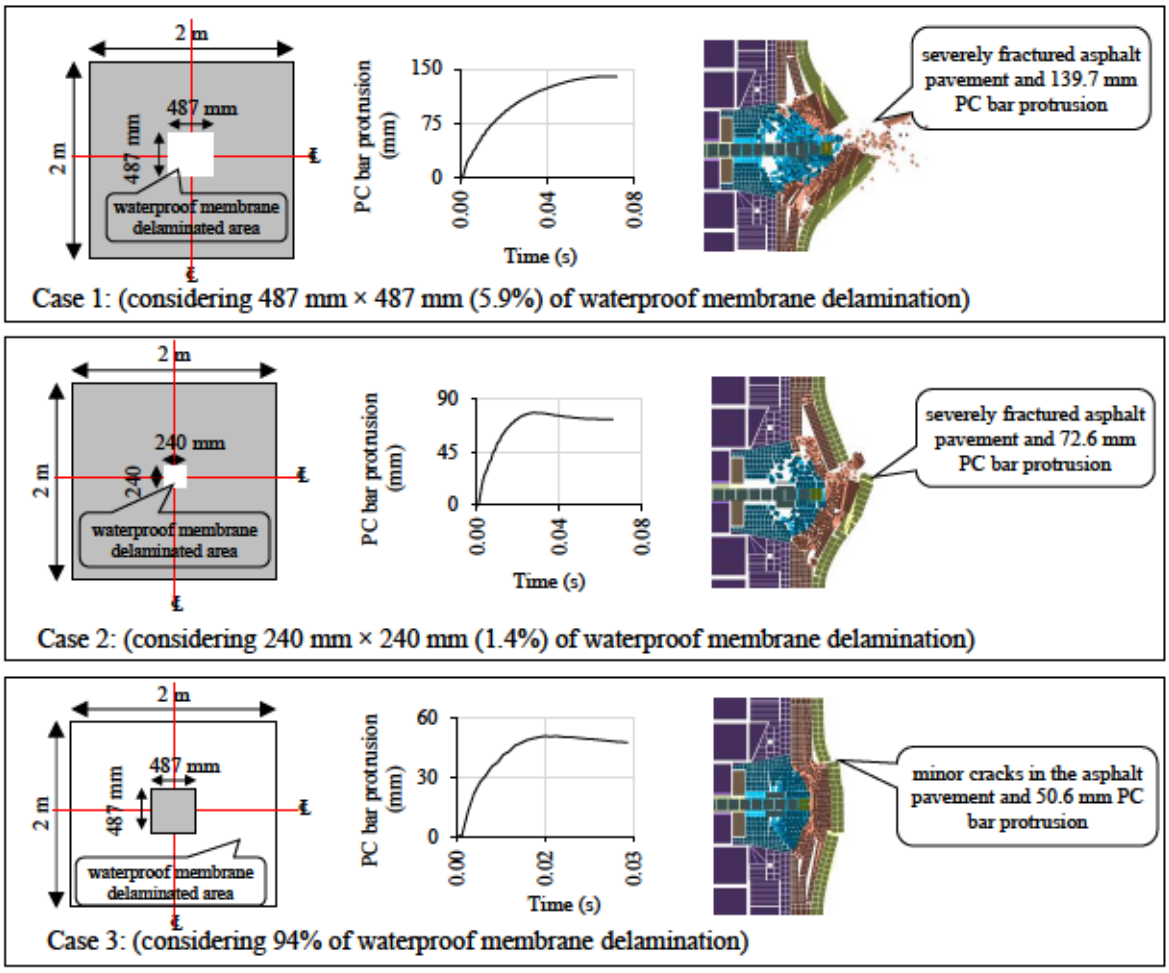

Fig. 7.5 The effect of waterproof membrane delamination in the PC bar protrusion and damage in the asphalt pavement

Fig. 7.7 shows the effect of waterproof membrane and tack coat delamination in the PC bar protrusion and damage in the asphalt pavements. These AEM simulations (Case 1 – 2 of Fig. 7.7) were the same as the AEM simulation shown in Fig. 4.29 except the waterproofing membrane and the tack coat delamination were considered. In Case 1 of Fig. 7.7, a 240 mm × 240 mm (1.4%) of waterproofing membrane and tack coat delamination were considered. In this case the asphalt pavement near the impacting area was severely fractured and the PC bar protrusions was 55.9 mm at 0.008 s and kept increasing. In Case 2 of Fig. 7.7, only a 487 mm × 487 mm (5.9%) of waterproofing membrane and tack coat were considered. In an area outside of the 487 mm × 487 mm, the waterproofing membrane and the tack coat were not considered. In this case however, minor cracks were observed in the asphalt pavement near the impacting area and the maximum PC bar protrusion was 43.3 mm.

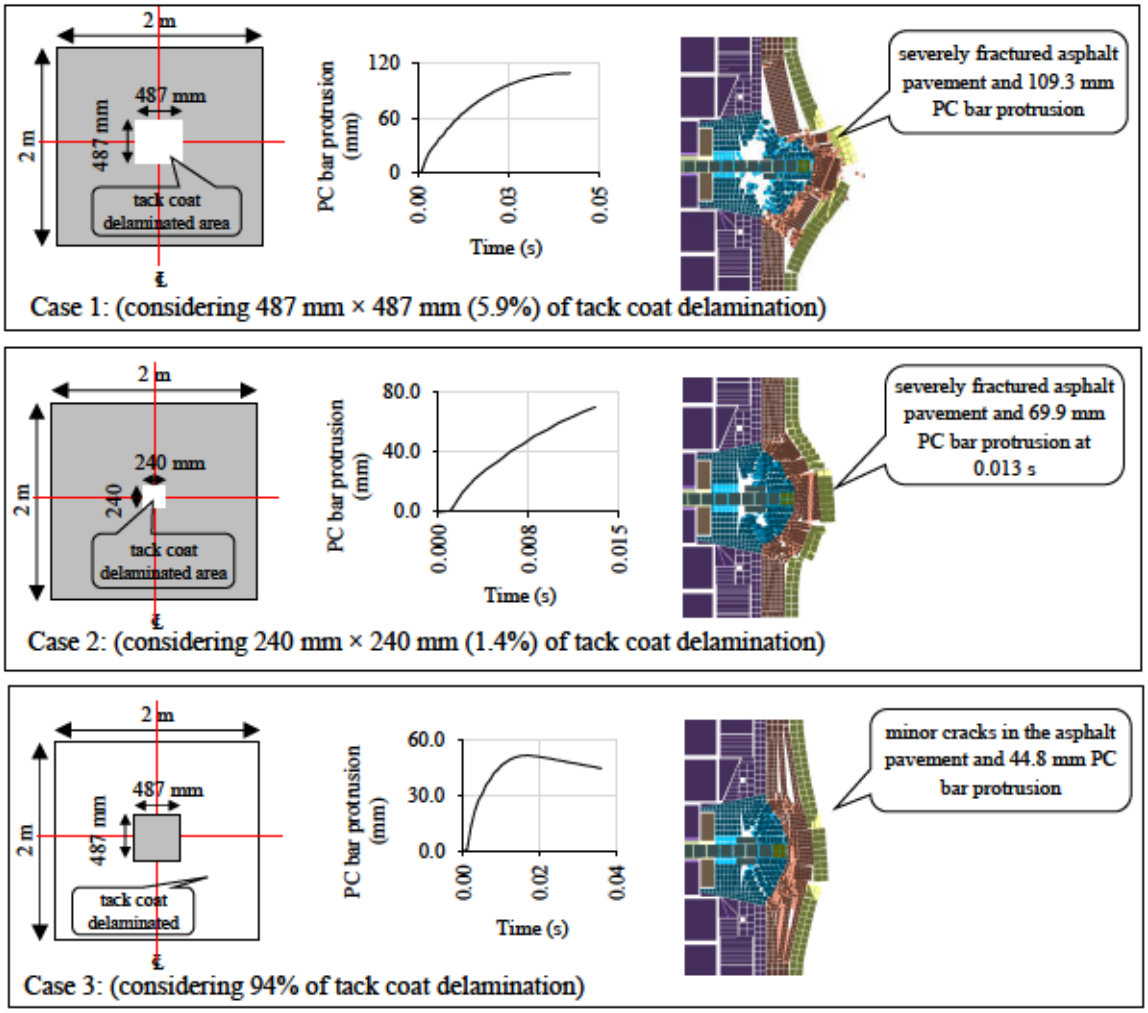

Fig. 7.6 The effect of tack coat delamination in the PC bar protrusion and damage in the asphalt pavement

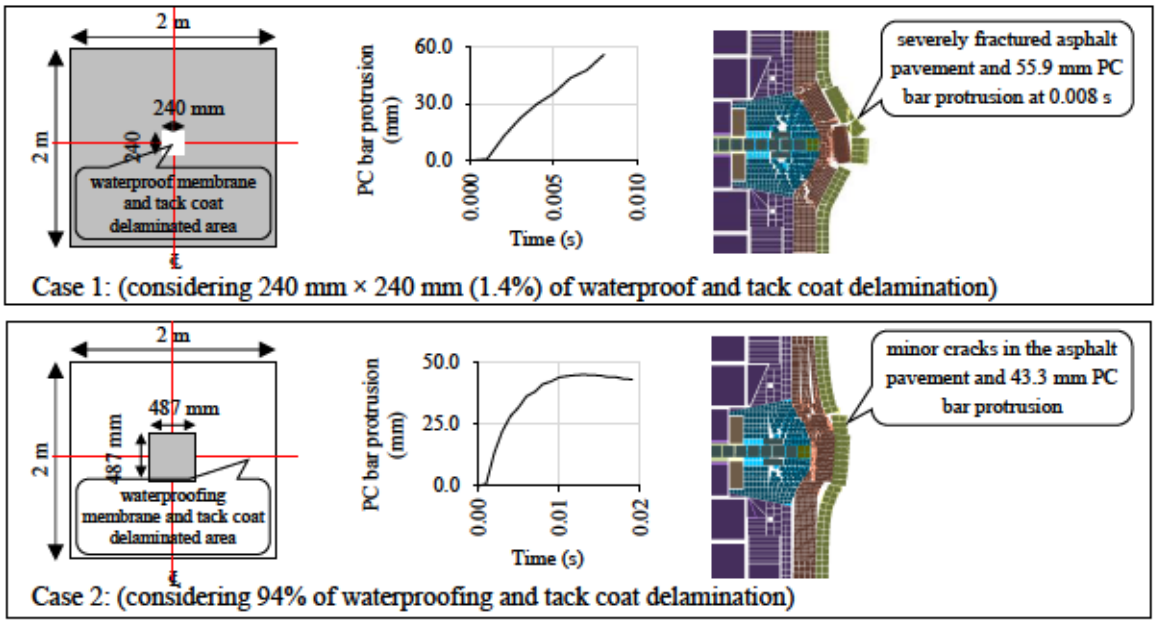

Fig. 7.7 The effect of waterproof membrane and tack coat delamination in the PC bar protrusion and damage in the asphalt pavement

According to the AEM simulation results (shown in Fig. 7.5 – 7.7), delamination of the waterproof membrane and the tack coat near the anchor had a significant effect in the PC bar protrusion and fracture in the asphalt pavement. A great attention should be paid during the application of the waterproof membrane and the tack coat at a location of a vertically prestressing bars in MEX.

Fig. 7.8 shows the effect of reducing strength of the base layer asphalt pavement in the PC bar protrusion and damage in the asphalt pavements. These AEM simulations (Case 1 – 6 of Fig. 7.8) were the same as the AEM simulation shown in Fig. 4.29 except strength of the base layer asphalt pavement was reduced. In Case 1 – 6 of Fig. 7.8, the strength of the base layer was reduced by 50%, 40%, 30%, 20%, 10% and 5% respectively. The AEM simulations with 50%, 40%, 30% and 20% strength reduction of the base layer resulted in a severely asphalt pavement fracture around the impact and a higher PC bar protrusion as shown in Case 1 – 4 of Fig. 7.8. The PC bar protrusions in Case 1 – 4 were 75.3 mm at 0.016 s, 72.2 mm at 0.014 s, 83.9 mm at 0.019 s and 75.7 mm at 0.020 s respectively and kept increasing in all cases. However, the AEM simulations with 10% and 5% strength reduction of the base layer resulted in minor cracks in the asphalt pavement around the impact and a smaller PC bar protrusion as shown in Case 5 and 6 of Fig. 7.8. The maximum PC bar protrusions in Case 5 and 6 were 42.2 mm at 0.015 s and 42.4 mm at 0.016 s respectively. According to the AEM simulation results (shown in Fig. 7.8), the base layer asphalt pavement is the most important material in impact energy dissipation and its strength reduction shall not exceed 10%.

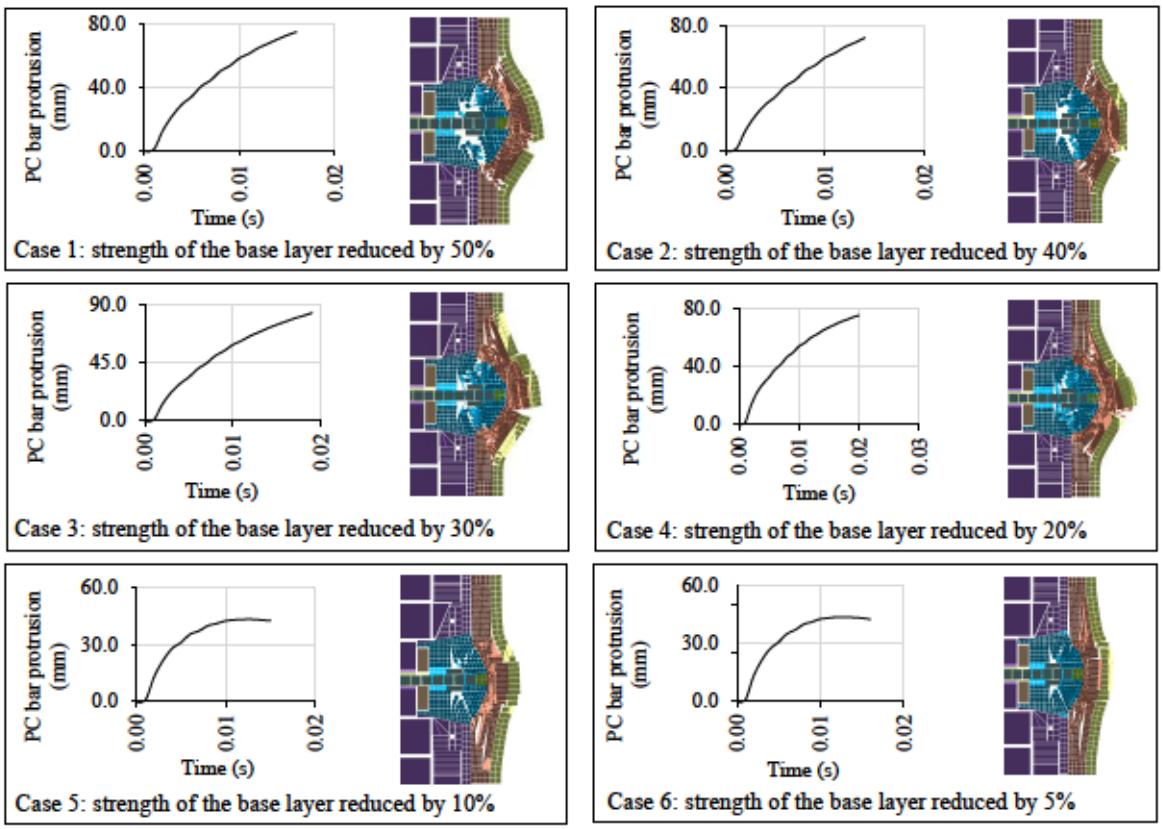

Fig. 7.8 The effect of reducing strength of base layer in the PC bar protrusion and damage in the asphalt pavement

Fig. 7.9 shows the effect of reducing strength of the cover layer asphalt pavement in the PC bar protrusion and damage in the asphalt pavements. These AEM simulations (Case 1 and 2 of Fig. 7.9) were the same as the AEM simulation shown in Fig. 4.29 except strength of the cover layer asphalt pavement was reduced. In Case 1 and 2 of Fig. 7.9, the strength of the cover layer was reduced by 50%, and 20% respectively. The AEM simulations with 50% and 20% strength reduction of the cover layer resulted in minor cracks in the asphalt pavement around the impact and a smaller PC bar protrusion as shown in Case 1 and 2 of Fig. 7.9. The maximum PC bar protrusions in Case 1 and 2 were 48.1 mm and 47.2 mm respectively. According to the AEM simulation result (shown in Fig. 7.9), the cover layer asphalt pavement had a smaller contribution in impact energy dissipation than the base layer asphalt pavement. The asphalt pavement system was effective against PC bar protrusion even though the strength of the cover layer reduced by 50%.

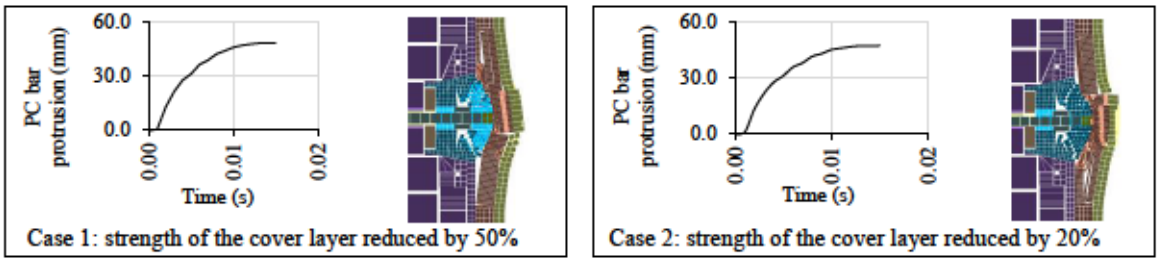

Fig. 7.9 The effect of reducing strength of cover layer in the PC bar protrusion and damage in the asphalt pavement

Fig. 7.10 shows the effect of reducing strength of the waterproofing membrane in the PC bar protrusion and damage in the asphalt pavements. These AEM simulations (Case 1 – 3 of Fig. 7.10) were the same as the AEM simulation shown in Fig. 4.29 except strength of the waterproofing membrane was reduced. In Case 1 – 5 of Fig. 7.10, the strength of the waterproofing membrane was reduced by 50%, 40%, 20%, 10% and 5% respectively. The maximum PC bar protrusions in Case 1 – 5 were 39.4 mm, 53.8 mm, 46.6 mm, 46.1 mm and 42.1 mm respectively as shown in Fig. 7.10. Reducing strength of the waterproofing membrane by 50%, 40% and 20% resulted in major cracks in the asphalt pavement around the impact. However, reducing strength of the waterproofing membrane by 10% and 5% resulted in minor cracks in the asphalt pavement around the impact. According to the AEM simulation result (shown in Fig. 7.10), reducing strength of the waterproofing membrane had a significant effect in asphalt pavement fracture and insignificant effect in the PC bar protrusion. Moreover, the waterproofing membrane strength reduction shall not exceed 10%.

Fig. 7.11 shows the effect of reducing strength of the tack coat in the PC bar protrusion and damage in the asphalt pavements. These AEM simulations (Case 1 – 3 of Fig. 7.11) were the same as the AEM simulation shown in Fig. 4.29 except strength of the tack coat was reduced. In Case 1 – 3 of Fig. 7.11, the strength of the tack coat was reduced by 50%, 40% and 20% respectively. The AEM simulation results of Case 1 – 3 exhibited a similar failure mode in the asphalt pavement and PC bar protrusions. The maximum PC bar protrusions in Case 1 – 3 were 48.5 mm, 47.9 mm and 48.7 mm respectively as

shown in Fig. 7.11. In all cases minor cracks were observed in the asphalt pavement around the impact. According to the AEM simulation result (shown in Fig. 7.11), the tack coat had a smaller contribution in impact energy dissipation than the waterproofing membrane. The asphalt pavement system was effective against PC bar protrusion even though the strength of the tack coat reduced by 50%.

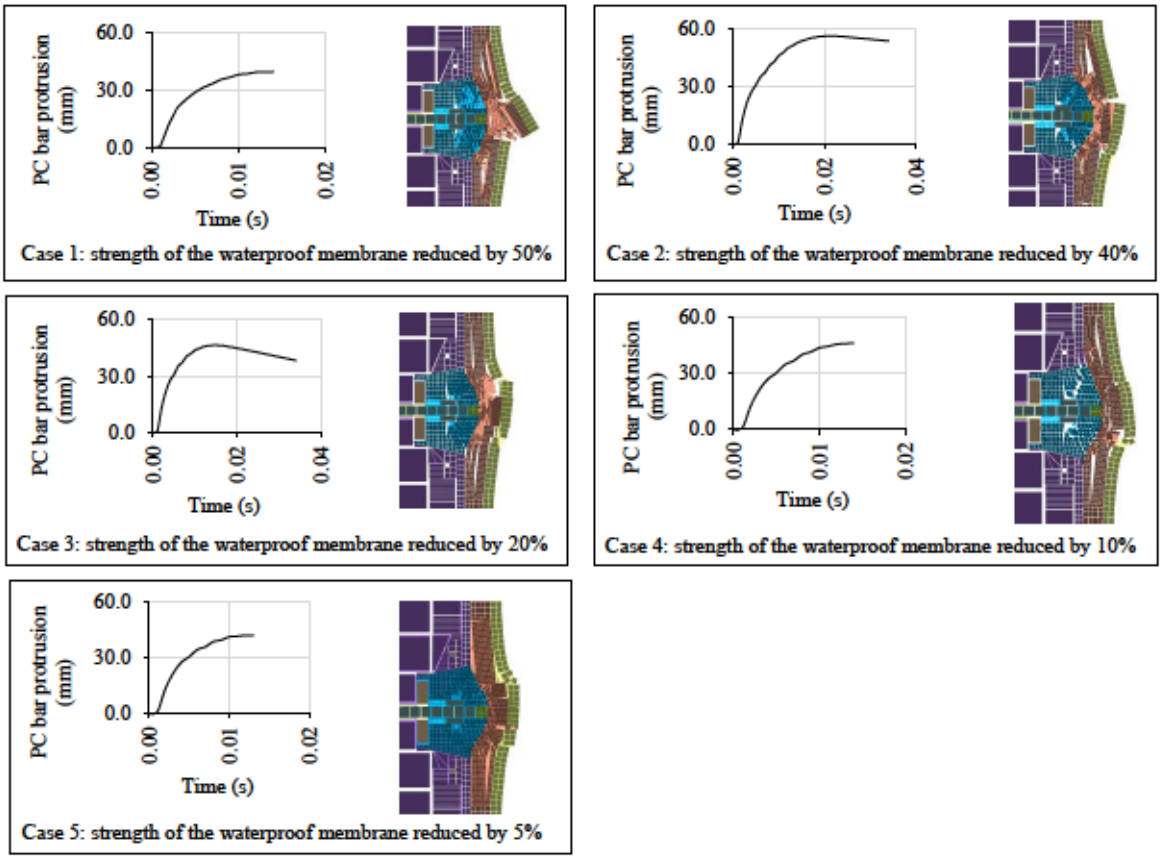

Fig. 7.10 The effect of reducing strength of waterproof membrane in the PC bar protrusion and damage in the asphalt pavement

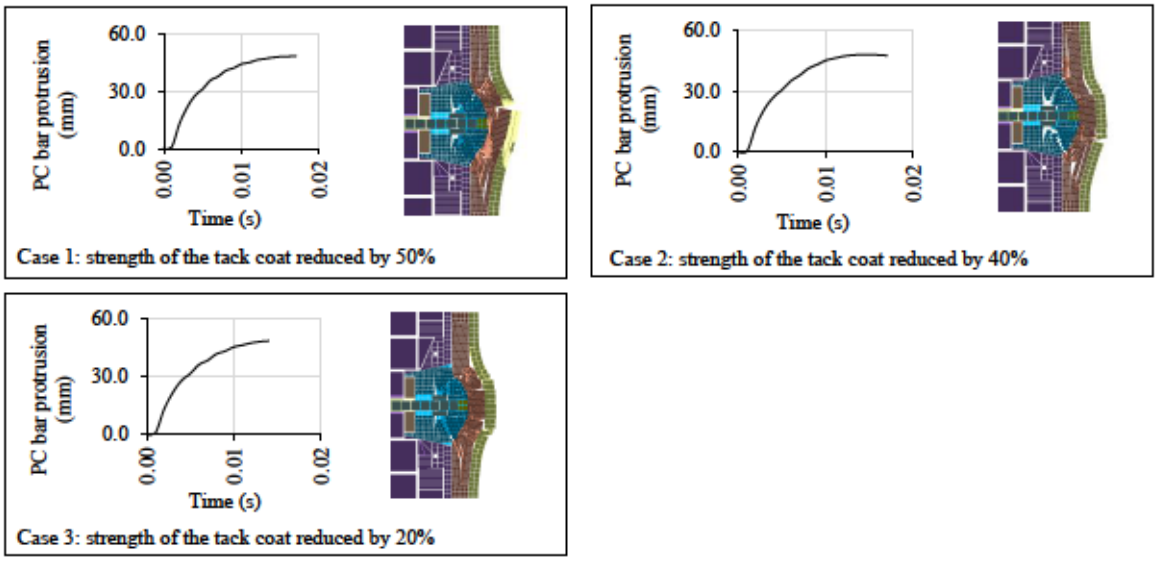

Fig. 7.11 The effect of reducing strength of tack coat in the PC bar protrusion and damage in the asphalt pavement

Fig. 7.12 shows the effect of reducing impact energy of the PC bar, reducing strength of the base layer and the cover layer and delamination of the interface bond materials in the PC bar protrusion and damage in the asphalt pavements. Case 1 of Fig. 7.12 was the same as the AEM simulation shown in Fig. 4.29. However, strength of the base layer and the cover layer was reduced by 10% and 50% respectively. Case 2 of Fig. 7.12 was the same as Case 1 of Fig. 7.12 except the impact energy of the prestressing steel bar was reduced (the PC bar rupture length changed from 4.5 m to 3.0 m). Case 1 resulted in a significant asphalt pavement fracture around the impact and 71.1 mm of maximum PC bar protrusion. However, Case 2 resulted in minor cracks in the asphalt pavement around the impact and 18.8 mm of maximum PC bar protrusion as the PC bar impact energy was smaller than Case 1.

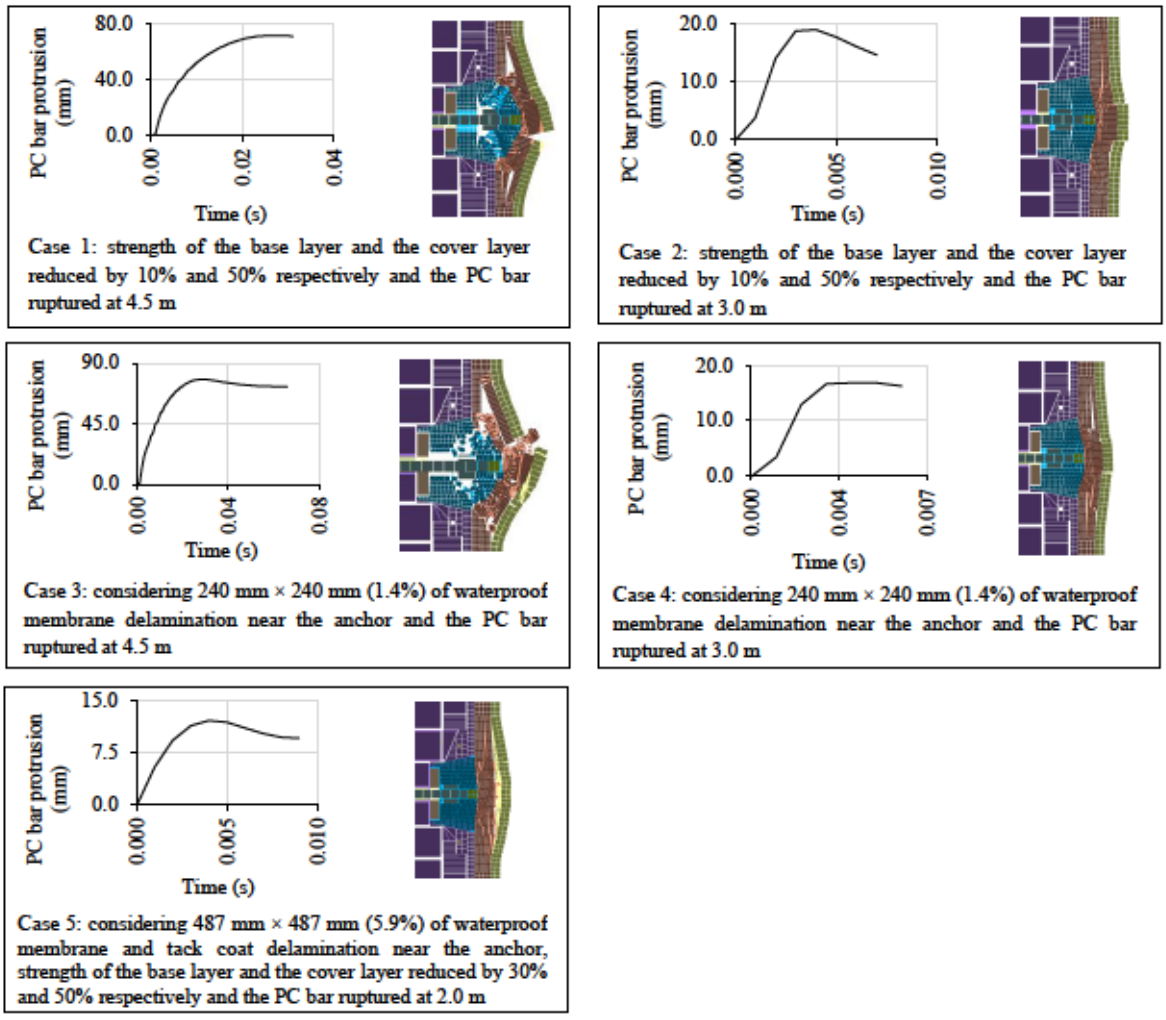

Fig. 7.12 The effect of reducing impact energy of the PC bar in the PC bar protrusion and damage in the asphalt pavement

Case 3 of Fig. 7.12 was the same as the AEM simulation shown in Fig. 4.29. However, 240 mm × 240 mm (1.4%) of waterproof membrane delamination near the anchor was considered. Case 4 of Fig. 7.12 was the same as Case 3 of Fig. 7.12 except the impact energy of the prestressing steel bar was reduced (the PC bar rupture length changed from 4.5 m to 3.0 m). Case 3 resulted in a significant asphalt pavement fracture around the impact and 77.6 mm of maximum PC bar protrusion. However, Case 4

resulted in minor cracks in the asphalt pavement around the impact and 16.8 mm of maximum PC bar protrusion as the PC bar impact energy was smaller than Case 3. The asphalt pavement systems simulated in Case 2 and 4 of Fig. 7.12 can cover 93% of vertically prestressing steel bars in MEX as 93% of vertically prestressing steel bars in MEX are less than 3.0 m in length.

Case 5 of Fig. 7.12 was the same as the AEM simulation shown in Fig. 4.29. However, 487 mm × 487 mm (5.9%) of waterproof membrane and tack coat delamination near the anchor were considered. In Case 5 the strength of the base layer and the cover layer was reduced by 30% and 50% respectively. Moreover, the impact energy of the prestressing steel bar was reduced (the PC bar rupture length changed from 4.5 m to 2.0 m). The AEM simulation in Case 5 resulted in minor cracks in the asphalt pavement around the impact and 12.1 mm of maximum PC bar protrusion as the PC bar impact energy was smaller. However, a significant tack coat delamination was observed. The asphalt pavement systems simulated in Case 5 of Fig. 7.12 can cover 56% of vertically prestressing steel bars in MEX as 56% of vertically prestressing steel bars in MEX are less than 2.0 m in length.

According to the AEM simulation results (shown in Fig. 7.12), decreasing the impact energy of the PC bar by reducing the PC bar rupture length produced a minor damage in the asphalt pavement and a small PC bar protrusion although several defects were considered in the asphalt pavement and in the interface bond martials.

b) AEM Simulation of Rupture of PC Bar with Two Layers of Asphalt Pavement at 0°C, 28°C and 50°C by Considering Strength Reduction in the Asphalt Pavement System

In this section, the effect of strength reduction of the asphalt pavement system and the effect of PC bar rupture length in the PC bar protrusion and damage in the asphalt pavement system were investigated using AEM simulation.

A verified AEM simulation (explained in section 4.4.2) was used to investigate the effect of strength reduction of the asphalt pavement system at 0°C in the failure mode and the effect of PC bar rupture length in the PC bar protrusion. Strength of the base layer, the cover layer, the waterproofing membrane and the tack coat in the verified AEM simulation (explained in section 4.4.2) was reduced by 20%. After considering 20% strength reduction in the asphalt pavement system, the PC bar was ruptured at 3.0 m, 3.5 m, 4.0 m and 4.5 m. The results of the AEM simulation are shown in Fig. 7.13. When the PC bar ruptured at 3.0 m, 3.5 m, 4.0 m and 4.5 m, the maximum PC bar protrusions were 20 mm, 33 mm, 49 mm and 98 mm respectively (Fig. 7.13a). When the PC bar ruptured at 3.0 m, 3.5 m and 4.0 m, minor cracks were observed in the asphalt pavement system as shown in Fig. 7.13b. However, when the PC bar ruptured at 4.5 m, the asphalt pavement system was severely fractured as shown in Fig. 7.13b.

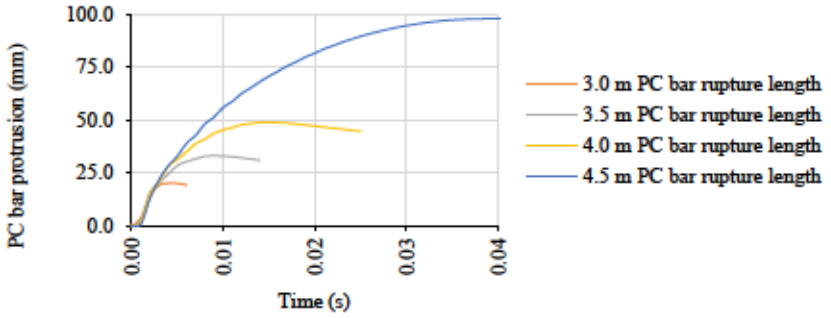

(a) The effect of PC bar rupture length in the PC bar protrusion

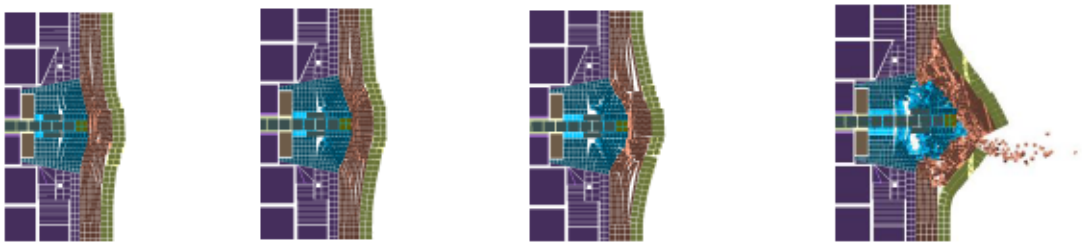

3.0 m PC bar rupture length 3.5 m PC bar rupture length 4.0 m PC bar rupture length 4.5 m PC bar rupture length

(b) The effect of PC bar rupture length in the failure mode

Fig. 7.13 The effect of PC bar rupture length in the PC bar protrusion and in the failure mode (AEM simulation of rupture of PC bar with asphalt pavement at 0°C by considering 20% strength reduction in the asphalt pavement system)

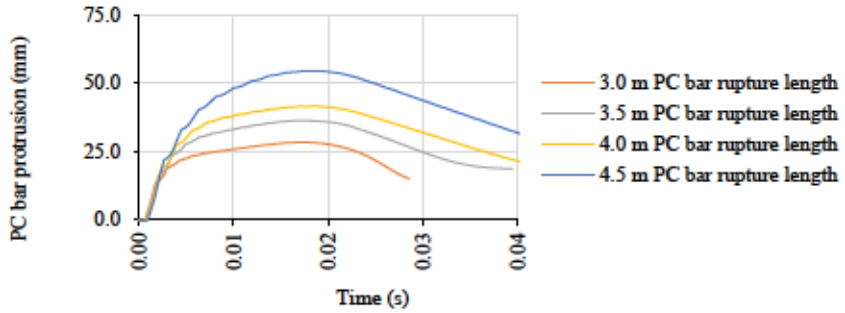

(a) The effect of PC bar rupture length in the PC bar protrusion

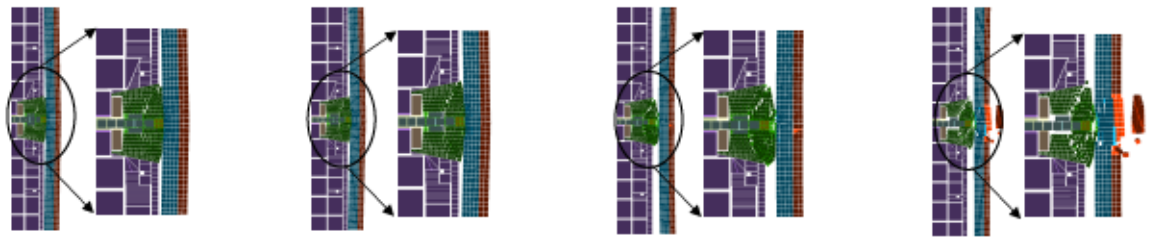

3.0 m PC bar rupture length 3.5 m PC bar rupture length 4.0 m PC bar rupture length 4.5 m PC bar rupture length

(b) The effect of PC bar rupture length in the failure mode

Fig. 7.14 The effect of PC bar rupture length in the PC bar protrusion and in the failure mode (AEM simulation of rupture of PC bar with asphalt pavement at 28°C by considering 20% strength reduction in the asphalt pavement system)

A verified AEM simulation (explained in section 4.2.2) was used to investigate the effect of strength reduction of the asphalt pavement system at 28°C in the failure mode and the effect of PC bar rupture length in the PC bar protrusion. Strength of the base layer, the cover layer, the waterproofing membrane and the tack coat in the verified AEM simulation (explained in section 4.2.2) was reduced by 20%. After considering 20% strength reduction in the asphalt pavement system, the PC bar was ruptured at 3.0 m, 3.5 m, 4.0 m and 4.5 m. The results of the AEM simulation are shown in Fig. 7.14. When the PC bar ruptured at 3.0 m, 3.5 m, 4.0 m and 4.5 m, the maximum PC bar protrusions were 28 mm, 36 mm, 41 mm and 54 mm respectively (Fig. 7.14a). When the PC bar ruptured at 3.0 m and 3.5 m no major damage was observed in the asphalt pavement system as shown in Fig. 7.14b. Impact energy of the PC bar was dissipated mainly by asphalt pavement deformation and delamination in the waterproofing membrane. However, when the PC bar ruptured at 4.0 m and 4.5 m the entire asphalt pavement system fell down as the waterproofing membrane was fully delaminated as shown in Fig. 7.14b.

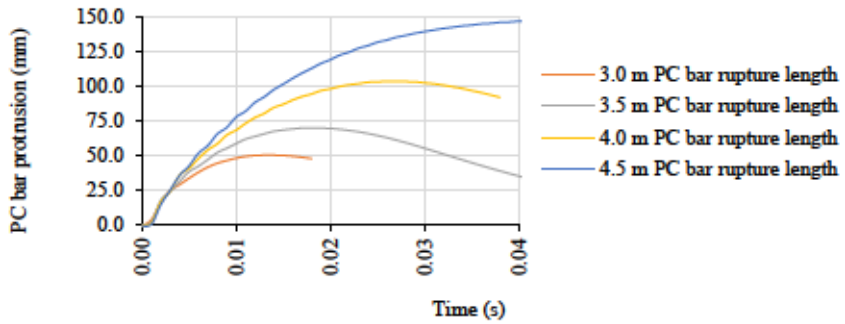

(a) The effect of PC bar rupture length in the PC bar protrusion

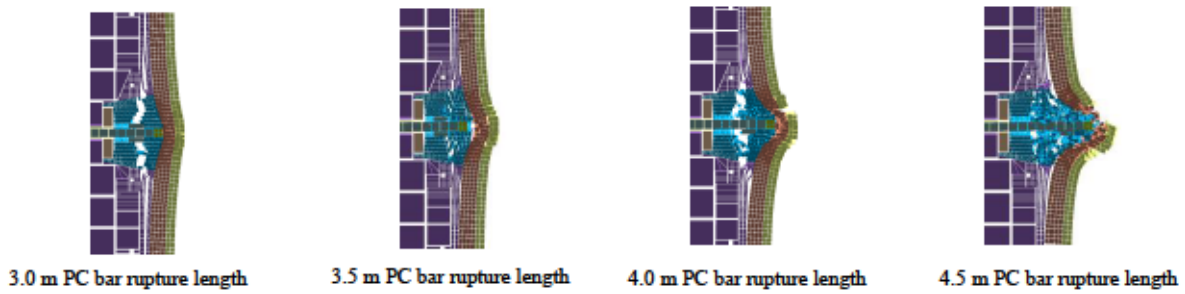

(b) The effect of PC bar rupture length in the failure mode

Fig. 7.15 The effect of PC bar rupture length in the PC bar protrusion and in the failure mode (AEM simulation of rupture of PC bar with asphalt pavement at 50°C by considering 20% strength reduction in the asphalt pavement system)

A verified AEM simulation (explained in section 4.3.2) was used to investigate the effect of strength reduction of the asphalt pavement system at 50°C in the failure mode and the effect of PC bar rupture length in the PC bar protrusion. Strength of the base layer, the cover layer, the waterproofing membrane and the tack coat in the verified AEM simulation (explained in section 4.3.2) was reduced by 20%. After considering 20% strength reduction in the asphalt pavement system, the PC bar was

ruptured at 3.0 m, 3.5 m, 4.0 m and 4.5 m. The results of the AEM simulation are shown in Fig. 7.15. When the PC bar ruptured at 3.0 m, 3.5 m, 4.0 m and 4.5 m, the maximum PC bar protrusions were 51 mm, 70 mm, 104 mm and 147 mm respectively (Fig. 7.15a). When the PC bar ruptured at 3.0 m and 3.5 m no major damage was observed in the asphalt pavement system as shown in Fig. 7.15b. The PC bar impact energy was dissipated mainly by deformation in the asphalt pavement and cracks in the concrete slab. However, when the PC bar ruptured at 4.5 m, the asphalt pavement system was severely fractured as shown in Fig. 7.15b.

7.5 Risk Reduction (Control) Interventions of Vertically Prestressing Steel Bar Protrusion

Performance of conventional asphalt pavement (using 50 mm thick dense graded base layer asphalt pavement + 30 mm thick porous cover layer asphalt pavement) was effective against 4,408 J (4.4 kN·m) impact energy at 0°C and 50°C as explained in chapter 4. Similarly, performance of two layers of asphalt pavement using 50 mm thick guss asphalt pavement base layer and 30 mm thick porous cover layer asphalt pavement was effective against 4,408 J (4.4 kN·m) impact energy at 28°C as explained in chapter 4. These asphalt pavements can be used as a countermeasure against PC bar protrusion for around 19,320 vertical PC bars (99.26%) in MEX. However, these asphalt pavements might not be effective against an impact energy of greater than 4,408 J (4.4 kN·m). For the remaining 144 vertical PC bars (0.74%), whose impact energies greater than 4,408 J (4.4 kN·m), a countermeasure which includes a conventional asphalt pavement (50 mm thick dense graded base layer asphalt pavement + 30 mm thick porous cover layer asphalt pavement), steel plate, aramid fiber and waterproofing sheet can be applied as shown in Fig. 7.16. This type of countermeasure was utilized by NEXCO central and it was effective against an impact energy of greater than 4,408 J (4.4 kN·m).

Those 144 vertical PC bars (0.74%), whose impact energies are greater than 4,408 J (4.4 kN·m), should be identified first before applying the countermeasure shown in Fig. 7.16. When a PC bar ruptured with this technique, the steel plate distributed the punching shear stress from the ruptured PC bar over a wider area and reduced localized failure. Aramid fiber and waterproofing sheet attached on a cover concrete surface with adhesive to prevent concrete spalling as they are good in tensile strength, stretch performance and energy absorption. However, this technique is not convenient for MEX as it takes a longer construction time. Reducing construction time of countermeasure is one of the criteria in this study as traffic volume in MEX is very harsh. Installation of the steel plate needs anchor drilling and more time is also needed for the adhesive material to cure.

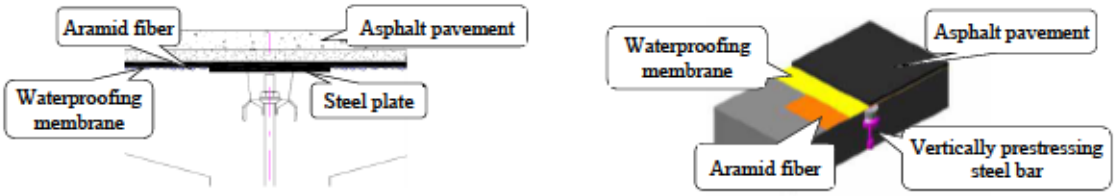

Fig. 7.16 Countermeasure using asphalt pavement, steel plate, aramid fiber and waterproofing sheet [2]

7.6 Summary of Chapter 7

Based on the results obtained in the present work, the following main summary and conclusions can be drawn:

- Basic information of vertical PC bars in Metropolitan Expressway (MEX) including the recent situations and onsite inspection of rupture of vertical PC bars were discussed briefly.
- Application of the AEM simulation in the preparation of a PC bar protrusion prevention guideline was discussed.
- The AEM simulation with two layers of asphalt pavement countermeasure at 0°C supported:
    - ❖ delamination of the waterproof membrane and the tack coat near the anchor had a significant effect in the PC bar protrusion and fracture in the asphalt pavement. A great attention should be paid during the application of the waterproof membrane and the tack coat at a location of a vertically prestressing bars in MEX.
    - ❖ the base layer asphalt pavement is the most important material in impact energy dissipation and its strength reduction shall not exceed 10%.
    - ❖ the cover layer asphalt pavement had a smaller contribution in impact energy dissipation than the base layer asphalt pavement. The asphalt pavement system was effective against PC bar protrusion even though the strength of the cover layer reduced by 50%.
    - ❖ reducing strength of the waterproofing membrane had a significant effect in asphalt pavement fracture and insignificant effect in the PC bar protrusion. Moreover, the waterproofing membrane strength reduction shall not exceed 10%.
    - ❖ the tack coat had a smaller contribution in impact energy dissipation than the waterproofing membrane. The asphalt pavement system was effective against PC bar protrusion even though the strength of the tack coat reduced by 50%.
    - ❖ decreasing the impact energy of the PC bar by reducing the PC bar rupture length produced a minor damage in the asphalt pavement and a small PC bar protrusion although several defects were considered in the asphalt pavement and in the interface bond martials.
- According to the AEM simulation, the asphalt pavement system developed in this study at 0°C, 28°C and 50°C with the PC bar rupture length of 3.5 m and with 20% strength reduction in the base layer, the cover layer, the water proofing membrane and the tack coat was effective against PC bar protrusion. The PC bar protrusion was small and the asphalt pavement damage was minor.
- Risk reduction (control) interventions of protrusion of vertical PC bars was also addressed.

References in Chapter 7:

[1] Bonger A.D, Hosoda A., Salem H., and Fukaya T., "Numerical simulation of rupture and protrusion of vertically tightened PC steel bars in PC girders with asphalt pavement using Applied Element Method," *Journal of Japan Society of Civil Engineers*, vol. 10, pp. 145–161, 2022.

[2] Central NEXCO (Central Nippon Expressway Company Ltd.), "Technical data on countermeasures for rupture of PC steel bar," 2009.

CHAPTER 8

CONCLUSIONS

8.1 General

The present research evaluated the performance of countermeasures against impact from corrosion induced ruptured vertical PC bars in PC bridges using AEM numerical simulation. The protrusion of a PC bar from a bridge can occur with no advance warning. This study evaluated the performance of countermeasures against eruption of PC bars to avoid damage to third party. The impact energies were applied on the countermeasures either using a ruptured PC bar or using a drop weight impact test. Performance of asphalt pavements was evaluated using extreme impact energy, 4,408 J, that could cover most of rupture of vertical PC bars in MEX. Performance of asphalt pavements was also evaluated by considering low and high temperatures to simulate winter and summer conditions in Tokyo area. The effect of time dependent deterioration of asphalt pavement by reducing the thickness of asphalt pavement was also investigated. Energy absorption capacity of polyurea and steel fiber reinforced polymer cement mortar (PCM) was investigated using a drop weight impact test. Methodology of the present research involved establishing the Applied Element Method (AEM) numerical simulation due to its advantages of simulating structural progressive collapse. The methodology followed three levelled systematic analysis schemes for AEM full scale simulation of performance evaluation of countermeasures. The AEM numerical simulations were verified with the experimental results. In the process of verification, many influential parameters, such as the effects of contact stiffness between separated elements, fracture energy of concrete and asphalt pavement, mesh sensitivity, time interval sensitivity, material properties, temperature effect, and strain rate effect were investigated. Failure modes in the countermeasures using the AEM simulations were investigated in detail. The numerical simulations developed in this study played a vital role in predicting experimental results. Based upon the experimental and analytical results, the following conclusions are summarized.

8.2 AEM Numerical Simulation of Rupture and Protrusion of Prestressing Steel Bars Without Considering Countermeasure

The effects of 15 mm cover concrete (assuming bottom of a bridge girder) on preventing protrusion of PC bars were investigated. Numerical simulation of rupture and protrusion of PC bars was conducted using the Applied Element Method. The numerical simulations were verified based on the experimental results. In the process of verification, many influential parameters, such as the effects of contact stiffness between elements, fracture energy of concrete, mesh sensitivity, time interval sensitivity, material properties, and strain rate effect, were investigated. The numerical simulation was required to investigate the protrusion behavior of PC bar and the failure mechanism of cover concrete. Based on experimental and numerical simulation using the AEM, the following conclusions were obtained:

- Appropriate numerical simulation with the AEM can be conducted with appropriate interface material property between the PC bar and the sheath, considering the fracture energy of concrete, with appropriate mesh discretization, appropriate time interval, appropriate Normal Contact Stiffness Factor (*NF*), and considering strain rate effects in concrete.
- Cover concrete of 15 mm alone could not prevent the protrusion of a PC bar of 4.5 m rupture length.

8.3 AEM Numerical Simulation of Rupture and Protrusion of Prestressing Steel Bars with Asphalt Pavement Considering the Effect of Temperature

A 3D AEM model was developed for simulating asphalt pavement at 0°C, 28°C and 50°C under extreme impact energy (4,408 J) generated from a corrosion induced ruptured vertically tightened PC bars in PC bridges. The asphalt pavement material models were calibrated using asphalt pavement bending test results. The bending properties of asphalt pavement at different temperature were numerically investigated. The interface bond material model was calibrated based on the pull-off adhesive test. The effects of temperature on asphalt pavement system on preventing the protrusion of PC bars and concrete spalling were numerically investigated. The *DIF* was employed to accurately capture the dynamic material behavior of the asphalt pavement under high loading rate. The failure mode of the asphalt pavement under 4,408 J impact energy was numerically investigated in detail. In MEX, the asphalt pavement over bridge deck has two layers. In this study, in order to simulate the worst condition in reality (time dependent deterioration), in one specimen, the cover layer was excluded and only the base layer (50 mm thickness) was investigated in terms of its performance in preventing the protrusion PC bars with 4,408 J impact energy at 20°C. The AEM simulation results support the following conclusions:

- Appropriate numerical simulation with the AEM can be conducted with appropriate interface material property between the slab concrete and the asphalt pavement layers, considering the fracture energy of concrete and asphalt pavement, with appropriate mesh discretization, appropriate time interval, appropriate Normal Contact Stiffness Factor (*NF*), and considering strain rate effects both in concrete and in asphalt pavement.
- The asphalt pavement system used in this study, without using a steel plate and FRP sheet, with appropriate material and thickness could prevent the protrusion of the PC bar of 4.5 m rupture length. The AEM simulation results proved that the two layers of asphalt pavement with 80 mm thick at 0°C, 28°C and 50°C was effective against 4,408 J impact energy and effective against PC bar protrusion and concrete spalling. Moreover, a single layer of guss asphalt pavement with 50 mm thick at 20°C was effective against PC bar protrusion which was around 22 mm in the AEM simulation. However, asphalt pavement fracture was observed near the anchorage area.

- Based on the analysis results, the effectiveness of the asphalt pavement system depends on impact energy of ruptured PC bars, material properties of asphalt pavements, material properties of interface bond materials, fracture energy, mesh discretization, strain rate and temperature.
- In the two layers of asphalt pavement system at 28°C, the PC bar protrusion was prevented by ductile deformation of asphalt pavement delaminated from slab concrete. The strain energy of the PC bar was dissipated by a simultaneous action of asphalt pavement deformation, cone-shaped crack in the mortar, and interface delamination between the slab concrete and the asphalt pavement.
- In the two layers of asphalt pavement system at 50°C, the strain energy of the PC bar (4,408 J) was dissipated by a synchronized action of a shear-cone shaped fracture in the concrete and in the non-shrinking mortar, deformation and cracks in the asphalt pavement.
- In the two layers of asphalt pavement system at 0°C, the strain energy of the PC bar (4,408 J) was dissipated by a synchronized action of a shear-cone shaped fracture in the base layer and in the non-shrinking mortar, deformation and cracks in the asphalt pavement and delamination of tack coat.
- In the single layer (50 mm tick) of guss asphalt pavement system at 20°C, the strain energy of the PC bar (4,408 J) was dissipated by a simultaneous action of a shear-cone shaped fracture in the asphalt pavement and in the non-shrinking mortar, interface bond delamination between the concrete slab and the asphalt pavement, and cracks in the asphalt pavement.
- The results of the numerical simulation had a good agreement with the experimental data.

8.4 AEM Numerical Simulation of Dynamic Punching Test of Polyurea Sheet

Punching tests for polyurea sheet with thickness of 3 mm, 5 mm and 10 mm under different impact loads were investigated. This study numerically investigates the effects of polyurea coating on impact resistance and on preventing concrete spalling. The results obtained are used to assess the extent of energy absorption and to identify the mode of failure of the polyurea as a function of the imposed impact conditions. The numerical simulations were verified with the experiments. Based on the results obtained in the present work, the following main conclusions can be drawn:

- Both numerical simulations and high-speed photography measurements indicated that the polyurea sheet significantly reduced impulsive loads.
- Effectiveness of the polyurea sheet depends on impact energy, polyurea thickness, bond strength, primer and quality of surface concrete, etc.
- The constitutive model using a bi-linear material for polyurea in the drop weight AEM simulation showed good agreement with the experimental results in terms of impact resistance and failure mode.

- A polyurea (500 mm × 500 mm) sheet with 5 mm thickness was effective in resisting against 758 J impact energy. However, 3 mm and 10 mm thick polyurea sheets with 500 mm × 500 mm were not effective in resisting against 758 J and 3,983 J impact energy respectively.

8.5 Drop Weight Impact Test of Steel Fiber Reinforced PCM for Investigating Energy Absorption Capacity

The impact resistance of a steel fiber reinforced polymer cement mortar (PCM) against drop weight impact were investigated numerically and experimentally. Effectiveness of the PCM depended on impact energy, depth of core, and material properties of the PCM. Based on the results obtained in the present work, the following main summary and conclusions can be drawn:

- The effect of PCM on impact resistance were investigated numerically and experimentally.
- The modeling of PCM in the drop weight AEM simulation showed good agreement with the experimental results in terms failure mode.
- The drop weight impact energy was dissipated by damages in the PCM, deflection of boundary and strain in the reinforcing bars.
- Both numerical simulations and high-speed photography indicated that the drop weight impact test were significantly affected by boundary conditions.
- The proposed boundary condition in this study greatly reduced deflection at the boundary and hence eliminate the energy absorbed by flexure.

8.6 Risk Management of Protrusion of Vertically Prestressing Steel Bars in MEX

- Basic information of vertical PC bars in Metropolitan Expressway (MEX) including the recent situations and onsite inspection of rupture of vertical PC bars were discussed briefly.
- Application of the AEM simulation in the preparation of a PC bar protrusion prevention guideline was discussed.
- The AEM simulation with two layers of asphalt pavement countermeasure at 0°C supported:
    - ❖ delamination of the waterproof membrane and the tack coat near the anchor had a significant effect in the PC bar protrusion and fracture in the asphalt pavement. A great attention should be paid during the application of the waterproof membrane and the tack coat at a location of a vertically prestressing bars in MEX.
    - ❖ the base layer asphalt pavement is the most important material in impact energy dissipation and its strength reduction shall not exceed 10%.
    - ❖ the cover layer asphalt pavement had a smaller contribution in impact energy dissipation than the base layer asphalt pavement. The asphalt pavement system was

effective against PC bar protrusion even though the strength of the cover layer reduced by 50%.

- ❖ reducing strength of the waterproofing membrane had a significant effect in asphalt pavement fracture and insignificant effect in the PC bar protrusion. Moreover, the waterproofing membrane strength reduction shall not exceed 10%.
- ❖ the tack coat had a smaller contribution in impact energy dissipation than the waterproofing membrane. The asphalt pavement system was effective against PC bar protrusion even though the strength of the tack coat reduced by 50%.
- ❖ decreasing the impact energy of the PC bar by reducing the PC bar rupture length produced a minor damage in the asphalt pavement and a small PC bar protrusion although several defects were considered in the asphalt pavement and in the interface bond martials.

- According to the AEM simulation, the asphalt pavement system developed in this study at 0°C, 28°C and 50°C with the PC bar rupture length of 3.5 m and with 20% strength reduction in the base layer, the cover layer, the water proofing membrane and the tack coat was effective against PC bar protrusion. The PC bar protrusion was small and the asphalt pavement damage was minor.
- Risk reduction (control) interventions of protrusion of vertical PC bars was also addressed.

8.7 Future Tasks

When a vertically prestressing steel bar ruptured, one piece erupts upward and the other piece erupts under a bridge girder. The countermeasures investigated in this study were effective against PC bar protrusion on the top of a bridge girder. However, performance evaluation of countermeasures against PC bar protrusion on the bottom of a bridge girder are equally important. Performance evaluation of type A FRP sheet and polyurea sheet simulating the bottom of a bridge girder were carried out. However, they were not effective against 4,408 J impact energy. Therefore, the systematic AEM simulation procedure established in the present study should include performance evaluation of countermeasures simulating the bottom of a bridge girder.

Further, utilizing the established AEM models, the energy absorption capacity of steel fiber reinforced polymer cement mortar (PCM) will be investigated by considering the effect of temperature.

Finally, the obtained knowledge will contribute to improve a guideline for prevention of protrusion of vertically prestressing steel bars in MEX. Ultimately, the expressway will be safe for traffic.